Development and surface modification of β-Titanium alloys produced by powder metallurgy for biomedical applications

by

Caterina Chirico Rodríguez

A dissertation submitted by in partial fulfillment of the
requirements for the degree of Doctor of Philosophy in

Materials Science and Engineering

Universidad Carlos III de Madrid

Advisor(s):

Elena Gordo Oderiz
Sophia Alexandra Tsipas

Tutor:

Sophia Alexandra Tsipas

July, 2021

A mis padres,
Mario y María Elena.

PREFACE

This PhD Thesis has been carried out at the Group of Powder Technology (GTP), belonging to the Department of Materials Science and Engineering and Chemical Engineering of the University Carlos III of Madrid (UC3M). This research has been carried out in the frame of the BIOHYB project (Ref. PCIN-2016-123), from the M.Era-Net 2015, in collaboration with University of Minho (Portugal) and University Estadual Paulista "Julio de Mesquita Filho" and University of Sao Paulo (Brazil).

Part of this Thesis has been performed in collaboration with different institutions through two research stays: at the Trento University (Italy), under the supervision of Prof. Alberto Molinari (3 months) with the financial support of the Institute of Chemistry and Materials Alvaro Alonso Barba (IAAB); and at the Estadual Paulista of Sao Paulo University (Brazil), under the supervision of Prof. Carlos Roberto Grandini (2 months), financed by the grant of the Iberoamerican Program of Santander Bank in Spain.

This Doctoral Thesis complies with the requirements for its mention as an International PhD that has been established in article 15 of the Real Decreto 99/2011 en la Ordenación de la Enseñanza Universitaria Oficial (B.O.E N° 35 of January 28, 2011, pp. 13909-13926) as is described in the Rules and Regulations for PhD studies at Universidad Carlos III de Madrid.

ACKNOWLEDGEMENTS

Una Tesis doctoral se resume, si así se puede decir, en un documento, en este documento, cuya sombra es más alargada de lo que a priori pudiera parecer. Sin embargo, las sombras no siempre son oscuras. En ocasiones albergan espacios de paz y tranquilidad al lado de personas que engrandecen cualquier experiencia vital. Sin ellas, sin su proximidad, su cercanía, su apoyo, su colaboración o su comprensión no hubiera concluido esta tarea que me propuse realizar hace varios años. No obstante, pese a la importancia de su contribución en este trabajo, me veo en la obligación de resumir, una vez más, las merecidas muestras de afecto que no me cansaría de repetir.

Un lugar primordial lo ocupan mis directoras de tesis, Elena Gordo y Sophia Tsipas. Juntas me han guiado con tenacidad, confianza y libertad en el continuo aprendizaje profesional y personal que requiere este proceso. Muchas gracias a las dos por el tiempo que hemos compartido, que va más allá de esta tesis.

También me gustaría agradecer este trabajo al Departamento de Ciencia e Ingeniería de Materiales de la Universidad Carlos III de Madrid. A los técnicos del Departamento: Juan Carlos, Luis y Cristina por su disposición a colaborar conmigo en todo momento. Muchas gracias, Cris, por esos ratos tan amenos que pasamos en el SEM, encontrando, entre otras muchas cosas, las "pinceladas" de este cuadro.

A los integrantes del Grupo de investigación de Tecnología de Polvos (GTP), José Manuel, Maru, Juan, Sandra, Elisa, Toñi, Mónica, Paula A., Tamara, Eva y Christian por ayudarme y hacer más llevadero este camino. Ha sido un placer compartir este tiempo con ustedes.

Gracias a los miembros del proyecto BIOHYB, Prof. Fatih Toptan, Alexandra Alves, Rodrigo Cardoso, Luis Rocha, Carlos Grandini e Ihsan Çaha por su colaboración y contribución en este trabajo.

Quiero agradecer al Departamento de Ingeniería Industrial de la Università di Trento y al Laboratorio de Anelasticidad y Biomateriales de la Universidade Estadual Paulista "Julio de Mesquita Filho" de Sao Paulo, por abrirme sus puertas para realizar mis estancias doctorales.

Ringrazio il Prof. Alberto Molinari, per tutto il suo aiuto e la collaborazione, per le sue parole di sostegno e per avermi guidato, sempre con un sorriso, durante questa esperienza. É stato un vero piacere poter lavorare con te. Ringrazio il Prof. Matteo Benedetti, per il suo aiuto con le prove di fatica. Alle tecniche Lorena Maines e Lorena per la costante disponibilità. Grazie anche a Marco, Daniele, Michelangelo e Silvia per la vostra amicizia nei giorni a Trento.

Agradeço ao Prof. Carlos Roberto Gandini por sua grande disposição em me ajudar e por me tratar como integrante de sua equipe durante todo este tempo. Agradeço também ao Prof. José Humberto Dias da Silva, ao Prof. Luís Augusto Sousa Marques da Rocha e aos colegas Lucas Affonco, Caio, Thiago, Pedro e Williams por toda ajuda e por facilitarem minha vivência no laboratório. Agradeço a Mariana e a Fernanda pelos momentos compartilhados, muito obrigada por fazerem me sentir em casa. Obrigada a todos pela hospitalidade e gentileza. Prazer em conhecê-los.

Hay personas cuya presencia no se mide en magnitudes físicas, pero su órbita es duradera e inagotable. La Dra. Begoña Ferrari despertó en mí el interés por la investigación, creyó en mí, en mi trabajo y me inculcó la determinación y el valor necesarios para afrontar nuevos retos. Bego, mi agradecimiento es infinito, gracias por todo tu apoyo.

Cuando se empieza un nuevo trabajo siempre hay algo de emoción e intriga. Hay numerosas expectativas que se aclaran cuando avanza el tiempo. Los compañeros son una de esas piezas y los míos han pasado de ser solamente compañeros para ser grandes AMIGOS. Eric me has ayudado siempre que lo he necesitado, a mí y a todos nosotros. Siempre lo has hecho con una sonrisa sincera que ejemplifica parte de tu inmensa amabilidad; te echo de menos Super Maci. Alberto, (Tru), tienes el don de ser fastidioso incluso a distancia y la magia de hacer sonreír eternamente, gracias por todo Tru. Con María de Nicolás ha crecido una amistad sincera al cobijo de un horno que perdurará al vacío o sin él. Sin Alberto y sin María la última etapa de la tesis se hubiera convertido en una historia interminable. Mi queridísimo Edu, por primera vez las palabras se me quedan cortas contigo. Sabes que sin ti este doctorado no hubiera sido el mismo; me has escuchado hasta el infinito, con una paciencia sobrehumana, me has enseñado a quitarme una pila, a veces hasta dos, cuando estaba a punto de saltar por los aires. Natalia, (Niiits), eres como una hermana para mí. Gracias por acogerme, por tu cariño, por tu amistad verdadera, gracias por todo mi Niiits. Queen me has traído calma y claridad frente a tempestades ingobernables; eres lo mejor de la realeza. Amaya, sencillamente eres maravillosa. Me has ayudado más de lo que te imaginas. Second, tu me has acompañado en los laboratorios y fuera de ellos; para serte sincera, ha sido un placer trabajar contigo. Andrea pH, tu sonrisa ha estado muy presente en todo este camino; me recibiste con ella y me has sacado muchas más con tu empane característico. Gracias también a Gleidys, Nieves, María F., Marquiños, Andrea G., Betty, Reverte por ser tan buenos compañeros. Sin duda, todos ustedes son la mejor parte de este trabajo. Son una razón para mirar atrás con admiración, cariño y entusiasmo. Son una razón para mirar hacia adelante con más certezas de las que traje cuando vine a España.

Dicen que la familia te toca y los amigos se escogen. Sin embargo, la vida me ha regalado una familia que he tenido el privilegio de escoger. Adrianna, Vanessa, Gaby, Kala, Melissa y Emil son algo más que compañeros de viaje. Las circunstancias, así como las experiencias a un y otro lado del océano, han forjado una unión que trasciende la palabra amistad. Las tesis doctorales, por muchas horas de dedicación que requieran, se acompañan de gente especial con la que compartir otras vivencias. Se acompañan de gente que te apoya, te escucha, se ríe, llora, se lamenta y te motiva. He sentido nuestra mano junto a la mía siempre que lo he necesitado. Me siento afortunada por tenerlos en mi vida.

Este viaje ha sido largo. La distancia me ha separado de los míos, aunque emocionalmente están todos a mi lado. Mis padres, Mario y María Elena, me han entregado incondicionalmente su apoyo. Desde el cariño y la disciplina me han dado la fuerza y los ánimos para afrontar las circunstancias con las que me he encontrado. Con ustedes he aprendido que la perseverancia te ayuda a no rendirte. Los dos, Mario y María Elena, me han hecho ser quien soy y me enorgullezco de llevar algo de ustedes conmigo. Sin embargo, hay ausencias que no terminan nunca. Papi, sé que disfrutarías compartiendo este momento conmigo. Confiaré en que desde lejos me observas y celebramos juntos.

Quiero agradecer a mi hermana Diocemar todo lo que se ha preocupado por mí. He notado tu compañía en situaciones complicadas que me has ayudado a sobrellevar. Gracias a mis primas Diocelis, Beberling y Gabriela, a las que podría llamar casi hermanas. Siempre he tenido su comprensión y apoyo en todo lo que hacía. El cariño de mis tías Milagros y Mayibe ha sido fundamental para mí. Y mis sobrinos, Danyelis, Eileen, Ariana, Miguel, Anto y Andrés, los más pequeños de la casa, todos ellos han sido parte de mi inspiración para mirar hacia adelante, para ser valiente, para demostrarme a mí misma que vale la pena embarcarse en los esfuerzos en los que se cree. Para mí sería un sueño poder devolver en algún momento toda esa inspiración que me dieron.

Por último, te agradezco a ti Fernando. Gracias por acompañarme y recorrer este camino de mi mano. Gracias por ser mi pañuelo, mi amigo, mi compañero. Gracias por tu ayuda, por todo el cariño que me das, por tu paciencia y comprensión en los momentos difíciles y por todos los momentos maravillosos que me has regalado.

A todos ustedes GRACIAS.

PUBLISHED AND SUBMITTED CONTENT

Publications from the doctoral thesis:

1. C. Chirico, S. Tsipas, F. Toptan, E. Gordo. Development of Ti–Nb and Ti–Nb–Fe beta alloys from TiH_2 powders. *Powder Metallurgy*, 2019, Volume 62, (1), p. 44-53. DOI: 10.1080/00325899.2018.1563953.

   The information of this paper is partly reported in Chapter 5. I participate in all the experimental part as well as the writing of the paper itself.
   This is an invited paper after being awarded with Keynote Award in the EuroPM2018 conference.

---

2. C. Chirico, S. Tsipas, P. Wilczynski, E. Gordo. Beta Titanium Alloys Produced from Titanium Hydride: Effect of Alloying Elements on Titanium Hydride Decomposition. *Metals*, 2020, Volume 10, (682). DOI: 10.3390/met10050682.

   The information of this paper is reported in Chapter 4. I participate in all the experimental part as well as the writing of the paper itself.

---

3. C. Chirico, S. Tsipas, A-Vaz-Romero, E. Gordo. Improvement of wear resistance of low-cost powder metallurgy β-Ti alloys. **To be submitted.**

   The information of this paper is reported in Chapter 6. I participate in all the experimental part as well as the writing of the paper itself.

Publications from BIOHYB collaboration:

1. I. Çaha, A.C. Alves, C. Chirico, S.A. Tsipas, I.R. Rodrigues, A.M.P. Pinto, C.R. Grandini, L.A. Rocha, E. Gordo, F. Toptan. Interactions between wear and corrosion on cast and sintered Ti-12Nb alloy in comparison with the commercial Ti-6Al-4V alloy, *Corrosion Science*, 2020, Volume 176, 108925. DOI: 10.1016/j.corsci.2020.108925.

---

2. I. Çaha, A.C. Alves, C. Chirico, A.M.P. Pinto, S.A. Tsipas, E. Gordo, F. Toptan. Corrosion and Tribocorrosion Behavior of Ti-40Nb and Ti-25Nb-5Fe Alloys Processed by Powder Metallurgy. *Metall Mater Trans A*, 2020, Volume 51, p. 3256–3267. DOI: 10.1007/s11661-020-05757-6.

---

3. I. Çaha, A.C. Alves, C. Chirico, A.M.P. Pinto, S.A. Tsipas, E. Gordo, F. Toptan. A promising method to develop TiO_2-based nanotubular surfaces on Ti-40Nb alloy with enhanced adhesion and improved tribocorrosion resistance, *Applied Surface Science*, 2021, Volume 542, 148658. DOI: 10.1016/j.apsusc.2020.148658.

National and International Conferences related to the doctoral Thesis:

1.

Author: C. Chirico, S. Tsipas, E. Gordo

Title: Effects of alloying element particle size on low cost β-Titanium alloys produced by powder metallurgy.

Communication type: Oral

Congress: Congreso Nacional de Materiales. Salamanca, Spain (4-6 July 2018)

2.

Author: C. Chirico, S. Tsipas, F. Toptan, E. Gordo

Title: Development of Ti-Nb and Ti-Nb-Fe beta alloys from TiH_2 powders.

Communication type: Oral (Keynote Paper Award)

Congress: EUROPM 2018. Bilbao, Spain (14-18 October 2018)

3.

Author: C. Chirico, S. Tsipas, A. Vaz-Romero, E. Gordo

Title: Study of TiB_2 and TiN reinforcement addition in beta titanium alloys processed by powder metallurgy

Communication type: Oral

Congress: VII Congreso Español de Pulvimetalurgia - II Congreso Iberoamericano de Pulvimetalurgia. Madrid, Spain (24-26 June 2019)

4.

Author: C. Chirico, S. Tsipas, A. Vaz-Romero, E. Gordo

Title: Development of TiB_2 and TiN reinforced beta titanium alloys produced by powder metallurgy route.

Communication type: Oral

Congress: EUROPM2019. Maastricht, Netherland (13-16 October 2019)

5.

Author: C. Chirico, S. Tsipas, E. Gordo

Title: Strategies for improving wear behaviour of powder metallurgy β-Ti alloys.

Communication type: Oral

Congress: EuroPM2020 Online (17-20 October 2020)

CONTENTS

CHAPTER 4: Study of titanium hydride decomposition 87

ABSTRACT

Titanium and its alloys have been widely used in biomedical applications. Ti-6Al-4V and Ti-6Al-7Nb are the most employed Ti alloys for dental and orthopaedic implants. Ti alloys are preferred over stainless steel and CrCo alloys due to their distinctive properties such as low density, high specific resistance, high corrosion resistance, especially in contact with human fluids and tissues, and biocompatibility. Despite their excellent properties, orthopaedic hip implants have three main issues, due to the alloy properties that compromise their durability.

Firstly, the currently used Ti alloys have higher elastic modulus values than the bone. The mismatch between the elastic moduli of the bone (10-30 GPa) and Ti alloys (100-110 GPa) produces the stress-shielding phenomenon. In the long term, stress-shielding produces bone resorption, which causes implant loosening. Secondly, due to the low wear resistance of Ti alloys, metal ions and wear particles are released, which could have harmful local and systemic effects, and cause cell tissue damage. Finally, the lack of bioactivity of Ti limits the bone growth around the implant, affecting the bonding between both surfaces (bone and implant), until its loosening. All these problems cause the premature failure of hip implants, increasing the revision surgeries rate, since the prosthesis must be replaced earlier than expected. Therefore, suitable Ti alloys for orthopaedic applications must exhibit low elastic modulus, high wear resistance, and high bioactivity, to prevent the occurrence of these problems.

This thesis attempts to cover the previous problems, pursuing the following goal: development of biocompatible and low modulus β-Ti alloys with improved wear resistance and a biofunctionalised surface to improve the interaction between the implant surface and bone tissue.

β-Ti alloys were processed using Nb and Fe as alloying elements and TiH_2 as Ti source. Both Fe and Nb are non-toxic and biocompatible β-stabiliser elements. Ti-Nb alloys have gained attention to produce biomedical Ti alloys, because they exhibit a lower elastic modulus. Fe alloying element reduces the Nb content necessary, and therefore the alloy cost, maintaining the β-Ti phase. Moreover, it has been reported that small Fe additions improve the Ti sinterability and mechanical properties. TiH_2 is cheaper than CP-Ti, and it offers higher sinterability than elemental Ti and provides an inert atmosphere during its decomposition, which protects the particle surface during the consolidation, preventing contamination issues. Therefore, TiH_2 is an attractive candidate to produce Ti-based components, while maintaining mechanical properties and reducing the processing costs. The design and development of these β-Ti alloys are described in detail in Chapter 4 and Chapter 5.

The success of TiH_2 use as a Ti substitute, highly depends on the dehydrogenation process, that is, how hydrogen is released when the sample is heated. Hence, this thesis includes a detailed study about the dehydrogenation process and how alloying elements (Nb and Fe) influence this process, considering the effect that they have, when they are incorporated individually and in a combination form. From this study, relevant principles were established to define the appropriate consolidation conditions that promote a controlled and complete transformation from TiH_2 to Ti. The details of this study are included in Chapter 4.

Wear resistance was improved following two strategies described in Chapter 6: (1) by developing Ti composite materials, incorporating TiB_2 and TiN particles as ceramic reinforcements, and (2) by promoting the formation of TiN coatings obtained by nitriding treatments. Finally, surface modification was performed by micro-arc oxidation treatments, obtaining a porous layer of titanium oxide on the sample surface, which is enriched with bioactive elements (Ca and P) and antibacterial agents (ZnO) that enhance the cellular response, improve osseointegration, and prevent the bacteria proliferation. This study is included in Chapter 7.

Processed samples were evaluated based on their microstructural features and mechanical properties (hardness, elastic modulus, fatigue behaviour), as well aswear resistance. Furthermore, the biocompatibility of the base alloys was studied, confirming the viability of these substrates for biomedical applications.

The main results obtained establish that the low-cost β-Ti alloys developed in this work are suitable candidates for biomedical applications. They show reduced elastic modulus values and improved wear resistance. Regarding biofunctionalised surfaces, samples presented a multiscale porous structure and a high Ca/P ratio. These are promising features to promote osseointegration and mimic the implant with the bone tissue.

RESUMEN

El titanio y sus aleaciones son materiales ampliamente utilizados en aplicaciones biomédicas. Entre estas aleaciones destacan el Ti-6Al-4V y Ti-6Al-7Nb que componen la mayoría de implantes dentales y ortopédicos. El principal motivo para el uso de estos materiales frente al acero inoxidable y aleaciones CrCo responde a su combinación de propiedades, tales como baja densidad, alta resistencia específica, alta resistencia a la corrosión, especialmente en contacto con fluidos y tejidos corporales, y biocompatibilidad. Pese a sus buenas propiedades, los implantes ortopédicos de cadera presentan tres problemas principales relacionados con las propiedades del material, que comprometen la durabilidad del implante.

Primero, las aleaciones de titanio más utilizadas presentan un elevado módulo de elasticidad en comparación con el hueso. La diferencia entre el módulo elástico del hueso (10-30 GPa) y el módulo elástico de las aleaciones de Ti (100-110 GPa) provoca el fenómeno conocido como "stress-shielding". A largo plazo, el stress-shielding produce la resorción ósea, que desencadena en el aflojamiento y pérdida del implante. Segundo, debido a la baja resistencia a desgaste de las aleaciones de Ti se liberan iones metálicos y partículas de desgaste que podrían causar efectos locales, sistémicos y daños en el tejido celular. Por último, la falta de bioactividad del Ti impide el crecimiento óseo alrededor del implante, perjudicando la unión entre ambas superficies (hueso-implante). Esto podría afectar a la fijación del implante hasta producir su desprendimiento.

Los problemas enumerados anteriormente están asociados al fallo prematuro de los implantes de cadera. A causa de ellos aumenta la tasa de cirugías de revisión y las prótesis deben ser reemplazadas antes de lo esperado. En consecuencia, con objeto de evitar su aparición, las aleaciones de Ti apropiadas para aplicaciones ortopédicas deben presentar bajo módulo elástico, alta resistencia al desgaste y alta bioactividad.

Esta tesis aborda la problemática anterior persiguiendo el siguiente objetivo: el desarrollo de aleaciones β-Ti de bajo módulo elástico, biocompatibles, con una resistencia al desgaste mejorada y una superficie biofuncionalizada a fin de mejorar la interacción entre la superficie del implante y el tejido óseo.

Las aleaciones β-Ti se procesaron utilizando Nb y Fe como elementos de la aleación y TiH_2 como fuente de Ti. El Fe y el Nb son elementos estabilizadores de la fase β, no tóxicos y biocompatibles. El uso de Nb en el desarrollo de aleaciones biomédicas de Ti es de gran interés debido a la significativa reducción del módulo elástico reportado en las aleaciones Ti-Nb. El Fe, por su parte, aporta interesantes ventajas: permite disminuir el contenido de Nb, manteniendo la microestructura constituida por fase β-Ti; reduce el coste total de la aleación, al reducir el contenido de Nb; y mejora la sinterabilidad del Ti y las propiedades

mecánicas. El TiH_2 es más barato que el Ti. Presenta mayor sinterabilidad que el Ti elemental y provee una atmósfera inerte durante su descomposición que protege la superficie de las partículas, reduciendo la contaminación de la pieza. Por ello, se considera un candidato atractivo para producir componentes base Ti manteniendo sus propiedades mecánicas y reduciendo los costes de procesamiento. El diseño y desarrollo de estas aleaciones de β-Ti se describe en detalle en el Capítulo 4 y Capítulo 5.

El proceso de deshidrogenación, es decir, cómo se libera el hidrógeno a medida que se caliente la muestra, determina, en gran medida, el éxito para sustituir el Ti por TiH_2. Por ello, esta tesis incluye un estudio detallado sobre el proceso de deshidrogenación, así como la influencia de los elementos de aleación (Nb y Fe) en este proceso, evaluando su efecto al añadirse de forma individual y combinada/conjunta. Como resultado de este estudio surgieron consideraciones relevantes, empleadas para definir las condiciones más adecuadas de consolidación de las muestras, a fin de promover una transformación controlada y completa de TiH_2 a Ti. Los detalles de este estudio se presentan en el Capítulo 4.

Para la mejora de la resistencia al desgaste de las aleaciones β se proponen dos estrategias, descritas en el Capítulo 6: (1) desarrollar materiales compuestos incorporando partículas de TiB_2 y TiN como refuerzos cerámicos; (2) producir recubrimientos de TiN mediante tratamientos de nitrurado. Finalmente, se modifica la superficie del material mediante tratamientos de *"micro-arc oxidation* (anodizado). Con este tratamiento se obtiene una capa porosa de óxido de titanio enriquecida con elementos bioactivos (Ca y P) y agentes antibacterianos (ZnO) que potencian la respuesta celular, mejoran la osteointegración y evitan/reducen la proliferación de bacterias. Este estudio se desarrolla en el Capítulo 7.

Las muestras procesadas con las premisas anteriores se evaluaron en función de sus características microestructurales, propiedades mecánicas (dureza, módulo de elasticidad, comportamiento a fatiga), y resistencia a desgaste. Además, se estudió la biocompatibilidad de las aleaciones base que confirma la viabilidad de estos sustratos en aplicaciones biomédicas.

Los resultados principales indican que las aleaciones β-Ti de bajo coste, producidas y modificadas en este trabajo son adecuadas para aplicaciones biomédicas: presentan valores de módulo elástico reducidos y mejor resistencia al desgaste. Los resultados obtenidos en las superficies biofuncionalizadas son prometedores ya que las muestras exhiben una estructura porosa multiescala y una alta relación Ca/P, útiles para mimetizar el implante con el tejido óseo y favorecer la osteointegración.

CHAPTER 1

Introduction

CHAPTER 1

1.1. Biomaterials for orthopaedic applications.

Biomaterials, whether of synthetic or natural origin, are defined as "materials that interact with biological systems to evaluate, treat, reinforce or replace any tissue, organ or function of the body" [1]. They are used in a wide range of applications, from contact lenses, heart valves, blood vessel prosthesis, cochlear implants, skin repair devices, dental and orthopaedic implants, etc. Since they are in intimate contact with living tissues, the main requirement of biomaterials is that they must be biocompatible as do not induce harmful effects to the host.

According to their chemical nature, biomaterials can be classified into four main groups: metals, ceramics, polymers and composites [2]. **Table 1.1** lists the main properties and common causes of failure of the different materials employed for orthopaedic implants. In the orthopaedic field, above 80% of load-bearing implants are metallic since their properties outperform ceramic and polymer implant properties [3]. Polymer bearings reduce the coefficient of friction in the joint, but exhibit a high wear rate, producing osteolysis and then aseptic implant loosening. Ceramic components reduce the wear rate due to their high hardness, but this also makes them brittle, so they present failure by fracture of the ceramic femoral head. [4]

Table 1.1. Features of different materials groups employed in orthopaedic implants. Adapted from [5]

Material group	Common materials	Properties	Failure	Cause of failure
Biometals	Stainless steel Cobalt-chrome Ti and Ti alloys	High mechanical properties, low elastic modulus, low density.	Adverse reaction due to corrosion.	Release of allergic substances and high elastic modulus.
Bioceramics	Alumina Zirconia	High biocompatibility, compression strength.	Low fracture toughness.	High elastic modulus compared to bone.
Biopolymers	PTFE UHMWPE PEEK	Appropriate primary fixation.	Inflammation and degradation of implants.	Releases monomers in the body.

Hip implant design, employed materials, and the combination of these have continuously evolved over the years, looking to find a balance between biocompatibility and good mechanical properties such as fatigue resistance, stiffness, and roughness, in order to guarantee hip replacement surgery success in the long term [6], [7].

The biocompatibility of a metallic implant is related to its corrosion resistance. Since implants are in contact with human fluids, that constitutes an aggressive environment, which may favour the generation of undesirable corrosion products, reducing the structural integrity of the implant [8]. Corrosion products may have possible biological effects caused by metal ions and debris particles released by wear. Hip implants are continuously exposed to wear, which are produced due to the continuous relative motion at the joint that causes friction between the surfaces. Wear debris may lead to adverse reactions leading to osteolysis and cytotoxic effects. To prevent this, the new implant generation must be made using non-toxic elements that do not risk the safety and health of the patient if wear debris is formed [9], [10]

Although metallic materials are biocompatible, they are bioinert, meaning that they lack bioactivity. This means no biological interactions between implant and tissue are naturally produced, limiting the fixation between the implant and bone. The challenge consists in improving the biological response by different surface modification techniques that have been developed, attempting to induce the osseointegration of the implant with the surrounding tissues.

The mechanical properties of metallic implants should be similar to those of the implanted host tissue, especially the Young modulus. Mismatch of Young modulus between implant material and bone leads to stress-shielding phenomenon that, in the long term, produces bone resorption, fixation loss and early implant loosening.

To summarise, an ideal material for load-bearing implants should have the following requirements: 1) high biocompatibility, 2) high corrosion resistance, 3) good mechanical properties (low Young's modulus, high fatigue resistance, high ultimate tensile strength), 4) high wear resistance and 5) osseointegration ability [9]–[11]. **Figure 1.1** shows some issues related to the lack of these requirements that affect implant functionality.

As it was mentioned before, most orthopaedic implants are metallic. Despite there being a wide variety of alloys available in the industry, the list of suitable materials for hip implants is rather reduced. Among the most commonly used alloys in hip implants are stainless steels, Cr-Co alloys and, titanium alloys [6], [12], [13]. **Table 1.2** shows the main features exhibited by these materials.

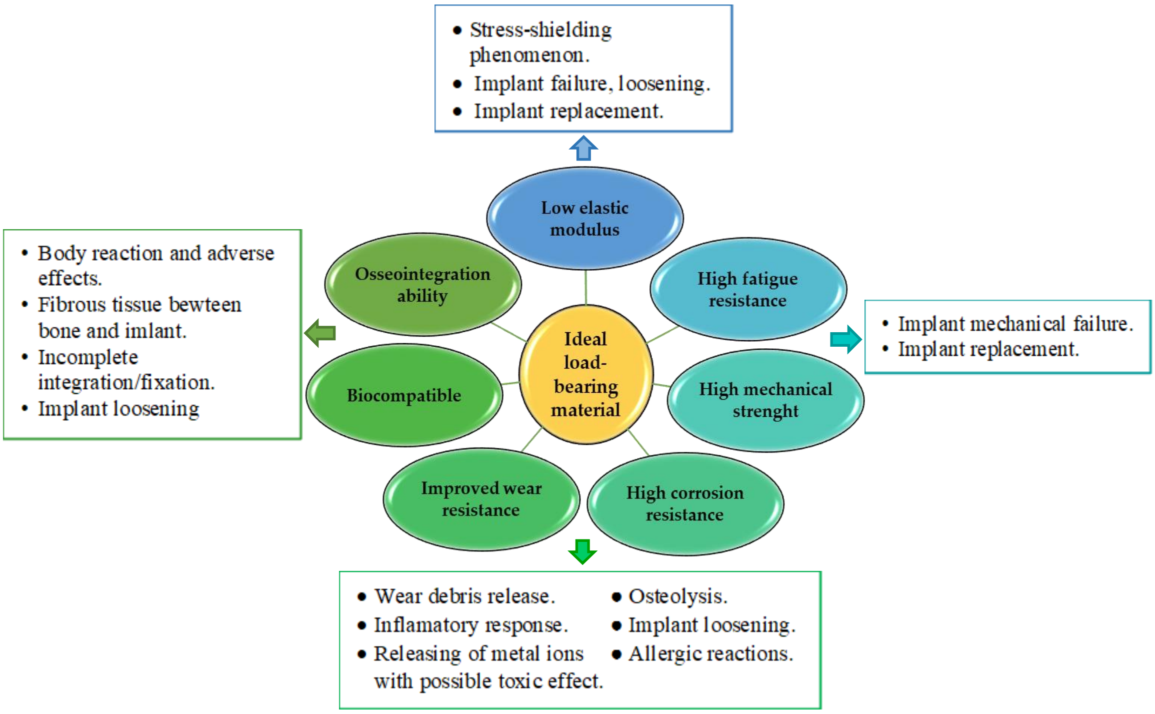

Figure 1.1. Requirement of ideal load-bearing material and problems associated with the lack of them. Adapted from [9].

Table 1.2. Features of the leading materials employed in hip implants compared to the bone. Adapted from [12], [14] .

Material	Density (g/cm^3)	Tensile strength (MPa)	Yield strength (MPa)	Elastic modulus (GPa)	Biocompatibility
Cortical bone		70-150	30-70	10-30	---
Type 316 Stainless Steel	7.9	490-1350	190-690	200-210	Poor
Co-Cr alloys	7.8	655-1793	310-1586	210-253	Moderate
Ti-based alloys	4.4-4.5	690-1100	585-1060	55-110	Good

Among these options, titanium presents superior corrosion resistance in contact with human fluids, and Ti and its alloys exhibit more suitable structural properties since they have half Young's modulus than Cr-Co alloys and stainless steel 316L. **Table 1.3** shows some properties of different Ti alloys commercially used for orthopaedic implants.

Ti6Al4V and Ti6Al7Nb are the most used alloys in the hip prosthesis; however, their elastic modulus is still higher (~ 100-115 GPa) compared to the cortical bone (10-30 GPa), so they are not the most suitable alloys for this application, since do not prevent the stress-shielding phenomenon. Besides, it is known that elements like aluminium or vanadium could be toxic for the human body as they have been linked to diseases such as Alzheimer; therefore, their use as alloying elements should be avoided to prevent adverse systemic effects.

Table 1.3. Properties of common Ti alloys (in annealed condition) used as implant material. Adapted from [15]

Material	**Microstruture**	**Elastic modulus (GPa)**	**Yield strength (MPa)**	**Tensile strength (MPa)**	**Fatigue limit, at 10^7 cycles (MPa)**
Cortical bone		10-30	---	90-140	---
CP-Ti (Grade 4)	α	105	480	550	350
Ti-6Al-4V	α + β	110	680	780	400
Ti-6Al-7Nb	α + β	105	800	900	500
Ti-5Al-2.5Fe	α + β	110	780	860	725
Ti-13Nb-13Zr	α + β	79	900	1030	500
Ti-11.5Mo-6Zr-4.5Sn	β	79	620	690	525
Ti-15Mo-5Zr-3Al	β	80	900	930	540
Ti-35Nb-5Ta-7Zr	β	55	530	590	265

Research on the development of novel Ti-based alloys designed for biomedical applications is focused on obtaining a material that combines mechanical properties and low elastic modulus, using biocompatible and non-toxic alloying elements. In the bibliography, two main strategies can be found in order to achieve this [16]–[21]. The first strategy is the development of porous materials, since elastic modulus decreases as increasing the porosity amount. However, given that strength also decreases with porosity fractions, this must be carefully controlled in order to guarantee an adequate mechanical performance of the material. On the other hand, porous structure enhances the stress distribution along the implant and provides channels suitable for the growth of bone tissue, promoting the osseointegration process [17], [18].

A second possibility is the development of β-Ti alloys, which are considered promising materials for hip implants since they exhibit lower Young's modulus than biphasic (α + β), as shown in **Table 1.3**. Several studies have reported on the development of biocompatible and low modulus β-phase Ti alloys, using different stabilisers such as Nb, Mo, Zr and Ta. Among these, Nb is considered the most biocompatible β-stabilising element [22]. Overall, the higher the β-stabiliser elements amount, the lower the elastic modulus values are achieved due to increased β-phase stability.

1.2. General aspects of Titanium and Titanium alloys.

Titanium and its alloys have been widely employed for high-performance components due to their unique combination of low density, high strength to weight ratio, excellent mechanical properties, improved corrosion resistance and good biocompatibility. All these make them suitable for several industries such as automotive, aviation, sports equipment, biomedical. Aerospace and biomedical are currently the most important sectors for applications of titanium products. In the biomedical sector, Ti and its alloys have been used in numerous medical devices such as heart valves, cardiac stents, bone plates, screws, dental and orthopaedic (hip and knee) implants. [2], [23]

Titanium (Ti) is the fourth most abundant structural metal on the Earth crust, after aluminium (Al), iron (Fe) and magnesium (Mg) [24]. Like many metals, Ti is not found in its pure metallic state; it is obtained from ilmenite ($FeTiO_3$) and rutile (TiO_2) mineral sources. Titanium was discovered in 1791, but it was not until 1940 that it was commercially attractive when Wilhelm Justin Kroll, who is recognised as the father of the titanium industry, developed a novel method to isolate Ti. This method, known as the "Kroll process", is still the most used method for titanium production. This method allowed an increase in the amount of Ti obtained, which made its commercial or industrial use viable.

Kroll process is based on reducing titanium tetrachloride with molten magnesium in an inert argon gas atmosphere. The reduction product is vacuum distilled to removed impurities, and then it is cut and crushed, to finally obtain "titanium sponge", which is used as raw material to produce different kinds of Ti powders and Ti components by vacuum arc remelting or electron beam cold hearth melting [25].

Like other metals, the large variety of structural properties of Ti is influenced by the arrangement of the atoms in the crystal structure. Ti presents two different crystal structures. At low temperature, Ti exhibits a hexagonal close-packed (HCP) structure, known as α-Ti phase, whereas, at temperatures higher than the allotropic transformation (882 °C), it changes to body-centred cubic (BCC) structure called β-Ti phase, which is kept up until the melting point at 1678 °C. The point at which the $\alpha \rightarrow \beta$ transformation occurs is known as beta transus temperature. [24], [26], [27]

According to their room temperature microstructure, Ti alloys can be classified as α, near α, α+β, β. The α-Ti and near α alloys present higher creep resistance compared to β-Ti alloys, so they are suitable for high-temperature applications. Due to the high stability of the α phase, they cannot be heat treated to improve their mechanical properties. The α+β alloys contain between 10-50 vol.% of β phase [28]. They are recognised to exhibit a good balance of strength, ductility, fatigue resistance and fracture properties. Moreover, α+β alloys can be strengthened by heat treatment. Ti-6Al-4V is the most popular α+β alloys, especially in the aerospace industry. Finally, β-Ti alloys are heat treatable to achieved high strength, usually by solution treatment, quenching and ageing. β-Ti alloys combine good mechanical properties, high corrosion resistance, similar and even higher than some (α+β)-Ti alloys. Besides, they could exhibit lower elastic modulus than other Ti alloys, which makes them suitable for biomedical application. [24], [28], [29]

Ti exhibits an incomplete shell in its electronic structure; hence, it tends to form solid-solution with most substitutional elements with a size factor within ± 20%, which has a strengthening effect that improves its mechanical properties [30]. Microstructure and allotropic transformation temperature are altered by adding alloying elements. According to their effect on the beta transus temperature, alloying elements are divided into three main groups: α-stabilisers, β-stabilisers and neutral. **Figure 1.2**. displays the influence of the different alloying elements on the Ti phase diagram.

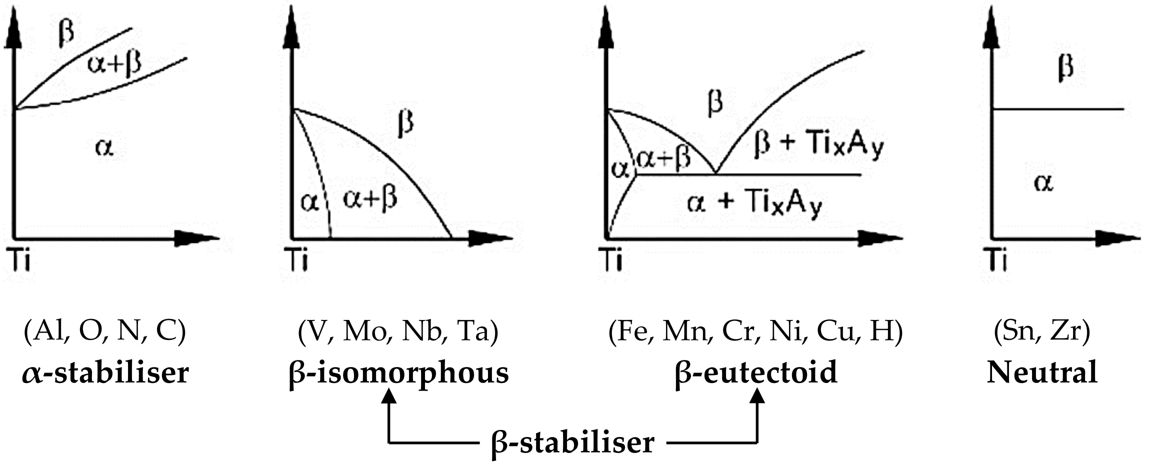

Figure 1.2. Schematic representation of the effect of alloying elements on Ti phase diagram. Adapted from [24], [31].

The α-stabiliser elements increase the beta transus temperature, displacing the α phase-field toward higher temperature as increases the solute content. Among α-stabiliser elements, aluminium is the most employed alloying element in Ti alloys. Interstitial elements such as O, C and N are also included within α-stabiliser elements, as long as their content is controlled to achieve improved mechanical properties. [32]

Most of the β-stabilisers elements are transition metals that present partial solubility in the α-Ti phase and reduce the beta transus temperature, allowing to obtain a β or biphasic α+β microstructure at room temperature. β-stabilisers elements are divided into β-isomorphous and β-eutectoid elements according to their effect on the phase diagram. β-isomorphous elements usually present complete mutual solubility with β-Ti, among this kind of alloying element are V, Mo, Nb and Ta. In contrast, β-eutectoid elements present limited solubility in β phase, and they may form intermetallic compounds through the eutectoid decomposition of the β phase. Some β-eutectoid elements are Fe, Mn, Cr, Ni, Cu and H. [33]

Neutral alloying elements, such as Sn or Zr, do not significantly affect the beta transus temperature. Nevertheless, they are used because they increase the ultimate strength of Ti alloys, with Sn more effective than Zr for lower additions. [34]

1.3. Processing of titanium alloys.

Ti-based components have been typically manufactured by ingot melting techniques that consist of a multi-step process of vacuum arc melting, thermo-mechanical processing, such as forging or hot rolling, scale removal, vacuum annealing, machining, and surface treatment. All these fabrication stages make the final product expensive, especially the machining stage that may involve about half of the total processing cost [35]. The weight ratio of raw material employed to produce the final component, known as the buy-to-fly ratio, is too high. It has been reported that some aircraft Ti components have a buy-to-fly ratio between 12:1 or 20:1 for components fabricated from plate or sheet, which supposes a significant amount of scrap material for each produced component. [36] Overall, Ti is an expensive material, about 4-5 times more expensive than stainless steel [25]. The high cost of Ti is because careful and controlled processing must be carried out to prevent contamination by interstitial elements due to the high reactivity of Ti.

In 1980 at The Minerals, Metals and Materials Society (TMS) Conference, the powder metallurgy (PM) approach was proposed as an attractive alternative to produce Ti components reducing the production cost and the manufacturing steps [37]. PM consists of three main stages: (1) powder production, (2) powder compaction to obtain near-net shape green components and (3) sintering, to provide final dimensions, microstructural development and mechanical properties. PM processing provides near-net-shape parts, minimising the machining steps and increasing the material yield [25], [38]. **Figure 1.3** reflects the reduction of processing stages offered by powder metallurgy techniques compared to conventional ingot metallurgy processing.

PM is a versatile technique that allows the production of components from refractory metals such as molybdenum (Mo), tungsten (W), or niobium (Nb), which are difficult to process by wrought ingot metallurgy due to their high melting point, above 2000 °C. Moreover, PM is a useful alternative over the wrought ingot metallurgy for processing components from elements with very different melting points that exhibit limited solubility in the liquid state and different density among them [4]. Hence, PM provides high flexibility in alloying design, overcoming limitations in casting, and achieving good homogenisation of the alloying elements.

Even though the PM approach reduces the processing steps, resulting in a processing cost reduction, the cost of Ti powder as raw material is still high. The cost of the powder represents a significant fraction of the total processing cost in PM components. Hence, reducing the powder cost could reduce the cost of Ti components [35], [39].

The performance of PM Ti components is highly influenced by the characteristics of the starting powder, such as particle size and morphology, and interstitial elements O, N, and C content [25], [40]–[43]. The choice of Ti powders is a key aspect to take into account in

PM components processing. Hence, in recent years, there have been great advances in Ti powders production in order to satisfy the requirements for specific applications or manufacturing methods. For instance, overall, fine powders with an irregular shape achieve higher densification than coarse powders, since they possess a higher specific surface, and therefore, they have a higher surface activity, which constitutes the driving force in the sintering process. Therefore, sinterability is improved, and lower sintering temperature might be required to obtain full-density samples [44]. Due to the higher specific surface, fine and irregular powders have a higher risk of contamination, so this kind of powders might contain a higher fraction of impurities, that must be controlled to prevent embrittlement of the alloy. In contrast, spherical powders, such as pre-alloyed powders, are not suitable for cold compaction because their particle surface becomes hardened, making it challenging to reach high green density values.

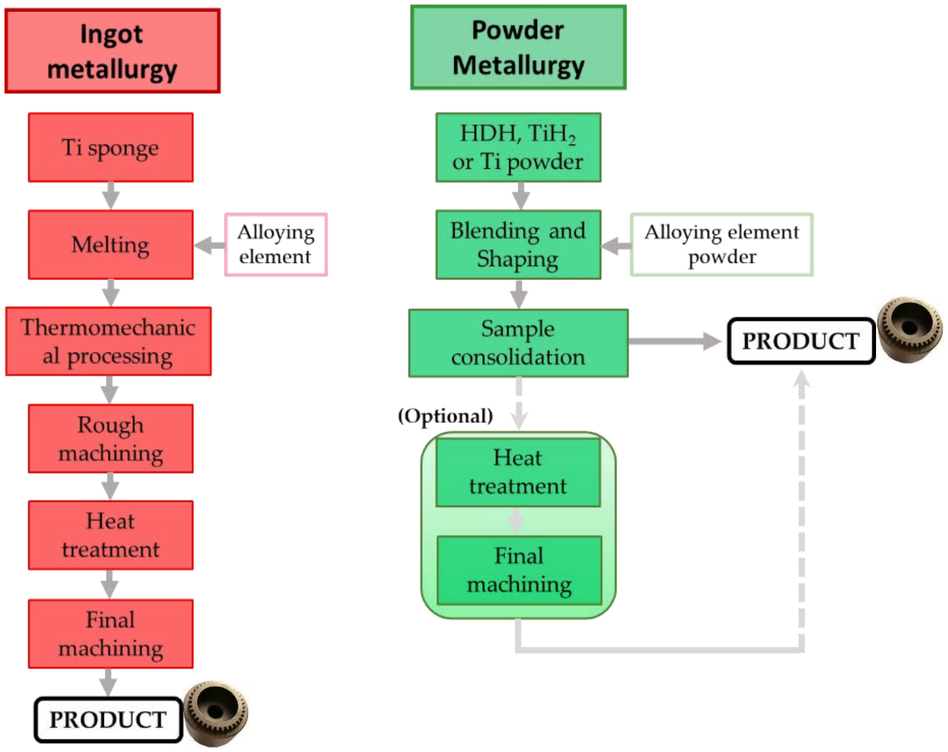

Figure 1.3. Processing stages involved ingot metallurgy and powder metallurgy techniques. Adapted from [25].

There are several processes to obtain commercial Ti powders from Ti sponge. Among them, the HDH (hydride-dehydride) technique uses by-products of Ti sponge which are submitted to hydrogenation, ground until they achieve the suitable particle size, and then powder dehydrogenation is carried out [25]. Ti HDH powders have an irregular shape, the oxygen content is low, and they are suitable for pressing and sintering. Ti powders can also be obtained by several atomisation techniques like gas atomisation, plasma atomisation and plasma rotating electrode process. Atomisation techniques allow to obtain pre-alloyed powders and lead to spherical powder morphology [8]. Atomised powders are widely used in components produced by additive manufacturing and metal injection moulding, where good flowability is required. [45], [46]

In general, regardless of the processing method, the cleaner the powder, the higher the cost [47]. Therefore, finding a cheap powder with the appropriate features, in terms of morphology, purity, and particle size, suitable to be processed by the different PM techniques is one of the main challenges of the PM Ti industry.

On the other hand, processing titanium powders to give final components by the conventional pressing and sintering route requires sintering temperatures around 1200-1400 °C employing long dwell times (2 to 5 h typically), which suppose high energy consumption. [39]

Hence, there is room to reduce processing costs through alternative routes or using alternative starting powders and alloying elements that help improve the sintering parameters while maintaining the final properties in terms of density and microstructure [25], [39], [47]. Producing low-cost Ti alloys will allow expanding the application sector of the Ti components, not only in the biomedical sector but also in more competitive sectors, such as automotive, where their use is limited due to the significant cost difference between Ti and steel components.

1.3.1. Processing of Ti alloys from TiH_2 powder.

Since 2000, titanium hydride (TiH_2) has become an attractive alternative to reducing the raw material cost for Ti alloys. This has lead to adjusting the processing parameters of Ti components toward lower sintering temperature, and hence, lower energy consumption.

The main advantages of using TiH_2, compared to Ti powders, are: (1) TiH_2 as raw material is cheaper because it is an intermediate product in HDH-Ti powder production. (2) It achieves higher densification compared to Ti sintered under the same conditions [48], [49]. (3) The brittle behaviour of TiH_2 helps to fragment particles during pressing, improving the compressibility of the powder [42], [49]–[51]. (4) The lattice defects generated by decomposition reactions of TiH_2 activate the diffusion process, which leads to pore healing and accelerates the chemical homogenization of the final product [50]. (5) Hydrogen released during the transformation to Ti, through the reaction $TiH_2 \rightarrow Ti + H_2$, provides a protective atmosphere for the Ti surface that reduces the contamination amount [51]–[53].

TiH_2 uses dates back to 1970 when Greenspan et al. produced titanium alloys and metal matrix composites by hot pressing using TiH_2 as starting powder; this process was called decomposition powder metallurgy [54]. Next, in 1974, Obara et al. patented the first press and sinter process, both in a vacuum and inert gas atmosphere, to produce Ti alloys from TiH_2 powder [54]. Since then, several works focused on the sintering of titanium hydride components.

All TiH_2 applications depend on the dehydrogenation process: how hydrogen is released when it is subjected to a heat treatment. The TiH_2 decomposition process has been widely researched through simultaneous thermal analysis under different atmospheres combined with structural analysis and in-situ methods [55]–[61]. Zeppelin et al. [62] found that the dehydrogenation process is dependent on the heating atmosphere. Dehydrogenation occurs at lower temperature when the sample is heated under vacuum, while it is delayed under helium and air atmosphere. The maximum hydrogen desorption was found at 516 °C, 620 °C, and 655 °C when the sample was heated under vacuum, helium, and air heating, respectively.

Concerning the different dehydrogenation reactions, some authors propose that dehydrogenation occurs in four stages [55], [59], [63], [64]. In where δ-TiH_2 is transformed to $TiH_{1.5}$ (stage I); then, in β-Ti hydrogen-rich phase (β_H, stage II); followed in α-Ti hydrogen-rich phase (α_H, stage III) and finally, after complete hydrogen removal, it is transformed into α-Ti. A representative model of the dehydrogenation process proposed by Liu et al. is shown in **Figure 1.4**.

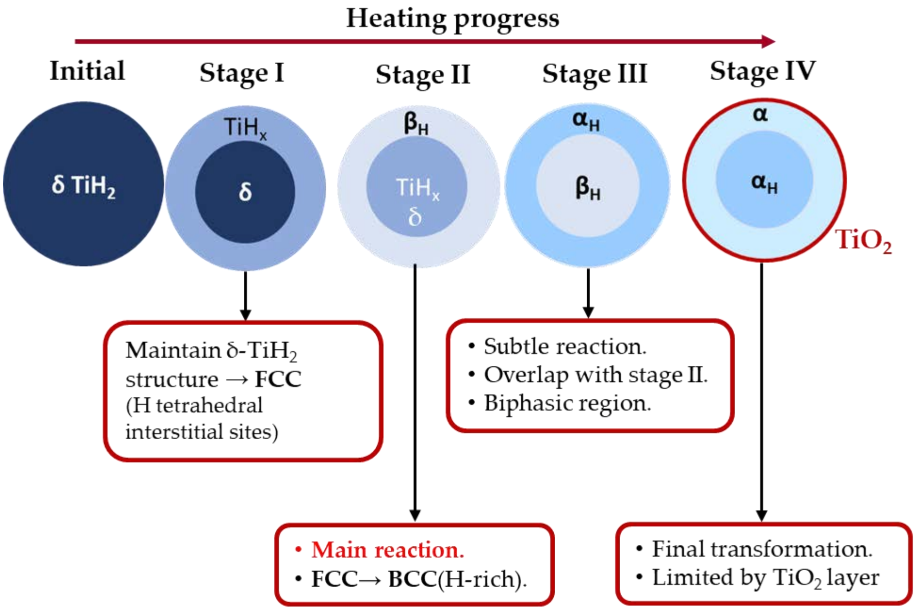

Figure 1.4. Schematic representation of non-isothermal dehydrogenation of TiH_2. Adapted from [59].

On the other hand, some authors disagree with this dehydrogenation sequence [61], [65]–[67]. Their approach supports that δ-TiH_2 is transformed to $TiH_{1.5}$, and then α_H is formed. Next, α_H and β_H coexist until hydrogen is completely released and α-Ti is obtained.

Although there are discrepancies about the sequence of the phases formed during TiH_2 decomposition process, researchers agree that this process is strongly dependent on samples' features, like the purity of the powder, particle size, and surface contamination, which can act as a barrier for the release of hydrogen. Besides, the heating rate is an important aspect to be taken into account in order to promote decomposition. Generally, dehydrogenation occurs between 400-800 °C [50]. Nevertheless, it has been reported that the temperature decomposition range can be reduced using a low heating rate. [57], [59], [64], [68]

Many studies have been conducted on the thermal behaviour of TiH_2 since its decomposition temperature is an essential aspect to consider in order to take advantage of its properties. TiH_2 decomposition has been widely studied to produce aluminium foam, since both pore morphology and porosity depend on the dehydrogenation process. In this process, delay of the beginning of dehydrogenation is required in order to avoid early hydrogen release [56], [69]–[71]. Moreover, TiH_2 has been evaluated to be employed as a foaming agent in TiNi scaffolds processing for biomedical applications [70].

Sintering of Ti alloys employing TiH_2 powders has also been extensively studied [57], [68], [72]–[74]. These studies propose TiH_2 as an attractive alternative to produce Ti-based components. They point out that components processed from TiH_2 require lower consolidation temperature and even may outperform the properties compared to Ti components.

However, there are few studies about the effect of alloying elements on TiH_2 decomposition. It is considered that understanding the interactions among hydrogen and alloying elements during and after the dehydrogenation process could become a powerful tool in achieving microstructure control of Ti alloys, especially in β-Ti alloys.

1.3.2. Addition of iron (Fe).

The alloys features depend on the alloying elements. Each alloying element provides certain properties to the alloy. For instance, aluminium increases mechanical properties, Nb improves corrosion resistance and decreases elastic modulus, Zr inhibits grain growth. To develop an economically viable alloy, the cost of the raw materials to be used must be considered. **Figure 1.5** displays the prices of some metals frequently used as alloying elements in Ti alloys. It can be seen that the price of Mo and Ta as alloying elements is even higher than that of titanium, while that of Nb and V is comparable.

Ti-Nb alloys, developed for biomedical applications, require at least 27.5 Nb wt.% to begin retaining the β-Ti phase [21]. As Nb is an expensive metal, large amounts of Nb additions increase the alloy cost [76]. One way to reduce the processing cost of Ti alloys is employing low-cost alloying elements, provided that these allow achieving materials with good properties.

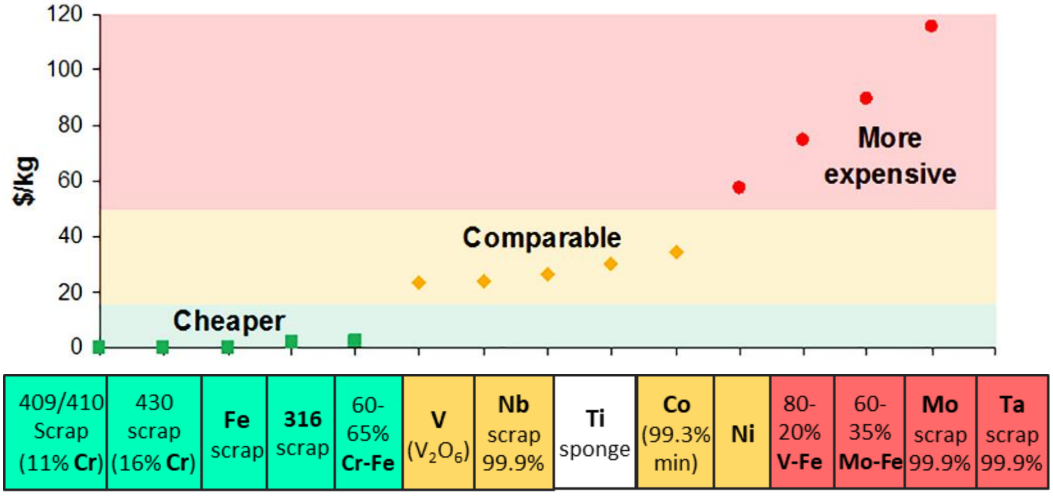

Figure 1.5. Price of common alloying elements employed for processing Ti alloys. [75]

In this regard, Fe is a suitable alternative since it is an abundant and low-cost material. Also, Fe is a strong β-stabiliser element that diffuses fast into β-Ti, which favours its quick dissolution during sintering. Small Fe addition increases the β-Ti stability; hence, it will lead to a reduction in the Nb content required to stabilise the β phase. Therefore, substituting Nb with Fe can contribute to the cost reduction of the alloy.

In addition to reducing the alloy cost, Fe addition has several advantages for Ti alloys processing. Fe provides a strong solid-solution strengthening effect on Ti alloys. Furthermore, several authors have indicated that densification rises with small Fe additions (2.5-5 wt.% Fe) [77], [78]. Wei et al. [78] found that the mean shrinkage of Ti-5 Fe wt.% is three times that exhibited for pure Ti, and that the most shrinkage occurs during heating instead of during holding time (at the sintering temperature), as it usually happens in pure Ti.

Densification of Ti-Fe alloys is influenced by heating rate and Fe particle size. Overall, it is considered that a slower heating rate and finer Fe powders favour diffusion and sample densification. In contrast, coarser Fe powders may promote Kirkendall porosity, causing worse densification and large porosity, presenting pores as large as powder size. [78], [79]

In addition, Fe enhances the sinterability of Ti alloys since it accelerates the mobility of Ti atoms by the rapid Fe diffusion. Furthermore, Fe increases the Ti auto-diffusion coefficient [78], which could enhance the diffusion process of slower diffusing alloying elements like Nb or Mo, promoting a homogeneous microstructure.

According to Ti-Fe phase diagram, the intermetallic TiFe can be formed around 1085 °C [80]. Even though it has been reported that Fe exhibits a slow intermetallic formation, the amount of Fe must be controlled in order to avoid the formation of TiFe, since it may have detrimental effects on mechanical properties, such as ductility loss [75], [80], [81]. TiFe formation could also be influenced by Fe particle size. O'Flynn et al. [77] reported for Ti-2.5 wt.% Fe alloy that as the size of Fe powder becomes smaller, the exothermic peak associated with TiFe formation disappears. This fact is because the smaller Fe particle size dissolves faster into Ti lattice, and then, once Fe is dissolved, the eutectic reaction is avoided.

1.4. Strategies to improve Ti properties.

Ti and its alloys are suitable materials for orthopaedic implants due to their good bulk properties like good corrosion resistance, high biocompatibility, good mechanical properties, low density and high fatigue resistance. The bulk properties of Ti are crucial for implant material choice. Nevertheless, Ti alloys present some intrinsic drawbacks that may affect their performance. Ti alloys present relative low hardness values, which make them susceptible to low wear resistance. Poor wear resistance impairs the functionality of the implant, causing premature failure. Therefore, it is mandatory to develop a material that provides improved mechanical properties, especially hardness, since harder materials are considered to exhibit higher wear resistance.

On the other hand, the contact surface features between the implant and bone are determinants to induce osseointegration. Therefore, the implant surface properties must be similar to the tissue where it is implanted to avoid possible rejection or adverse responses. Several authors agree that implant surface should exhibit certain roughness and higher wettability, and a hydrophilic surface, in order to facilitate cell adhesion and proliferation. Also, it is suggested that porous surface are favourable to promote inward bone growth, resulting in a better fixation between the implant and surrounding tissue. [21], [82]

Many modification treatments have been extensively studied in order to improve the Ti alloys qualities and provide them with similar features to the bone/host tissue. There are modifications treatments for Ti alloys, affecting the whole material, so changing the bulk properties. These kinds of treatments are focused on improving mechanical properties changing the microstructure. On the other hand, the development of titanium matrix composites (TMC) materials is an alternative strategy employed to achieve improved mechanical properties.

A wide variety of surface modification treatments have been developed to adapt implant surface. These treatments alter just the surface region, maintaining the internal properties of the alloy. Surface modification treatments have been widely studied to improve the biocompatibility and bioactivity of implant materials, employing bioactive compounds that promote the osseointegration process. Nevertheless, some of these treatments are also performed looking to enhance wear and corrosion resistance.

According to the surface interaction, they can be classified as mechanical, chemical or physical. **Figure 1.6** shows different treatments usually employed to improve bulk properties and surface features on Ti alloys.

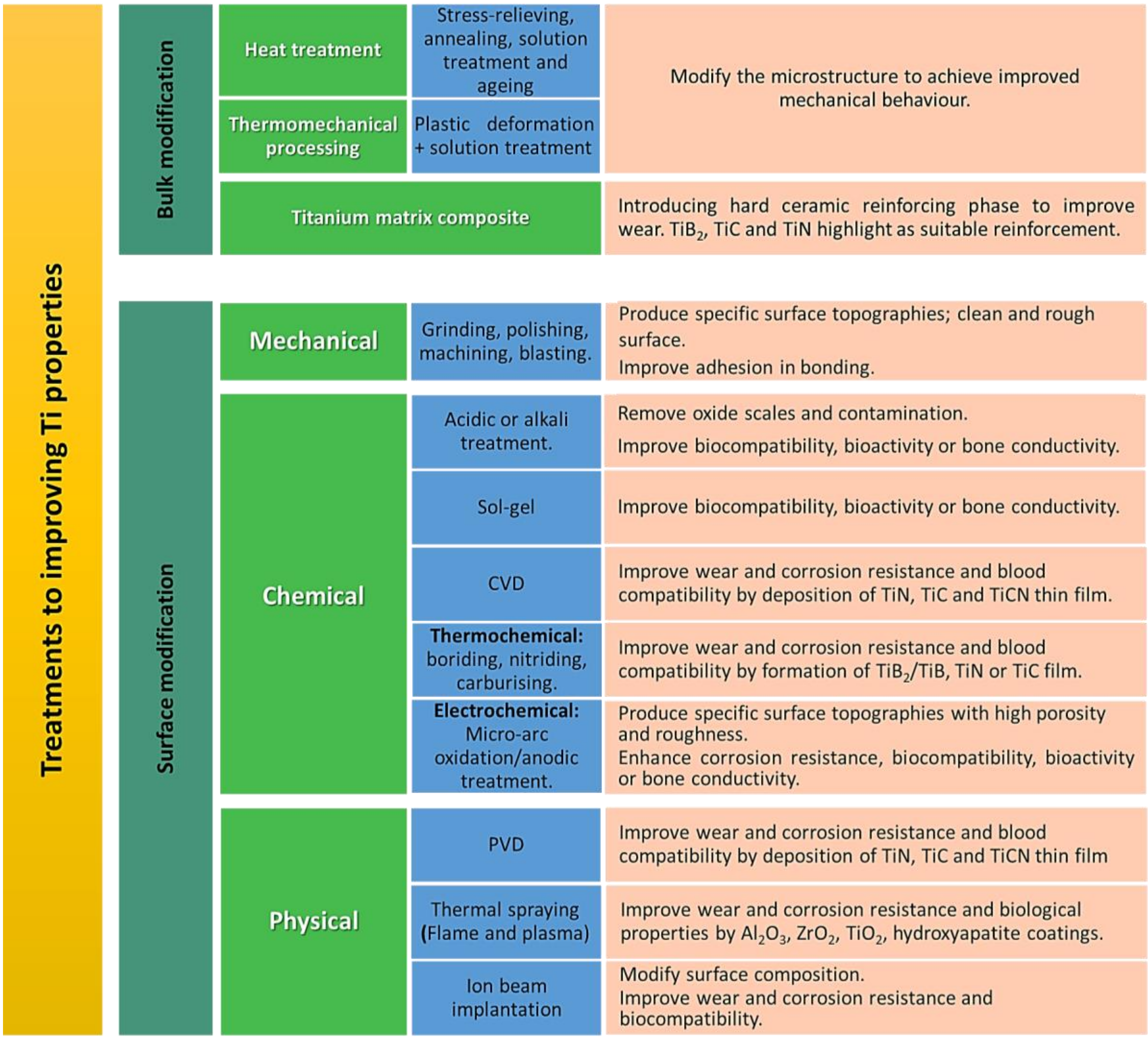

Treatments to improving Ti properties	Bulk modification	Heat treatment	Stress-relieving, annealing, solution treatment and ageing	Modify the microstructure to achieve improved mechanical behaviour.
		Thermomechanical processing	Plastic deformation + solution treatment	
		Titanium matrix composite		Introducing hard ceramic reinforcing phase to improve wear. TiB_2, TiC and TiN highlight as suitable reinforcement.
	Surface modification	Mechanical	Grinding, polishing, machining, blasting.	Produce specific surface topographies; clean and rough surface. Improve adhesion in bonding.
		Chemical	Acidic or alkali treatment.	Remove oxide scales and contamination. Improve biocompatibility, bioactivity or bone conductivity.
			Sol-gel	Improve biocompatibility, bioactivity or bone conductivity.
			CVD	Improve wear and corrosion resistance and blood compatibility by deposition of TiN, TiC and TiCN thin film.
			Thermochemical: boriding, nitriding, carburising.	Improve wear and corrosion resistance and blood compatibility by formation of TiB_2/TiB, TiN or TiC film.
			Electrochemical: Micro-arc oxidation/anodic treatment.	Produce specific surface topographies with high porosity and roughness. Enhance corrosion resistance, biocompatibility, bioactivity or bone conductivity.
		Physical	PVD	Improve wear and corrosion resistance and blood compatibility by deposition of TiN, TiC and TiCN thin film
			Thermal spraying (Flame and plasma)	Improve wear and corrosion resistance and biological properties by Al_2O_3, ZrO_2, TiO_2, hydroxyapatite coatings.
			Ion beam implantation	Modify surface composition. Improve wear and corrosion resistance and biocompatibility.

Figure 1.6. Modification methods employed for improving mechanical and surface properties of Ti and its alloys. Adapted from [83].

1.4.1. Improvement of Bulk properties.

It is well known that the bulk properties of Ti alloys, such as elastic modulus, strength, fatigue resistance and hardness, and consequently wear resistance, are highly dependent on microstructural features. The phases present on the microstructure may promote or affect a specific property. For instance, it has been reported that hardness and elastic modulus values increase from $\beta < \alpha'' < \alpha' < \alpha < \omega$-Ti phase [84]. Therefore, by varying the fraction of these Ti phases in the material, mechanical properties can be modified. The grain size also affects the mechanical behaviour. Overall, it is considered that fine microstructures are favourable for mechanical properties compared to coarse ones. [39].

There are different ways to modify the microstructure. Before consolidation, it can be achieved by adjusting the chemical composition using suitable alloying elements to promote the desired microstructure [39], [85]. After the material consolidation, the microstructure may be altered by performing heat treatments and/or thermomechanical processing. The latter combines plastic deformation process and solution heat treatment. Plastic deformation produces high dislocation amount, reducing the driving force for further recrystallisation and nucleation sites of α precipitates that provide enhanced strength. Meanwhile, heat treatment alleviates the internal stress generated during plastic deformation and produce microstructural changes as well. For Ti PM components, it can also be used to eliminate residual porosity.[25]

It should be considered that these kinds of treatment may promote surface contamination leading to the formation of a hard and brittle O/N-rich α phase, which is denominated as alpha case. Hence, the sample surface must be cleaned after treatment to remove the alpha case either by mechanical or chemical methods. [86]

1.4.1.1. Heat treatments.

Depending on microconstituents distribution, Ti alloys may exhibit different types of microstructures like lamellar, bimodal, Widmanstätten, equiaxed, basket-weave, martensite, acicular and bilamellar. Each of these determines material behaviour [87]. Heat treatments comprise changing the starting microstructure obtained during consolidation into an enhanced microstructure that provides better performance [88]. The desired microstructure is obtained by controlled phase transformations that take place during heat treatment. Heat treatments allow to obtain enhanced ductility, strength, impact resistance, creep resistance, fracture toughness and fatigue resistance [89]–[91].

Beta transus temperature is an essential aspect for the design of heat treatment since it highly influences the phase transformations. Beta transus is a reference point to define the heat treatment conditions (heat treatment temperature, time and heating/cooling rate) more suitable for the alloy to be treated.

The heat treatment response depends on the alloy type. α and near-α Ti alloys cannot be hardened by heat treatments because of the high thermal stability of HCP Ti. In contrast, α+β and β alloys have a better response to heat treatments due to they could experiment martensitic transformations during cooling, whereas α-Ti alloys not, as evidence in **Figure 1.7.** Thus, α+β and β alloys can present a large variety of phase compositions, and similarly, a wide range of properties through appropriate conditions choice. β-Ti alloys can be heat treated at lower temperatures compared to α+β alloys because they exhibit lower beta transus temperature. Thus, the phase transformations in β-Ti are also produced at lower temperatures.

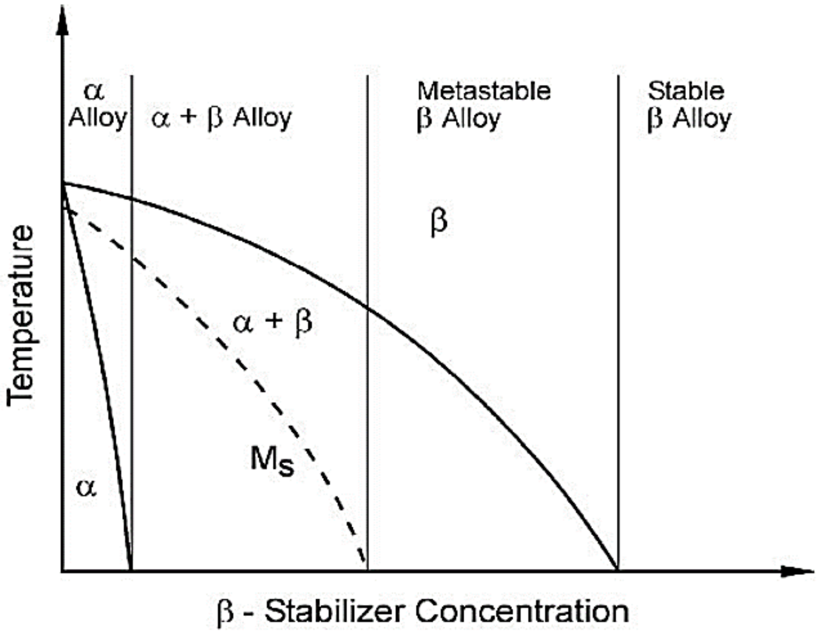

Figure 1.7. Pseudo-binary phase diagram indicating the martensitic transformation line according to the β-stabiliser element concentration. Adapted from [92]

Stress-relieving, annealing (including mill annealing, duplex annealing, recrystallization annealing or β-annealing), solution treatment and ageing are the main heat treatments performed in Ti alloys. Given the relevance of β-Ti alloys in developing implant materials that replace the high-modulus (α+β)-Ti alloys, the most used heat treatments in β-Ti alloys will be described in this section. These are solution treatment and ageing. [86], [87]

Solution treatments (ST) are performed slightly above (super transus) or below (sub transus) the beta transus temperature. Sample is maintained at the selected temperature, seeking to homogenise the alloying elements into β phase. Super transus ST of β alloys attempts to retain 100% β-phase with equiaxed grains after quenching. In this case, the holding time of ST (above beta transus temperature) must be carefully controlled, avoiding long dwell time, because of the fast grain growth in the β field that may decrease the mechanical properties [86], [91].

In contrast, sub transus ST (conducted from α+β field) promote the formation of primary elongated or globular α phase into β grains to inhibit the excessive growth of β grains [93], [94]. The ST temperature highly influences the morphology of the primary α phase. As temperature become closer to beta transus, the primary α phase precipitates exhibit a globular morphology, whereas when it is much lower, elongated precipitates are obtained [94].

Some authors report better strength-ductility balance for sub transus ST than super transus ST [33], [89], [93]. Ti-6Cr-5Mo-5V-4Al alloy solution treated from α+β field (760 °C, -30 °C below beta transus temperature) exhibits similar ductility to alloy solution treated from β field (800 °C, +10 °C upon beta transus temperature), achieving about 22% elongation and

57-60% area reduction. Sample treated below beta transus temperature achieves 973 MPa of strength, which is 100 MPa higher than alloy treated from β field [93]. The improved strength is due to α precipitates, formed during sub transus ST, which hinder the dislocation movement, avoid the β grain recrystallisation and have a grain refinement effect that strengthens the alloy. [93]

Once the sample is homogenised, it is subjected to rapid cooling to "freeze" the modified microstructure. Quenching may produce a martensitic microstructure. This is related to fast cooling rate that limits the rearrangement of the atoms, distorting the lattice during the reverse transformation from β-Ti(BCC) to α-Ti(HCP). There are two martensite phases in Ti alloys: the hexagonal martensite, α' and, the orthorhombic martensite, α'', both are a supersaturated substitutional solid solution of elements in α-Ti, which is formed in zones where β phase become depleted in β-stabiliser elements [95]. α'' is usually formed in β-Ti containing Nb, Mo, Ta, Mo, V, W and Re. Nevertheless, martensitic transformation (from $\beta \rightarrow \alpha'/\alpha''$) could be suppressed increasing the amount of β-stabiliser elements, since these elements exhibit slow diffusion and reduced diffusion rate, which increase the stability of β-phase and limit the element mobility [91], [96]–[98]. Bonish et al. [98] and Wang et al. [99] stated that martensitic transformation is hindered for Nb content higher than 25 at.% (40 wt.%). Ehtemam et al. [97] reported that the amount of α'' into Ti-7Fe alloy is reduced as the Nb content increases from 1 to 9 wt.%, and with 11 Nb wt.% no martensitic phases are observed.

Martensitic phases increase the strength, but at the same time, they reduce the alloy's ductility. Hence, martensitic phases are not desirable for some applications. Nevertheless, martensitic phases can act as intermediate phases in subsequent heat treatments, in which they decompose to obtain lamellar α+β microstructure, improving mechanical behaviour. [100]

Ageing treatments (AT) are usually performed from solution treated condition for most Ti alloys. However, in the case of β-Ti alloys, ageing may be carried out without previous solution treatment. This is known as direct ageing. AT increases the strength and hardness of the alloy, but it reduces the ductility of the alloy by refinement of α precipitates.

During ageing, β-phase is decomposed to form α phase precipitates that improve mechanical properties by precipitation strengthening effect. Overall, fine α precipitates are distributed within the β-grains. In contrast, when ageing is preceded by solution treatment, primary and secondary α phase precipitates are formed, hence, the microstructure exhibit bimodal α morphologies associated with enhanced mechanical properties. [33], [86]

Ageing may be conducted at high or low temperature. It is considered high-temperature ageing when the sample is heated up between 85 and 195 °C below the beta transus temperature, which means about 450-650 °C [33]. Meanwhile, low-temperature ageing is usually conducted between 200-450 °C. High-temperature ageing reduces the hardening effect, but the treatment time is shortened. On the contrary, low-temperature ageing requires prolonged dwell time in order to complete the phase transformations [101].

1.4.1.2. Titanium matrix composites.

Titanium matrix composites (TMC), where hard ceramic reinforcing phases into the Ti matrix are incorporated, are an alternative to improved wear properties since they exhibit increased hardness compared to unreinforced alloy.

According to the reinforcement, there are two types of TMC: the composed of continuous reinforcements, such as fibres or wires, and those containing discontinuous reinforcements like particulate compounds [102]–[104]. Processing TMC with continuous reinforcements is an expensive and complex process due to the difficulty to align the fibre and to obtain a homogeneous distribution within the metal matrix [105]. Continuous TMC component may exhibit twice the strength and stiffness of Ti alloys; however, their properties are anisotropic, depending on the fibre direction. They are structurally efficient in the longitudinal direction but present reduced transversal properties. [106]

The main advantage of particulate reinforced TMC is that they can be manufactured using less expensive methods, such as powder metallurgy [107]. Indeed, PM processing is considered one of the most cost-effective manufacturing methods for discontinuous TMC components. Furthermore, discontinuous TMC exhibit isotropic properties, which only depend on the reinforcement´s homogeneity in the matrix. Therefore, the mixing of powders and particle dispersion must be carefully controlled to achieve suitable properties. Moreover, the reinforcement properties are also important to enhance the properties of Ti components. An optimal reinforcement should have high specific strength and hardness; thermodynamic stability at the consolidation temperature; similar thermal expansion coefficient with the Ti matrix; and strong interfacial bonding between the Ti matrix and reinforcement to avoid the detachment of hard particles that could affect the wear resistance, worsening the wear damage [108], [109]. Last but not least, reinforcements of TMC for biomedical applications must be biocompatible. [110]

Table 1.4 lists the physical and mechanical properties exhibited by the most used reinforcements in TMC processing compared to Ti properties.

As the reinforcement amount increases, the wear behaviour of TMC is enhanced [103], [111]. Choi et al. [112] found that wear volume loss is reduced a 32%, 35% and 64% for Ti-(TiB+TiC) with 5, 10, and 20 vol.% of (TiB+TiC) compared to pure Ti. Moreover, it was reported that the coefficient of friction of Ti6Al4V reinforced with TiN particles decreases as the TiN amount increases. [110]

Table 1.4. Properties of some reinforcements used in continuous reinforced TMC. [107], [108]

Reinforcement	Density (g/cm^3)	Melting point (°C)	Elastic modulus (GPa)	Vickers Hardness (GPa)	CTE at RT ($x10^{-6}/°C$)
Ti	4.57	1668	110	2.2	8.6
TiB	4.56	2200	425-480	17.7	7.15
TiB_2	4.52	2980	529	21.6	6.2
TiC	4.92	3160	440	31.4	7.95
TiN	5.43	3220	390	22.5	9.35

CTE: Coefficient of thermal expansion. RT: Room temperature.

Although a greater amount of reinforcement improves wear resistance, this could bring unfavourable effect concerning elastic modulus. As shown in **Table 1.4**, ceramic reinforcements have elastic modulus values much higher than Ti; hence, the elastic modulus of TMC will also be higher [111]. Atri et al. [113] reported that the elastic modulus increases from 110 to 160 and 210 MPa for Ti, Ti-30 TiB vol.% and Ti-54 TiB vol.%, respectively. Therefore, the amount of reinforcement must be controlled, looking to achieve balanced properties that lead to improving wear resistance without highly increasing Young's modulus.

Alternatively, for orthopaedic and dental implants, TMC can be used as a coating or develop a functionally graded material (FGM) in unreinforced β-Ti alloys [114], [115]. In this way, surface wear resistance will be improved, maintaining part of the internal properties of the base alloy, such as low elastic modulus. Several works have reported improved wear performance of TMC coatings [111], [115]–[119]. Cui et al. [115] investigated the wear behaviour of Ti/TiN TMC coating on pure titanium and found that TMC coating shows significant lower wear than Ti sample. This fact is attributed to the gradient microstructure developed from the surface inwards, leading to a gradient in properties, with higher hardness and wear resistance at the surface. Similar findings were reported by Das et al. [111] for Ti6Al4V/TiB-TiN TMC coating on pure Ti substrate. They found good interfacial bonding between coating and substrate and similar bioactivity compared to uncoated Ti. So, TiB and TiN as reinforcements are suitable for biomedical applications, due to enhanced wear properties, and no effect on the biocompatibility have been observed.

1.4.2. Surface modifications.

Both bulk and surface properties of implant materials play an essential role in implant success. Bulk properties determine the cytotoxicity and appropriate mechanical behaviour during the implant lifetime. On the other hand, surface properties gain especially relevance after implantation. After implantation, the implant surface is exposed to an aggressive environment, so it must be corrosion resistant; it is continuously in contact with bone tissues; then, the implant surface must be suitable to provide good biological interaction and osseointegration process. Finally, the implant surface is subjected to wear because it withstands cyclic loads; then, it must exhibit high wear resistance. [21]

Achieve a material with good bulk and surface properties is desired for orthopaedic applications. However, to develop a Ti-based material that complies both requirements is usually difficult, since the nature of Ti and its alloys impede obtaining suitable surface properties [5], [120]. Ti-based components exhibit a bioinert behaviour that limits the formation of strong bonding between the implant surface and the surrounding tissue. Moreover, Ti and its alloys are characterised by exhibiting relatively low hardness values, which brings them poor tribocorrosion resistance. Therefore, surface modification techniques are employed to overcome these drawbacks associated with the Ti nature, looking to develop more suitable implant materials that could mimic better with the environment.

Many surface modification treatments are based on obtaining coatings focused on improving the implants' wear and corrosion resistance or biocompatibility. Depending on the nature of the coating, surface roughness, surface hardness, bone/implant interface and osseointegration ability could be adapted to improve the material performance. [121]

1.4.2.1. Nitride coatings.

Low wear resistance is one of the main drawbacks of Ti alloys for load-bearing implants [122], [123]. Wear generates metal ions and wear debris that are related to cell tissue damage and possible further implant loosening, reducing the lifetime of implants [10], [12], [15]. The release of metal ions and wear debris during wear action have been related to cell tissue damage and possible long term implant loosening [9], [30]. These issues can be overcome by surface engineering techniques that have been developed to obtain materials with improved tribological properties by surface hardening since harder materials exhibit better wear performance [124]–[126].

Most of the surface modifications methods to increase wear resistance consist of coating development by physical deposition techniques such as plasma spraying[127], ion implantation [128], [129], physical vapour deposition [130], [131]. Moreover, thermochemical treatments like boriding, oxidation, carburising and nitriding have also been broadly used to improve the surface hardness of titanium alloys [132].

Titanium nitride (TiN) coatings are considered an attractive candidate to protect Ti surface against wear, since they exhibit high hardness, and thus, increased wear resistance, high corrosion resistance, good biocompatibility, haemocompatibility, chemical stability and good interfacial bonding between the coating and substrates [126], [133]–[135]. TiN-coated orthopaedic implants, indeed, are already commercially available. Corin Group employs TiN coated knee and ankle implants which are obtained by plasma spraying technique. They state a reduction of 60% and 80% in the wear rate and metal ion release, respectively, compared to CrCo alloys. [136].

Nitriding treatments have been successfully used for Ti protection against wear. There are different kinds of nitriding methods, like ion-beam, laser, plasma and gas. All these involve interactions between nitrogen and the metal surface to produce a hard external layer composed of TiN and Ti_2N phases that protects Ti substrate [137]–[140]. Moreover, due to the high affinity of Ti with nitrogen, nitrogen is able to diffuse inward, having a strengthening effect, by interstitial solid solution in α-Ti. As nitrogen reacts with the Ti substrate, a diffusion zone is formed, producing a hardness gradient. Hardness values decrease from the surface inward due to the decrease in nitrogen concentration. [115], [141], [142]. It has been reported that nitrided Ti alloys hardness varies as follow: >1500 $HV_{0.5}$ at the surface (nitride layer), between 700-900 $HV_{0.5}$ in the diffusion zone, while the core exhibits about 150-400 $HV_{0.5}$ [141]. Zhecheva et al. [142] investigated the effect of gas nitriding treatment in four commercial Ti alloys: two near-α alloys, Ti-8Al-1Mo-1V, Ti-6Al-2Sn-4Zr-2Mo; one biphasic (α+β), Ti-6Al-4V, and one near-β, Ti-10V.2Fe-3Al. After gas nitriding at 850 °C for 10 h, surface hardness values vary from 570-700 $HK_{0.1}$, while the cores exhibit between 350-410 $HK_{0.1}$. In all cases, the diffusion zone was at least 100 μm.

The hardness increases depend on the diffusion kinetics of nitrogen; hence alloying elements play an important role. Alloying elements can alter the diffusion front of nitrogen, since the diffusivity and solubility of nitrogen in each element may vary. Moreover, usually the highest nitride layer thickness, the greatest hardness improvement is achieved. It is considered that both nitride layer thickness and diffusion region increase with increasing nitriding temperature, which, usually, is found between 0.55 and 0.65 of the solidus temperature. [141], [143], [144]

1.4.2.2. *Bioactive coatings.*

Although titanium is a biocompatible metal, it is bio-inert, which means biological interactions with the tissue do not occur. The absence of bioactivity limits the growth of bone tissue through the implant surface, and therefore the fixation of the implant. Moreover, inflammatory response and early infection due to foreign body response are common issues in hip implant surgery. Bio-functionalised Ti alloys are required to solve these drawbacks. Cell adhesion, proliferation, and osseointegration are promoted by incorporating bioactive elements found in natural bone, like calcium (Ca), phosphorous (P) and magnesium (Mg) [145]. In contrast, infections could be prevented by adding antimicrobial agents as Ag, Zn and Cu, which have been shown to inhibit the adhesion of bacteria on the material surface, thus reducing the infection risk [145].

Along with biocompatibility, implant surface features, such as roughness, chemical composition, wettability, and morphology, determine biomaterials' biological response and viability. So, the study and optimisation of these factors is considered decisive for developing and designing implant materials.

Surface modification techniques have been developed, focused on adapting the implant surface features to mimic the surrounding bone tissue with the aim to provide a better biological response [114]. These include ion implantation[128], [129], sol-gel method [146], [147], thermal spraying [148], [149], chemical vapour deposition [150], [151], physical vapour deposition [130], [131], and micro-arc oxidation (MAO) [152]–[155]. Among these surface treatments, MAO has gained attention because of its versatility to produce biocompatible coatings.

MAO is a low-cost electrochemical treatment that does not need expensive equipment and offers the possibility to coat complex shapes. The coating obtained presents excellent adhesion with the substrate. Bio-functionalised MAO surfaces improve osseointegration and promote *in vivo* bone growth [145]. Furthermore, it is known that corrosion and wear behaviour is also improved due to the formation of TiO_2. [156]–[158]

MAO treatments combine electrochemical oxidation, plasma chemical reaction and thermal diffusion in an electrolyte bath [159]. It consists of immersing the sample in an electrolyte bath; then, an electric current passes through the sample. The sample acts as the anode, while platinum or stainless steel is used as cathode. During MAO treatment, a TiO_2 layer is formed by electrochemical oxidation. As the TiO_2 layer grows, localised spark discharges are produced, which raise the temperature in these zones. This temperature increase produces the melting of the TiO_2, which facilitates the incorporation of bioactive species into the coating during solidification. TiO_2 can be formed as anatase, rutile or amorphous titania, depending on the temperature and pressure during the MAO process. [160]

MAO treatments are typically performed using a voltage between 250-450 V during short times, about 1-10 min [114], [145]. MAO treatment provides a multiscale volcano-like porous and rough coating, maintaining the starting properties of the alloys. Porous coatings, showing moderated roughness, favour the biological response, providing a more natural environment for cell attachment and enhancing cell migration and proliferation [161]–[163]. The features of MAO coatings depend highly on operating conditions. Overall, it is considered that pores size increases as applied voltage and time increase. Even though pore diameter increases with time, the number of pores at the surface decreases [159]. MAO treated Ti-13Zr-13Nb exhibit higher roughness an increased average pore diameter, varying from 1.8 to 26.8 μm as voltage increases from 200 to 400 V [164]. Moreover, it has been reported that higher voltage (500 V) induce apatite formation; however, at very high voltage, the apatite formed could cover the surface, destroying the porous structure, which may limit the bone growth into the implant surface [165].

MAO is a versatile method since the chemical composition of coatings can be easily modified by varying the electrolyte bath composition. It is possible to add both bioactive and antibacterial agents into the electrolyte bath [163], [166]. In general, it is sought that MAO coating achieves a Ca/P ratio close to hydroxyapatite (1.67) in order to stimulate the osteogenic differentiation of cells and promote bone growth. Electrolytes containing calcium acetate and β-glycerophosphate, as Ca and P sources, are frequently found in the bibliography [167]–[170]. On the other hand, it has been stated that electrolytes containing nanoparticles (NPs) exhibit improved tribological behaviour, high corrosion resistance and higher antibacterial effect. Roknian et al. [171] evaluated the effect of ZnO NPs on titanium samples treated by MAO. They found that the corrosion resistance of samples containing 15 g/L of ZnO is 27 higher than that obtained without ZnO NPs. Furthermore, they report that as the ZnO NPs concentration increases from 5 to 15 g/L, the bacteria colonies (Staphylococcus aureus and Escherichia coli) decreases. Samples without ZnO NPs presented a limited antibacterial effect, but higher than the uncoated sample. This fact suggests that the rutile and anatase in the coating are beneficial, enhancing the antibacterial effect. Several authors stated that the presence of anatase and rutile might enhance the biological, electrochemical and tribological properties of Ti alloys [169]. Anatase contributes to enhanced cell behaviour and promotes apatite formation in simulated body fluid [172], whereas rutile provides a reduction of coefficient of friction, having a self-lubricant effect, and improves wear resistance. [160], [169], [173]

References

[1] V. Hasirci and N. Hasirci, *Fundamentals of Biomaterials*. New York: Springer, 2018.

[2] G. Kapusetti, N. More, and M. Choppadandi, "Introduction to Ideal Characteristics and Advanced Biomedical Applications of Biomaterials," in *Biomedical Engineering and its Applications in Healthcare*, P. Sudip, Ed. Singapore: Springer Nature, 2019, pp. 171–204.

[3] T. Hanawa, "Research and development of metals for medical devices based on clinical needs," *Sci. Technol. Adv. Mater.*, vol. 13, no. 6, 2012.

[4] C. Y. Hu and T. R. Yoon, "Recent updates for biomaterials used in total hip arthroplasty," *Biomater. Res.*, vol. 22, no. 1, pp. 1–12, 2018.

[5] S. Devgan and S. S. Sidhu, "Evolution of surface modification trends in bone related biomaterials: A review," *Mater. Chem. Phys.*, vol. 233, pp. 68–78, 2019.

[6] M. Merola and S. Affatato, "Materials for Hip Prostheses: A Review of Wear and Loading Considerations," *Materials (Basel).*, vol. 12, no. 495, 2019.

[7] M. I. Z. Ridzwan, S. Shuib, A. Y. Hassan, A. A. Shokri, and M. N. Mohammad Ibrahim, "Problem of stress shielding and improvement to the hip implant designs: A review," *Journal of Medical Sciences*, vol. 7, no. 3. pp. 460–467, 2007.

[8] V. Sáenz and E. Fuentes, "Titanium and Titanium alloys as Biomaterials," in *Tribology-Fundamentals and Advancements*, IntenchOpen, 2013, pp. 155–181.

[9] M. B. Nasab, M. R. and Hassan, and B. Bin Sahari, "Metallic Biomaterials of Knee and Hip-A Review," *Trends Biomater. Artif. Organs*, vol. 24, no. 2, pp. 69–82, 2010.

[10] Q. Chen and G. A. Thouas, "Metallic implant biomaterials," *Mater. Sci. Eng. R Reports*, vol. 87, pp. 1–57, 2015.

[11] L. Cvrcek and M. Horáková, "Plasma Modified Polymeric Materials for Implant Applications," in *Non-Thermal Plasma Technology for Polymeric Materials*, T. Sabu, M. Miran, C. Uros, S. Petr, and P. Praveen K, Eds. Amsterdam: Elsevier Inc, 2019, pp. 367–407.

[12] M. Kaur and K. Singh, "Review on titanium and titanium based alloys as biomaterials for orthopaedic applications," *Mater. Sci. Eng. C*, vol. 102, pp. 844–862, 2019.

[13] Q. Chen and G. A. Thouas, "Metallic implant biomaterials," *Mater. Sci. Eng. R*, vol. 87, pp. 1–57, 2015.

[14] R. Narayan, *ASM Handbook Volume 23: Materials for Medical Devices*, vol. 23. Ohio: ASM International, 2012.

[15] M. Abdel-Hady Gepreel and M. Niinomi, "Biocompatibility of Ti-alloys for long-term implantation," *J. Mech. Behav. Biomed. Mater.*, vol. 20, pp. 407–415, 2013.

[16] G. He, P. Liu, and Q. Tan, "Porous titanium materials with entangled wire structure for load-bearing biomedical applications," *J. Mech. Behav. Biomed. Mater.*, vol. 5, pp. 16–31, 2012.

[17] K. Palka and R. Pokrowiecki, "Porous Titanium Implants: A Review," *Adv. Eng.*

Mater., p. 1700648, 2018.

[18] M. Niinomi, "Mechanical biocompatibilities of titanium alloys for biomedical applications," *J. Mech. Behav. Biomed. Mater.*, vol. 1, no. 1, pp. 30–42, 2008.

[19] H. Attar, S. Ehtemam-haghighi, N. Soro, D. Kent, and M. S. Dargusch, "Additive manufacturing of low-cost porous titanium-based composites for biomedical applications: Advantages, challenges and opinion for future development," *J. Alloys Compd.*, vol. 827, p. 154263, 2020.

[20] T. Akahori, M. Niinomi, H. Fukui, M. Ogawa, and H. Toda, "Improvement in fatigue characteristics of newly developed beta type titanium alloy for biomedical applications by thermo-mechanical treatments," *Mater. Sci. Eng. C*, vol. 25, no. 3, pp. 248–254, 2005.

[21] Y. Kirmanidou *et al.*, "New Ti-Alloys and Surface Modifications to Improve the Mechanical Properties and the Biological Response to Orthopedic and Dental Implants: A Review," *Biomed Res. Int.*, vol. 2016, p. 2908570, 2016.

[22] M. Delshadmanesh, G. Khatibi, M. Z. Ghomsheh, M. Lederer, M. Zehetbauer, and H. Danninger, "Influence of microstructure on fatigue of biocompatible β-phase Ti-45Nb," *Mater. Sci. Eng. A*, vol. 706, pp. 83–94, 2017.

[23] C. N. Elias, J. H. C. Lima, R. Valiev, and M. A. Meyers, "Biomedical applications of titanium and its alloys," *Jom*, vol. 60, no. 3, pp. 46–49, 2008.

[24] G. Lutjering and J. Williams, *Titanium*, 2nd editio. Berlin: Springer, 2007.

[25] Z. Z. Fang *et al.*, "Powder metallurgy of titanium-past, present, and future," *Int. Mater. Rev.*, vol. 63, no. 7, pp. 407–459, 2017.

[26] W. Sha and S. Malinov, *Titanium alloys: modelling of microstructure, properties and applications*. Cambrige: Woodhead Publishing Limited, 2009.

[27] C. Leyens and M. Peters, *Titanium and Titanium Alloys: Fundamentals and Applications*. 2003.

[28] Y. Oshida, "Materials Classification," in *Bioscience and Bioengineering of Titanium Materials*, 1st Editio., Elsevier Science, 2006, pp. 11–22.

[29] L. Zhang and L. Chen, "A Review on Biomedical Titanium Alloys: Recent Progress and Prospect," *Adv. Eng. Mater.*, 2019.

[30] M. Long and H. J. Rack, "Titanium alloys in total joint replacement- a materials science perspective," *Biomaterials*, vol. 19, pp. 1621–1639, 1998.

[31] C. Leyens and M. Peters, *Titanium and Titanium Alloys*. Weinheim: WILEY-VCH, 2003.

[32] K. S. Krishnan and R. S. Mishra, "Titanium Alloys," in *Metallurgy and Design of Alloys with Hierarchical Microstructures*, K. S. Krishnan and R. S. Mishra, Eds. E, 2017, pp. 177–288.

[33] R. Prakash Kolli and A. Devaraj, "A Review of Metastable Beta Titanium Alloys," *Metals (Basel).*, vol. 506, no. 8, 2018.

[34] Y. Okazaki, Y. Ito, A. Ito, and T. Tateishi, "Effect of Alloying Elements on Mechanical Properties of Titanium Alloys for Medical Implants," *Mater. Trans. JIM*, vol. 34, no. 12, pp. 1217–1222, 1993.

[35] F. H. S. Froes, M. N. Gungor, and M. A. Imam, "Cost-Affordable Titanium: The Component Fabrication Perspective," *JOM*, vol. 59, pp. 28–31, 2007.

[36] Z. Zak Fang and P. Sun, "Pathways to Optimize Performance/Cost Ratio of Powder Metallurgy Titanium- A Perspective," *Key Eng. Mater.*, vol. 520, pp. 15–23, 2012.

[37] F. Froes, "A Historical Perspective of Titanium Powder Metallurgy," in *Titanium Powder Metallurgy: Science, Technology and Application*, First edii., M. Qian and F. Froes, Eds. Waltham: Butterworth-Heinemann, 2015, pp. 1–21.

[38] Q. Zhao, Y. Chen, Y. Xu, R. Torrens, L. Bolzoni, and F. Yang, "Cost-affordable and quali fi ed powder metallurgy metastable beta titanium alloy by designing short-process consolidation and processing," *Mater. Des.*, vol. 200, p. 109457, 2021.

[39] A. Hidalgo Amherd, R. Frykholm, T. Ebel, and F. Pyczak, "Powder Metallurgy Strategies to Improve Properties and Processing of Titanium Alloys: A Review," *Adv. Eng. Mater.*, vol. 19, no. 6, pp. 1–14, 2017.

[40] H. Sibum, "Titanium and Titanium Alloys – From Raw Material to Semi-finished Products," in *Titanium and Titanium Alloys. Fundamentals and Applications*, C. Leyens and M. Peters, Eds. WILEY-VCH, 2003, pp. 231–245.

[41] K. S. Narasimhan and M. O. H. Amuda, "Powder Characterization," *Ref. Modul. Mater. Sci. Mater. Eng.*, 2017.

[42] C. G. McCracken, D. P. Barbis, and R. C. Deeter, "Key characteristics of hydride – dehydride titanium powder," *Powder Metall.*, vol. 54, no. 3, pp. 180–183, 2011.

[43] E. Baril, L. P. Lefebvre, and Y. Thomas, "Interstitial elements in titanium powder metallurgy: sources and control," *Powder Metall.*, vol. 54, no. 3, pp. 183–187, 2011.

[44] F. Thümmler and W. Thomma, "The sintering process," *Metall. Rev.*, vol. 115, pp. 69–108, 1967.

[45] I. E. Anderson, E. M. H. White, and R. Dehoff, "Feedstock powder processing research needs for additive manufacturing development," *Curr. Opin. Solid State Mater. Sci.*, vol. 22, pp. 8–15, 2018.

[46] S. Eddine, M. Letenneur, C. Alex, and V. Brailovski, "Influence of particle morphology and size distribution on the powder flowability and laser powder bed fusion manufacturability of Ti-6Al-4V alloy," *Addit. Manuf.*, vol. 31, p. 100929, 2020.

[47] L. Bolzoni and E. Gordo, "Quantifying the properties of low-cost powder metallurgy titanium alloys," *Mater. Sci. Eng. A*, vol. 687, pp. 47–53, 2017.

[48] C. Wang, Y. Zhang, S. Xiao, and Y. Chen, "Sintering densification of titanium hydride powders," *Mater. Manuf. Process.*, vol. 32, no. 5, pp. 517–522, 2017.

[49] L. Mei, C. Wang, Y. Wei, S. Xiao, and Y. Chen, "Effects of hydrogen content on powder metallurgy characteristic of titanium hydrides," *Int. J. Hydrogen Energy*, vol. 43, no. 14, pp. 7102–7107, 2018.

[50] O. Ivasishin and V. Moxson, "Low-cost titanium hydride powder metallurgy," in *Titanium Powder Metallurgy*, Elsevier Inc., 2015, pp. 117–148.

[51] I. M. Robertson and G. B. Schaffer, "Comparison of sintering of titanium and titanium hydride powders," *Powder Metall.*, vol. 53, no. 1, pp. 12–19, 2010.

[52] D. H. Savvakin, M. M. Humenyak, M. V Matviichuk, and O. H. Molyar, “Role of Hydrogen in the Process of Sintering of Titanium Powders,” *Mater. Sci.*, vol. 47, no. 5, pp. 72–81, 2012.

[53] E. Nyberg, M. Miller, K. Simmons, and S. Weil, “Manufactures ‘need better quality titanium PM powders,’” *Met. Powder Rep.*, vol. 60, no. 10, pp. 8–13, 2005.

[54] J. D. Paramore, Z. Fang, and P. Sun, “Hydrogen sintering of Titanium and its alloys,” in *Titanium Powder Metallurgy*, Elsevier Inc., 2015, pp. 163–182.

[55] D. Y. Kovalev, V. K. Prokudina, V. I. Ratnikov, and V. I. Ponomarev, “Thermal decomposition of TiH2: A TRXRD study,” *Int. J. Self-Propagating High-Temperature Synth.*, vol. 19, no. 4, pp. 253–257, 2010.

[56] D. Lehmhus and G. Rausch, “Tailoring titanium hydride decomposition kinetics by annealing in various atmospheres,” *Adv. Eng. Mater.*, vol. 6, no. 5, pp. 313–330, 2004.

[57] N. Peillon, J. B. Fruhauf, S. Gourdet, J. Feraille, S. Saunier, and C. Desrayaud, “Effect of TiH2 in the preparation of MMC Ti based with TiC reinforcement,” *J. Alloys Compd.*, vol. 619, pp. 157–164, 2015.

[58] V. Bhosle, E. G. Baburaj, M. Miranova, and K. Salama, “Dehydrogenation of TiH2,” *Mater. Sci. Eng. A*, vol. 356, pp. 190–199, 2003.

[59] H. Liu, P. He, J. C. Feng, and J. Cao, “Kinetic study on nonisothermal dehydrogenation of TiH2 powders,” *Int. J. Hydrogen Energy*, vol. 34, pp. 3018–3025, 2009.

[60] Y. L. Zhou *et al.*, “In-situ EXAFS study on the thermal decomposition of TiH2,” *Chinese Phys. C*, vol. 38, no. 3, pp. 1–9, 2014.

[61] C. Jiménez *et al.*, “Decomposition of TiH2 studied in situ by synchrotron X-ray and neutron diffraction,” *Acta Mater.*, vol. 59, pp. 6318–6330, 2011.

[62] F. Von Zeppelin, M. Hirscher, H. Stanzick, and J. Banhart, “Desorption of hydrogen from blowing agents used for foaming metals,” *Compos. Sci. Technol.*, vol. 63, pp. 2293–2300, 2003.

[63] Z. Ying-li *et al.*, “In-situ EXAFS study on the thermal decomposition of TiH 2 *,” no. 10875143, pp. 1–9.

[64] M. Ma *et al.*, “Phase transformations of titanium hydride in thermal desorption process with different heating rates,” *Int. J. Hydrogen Energy*, vol. 40, pp. 8926–8934, 2015.

[65] G. Chen, K. D. Liss, G. Auchterlonie, H. Tang, and P. Cao, “Dehydrogenation and Sintering of TiH2: An In Situ Study,” *Metall. Mater. Trans. A Phys. Metall. Mater. Sci.*, vol. 48A, no. 6, pp. 2949–2959, 2017.

[66] H. R. Z. Sandim, B. V. Morante, and P. A. Suzuki, “Kinetics of thermal decomposition of titanium hydride powder using in situ High-temperature X-ray Diffraction (HTXRD),” *Mater. Res.*, vol. 8, no. 3, pp. 293–297, 2005.

[67] Y. Li, X. M. Chou, L. Yu, Y. Li, X. M. Chou, and L. Yu, “Dehydrogenation debinding process of MIM titanium alloys by TiH2 powder,” vol. 5899, no. March, 2016.

[68] K. G. Prashanth, “Influence of Mechanical Activation on Decomposition of Titanium Hydride,” *Mater. Manuf. Process.*, vol. 25, pp. 974–977, 2010.

[69] B. Matijasevic-lux, J. Banhart, S. Fiechter, O. Gorke, and N. Wanderka, "Modification of titanium hydride for improved aluminium foam manufacture," *Acta Mater.*, vol. 54, pp. 1887–1900, 2006.

[70] S. Wu *et al.*, "Hydrogen release from titanium hydride in foaming of orthopedic NiTi scaffolds," *Acta Biomater.*, vol. 7, no. 3, pp. 1387–1397, 2011.

[71] D. Yang and B. Hur, "The relationship between thermal decomposition properties of titanium hydride and the Al alloy melt foaming process," *Mater. Lett.*, vol. 60, pp. 3635–3641, 2006.

[72] B. Sharma, S. K. Vajpai, and K. Ameyama, "Microstructure and properties of beta Ti–Nb alloy prepared by powder metallurgy route using titanium hydride powder," *J. Alloys Compd.*, vol. 656, pp. 978–986, Jan. 2016.

[73] C. Chirico, S. Tsipas, F. Toptan, and E. Gordo, "Development of Ti–Nb and Ti–Nb–Fe beta alloys from TiH2 powders," *Powder Metall.*, vol. 62, no. 1, pp. 44–53, 2019.

[74] Y. Zhang *et al.*, "Fabrication of Low-cost Ti-1Al-8V-5Fe by Powder Metallurgy with TiH 2 and FeV 80 Master Alloy Fabrication of low-cost Ti-1Al-8V-5Fe by powder metallurgy with TiH 2 and FeV 80 alloy," *Mater. Manuf. Process.*, vol. 32, no. 16, pp. 1869–1873, 2017.

[75] L. Bolzoni, "Low-cost Fe-bearing powder metallurgy Ti alloys," *Met. Powder Rep.*, vol. 74, no. 6, pp. 308–313, 2019.

[76] Y. Zhang, D. Sun, J. Cheng, J. Kit, H. Tsoi, and J. Chen, "Mechanical and biological properties of Ti-(0-25 wt %) Nb alloys for biomedical implants application," *Regen. Biomater.*, vol. 7, no. 1, pp. 119–127, 2020.

[77] J. O'Flynn and S. F. Corbin, "The influence of iron powder size on pore formation, densification and homogenization during blended elemental sintering of Ti-2.5Fe," *J. Alloys Compd.*, vol. 618, pp. 437–448, 2015.

[78] W. Wei, Y. Liu, K. Zhou, and B. Huang, "Effect of Fe addition on sintering behaviour of titanium powder," *Powder Metall.*, vol. 46, no. 3, pp. 246–250, 2003.

[79] O. M. Ivasishin, V. Bondarchuk, and D. G. Savvakin, "Diffusion during Powder Metallurgy Synthesis of Titanium Alloys," *Defect Diffus. Forum*, vol. 277, pp. 177–185, 2008.

[80] P. G. Esteban, L. Bolzoni, E. M. Ruiz-Navas, and E. Gordo, "PM processing and characterisation of Ti-7Fe low cost titanium alloys," *Powder Metall.*, vol. 54, no. 3, pp. 242–252, 2011.

[81] Y. Liu, L. F. Chen, H. P. Tang, C. T. Liu, B. Liu, and B. Y. Huang, "Design of powder metallurgy titanium alloys and composites," *Mater. Sci. Eng. A*, vol. 418, pp. 25–35, 2006.

[82] L. Ponsonnet *et al.*, "Relationship between surface properties (roughness, wettability) of titanium and titanium alloys and cell behaviour," *Mater. Sci. Eng. C*, vol. 23, pp. 551–560, 2003.

[83] X. Liu, P. K. Chu, and C. Ding, "Surface modification of titanium, titanium alloys, and related materials for biomedical applications," *Mater. Sci. Eng. R Reports*, vol. 47, no.

3–4, pp. 49–121, 2004.

[84] P. Akira *et al.*, "Effect of Thermomechanical Treatments on the Phases, Microstructure, Microhardness and Young's Modulus of Ti-25Ta-Zr Alloys," *Materials (Basel).*, vol. 12, p. 3210, 2019.

[85] G. He and M. Hagiwara, "Ti alloy design strategy for biomedical applications B," *Mater. Sci. Eng. C*, vol. 26, pp. 14–19, 2006.

[86] J. Matthew and J. Danachie, "Heat Treating Titanium and its Alloys," *Heat Treat. Prog.*, vol. 1, no. July, pp. 47–57, 2001.

[87] P. Yadav and K. K. Saxena, "Effect of heat-treatment on microstructure and mechanical properties of Ti alloys: An overview," *Mater. Today Proc.*, vol. 26, pp. 2546–2557, 2020.

[88] O. M. Ivasishin and P. Markovsky, "Enhancing the mechanical properties of titanium alloys with rapid heat treatment," *JOM*, vol. July, pp. 48–52, 1996.

[89] M. Santhosh, R. Geetha, and M. Nageswara Rao, "Recent Developments in Heat Treatment of Beta Titanium Alloys for Aerospace Applications," *Trans. Indian Inst. Met.*, vol. 70, no. 7, pp. 1681–1688, 2017.

[90] S. Rajan Soundararajan, J. Vishnu, G. Manivasagam, and N. Rao Muktinutalapati, "Heat Treatment of Metastable Beta Titanium Alloys," in *Welding*, S. Alfaro, Ed. IntenchOpen, 2021.

[91] N. Yumak and K. Aslantas, "A review on heat treatment efficiency in metastable β titanium alloys: the role of treatment process and parameters," *J. Mater. Res. Technol.*, vol. 9, no. 6, pp. 15360–15380, 2020.

[92] G. Lutjering and J. Williams, "Fundamental Aspects," in *Titanium*, 2nd ed., G. Lutjering and J. Willimas, Eds. Berlin, 2007, pp. 15–52.

[93] C.-L. Li, X.-J. Mi, W.-J. Ye, S.-X. Hui, Y. Yu, and W.-Q. Wang, "Effect of solution temperature on microstructures and tensile properties of high strength Ti-6Cr-5Mo-5V-4Al alloy," *Mater. Sci. Eng. A*, vol. 578, pp. 103–109, 2013.

[94] Z. Wang, L. Liu, L. Zhang, J. Sheng, D. Wu, and M. Yuan, "Effect of Heat Treatment on the Microstructure and Mechanical Properties of High-Strength Ti6Al4V5Fe Alloy," *Mater. Trans.*, vol. 60, no. 2, pp. 269–276, 2019.

[95] M. Motyka, K. Kubiak, J. Sieniawski, and W. Ziaja, "Phase Transformations and Characterization of α+β Titanium Alloys," in *Comprehensive Materials Processing*, vol. 2, S. Hashmi, G. Ferreira Batalha, C. J. Van Tyne, and Y. Bekir, Eds. Elsevier, 2014, pp. 7–36.

[96] M. Bönisch *et al.*, "Thermal stability and phase transformations of martensitic Ti-Nb alloys," *Sci. Technol. Adv. Mater.*, vol. 14, no. 5, 2013.

[97] S. Ehtemam-Haghighi, Y. Liu, G. Cao, and L.-C. Zhang, "Influence of Nb on the $\beta \rightarrow \alpha''$ martensitic phase transformation and properties of the newly designed Ti-Fe-Nb alloys," *Mater. Sci. Eng. C*, vol. 60, pp. 503–510, 2016.

[98] M. Bönisch, T. Waitz, M. Calin, W. Skrotzki, and J. Eckert, "Tailoring the Bain strain of martensitic transformations in Ti-Nb alloys by controlling the Nb content," *Int. J.*

Plast., vol. 85, pp. 190–202, 2016.

[99] Q. Wang *et al.*, "Effect of Nb content on microstructure, property and in vitro apatite-forming capability of Ti-Nb alloys fabricated via selective laser melting," *Mater. Des.*, vol. 126, pp. 268–277, 2017.

[100] M. Motyka, A. Baran-Sadleja, J. Sieniawski, M. Wierzbinska, and K. Gancarczyk, "Decomposition of deformed $\alpha'(\alpha'')$ martensitic phase in Ti-6Al-4V alloy," *Mater. Sci. Technol.*, vol. 35, no. 3, pp. 260–272, 2019.

[101] C. Sauer and G. Luetjering, "Thermo-mechanical processing of high strength β-titanium alloys and effects on microstructure and properties," *J. Mater. Process. Technol.*, vol. 117, pp. 311–317, 2001.

[102] W. Zhang, Y. Liu, B. Liu, X. Li, H. Wu, and J. Qiu, "A new titanium matrix composite reinforced with Ti-36Nb-2Ta-3Zr-0.35O wire," *Mater. Des.*, vol. 117, pp. 289–297, 2017.

[103] M. D. Hayat, H. Singh, Z. He, and P. Cao, "Titanium metal matrix composites: An overview," *Compos. Part A Appl. Sci. Manuf.*, vol. 121, no. April, pp. 418–438, 2019.

[104] S. C. Tjong and Y. Mai, "Processing-structure-property aspects of particulate- and whisker-reinforced titanium matrix composites," *Compos. Sci. Technol.*, vol. 68, pp. 583–601, 2008.

[105] B. C. Leyens, J. Hausmann, and J. Kumpfert, "Continuous Fiber Reinforced Titanium Matrix Composites: Fabrication, Properties and Applications," *Adv. Eng. Mater.*, vol. 5, no. 6, pp. 399–410, 2003.

[106] G. Lutjering and J. Williams, "Titanium Matrix Composite," in *Titanium*, 2nd Editio., he: Springer Berlin Heidelberg, 2007, pp. 367–382.

[107] K. S. Ravi Chandran, K. B. Panda, and S. S. Sahay, "TiBw-reinforced Ti composites: Processing, properties, application prospects, and research needs," *Jom*, vol. 56, no. 5, pp. 42–48, 2004.

[108] T. Saito, "The automotive application of discontinuously reinforced TiB-Ti composites," *Jom*, vol. 56, no. 5, pp. 33–36, 2004.

[109] J. A. Otte, J. Zou, R. Patel, M. Lu, and M. S. Dargusch, "TiB Nanowhisker Reinforced Titanium Matrix Composite with Improved Hardness for Biomedical Applications," *Nanomaterials*, vol. 10, p. 2480, 2020.

[110] S. Kundu, M. Hussain, V. Kumar, S. Kumar, and A. K. Das, "Direct metal laser sintering of TiN reinforced Ti6Al4V alloy based metal matrix composite: Fabrication and characterization," *Int. J. Adv. Manuf. Technol.*, vol. 97, no. 5–8, pp. 2635–2646, 2018.

[111] M. Das, K. Bhattacharya, S. A. Dittrick, and C. Mandal, "In situ synthesized TiB-TiN reinforced Ti6Al4V alloy composite coatings: Microstructure, tribological and in-vitro biocompatibility," *J. Mech. Behav. Biomed. Mater.*, vol. 29, pp. 259–271, 2014.

[112] B.-J. Choi, I.-Y. Kim, Y.-Z. Lee, and Y.-J. Kim, "Microstructure and friction/ wear behavior of (TiB+TiC) particulate-reinforced titanium matrix composites," *Wear*, vol. 318, pp. 68–77, 2014.

[113] R. R. Atri, K. S. Ravichandran, and S. K. Jha, "Elastic properties of in-situ processed Ti-TiB composites measured by impulse excitation of vibration," *Mater. Sci. Eng. A*,

vol. 271, pp. 150–159, 1999.

[114] I. Çaha, A. C. Alves, L. . Rocha, and F. Toptan, "A Review on Bio-functionalization of β-Ti Alloys," *J. Bio- Tribo-Corrosion*, vol. 135, no. 6, 2020.

[115] Z. D. Cui, S. L. Zhu, H. C. Man, and X. J. Yang, "Microstructure and wear performance of gradient Ti/TiN metal matrix composite coating synthesized using a gas nitriding technology," *Surf. Coatings Technol.*, vol. 190, no. 2–3, pp. 309–313, 2005.

[116] J. J. Candel, V. Amigó, J. A. Ramos, and D. Busquets, "Sliding wear resistance of TiCp reinforced titanium composite coating produced by laser cladding," *Surf. Coatings Technol.*, vol. 204, pp. 3161–3166, 2010.

[117] Y. Lin, Y. Lei, H. Fu, and J. Lin, "Mechanical properties and toughening mechanism of TiB2/NiTi reinforced titanium matrix composite coating by laser cladding," *Mater. Des.*, vol. 80, pp. 82–88, 2015.

[118] Y. Lin, Z. Lin, Q. Chen, Y. Lei, and H. Fu, "Laser in-situ synthesis of titanium matrix composite coating with TiB-Ti network-like structure reinforcement," *Trans. Nonferrous Met. Soc. China*, vol. 29, pp. 1665–1676, 2019.

[119] V. Ocelík, D. Matthews, and J. T. . De Hosson, "Sliding wear resistance of metal matrix composite layers prepared by high power laser," *Surf. Coatings Technol.*, vol. 197, pp. 303–315, 2005.

[120] X. Liu, P. K. Chu, and C. Ding, "Surface modification of titanium, titanium alloys, and related materials for biomedical applications," *Mater. Sci. Eng. R Reports*, vol. 47, no. 2004, pp. 49–121, 2005.

[121] A. A. John, S. K. Jaganathan, E. Supriyanto, and A. Manikandan, "Surface modification of titanium and its alloys for the enhancement of osseointegration in orthopaedics," *Curr. Sci.*, vol. 111, no. 6, pp. 1003–1015, 2016.

[122] OECD, "Health at a Glance 2011: OECD Indicators," *OECD Publ.*, 2011.

[123] K. . Sipek, M. . Lyvers, and M. . Mathew, "Failure Causes in Total Hip Replacements: A Review.," *Austin J. Orthop. Rheumatol.*, vol. 5, no. 1, 2018.

[124] H. Mohseni, P. Nandwana, A. Tsoi, R. Banerjee, and T. W. Scharf, "In situ nitrided titanium alloys: Microstructural evolution during solidification and wear," *Acta Mater.*, vol. 83, pp. 61–74, 2015.

[125] W. Qu, X. Sun, B. Yuan, K. Li, and Z. Wang, "Tribological behaviour of biomedical Ti – Zr-based shape memory alloys," *Rare Met.*, vol. 36, no. 6, pp. 478–484, 2017.

[126] M. Geetha, A. K. Singh, R. Asokamani, and A. K. Gogia, "Ti based biomaterials, the ultimate choice for orthopaedic implants- A review.," *Prog. Mater. Sci.*, vol. 54, no. 3, pp. 397–425, 2009.

[127] G. M. Ingo, S. Kaciulis, A. Mezzi, T. Valente, F. Casadei, and G. Gusmano, "Characterization of composite titanium nitride coatings prepared by reactive plasma spraying," *Electrochim. Actaochimica*, vol. 50, pp. 4531–4537, 2005.

[128] T. R. Rautray, R. Narayanan, T. Y. Kwon, and K. H. Kim, "Surface modification of titanium and titanium alloys by ion implantation," *J. Biomed. Mater. Res. - Part B Appl. Biomater.*, vol. 93, no. 2, pp. 581–591, 2009.

[129] L. Thair, U. K. Mudali, N. Bhuvaneswaran, K. G. M. Nair, R. Asokamani, and B. Raj, "Nitrogen ion implantation and in vitro corrosion behavior of as-cast Ti-6Al-7Nb alloy," *Corros. Sci.*, vol. 44, pp. 2439–2457, 2002.

[130] R. Ali, M. Sebastiani, and E. Bemporad, "Influence of Ti-TiN multilayer PVD-coatings design on residual stresses and adhesion," *Mater. Des.*, vol. 75, pp. 47–56, 2015.

[131] G. M. Uddin *et al.*, "Experimental investigation of tribo-mechanical and chemical properties of TiN PVD coating on titanium substrate for biomedical implants manufacturing," *Int. J. Adv. Manuf. Technol.*, vol. 102, pp. 1391–1404, 2019.

[132] A. Zhecheva, W. Sha, S. Malinov, and A. Long, "Enhancing the microstructure and properties of titanium alloys through nitriding and other surface engineering methods," *Surf. Coatings Technol.*, vol. 200, no. 7, pp. 2192–2207, 2005.

[133] A. Nemati, M. Sagha, S. Khamseh, E. Alibakhshi, and P. Zarrintaj, "Technology Magnetron-sputtered TixN y thin fi lms applied on titanium-based alloys for biomedical applications: Composition-microstructure-property relationships," *Surf. Coatings Technol.*, vol. 349, pp. 251–259, 2018.

[134] R. P. Van Hove, I. N. Sierevelt, B. J. Van Royen, and P. A. Nolte, "Titanium-Nitride Coating of Orthopaedic Implants: A Review of the Literature," *Biomed Res. Int.*, vol. 2015, p. 485975, 2015.

[135] A. Kurup, P. Dhatrak, and N. Khasnis, "Surface modification techniques of titanium and titanium alloys for biomedical dental applications: A review," *Mater. Today Proc.*, vol. 39, pp. 84–90, 2021.

[136] "Corin Group: UniglideTM," *https://www.coringroup.com/healthcare-professionals/solutions/uniglide/*, 2021. .

[137] F. Yildiz, A. F. Yetim, A. Alsaran, and A. Çelik, "Plasma nitriding behavior of Ti6Al4V orthopedic alloy," *Surf. Coatings Technol.*, vol. 202, no. 11, pp. 2471–2476, 2008.

[138] J. Kang *et al.*, "Tribological behavior of titanium alloy treated by nitriding and surface texturing composite technology," *Materials (Basel).*, vol. 12, no. 2, 2019.

[139] C. W. Chan *et al.*, "Enhancement of wear and corrosion resistance of beta titanium alloy by laser gas alloying with nitrogen," *Appl. Surf. Sci.*, vol. 367, pp. 80–90, 2016.

[140] X. Liu, P. K. Chu, and C. Ding, "Surface modification of titanium, titanium alloys, and related materials for biomedical applications," *Mater. Sci. Eng. R*, vol. 47, pp. 49–121, 2005.

[141] H. Spies, B. Reinhold, K. Wilsdorf, H. Spies, B. Reinhold, and K. Wilsdorf, "Gas nitriding-Process control and nitriding non-ferrous alloys," *Surf. Eng.*, vol. 17, no. 1, pp. 41–54, 2001.

[142] A. Zhecheva, S. Malinov, and W. Sha, "Titanium alloys after surface gas nitriding," *Surf. Coatings Technol.*, vol. 201, no. 6, pp. 2467–2474, 2006.

[143] I. N. Pogrelyuk, "On the problem of intensification of nitriding of titanium alloys," *Met. Sci. Heat Treat.*, vol. 41, no. 5–6, pp. 242–245, 1999.

[144] K. Tokaji, T. Ogawa, and H. Shibata, "The Effects of Gas Nitriding on Fatigue Behavior in Titanium and Titanium Alloys," *J. Mater. Eng. Perform.*, vol. 8, no. 2, pp. 159–167,

1999.

[145] I. A. J. van Hengel, M. W. A. M. Tierolf, L. . Fratila-Apachitei, I. Apachitei, and A. A. Zadpoor, “Antibacterial titanium implants biofunctionalized by plasma electrolytic oxidation with silver, zinc, and copper: a systematic review,” *Int. J. Mol. Sci.*, vol. 22, no. 7, 2021.

[146] E. Peón Avés *et al.*, “Hydroxyapatite coating by sol-gel on Ti-6Al-4V alloy as drug carrier,” *J. Mater. Sci. Mater. Med.*, vol. 20, pp. 543–547, 2009.

[147] H. Q. Nguyen, D. A. Deporter, R. M. Pilliar, N. Valiquette, and R. Yakubovich, “The effect of sol-gel-formed calcium phosphate coatings on bone ingrowth and osteoconductivity of porous-surfaced Ti alloy implants,” *Biomaterials*, vol. 25, no. 5, pp. 865–876, 2004.

[148] C. S. Yip, K. A. Khor, N. L. Loh, and P. Cheang, “Thermal spraying of Ti-6Al-4V/hydroxyapatite composites coatings: Powder processing and post-spray treatment,” *Journal of Materials Processing Technology*, vol. 65. pp. 73–79, 1997.

[149] J. G. Odhiambo, W. G. Li, Y. T. Zhao, and C. L. Li, “Porosity and Its Significance in Plasma-Sprayed Coatings,” *Coatings*, vol. 9, 2019.

[150] Q. An, J. Chen, Z. Tao, W. Ming, and M. Chen, “Experimental investigation on tool wear characteristics of PVD and CVD coatings during face milling of Ti[sbnd]6242S and Ti-555 titanium alloys,” *Int. J. Refract. Met. Hard Mater.*, vol. 86, no. 800, p. 105091, 2020.

[151] J. Li *et al.*, “CVD growth of graphene on NiTi alloy for enhanced biological activity,” *ACS Appl. Mater. Interfaces*, vol. 7, pp. 19876–19881, 2015.

[152] M. Shokouhfar and S. R. Allahkaram, “Formation mechanism and surface characterization of ceramic composite coatings on pure titanium prepared by micro-arc oxidation in electrolytes containing nanoparticles,” *Surf. Coatings Technol.*, vol. 291, pp. 396–405, 2016.

[153] A. Santos-Coquillat, R. Gonzalez Tenorio, M. Mohedano, E. Martinez-Campos, R. Arrabal, and E. Matykina, “Tailoring of antibacterial and osteogenic properties of Ti6Al4V by plasma electrolytic oxidation,” *Appl. Surf. Sci.*, vol. 454, pp. 157–172, 2018.

[154] M. Mohedano, R. Guzman, R. Arrabal, J. . López Lacomba, and E. Matykina, “Bioactive plasma electrolytic oxidation coatings-The role of the composition, microstructure, and electrochemical stability,” *J. Biomed. Mater. Res. B Appl. Mater.*, vol. 101B, no. 8, pp. 1524–1537, 2013.

[155] D. R. N. Correa, L. A. Rocha, A. R. Ribeiro, S. Gemini-piperni, B. S. Archanjo, and T. Hanawa, “Growth mechanisms of Ca- and P-rich MAO films in Ti-15Zr-xMo alloys for osseointegrative implants,” *Surf. Coat. Technol.*, vol. 344, pp. 373–382, 2018.

[156] A. Fattah-Alhosseini, M. Molaei, N. Attarzadeh, K. Babaei, and F. Attarzadeh, “On the enhanced antibacterial activity of plasma electrolytic oxidation (PEO) coatings that incorporate particles: A review,” *Ceram. Int.*, vol. 46, no. 13, pp. 20587–20607, 2020.

[157] M. Shokouhfar and S. R. Allahkaram, “Effect of incorporation of nanoparticles with different composition on wear and corrosion behavior of ceramic coatings developed

on pure titanium by micro arc oxidation," *Surf. Coatings Technol.*, vol. 309, pp. 767–778, 2017.

[158] M. Shokouhfar, C. Dehghanian, M. Montazeri, and A. Baradaran, "Preparation of ceramic coating on Ti substrate by plasma electrolytic oxidation in different electrolytes and evaluation of its corrosion resistance: Part II," *Appl. Surf. Sci.*, vol. 258, no. 7, pp. 2416–2423, 2012.

[159] Y. Wang, H. Yu, C. Chen, and Z. Zhao, "Review of the biocompatibility of micro-arc oxidation coated titanium alloys," *Mater. Des.*, vol. 85, pp. 640–652, 2015.

[160] F. G. Oliveira *et al.*, "Understanding growth mechanisms and tribocorrosion behaviour of porous TiO2 anodic films containing calcium, phosphorous and magnesium," *Appl. Surf. Sci.*, vol. 341, pp. 1–12, 2015.

[161] W. H. Song, S. R. Hyun, and S. H. Hong, "Antibacterial properties of Ag (or Pt)-containing calcium phosphate coatings formed by micro-arc oxidation," *J. Biomed. Mater. Res. Part A*, vol. 88, no. 1, pp. 246–254, 2009.

[162] X. Lu *et al.*, "Plasma electrolytic oxidation coatings with particle additions – A review," *Surf. Coatings Technol.*, vol. 307, pp. 1165–1182, 2016.

[163] C. Garcia-Cabezon *et al.*, "Application of Plasma Electrolytic Oxidation Coating on Powder Metallurgy Ti-6Al-4V for Dental Implants," *Metals (Basel).*, vol. 10, p. 1167, 2020.

[164] M. Dziaduszewska, M. Shimabukuro, T. Seremak, A. Zieliniski, and T. Hanawa, "Effects of Micro-Arc Oxidation Process Parameters on Characteristics of Calcium-Phosphate Containing Oxide Layers on the Selective Laser Melted Ti13Zr13Nb alloy," *Coatings*, vol. 745, no. 10, 2020.

[165] M. Montazeri, C. Dehghanian, M. Shokouhfar, and A. Baradaran, "Investigation of the voltage and time effects on the formation of hydroxyapatite-containing titania prepared by plasma electrolytic oxidation on Ti-6Al-4V alloy and its corrosion behavior," *Appl. Surf. Sci.*, vol. 257, no. 16, pp. 7268–7275, 2011.

[166] B. L. Jiang and Y. M. Wang, "Chapter 5: Plasma electrolytic oxidation treatment of aluminium and titanium alloys," in *Surface Engineering of Light Alloys: Aluminium, Magnesium and Titanium Alloys*, D. Huang, Ed. Woodhead, 2010, pp. 110–154.

[167] A. C. Alves *et al.*, "Effect of bio-functional MAO layers on the electrochemical behaviour of highly porous Ti," *Surf. Coatings Technol.*, vol. 386, p. 125487, 2020.

[168] M. Qadir, Y. Li, K. Munir, and C. Wen, "Calcium Phosphate-Based Composite Coating by Micro-Arc Oxidation (MAO) for Biomedical Application: A Review," *Crit. Rev. Solid State Mater. Sci.*, vol. 43, no. 5, pp. 392–416, 2018.

[169] F. Toptan, A. C. Alves, A. M. P. Pinto, and P. Ponthiaux, "Tribocorrosion behavior of bio-functionalized highly porous titanium," *J. Mech. Behav. Biomed. Mater.*, vol. 69, no. December 2016, pp. 144–152, 2017.

[170] X. He, X. Zhang, X. Wang, and L. Qin, "Review of Antibacterial Activity of Titanium-Based Implants' Surfaces Fabricated by Micro-Arc Oxidation," *Coatings*, vol. 7, no. 3, p. 45, 2017.

[171] M. Roknian, A. Fattah-alhosseini, S. O. Gashti, and M. K. Keshavarz, "Study of the effect of ZnO nanoparticles addition to PEO coatings on pure titanium substrate: Microstructural analysis, antibacterial effect and corrosion behavior of coatings in Ringer's physiological solution," *J. Alloys Compd.*, vol. 740, pp. 330–345, 2018.

[172] A. Dos Santos *et al.*, "A study of the physical, chemical and biological properties of TiO2 coatings produced by micro-arc oxidation in a Ca-P-based electrolyte.," *J. Mater. Sci. Mater. Med.*, vol. 25, no. 7, pp. 1769–1780, 2014.

[173] A. F. Yetim, "Investigation of wear behavior of titanium oxide films, produced by anodic oxidation, on commercially pure titanium in vacuum conditions," *Surf. Coat. Technol.*, vol. 205, pp. 1757–1763, 2010.

CHAPTER 2

Motivation and objectives

CHAPTER 2

2.1. Motivation.

During the last decades, the research and development activities concerning hip implants have gain interest worldwide. A probe of that is the large variety of materials and design of implants available nowadays.

The need to further investigate this research field arises by the increase in the revision surgeries rate, where the prosthesis must be replaced earlier than expected. Prosthesis should ensure safety and effectiveness for at least 20 or 25 years. Nevertheless, in 2012, the European Commission stated that about 80, 75 and 55% of the prosthesis survives successfully, after 15, 20 and 25 years of the surgery, respectively. [1], [2]

It is considered that more than one million of total hip arthroplasty (THA) surgeries are performed every year around the world. According to the Organisation for Economic Co-operation and Development (OECD), the rate of primary THA surgeries increased by 25% between 2000 and 2009 [3]. The OECD also reported that this percentage is expected to continue to rise over time. Revision surgeries rate is also increasing; it is expected the total number of revision surgery will rise by 137% between 2005 and 2030 [4]. This rise is, in part, due to the increase in people's life expectancy owing to improvement in medical care; as well as, the decrease of patient age, generated by the increase in physical activity of people and the practice of extreme sports, which can cause severe injuries. The younger the patient, the higher the probability to be subjected to revision surgery for hip implant replacement, considering the short lifespan of the hip implants.

In 2009, Spain recorded a THA incidence of 93 per 100.000 habitants per year, which means close to 42.700 THA (including primary THA and revision surgery). Thus, taking into account the earlier failure of the implant, around 20% of these prostheses should be replaced after 15 years, which is a large number of new THA to perform. This fact is not desirable, since it implies problems for the patient who must be subjected again to a painful recovery; and also represents a high cost in healthcare, considering the estimated cost for a THA surgery is USD 12.000. [2]

THA surgery improves the quality of life of the patient, relieving the pain and allowing mobility almost immediately. However, this surgery only represents the beginning of treatment since, over time, revision surgery is required to bring back the quality of life and mobility to the patient. [2], [3].

There are long-term issues associated with implant material that reduce the lifespan of the hip prostheses. Many factors are involved in the long-term clinical success of THA procedures. These are associated with the implant material, its design, the expertise of the surgeon, surgical technique, the health status of the patient, patient age, obesity, bone density and gender that influence the recovery process, the post-operative activities, etc. In this work, aspects related to the implant material will be discussed.

Implant loosening, low fatigue strength, high wear level and lack of bioactivity are the leading causes of failure in hip implants [1], [4]–[6]. Implant loosening is produced by the stress-shielding phenomenon caused by the mechanical mismatch due to a significant difference in elastic modulus between bone and implant. The bone exhibits elastic modulus from 4 to 30 GPa [7], while, the currents Ti alloys employed in hip implants, such as Ti6Al4V and Ti6Al7Nb, reach much higher values, about 100-120 GPa [8].

Stress-shielding involves a non-homogeneous stress transfer between the implant and bone [9]. In a healthy femur, the load is carried out from the femur head to the cortical bone. When the bone is subjected to stress, it is continuously remodelled by the osteoclasts cells that dissolve the bone and osteoblasts cells, that allow the ossification forming new bone. Hence, the load/stress transfer helps to maintain the cellular balance between the osteoblasts and osteoclasts in response to the local load conditions. This difference on elastic modulus produces a heterogeneous stress transfer where, the upper femur part carried out a few loads, while the section closes to the stem tip is overloaded [10]. As the regular load transfer has been altered, the cellular behaviour/activity changes and bone resorption may occur in the surrounding region/area to the implant. Over time, implant losses gradually fixation to the bone. When the bone resorption is too high, implant loosening is produced, and the patient would require revision surgery to replace the damaged prosthesis. [1]

Another issue related to metallic prosthesis is the wear and its consequences. Wear damage causes the release of metal ions and wear debris from the implant to the surrounding tissue or bloodstream [5]. Wear debris size is a factor to take into account since, in the nanometric range, it can have nanotoxicity effects. The smaller is the particle size of wear debris, the higher the risk that these particles can be introduced into the cells, changing their biological effect. For instance, wear debris can migrate to the phagosome of macrophages, which activates the osteoclast cells promoting bone resorption [1], [11].

Excessive wear may produce adverse tissue reaction. It has been reported that high concentration of alloying elements, frequently used in hip implant material, such as aluminium (Al), vanadium (V), in Ti-6Al-4V alloy, are associated with adverse effects concerning to cell viability; and long-term health issues, like neurotoxic effects and local inflammation. Besides, Al delays bone mineralisation and has been associated with Alzheimer's disease [12]–[14]. Hence, a suitable implant material must improve wear resistance in Ti alloys, incorporating biocompatible alloying elements, in such way that, if these particles are released, they do not involve toxic effects.

The lack of bioactivity may promote implant failure in the early stage after surgery, as well as, lead to the gradual loosening of the implant in the long term [15], [16]. Although Ti is the most biocompatible metal, it cannot induce or promote bone formation itself, since it cannot form a direct bond with the bone. This fact causes fixation issues that compromise the THA success. Hence, implants must be subjected to surface treatments that modify the topography, incorporating bioactive agents that enhance the osseointegration process between the implant and surrounding bone/tissue. [15]

Therefore, the development of new Ti alloys that allow an increase in the lifetime of hip prostheses, must be focused on achieving a material with an elastic modulus closer to the bone values, with higher wear resistance, that incorporates non-toxic alloying elements and promotes bioactivity and osseointegration.

2.2. Objectives.

This PhD work aims to develop a new β-Ti alloy, suitable to be used as an implant material. These materials would increase the prosthesis lifetime, preventing the appearance of the main failures associated with implant replacement.

Additionally, a low-cost powder metallurgy processing route is proposed, that employs titanium hydride (TiH_2) as Ti source, and reduces the niobium (Nb) content by adding a small iron (Fe) addition.

To achieve this goal, the work was divided into three sections:

The first section consists of reducing the elastic modulus by developing β-Ti alloys, using Nb and Fe as alloying elements. The partial objectives in this section are:

- To design of composition suitable to be processed by PM using/studying the Ti-Nb and Ti-5Fe-Nb system.
- To study the phenomena associated with the dehydrogenation process and the effect of alloying elements in this process
- To design an appropriate sintering cycle that ensures the complete dehydrogenation and promotes the diffusion process achieving higher densification of the substrates
- To perform the mechanical characterisation determining elastic modulus, hardness and fatigue behaviour of the processed alloys.
- To evaluate the biological response of the substrate surface.

The aspects concerning the design of composition and study of the dehydrogenation process are discussed in Chapter 4, while aspects of the processing of the β-Ti alloys are found in Chapter 5.

The second section is based on improving wear resistance by modification of processed β-Ti alloys. Alloys are modified employing two strategies: (a) incorporating ceramic particles as reinforcement; and (b) performing nitriding treatment using gas and plasma, to obtain a wear-resistant TiN layer on the surface. The partial objectives in this section are:

- To optimise the consolidation parameters for composite samples, in terms of kind and amount of ceramic reinforcement.
- To compare the improved wear resistance of modified β-Ti alloys to the substrates by dry sliding wear tests applying different loads.

The aspects concerning the processing of modified β-Ti alloys and the evaluation of their mechanical properties and wear resistance are found in Chapter 6.

Finally, the third section consists of inducing bioactivity by an anodic treatment, modifying the topography and, at the same time, incorporating bioactive and antimicrobial agents like calcium (Ca), phosphorus (P) and zinc oxide (ZnO). These results are discussed in Chapter 7.

References

[1] U. Holzwarth and G. Cotogno, “Total Hip Arthroplasty,” 2012.

[2] B. M. Wroblewski, P. D. Siney, and P. A. Fleming, "The Charnley Hip Replacement – 43 Years of clinical success.," *Acta Chir. Orthop. Traumatol. Cech.*, vol. 73, no. 2006, pp. 6–9, 2015.

[3] OECD, "Health at a Glance 2011: OECD Indicators," *OECD Publ.*, 2011.

[4] M. Abdel-Hady Gepreel and M. Niinomi, "Biocompatibility of Ti-alloys for long-term implantation," *J. Mech. Behav. Biomed. Mater.*, vol. 20, pp. 407–415, 2013.

[5] K. . Sipek, M. . Lyvers, and M. . Mathew, "Failure Causes in Total Hip Replacements: A Review.," *Austin J. Orthop. Rheumatol.*, vol. 5, no. 1, 2018.

[6] C. Delaunay, M. Hamadouche, J. Girard, and A. Duhamel, “What are the causes for failures of primary hip arthroplasties in France?,” *Clin. Orthop. Relat. Res.*, vol. 471, no. 12, pp. 3863–3869, 2013.

[7] V. Sáenz and E. Fuentes, "Titanium and Titanium alloys as Biomaterials," in *Tribology-Fundamentals and Advancements*, INTECH Open Science, 2013, pp. 155–181.

[8] M. Niinomi, Y. Liu, M. Nakai, H. Liu, and H. Li, "Biomedical titanium alloys with Young's moduli close to that of cortical bone," *Regen. Biomater.*, vol. 3, no. 3, pp. 173–185, 2016.

[9] M. Niinomi and M. Nakai, "Titanium-Based Biomaterials for Preventing Stress Shielding between Implant Devices and Bone," *Int. J. Biomater.*, vol. 2011, 2011.

[10] M. I. Z. Ridzwan, S. Shuib, A. Y. Hassan, A. A. Shokri, and M. N. Mohammad Ibrahim, "Problem of stress shielding and improvement to the hip implant designs: A review," *Journal of Medical Sciences*, vol. 7, no. 3. pp. 460–467, 2007.

[11] G. M. Keegan, I. D. Learmonth, and C. P. Case, "Orthopaedic metals and their potential toxicity in the arthroplasty patient. A review of current knowledge and future strategies," *J. Bone Jt. Surg. - Ser. B*, vol. 89, no. 5, pp. 567–573, 2007.

[12] P. Afzali, R. Ghomashchi, and R. H. Oskouei, "On the corrosion Behaviour of low modulus titanium alloys for medical implant applications: A review," *Metals (Basel).*, vol. 9, no. 8, 2019.

[13] Jairo M. Cordero y Valentin A.R. Barao, "Is there scientific evidence favoring the substitution of commercialy pure titanium with titanium alloys for the manufacture of dental implants?" *Mater. Sci. Eng. C*, 2016.

[14] J. W. Nicholson, "Titanium Alloys for Dental Implants: A Review," *Prosthesis*, vol. 2, no. 2, pp. 100–116, 2020.

[15] B. Priyadarshini, M. Rama, and U. Vijayalakshmi, "Bioactive coating as a surface modification technique for biocompatible metallic implants : a review," *J. Asian Ceram. Soc.*, vol. 7, no. 4, pp. 397–406, 2019.

[16] F. J. Gil, A. Padrós, J. M. Manero, C. Aparicio, M. Nilsson, and J. A. Planell, "Growth of bioactive surfaces on titanium and its alloys for orthopaedic and dental implants,"

Mater. Sci. Eng. C, vol. 22, no. 1, pp. 53–60, 2002.

CHAPTER 3

Experimental procedure

CHAPTER 3

3.1. Experimental work scheme.

This research studies different beta titanium alloys (β-Ti) containing niobium (Nb) and iron (Fe) as alloying elements; and titanium hydride (TiH_2) as Ti source, from the development of the alloy until the assessment of the mechanical and biological properties. **Figure 3.1** displays the scheme of the experimental framework carried out during this thesis.

This thesis aims to study strategies to prevent the appearance of the three main issues related to the current hip implants (see **Chapter 2**), by the development of an alloy and surface treatments that fulfil all requirements to avoid premature failure in hip implants. Therefore, this experimental procedure has been structured into three blocks, which are focused on (1) reducing the elastic modulus by the development of β-Ti substrates; (2) improving wear resistance by different techniques and (3) increasing the bioactivity of modified β-Ti alloys.

3.2. Starting materials.

The beta titanium (β-Ti) substrates were prepared from TiH_2, Nb and Fe elementary powders as raw material. With the aim to optimise the sintering conditions, two kinds of Fe and Nb elemental powders were employed, to evaluate the effect of particle size on the densification process. **Table 3.1** summarises the powders employed and their main characteristics. **Figure 3.2** displays the morphology and particle size distribution of the raw powders employed for processing of β-Ti alloys.

In the case of reinforced samples, boron nitride (BN), titanium diboride (TiB_2) and titanium nitride (TiN) powders were used as ceramic reinforcement to modify the β-Ti base alloys. **Figure 3.2** shows the morphology and particle size distribution of the reinforcements used in this work.

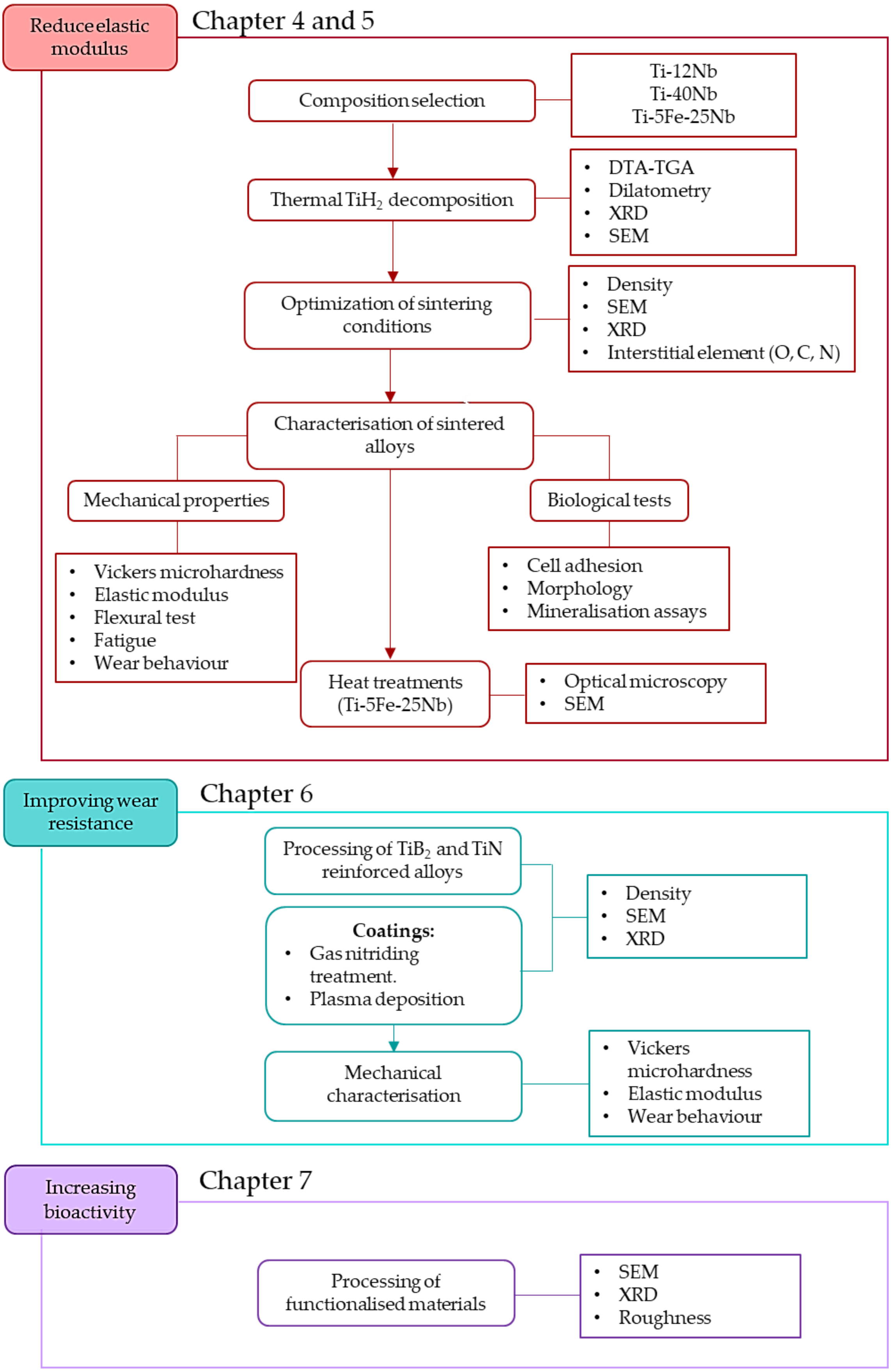

Figure 3.1. General work scheme followed during this work.

Table 3.1. Powders employed during processing of β-Ti substrates and reinforced materials.

Powder	Supplier	Density * (g/cm^3)	D_{50} (µm)
TiH_2	GfE	3.83 ± 0.01	24.3
Nb-1	Alfa Aesar	8.56 ± 0.03	13.7
Nb-2	Sat Nano	8.54 ± 0.02	21.5
Fe-1	Pomenton	7.79 ± 0.01	34.0
Fe-2	H.C. Starck	7.88 ± 0.01	3.4
TiB_2	Sigma Aldrich	4.33 ± 0.01	5.4
TiN	Sigma Aldrich	5.21 ± 0.01	4.1

* Determined by Helium pycnometry. ± Calculated by the standard deviation

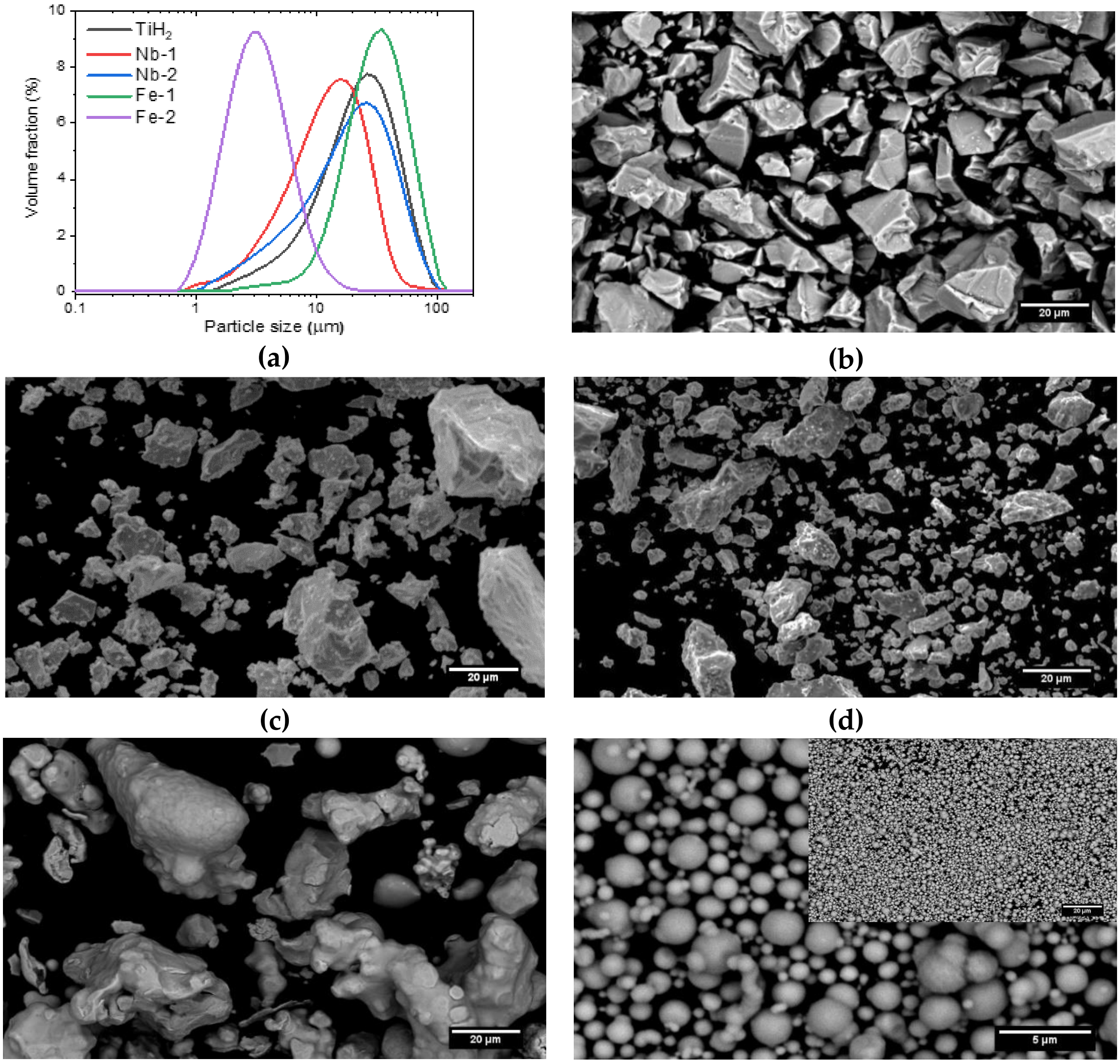

(a) (b)

(c) (d)

(e) (f)

Figure 3.2. Features of the elementary powders employed in this work. a) Particle size distribution of the starting powders; SE-SEM images of the powders: b) TiH_2; c) Nb-1; d) Nb-2; e) Fe-1 and f) Fe-2.

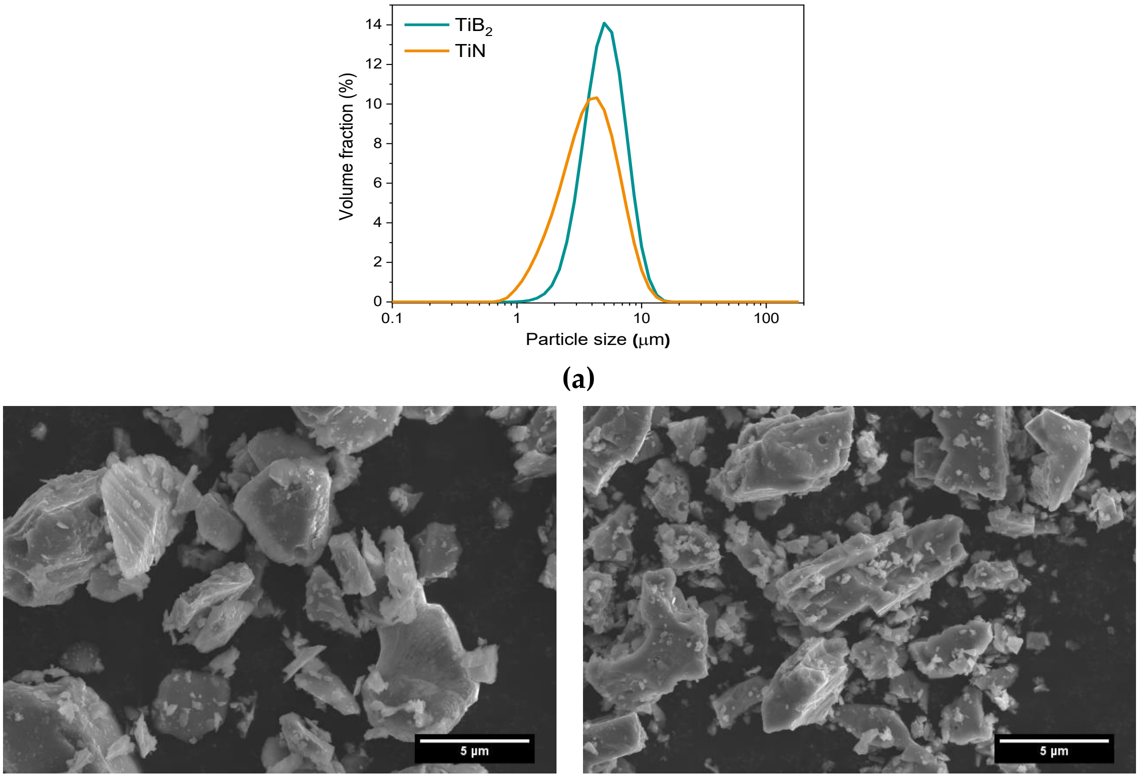

(a)

(b) (c)

Figure 3.3. Features of the elementary powders employed in this work. a) Particle size distribution of the reinforcement particles; SE-SEM images of the powders: b) TiB_2; c) TiN.

- ***Particle size distribution measurements:***

Particle size distribution was obtained using a laser diffraction particle size analyser (DLS Mastersizer 2000; Malvern Instruments Ltd., UK*)* equipped with a wet sample dispersion unit Hydro Sm (Malvern Instrument Ltd., UK). The dispersion unit was filled with distilled water and five drops of dispersant in order to avoid the formation of the agglomerates during the measurement, which could mask the results. Subsequently, the powder sample was incorporated under mechanical stirring to maintain the particles dispersed.

The principle of this technique is based on measuring angular variation in the intensity of the scattered light when the laser beam hit the particle dispersed in water. If particles are small, a large angle light scattering is produced, relative to the laser beam, [1]. This is a useful technique since a small amount of powder is required to obtain an accurate measurement in a short time.

3.3. Thermodynamic studies.

The compositions assessed in this work were selected by thermodynamic simulation for Ti-xNb and Ti-5Fe-xNb systems. The phase diagrams were predicted by Thermo-Calc software (Thermo-Calc Software Inc., McMurray, PA) using the Ti alloys database V3.1 (TTTI3).

3.4. Study of titanium hydride decomposition.

This work section aims to identify the phases that are formed during the titanium hydride (TiH_2) decomposition, as well as, evaluate the effect of the addition of β-stabilising elements such as Fe and Nb (Fe-2 and Nb-2 were used in this study) on the dehydrogenation process, in order to be able to control the decomposition process and produce β-Ti alloys from TiH_2 powders, avoiding pores and crack formation produced due to the hydrogen release.

Dehydrogenation process was analysed for two environments: under high purity argon flow by thermal analysis, and in high vacuum conditions. This study was performed controlling shrinkage, the mass loss associated with released hydrogen, densification, as well as the sequence of phase transformations and the evolution of the microstructure in the different stages of the process.

Samples were prepared by blending the required amount of powders for 1 h in a multidirectional mixer (Turbula®; WAB, CH). **Table 3.2** summarises the compositions prepared, as well as the method employed for their analysis. The amount of TiH_2 in the mixtures was calculated to obtain the mentioned final compositions of Ti, after the dehydrogenation process.

Table 3.2. Compositions prepared and analysing methods employed.

Composition [1]	DTA/TGA/DIL *	VAC
TiH_2	X	X
TiH_2-5Fe	X	X
TiH_2-7Fe	X	-
TiH_2-12Nb	X	X
TiH_2-25Nb	X	-
TiH_2-5Fe-25Nb	X	X
TiH_2-7Fe-25Nb	X	-
TiH_2-40Nb	X	X
TiH_2-5Fe-40Nb	X	-
TiH_2-7Fe-40Nb	X	-

[1] Nomenclature indicates the compositions in weight per cent.

* Performed using a high purity argon flow of 80 mL/min

3.4.1. Thermal analysis.

Differential thermal analysis (DTA) and thermogravimetric analysis (TGA) were carried out on a Setaram Setsys' Evolution 16/18' (Setaram Instrumentation, FR) for mixtures of powders, filling the alumina crucible with 80 mg of powders and with argon flow of 80 mL/min. Samples were heated at 10 °C/min up to 1250 °C, and were cooled at 10 °C/min.

DTA results led to identifying the critical decomposition temperature of the different stages of the dehydrogenation process and how the presence of alloying elements modifies them. Furthermore, DTA allows validating the expected reduction of the beta transus temperature, according to thermodynamic simulation.

From the mass loss observed in the TGA analysis, it can be discerned if the complete TiH_2 decomposition to Ti has occurred by calculating the relative hydrogen loss (RHL) during TGA analysis. For this, it is assumed that the mass loss corresponds to the hydrogen released during dehydrogenation, since no mass loss is expected for the alloying elements. For each composition, the theoretical hydrogen amount contained in the TiH_2 fraction in each composition was considered. It was assumed that starting TiH_2 powder contains 4.04 wt.% of hydrogen. For instance, sample TH12Nb contains 88.4 TiH_2 wt.%; of this, a 4.04 wt.% corresponds to hydrogen. Hence, the total hydrogen content in TH12Nb composition would correspond to 3.57 wt.%.

The RHL was calculated, following **Equation 3.1** and **Equation 3.2.**

$$RHL = \frac{\Delta m}{m_{0\,(H)}} \times 100 \ \ [\%]$$

Equation 3.1

$$m_{0\,(H)} = \frac{X_{m(TiH2)} \times 4.04\ (wt.\%\,H)\ \times m_{0\,(sample)}}{100}\ \ [g]$$

Equation 3.2

Where $m_{0\,(H)}$ is the total mass of hydrogen for each composition before heating; $X_{m(TiH2)}$ is the mass fraction of TiH_2, and $m_{0\,(sample)}$ corresponds to the starting mass of the samples before heating.

Thermal analyses were conducted in the Institute for Ceramic and Glass, CSIC in Madrid.

3.4.2. Dilatometry.

Dilatometry (DIL) measurements were performed to evaluate the different length changes that occur during the dehydrogenation process and to identify the starting sintering temperature of the alloys. DIL was made for square pressed samples at 700 MPa (about 1 cm side length), using a dilatometer Setaram Setsys Evolution TMA (Setaram Instrumentation, FR) with a vertical configuration. Samples were heated at 10 °C/min up to 1250 °C, and were cooled at 10 °C/min. This experimental section was performed in the Institute for Ceramic and Glass, CSIC in Madrid.

3.4.3. Thermal behaviour under high vacuum conditions.

Heat treatments using high-vacuum conditions (VAC) were done to corroborate the transformation reactions and dimensional changes observed by thermal analysis, as well as to evaluate the microstructural evolution during the decomposition stages, using similar processing conditions as those employed in the Ti industry.

VAC treatments were carried out for green compacts obtained by uniaxial pressing at 700 MPa, obtaining disks of 14 mm in diameter and 2-3 mm in thickness. Samples were treated in a high-vacuum tube furnace, model Carbolite-Hut 15/50/450 (Carbolite, UK), equipped with a diffusion pump coupled to a rotary pump, reaching a pressure of 10^{-5} mbar.

The VAC treatments performed are shown schematically in **Figure 3.4.** They were performed between 400 and 1100 °C. For heat treatments from 400 °C to 800 °C, samples were heated with a heating rate of 2 °C/min. Samples treated at 1100 °C were heated to 800 °C at 2 °C/min, and from 800 to 1100 °C, the heating rate was 5 °C/min. In all cases, once the chosen temperature was reached, it was maintained for 5 min; the furnace was cooled to room temperature with a cooling rate of 5 °C/min. During dehydrogenation, a heating rate of 2 °C/min was used to promote hydrogen elimination, according to previous results [2]. Afterwards, the heating rate was increased to 5 °C/min between 800 to 1100 °C to promote sintering and alloying elements diffusion after dehydrogenation. Five specimens were analysed for each heat treatment.

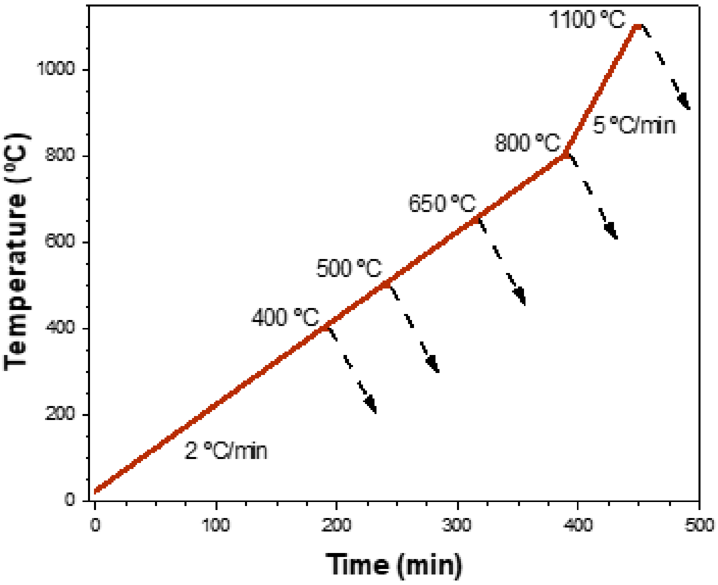

Figure 3.4. Heat treatment performed under high vacuum conditions (VAC).

3.5. Materials processing.

3.5.1. Beta-titanium (β-Ti) substrates.

Three different β-Ti substrates containing Ti-12Nb, Ti-40Nb and Ti-5Fe-25Nb (compositions are specified in weight per cent) were prepared in this work. **Table 3.3** displays the nomenclature used, as well as the nominal composition for each mixture of powder. The amount of TiH_2 used for each mixture was calculated to reach the aforementioned final composition after the dehydrogenation process; considering the theoretical weight loss of 4.04 wt.%, related to the total amount of hydrogen in TiH_2 powder.

Table 3.3. Nomenclature and nominal compositions prepared (wt.%).

Nominal composition (wt. %)			Label
TiH_2 */ Ti	Nb	Fe	
88.4 / 88	12		TH12Nb
60.9 / 60	40		TH40Nb
70.8 / 70	25	5	TH5Fe25Nb

* TiH_2 amount to achieve the fixed composition considering the hydrogen loss.

3.5.1.1. *Sample preparation.*

Substrates were processed by conventional powder metallurgy route, that is a pressing and sintering process. **Figure 3.5** summarises the steps followed for the manufacturing of the substrates. First, the raw powders were homogenised by dry blending for 1 h in a multidirectional mixer (Turbula®; WAB, CH). Then, green compacts were obtained by uniaxial pressing with a floating die at 700 MPa, using a cylindrical die of 16 mm in diameter and about 2-3 g of powder. Zinc stearate was used as a wall-die lubricant. Finally, green powder compacts were sintered under high-vacuum conditions (10^{-5} mbar), using a tube furnace (Carbolite-Hut 15/50/450; Carbolite, UK), equipped with a diffusion pump coupled to a rotary pump.

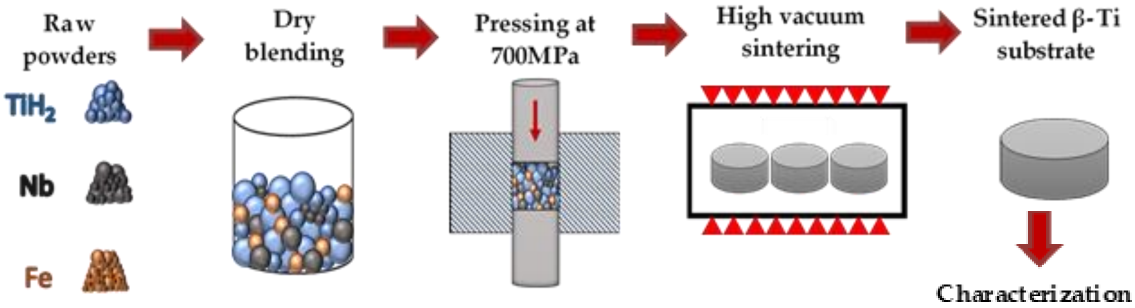

Figure 3.5. Schematic of experimental procedure carried out for β-Ti substrates.

3.5.1.2. *Consolidation parameters optimisation.*

Consolidation parameters were studied focusing on two aspects: dehydrogenation process, which takes place at low temperature between 400-800 °C [3]–[6]; and, densification and diffusion of alloying elements (especially of Nb) into Ti matrix, at high temperature (above 800 °C). The optimal sintering cycle should promote these two processes.

Due to the significant influence of the heating rate on TiH_2 decomposition, different heating rates during the dehydrogenation stage were assessed. Both time and maximum sintering temperature were varied, in order to evaluate the densification and diffusion process of the alloying elements. Five sintering cycles were performed, which are described in **Table 3.4**.

Table 3.4. Heating conditions for sintering cycles designed.

	Heating at low temperature				**Heating at high temperature**			
Cycle	**HR (°C/min)**	**IT (°C)**	**HR (°C/min)**	**IT (°C)**	**HR (°C/min)**	**Sintering temperature (°C)**	**Holding time (h)**	**CR (°C/min)**
C1	5	---			5	1200	2	5
C2	5	700 for 1h	---					
C3	5	450	2	450-650				
C4						1250	4	
C5						1450	4	

HR: Heating rate. IT: Intermediate temperature. CR: Cooling rate.

The physicochemical characteristics of the starting powders influence the final properties and performance of PM alloys profoundly. Hence, sintering cycles were also analysed for two kinds of Fe, and Nb elementary powders, with different particle size distribution and morphology (**See section 3.2**). **Table 3.5** summarises the type of powder employed in each sintering cycle.

Table 3.5. Powders employed in each sintering cycle.

Sintering cycle	Nb	Fe
C1	1	1
C2	1	1
C3	1	1 / 2
C4	1 / 2	1 / 2
C5	2	2

3.5.1.3. Heat treatment (HT) for dissolution of titanium carbide

This experimental section was performed in the Department of Industrial Engineering in the Università di Trento in Italy.

Titanium carbide (TiC) formation, especially along the grain boundaries, increases Young's modulus, but overall has detrimental effects on the fatigue life, ductility and corrosion resistance of Ti alloys [7]. These carbides influence the mechanical behaviour, producing premature failure of the alloy, due to cracks nucleating and propagating from the titanium carbides particles.

Preliminary studies on mechanical properties by static and dynamic flexural test revealed a marked intergranular fracture for sample TH5Fe25Nb, at lower stresses than expected. This fact is related to both big grain size and TiC detachment. Hence, several heat treatments (HT) that promote dissolution or reduction in the size of the TiC precipitates were proposed in order to improve the mechanical behaviour.

The carbon solubility in Ti-5Fe-25Nb-xC system was previously evaluated, by thermodynamic simulation, using Thermocalc software, to evaluate how the carbon content modifies the phase diagram. From the resulting phase diagram, various temperatures were chosen in order to study the TiC dissolution by cooling from different regions.

Table 3.6. Conditions of heat treatment for dissolution of TiC.

TT	HR (°C/min)	T (°C)	HT (h)	CR (°C/min)	T (°C)	HT (h)	CR (°C/min)	T (°C)
HT1	10	1300	0.5	600				25
HT2		1300	1					
HT3		1050	1					
HT4		1050	2					
HT5		900	2					
HT6		900	6					
HT7		1050	1	10	650	5	600	

TT: Thermal treatment. HR: Heating rate. HT: Holding time CR: Cooling rate

The HT were done using a quenching dilatometer (DIL805A/D/T; TA® Instruments, US) equipped with an induction heating system, that allows applying rapid heating and cooling rates, as well as changes of the atmosphere while the test is taking place. **Table 3.6** summarises the heat treatments performed in this work. For all treatments, samples were heated under vacuum (10^{-3} mbar) while cooling was carried out under argon atmosphere until room temperature.

3.5.2. Reinforced β-Ti alloys.

The alloys containing Ti-40Nb and Ti-5Fe25Nb were chosen to be reinforced with ceramic particles, due to their higher fraction of β-Ti phase compared to composition Ti-12Nb, which exhibits a biphasic (α+β) microstructure. A higher amount of β-Ti phase is related to lower elastic modulus values, which is desired in Ti alloys for biomedical application.

Titanium diboride (TiB_2) and titanium nitride (TiN) powders were used as ceramic reinforcement for the β-Ti matrix/alloys. Mixtures were prepared from TiH_2, Nb-2, Fe-2, and 5 vol.% of TiB_2 and TiN as starting powders. The nominal composition for each mixture of the powder prepared, and the nomenclature used for the reinforced samples are shown in **Table 3.7.**

Table 3.7. Nominal compositions for wet-milled (WM) reinforced samples.

Samples	TiH_2*/ Ti	Nb-2	Fe-2	TiB_2	TiN
TH40-TiB_2	58.5 / 57.5	38.4		4.1	
TH40-TiN	58.1 / 57.2	38.1			4.7
TH525-TiB_2	67.8 / 67.0	23.9	4.8	4.3	
TH525-TiN	67.4 / 66.5	23.8	4.8		4.9

* TiH_2 amount to achieve the fixed composition considering the hydrogen loss.

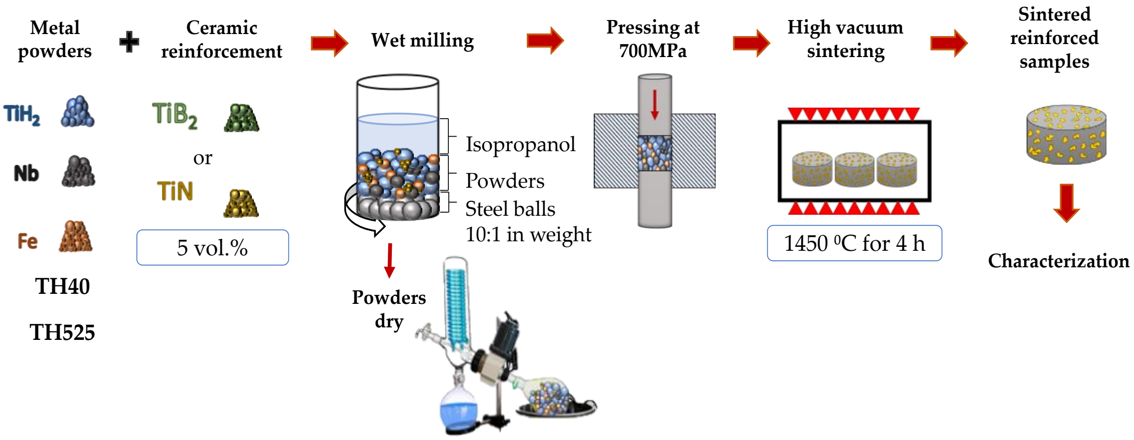

Figure 3.6. Schematic diagram for manufacturing of reinforced β-Ti alloys.

Mixtures were obtained by wet blending in order to improve the dispersion of the ceramic reinforcements into the β-Ti matrix. Milling was carried out on a planetary ball mill for 2 h, at 150 rpm using isopropanol as milling medium. The ratio of steel balls-powder employed was 10:1 in weight. Mixtures were dried employing a rotary evaporator. Subsequently, the mixtures were uniaxially pressed at 700 MPa, obtaining disks of 16 mm in diameter and 2-3 mm in thickness. Green compacts were sintered under high vacuum conditions at 1450 °C, with a holding time of 4 h, following sintering cycle 5 (C5). Processing of reinforced samples is summarised in **Figure 3.6**.

3.5.3. Coating treatments.

3.5.3.1. Gas nitriding treatment.

For gas nitriding treatment, samples were ground with sandpaper and then, were cleaned for 10 min using an ultrasonic bath in distilled water. Then, samples were heated in a horizontal tubular furnace Carbolite STF 15/75/450 up to 900 °C, employing a heating rate of 5 °C/min and maintaining it for 12 h; finally, samples were cooled to room temperature at 5 °C/min. The whole process was carried out using a high purity nitrogen gas environment.

Samples were heated using two overlapped alumina crucibles, as shown in **Figure 3.7.** Samples were put on the internal crucible. Ti powder was used in the external crucible, as a scavenger of oxygen, in order to prevent their oxidation.

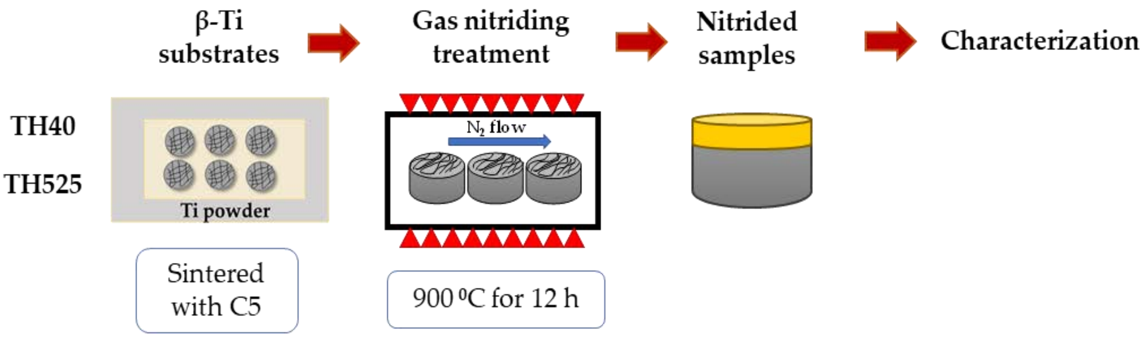

Figure 3.7. Schematic diagram for gas nitriding treatment.

Samples coated by gas nitriding treatment will be referred from now onwards like GN-followed by the sample composition (GN-TH40 and GN-TH525).

3.5.3.2. Plasma deposition coating.

Plasma deposition coatings (PDC) were deposited in the Laboratory of Semiconductors Films of the Universidade Estadual Paulista "Julio de Mesquita Filho", campus Bauru in Brasil.

PDC were deposited by radiofrequency (RF) magnetron sputtering techniques. This technique is useful to deposit a film formed by a chemical reaction between the target atoms to be deposited onto the substrate surface, and the gas atoms contained into the vacuum chamber. In this way, films of nitrides and oxide can be easily deposited controlling the gas pressure of the atmosphere. RF magnetron sputtering systems is shown in **Figure 3.8a**. A magnetic field is produced close to the target, which removes the target atoms from the surface (**Figure 3.8b**). Plasma is concentrated near the target area and the ionised gas atoms (Ar^+, N_2 atoms), collide with target atoms (Ti). The reaction between Ti-N_2 atoms forms stoichiometric TiN compound, which is deposited in thin layers on the sample surface.

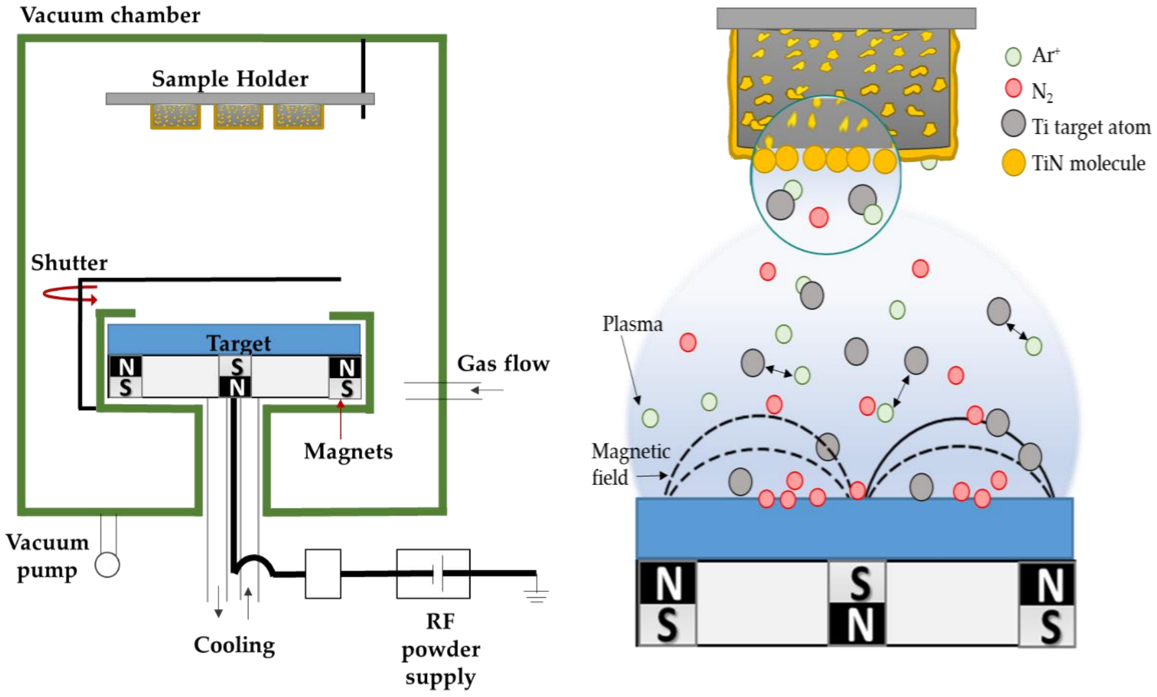

(a) (b)

Figure 3.8. Radiofrequency (RF) magnetron sputtering **(a)** System assembly, and **(b)** Process for TiN film coating.

PDC were carried out using a reactive magnetron sputtering system (Kurt. J. Lesker©, US), equipped with a Torus sputtering cathode of 3" in diameter (Kurt. J. Lesker©, US). A pure Ti target was used (AJA International Inc., US).

TiN coatings were deposited on the TiN reinforced substrates, using a power supply frequency of 13.6 MHz. Samples were ground with sandpaper. After grinding, samples were cleaned in an ultrasonic bath in deionised water, propanol and deionised water for 10 min, respectively.

Before TiN deposition, the sputtering chamber was evacuated down to residual pressure of < $5x10^{-6}$ Torr. Then, the substrate surface was sputter-cleaned in two stages to minimise the surface impurities. First, it was cleaned with pure argon flow of 40 sccm (standard cubic centimetre per minute) for 3 min and then with a mix of high purity 40 sccm argon and 10 sccm nitrogen gas flow for 2 min.

A resistance heater was used to maintain the sample holder temperature at 400 °C. The TiN layer was deposited applying RF power of 240 W and using 40 sccm of argon and 10 sccm of nitrogen flow, at a constant total pressure of $5x10^{-3}$ Torr. The total deposition time was 520 min.

Samples nitrided by plasma deposition method will be referred to from now onwards as PN-followed by the sample composition (PN-TH40(TiN) and PN-TH525(TiN)).

3.5.4. Functionalised materials.

This work section was performed in the Anelasticy and Biomaterials Laboratory of the Universidade Estadual Paulista, campus Bauru in Brasil.

TiN reinforced samples were functionalised by Micro-Arc Oxidation process (MAO), also called, electrochemical anodic treatment. This technique consists of immersing the sample in an electrolyte medium and applying a high voltage between an anode and cathode for a short time. The sample surface is maintained in anodic conditions that promote plasma sparkling and oxidation reactions, generating an inner porous oxide layer connected to the surface. During the plasma sparkling, the elements dissolved into the electrolyte are incorporated into the anodic layer. The anodic layer leads to better tribocorrosion behaviour. It allows improving the bioactivity in the Ti surface, by incorporation of bioactive elements like Ca and P, which can promote osteointegration by precipitation of hydroxyapatite. Furthermore, controlled porosity and roughness may promote specific cellular processes and cellular fixation, like adhesion and proliferation of osteoblasts, favouring bioactivity.

Before MAO treatment, TiN reinforced samples were ground with sandpaper and etched with Kroll's reagent for 3 min. Then, they were ultrasonically cleaned in propanol and distilled water for 15 min, respectively each.

Figure 3.9 shows the experimental configuration carried out for the anodic treatment. Samples (anode) were placed in an electrochemical cell and immersed in a conductive electrolyte. A platinum sheet, located on the opposite side, was employed as a cathode to allow the electrochemical reaction.

The electrolyte consists of an aqueous solution containing β-glycerophosphate disodium salt pentahydrate (β-GP) (Fluka-BioChemika) and calcium acetate monohydrate (CaA) (Sigma-Aldrich) as Ca and P sources, and zinc oxide nanoparticles (ZnO NPs) (Sigma-Aldrich). **Figure 3.10** shows the morphology of ZnO NPs used in this section.

The electrolyte was chosen to incorporate bioactive species (Ca and P) that promote apatite formation, increasing sample bioactivity. While ZnO was incorporated since it has an antibacterial effect, and could also improve the tribological behaviour [8]. On the other hand, Zn enhances the protein synthesis, promoting proliferation and differentiation of osteoblast cells, which stimulates bone formation, avoiding failure during the early stage of implantation [9]

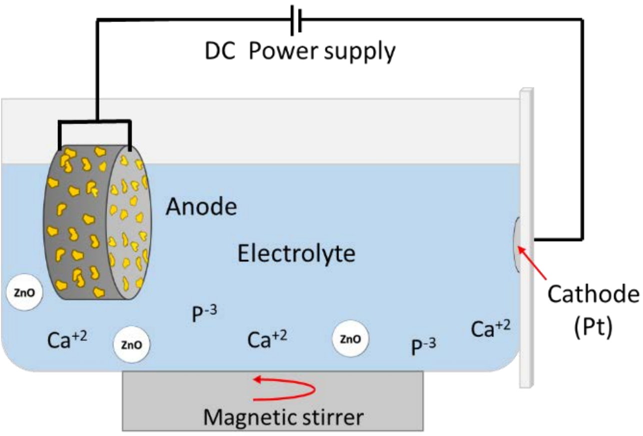

Figure 3.9. Schematic representation of MAO treatment setup.

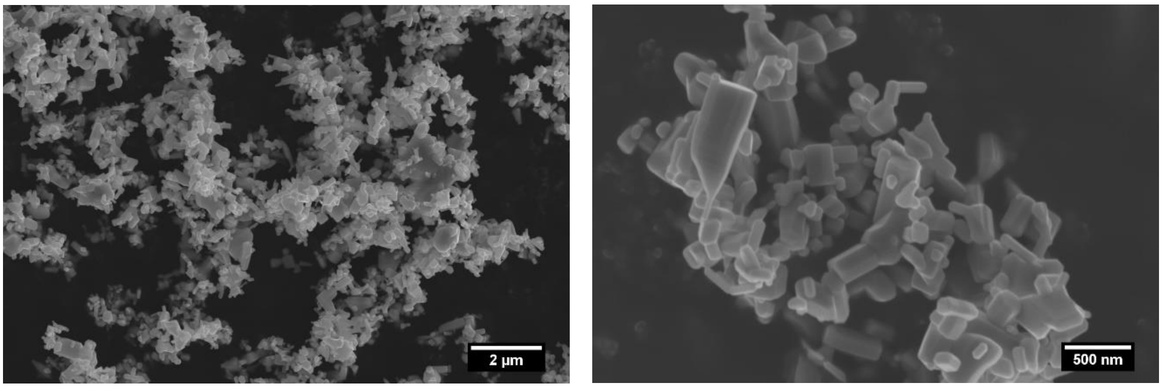

(a) **(b)**

Figure 3.10. SE-SEM images of ZnO nanoparticles taken at different magnification.

The electrolyte used for MAO treatment was a solution containing 0.02 M of β-GP and 0.35 of CaA. This electrolyte was modified by the addition of 0.02 M, 0.05 M and 0.07 M of ZnO NPs. Mixing of β-GP and CaA was carried out by simple magnetic stirring. Addition of ZnO NPs was performed by ultrasonic dispersion during 5 min using an ultrasonic processor (Sonics VCX-750) operating at 20 kHz and 300 W, right before the MAO treatment.

The anodic treatment was performed at room temperature using a DC power supply (Agilent N5772A), under a constant voltage of 300 V and restricting the current to 2.5 A for 1 min. The MAO treatments were carried out under magnetic stirring to prevent ZnO NPs agglomeration, ensuring homogeneous ions flow in the bath.

Anodised samples were cleaned in distilled water at 50 °C to remove the ZnO NPs that did not adhered to the surface. Then, samples were examined by SEM to evaluate the Ca, P and ZnO NPs distribution and to analyse the porosity in the anodised layer. Profilometry was carried out to measure the roughness and XRD analysis to detect anatase and rutile formation, which are key aspects of improving the biological response.

3.6. Characterisation of powders and processed samples.

3.6.1. Density measurement.

For each sample type, different techniques were employed to determine the density.

- ***Helium pycnometer:***

This method is used to measure the density of the body of the solids, using helium as displacement medium. It uses the gas displacement method to measure the sample volume; knowing the sample mass value, density can be calculated. The pycnometer density is also known as absolute density or true density; it considers surface pores accessible to the gas, excluding closed porosity. Usually, the values obtained are close to the theoretical density but always lower due to the defects or impurities generated during processing.

Helium pycnometer (AccuPyc 1330; Micrometric, US) was employed to measure the density of the starting powders. The measurement was performed three times for each powder.

- ***Geometrical method:***

The apparent density of green compacts and consolidated samples (β-Ti substrates, TiN reinforced and nitrided samples) was determined by the geometrical method, assuming the cylindrical geometry of the specimens. The volume calculated by this method includes both open and closed porosity. It is a method with limited accuracy, but an accepted approach to control the uniformity between the batches of samples processed.

- ***Immersion method:***

The density of the consolidated samples (β-Ti substrate and all modified alloy) was measured using Archimedes' Principle. Samples were immersed in ethanol ($\rho_{ethanol}$= 0.789 g/cm^3 at room temperature), recording the weight both in air (m_{air}) and immersed ($m_{immersed}$). According to the Archimedes Principles, density was calculated following **Equation 3.3**.

$$\rho = \frac{m_{air}}{m_{immersed}} \times \rho_{ethanol}\ [g/cm^3]$$

Equation 3.3

Relative density (ρ_{rel}) was obtained by the relationship between the Archimedes density (ρ) and the theoretical density (ρ_{th}), as shown in **Equation 3.4**. The theoretical density was calculated by the rule of mixture for each composition by **Equation 3.5**.

$$\rho_{rel} = \frac{\rho}{\rho_{th}} \times 100 \ [\%]$$ **Equation 3.4**

$$\rho_{th} = \frac{X_{m,1}}{\rho_1} + \frac{X_{m,2}}{\rho_2} + \cdots + \frac{X_{m,n}}{\rho_n} \ [g/cm^3]$$ **Equation 3.5**

Where, $X_{m,i}$ is the mass fraction of each component and ρ_i corresponds to its theoretical density. The TiH_2 density (3.75 g/cm^3) was considered for the green samples, and the Ti density (4.51 g/cm^3) was used for sintered samples.

This measurement method includes the open and closed porosity of the sample. Hence, Total porosity (P_T) can be calculated as a function of relative density values by **Equation 3.6**.

$$P_T = 100 - \rho_{rel} \ [\%]$$ **Equation 3.6**

3.6.2. Chemical analysis of interstitials elements.

It is well known that Ti has a high affinity for interstitial elements such as C, O and N. The presence of these elements, causes significant changes in the mechanical behaviour of Ti alloys, influencing mainly the elastic properties. Since toughness decreases as the interstitial concentration increases, the alloys become brittle. The most critical element that affects the mechanical properties is oxygen, because it is picked up preferentially compared to the others. Moreover, these elements are soluble in α-Ti phase, favouring the alpha phase formation, which is not desirable in this specific research, as it contributes to higher elastic modulus values.

Therefore, it is essential to control the presence of interstitial elements, both in the starting powders and in the sintered components. The interstitial content was analysed by Leco equipment (LECO, US); using a Leco TC-500 to determine O and N amount, and a Leco CS-200 to measure the C content.

The sample is deposited in an alumina crucible for C measurement, using about 250-300 mg. At that moment, an accelerator reagent (Lecocel II) is added to facilitate the combustion. The procedure consists of melting the sample under oxygen gas flow, in an induction furnace located inside the equipment. When combustion is reached, the C in the sample reacts with the gas, forming CO and CO_2 as combustion gases. These gases pass through powder and moisture and finally, are analysed using an infrared (IR) cell. The results obtained are expressed in weight per cent. The measure was performed three times for each sample.

In the case of O and N measurement, the sample is placed in a graphite crucible, using about 100-150 mg for samples containing Ti and Nb; while for Fe samples, about 1 g of sample was used. The sample is melted in the induction furnace, under Helium atmosphere. The O in the sample is combined with the C of the crucible, forming CO and CO_2. The N contained in the sample is released as molecular N_2. Helium gas carries the sample gases through filters to an IR cell where O is measured from CO_2; while N_2 passes through a thermal conductivity cell to be measured. The results obtained are expressed in weight per cent. The measurements were performed three times for each sample.

3.6.3. Mass loss and quantification of hydrogen released.

Mass loss (Δm) after sintering was calculated using **Equation 3.7**

$$\Delta m = \frac{m_0 - m_f}{m_0} \times 100\ [\%] \qquad \textbf{Equation 3.7}$$

Where, m_0 and m_f correspond to the sample mass before and after sintering, respectively.

Based on the assumption that the mass loss is produced only by the dehydrogenation process, quantification of hydrogen released in vacuum sintered samples was estimated as described in **Section 3.4.1**.

3.6.4. Microstructural analysis.

Microstructural analysis was performed by scanning electron microscopy (SEM). Different microscopes were employed for the analysis, based on the equipment availability and the sensitivity or accuracy required for each analysis. The microscopes used in this work are indicated below:

- Phillips XL-30 (Phillips, NL) coupled with energy-dispersive X-ray spectroscopy (EDAX, US).
- JSM-IT300LV (JEOL, JP) microscope equipped with an EDS detector XFlash 630M (Bruker, UK).
- EVO-015 (Carl Zeiss, DE) microscope.
- Field emission scanning electron microscopy, FE-SEM Teneo (FEI, US) equipped with an EDS X-ray analyser DX-4 detector.
- Optical microscope model Axiophot (Zeiss, DE).

Surface preparation was different according to the kind of sample to be analysed. Overall, samples were mounted in a conductive resin. Then, samples were ground using sandpaper until a final step of P1000 and polished with alumina suspension of 1 and 0.3 µm.

Polishing was completed with colloidal silica of 0.04 μm (Struers, DK), wetting the polishing cloth with hydrogen peroxide, in this step. Hydrogen peroxide has a slight etching effect that helps to reveal the microstructure. Finally, samples were coated with a thin carbon film. The gold coating usually used for this purpose was avoided as the emission line of gold is very close to that of Nb, producing overlap.

After the polished surface evaluation, TiB_2 reinforced samples were deep etched in Kroll's reagent for about 5 minutes in order to remove the metal matrix and reveal the morphology of precipitates. Kroll's etchant was prepared using 100 ml distilled water, 3 ml hydrofluoric acid and 6 ml nitric acid. Samples with surface modification (gas nitriding treatment, plasma deposition coating, and anodising treatment) were treated prior to metallographic preparation, in order to ensure that the modified surface is not damaged during the metallographic preparation process. Firstly, samples were coated with a thin gold film to ensure their conductivity. Then, samples were coated with a Cu film by electrolysis process, where the sample is immersed in a $CuSO_4$ solution, and an electric current passes through a piece of Cu, which acts as anode; and sample acts as a cathode. The Cu ions are deposited into the sample surface, protecting the coated surface during metallographic preparation. Finally, Cu coated samples are metallographically prepared, following the procedure mentioned above.

3.6.5. X-ray diffraction.

- ***Conventional measurement:***

The phase structures for the processed samples were analysed by X-ray diffraction (XRD) using X'pert Phillips (Phillips, US) with Cu K_α radiation 1.54 Å, and an accelerating voltage of 40 kV and a current of 40 mA. Pattern diffraction was obtained between 20° to 80° using a step size of 0.02° and a time per step of 2.5 s. X'pert High Score software was used to identify the different phases.

- ***Grazing incidence X-ray diffraction:***

Depending on the material features, conventional X-rays may penetrate deep, reaching several microns. For thin film characterisation, this is not desirable since the substrate contributions could mask the contribution of coating phases. GIXRD permits to control the X-ray penetration depth by changing the incidence angle between the X-ray beam and the sample surface. The incidence angle is known as α; it is very small and generally ranges from 0.1° to 1°[10]. Using GIXRD ensures, at least, most of the incident X-ray beam is confined within the film, and substrate contributions are eliminated or considerably reduced [10]–[12]. Hence, the phases detected by GIXRD will correspond to film instead of substrate.

Coatings obtained by nitriding treatment were analysed using grazing incidence X-Ray diffraction (GIXRD) in order to determine, more accurately, the phases present in the outer compound layer. GIXRD measurements were performed using an X'pert Pro Phillips (Phillips, US) diffractometer with Cu K_α radiation, an accelerating voltage of 45 kV and a current of 40 mA. An incidence angle (α) of 1° was used.

3.7. Mechanical characterisation.

3.7.1. Microhardness.

The hardness of processed samples was evaluated by Vickers microhardness measurement using a hardness tester ZHVμ (Zwick Roell, DE), applying a load of 50 gf ($HV_{0.05}$) with a diamond tip during 10 s. The values reported correspond to the average obtained after 20 indentations, which were randomly done following the ISO 6507-1:2018 standard. [13]

For comparison purposes, this test was performed in the cross-section of the processed samples. Samples were cut and embedded in a resin; then, they were ground with sandpaper with a final step of 1200 and polished until a mirror surface was obtained. Hardness in the cross-section was measured to evaluate the hardness in the matrix and not only on the surface; since, in the case of coated samples, it is expected that hardness values will be considerably higher on the surface, due to the external TiN layer. Additionally, hardness was measured at the top surface of nitrided samples, in order to compare the hardness of coatings achieved by plasma and gas nitriding treatment.

3.7.2. Elastic modulus.

Elastic modulus was determined for all processed materials using indentation tests. Indentations were done in the cross-section of the samples using a universal durometer ZHU2.5 (Zwick Roell, DE), applying a load of 10 N for 10 s. Samples were cut and embedded in a resin; then, they were ground and polished to ensure a planar surface. Values reported correspond to the average of at least 20 measurements for each material.

In this test, the load (P) displacement (h) data is recorded during the load-unload cycle. **Equation 3.8** shows the relationship between the initial unloading contact stiffness (S), to the elastic modulus (E) of the sample, as stated by Oliver and Pharr theory [14].

$$S = \frac{dP}{dh} = \beta \frac{2}{\sqrt{\pi}} E \sqrt{A}$$

Equation 3.8

Where, $\frac{dP}{dh}$ is the slope in the upper portion of the unloading curve, during its initial stage; β is a correction factor, according to the indenter symmetry employed; A is the projected contact area when the maximum load is applied.

3.7.3. Fatigue test.

This experimental section was performed in the Department of Industrial Engineering in the Università degli Studi di Trento in Italy.

Fatigue is a material degeneration process in which material failure occurs when it is subjected to cyclic stresses, which are lower than the material fracture strength. Fluctuating stresses are considered to produce small amounts of plastic strain. These deformations accumulate until they lead to the formation of microcracks that usually nucleate near the surface. The crack grows into the material in a direction normal to the applied load, until reaches a critical size, then it propagates through the material and producing the failure by fracture. [15], [16]

Fatigue behaviour of the β-Ti substrate was evaluated by three-point bending fatigue test using an Instron 1341 machine (Instron). Samples were cut by electrical discharge machining, using a brass wire to achieve a rectangular specimen of 17x2x1.5 mm.

The three-point bending fatigue tests were conducted at room temperature on 12 specimens for each composition. **Figure 3.11** shows a schematic representation of the sample position for fatigue tests. The stress produced in this test are bending stress which can be calculated using **Equation 3.9**.

$$\sigma = \frac{3FL}{2bh^2}\ [MPa]$$

Equation 3.9

Where F is the load (N); L is the support span length (mm); b is the sample width, and h is the sample thickness.

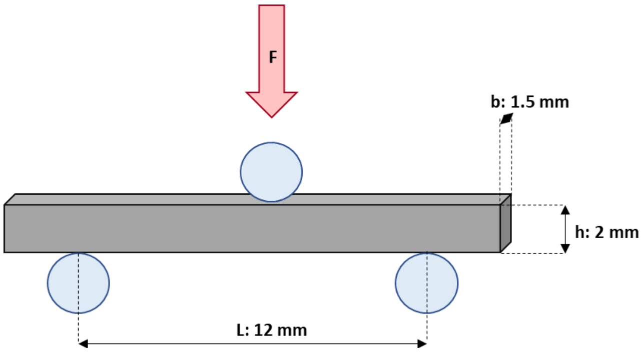

Figure 3.11. Schematic representation of bending fatigue test.

The sinusoidal load was applied at a frequency of 25 Hz. The number of cycles was set on value 2x10^6 cycles, which represents the run-out condition.

During fatigue tests, the sample is exposed to different stress amplitude levels. The stress amplitude (σ_a) is defined as half of the difference between the maximum (σ_{max}) and minimum (σ_{min}) applied stress (**Equation 3.10**). The mean stress (σ_m) applied can be defined using **Equation 3.11**. Tests were performed using a stress ratio, R= 0.1 (**Equation 3.12**).

$$\sigma_a = \frac{\sigma_{max} - \sigma_{min}}{2}$$ **Equation 3.10**

$$\sigma_m = \frac{\sigma_{max} + \sigma_{min}}{2}$$ **Equation 3.11**

$$R = \frac{\sigma_{min}}{\sigma_{max}}$$ **Equation 3.12**

The initial load applied, was defined about 40% of flexural strength, which was previously measured in three samples for each composition by static three-point bending test. Then, the load was increased or reduced depending on the number of cycles reached, looking towards determining the run-out stress condition or the infinite life.

Fatigue limit or fatigue strength (σ_f) is the maximum fluctuating stress that a material may resist for a high number of cycles, above 10^6 cycles. It can be estimated empirically from the S-N curves, applying the Basquin equation (**Equation 3.13**).

$$\sigma_a = \sigma'_f \times \left(2N_f\right)^b$$ **Equation 3.13**

Where σ'_f is the fatigue strength coefficient and b the fatigue strength exponent which corresponds to the slope in the Wohler line. This parameter was determined plotting $log\sigma_a - logN$ and using a linear fit.

After fatigue test, the fracture surface was observed by SEM.

3.7.4. Wear test.

Wear resistance was evaluated for β-Ti substrates and modified β-Ti alloys, in order to assess the improvement reached for each surface modification technique. Wear behaviour was studied by dry sliding tests; which were carried out on a ball-on-plate tribometer (UMT; Bruker, UK), using reciprocal movement. They were performed in ambient air under unlubricated conditions. Materials were tested by rubbing a 6 mm alumina ball under a load of 10 and 20 N at a frequency of 1 Hz. The tests had a duration of 1800 s with a total stroke length of 10 mm.

The surface of β-Ti substrate samples and TiN reinforced samples, was polished; while coated samples were tested in as-treated condition, to maintain the TiN layer. Each material was evaluated at least three times for each load condition.

After the dry sliding test, wear tracks were observed by SEM to analyse the wear mechanism produced. In addition, wear tracks volume was measured by an optical profilometer Zeta-20 (KLA, US). Profilometer obtains a 2D and 3D profile of the wear tracks, which is useful to determine the wear track geometrical features. Wear track can be represented by the model shown in **Figure 3.12**. For each wear track, four 2D profiles were measured along the track to describe it.

First, the average wear area loss, $\bar{A}_w$ (mm^2) is calculated from depth (Y) and width (X) values, taken by the 2D profile data and using **Equation 3.14**. For $\bar{A}_w$ calculation, four 2D profile were measured (numbered lines in **Figure 3.12**) for each wear track.

$$\bar{A}_w = \sum_{i=0}^{n} 0.5(Y_i + Y_{i-1})(X_i - X_{i-1})$$

Equation 3.14 [17]

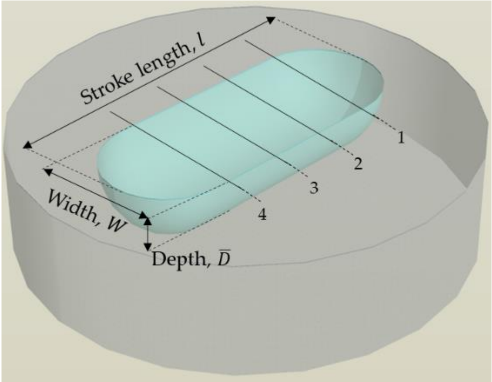

Figure 3.12. Model of wear track considered to calculate the wear parameters.

Once the $\bar{A}_w$, was obtained the average depth, $\bar{D}$ (mm) can be calculated by **Equation 3.15**.

$$\bar{D} = \frac{\overline{A_w}}{\bar{W}}$$ **Equation 3.15** [17]

Where, $\bar{W}$ is the average width of all wear tracks, measured in each wear track, for four 2D profiles. Volume loss value, V (mm^3) was calculated following **Equation 3.16**.

$$V = \left[\frac{1}{3} * \pi * \bar{D}^2 * (3R - \bar{D})\right] + \overline{A_w} * l$$ **Equation 3.16** [17]

Where R corresponds to the radius of the alumina ball (6 mm) and l, is the total stroke length (10 mm). Finally, the wear rate, W_v (mm^3/mm) was calculated considering V and the total sliding distance, S (mm) with **Equation 3.17**.

$$W_v = \frac{V}{S}$$ **Equation 3.17** [17]

3.8. Biological characterisation.

The biological characterisation performed in this work was performed in the Biochemical Laboratory of Dentistry Faculty of The Universidade de São Paulo, campus Bauru in Brazil.

This characterisation was carried out for the substrates TH-12Nb, TH40Nb and TH-5Fe-25Nb, sintered under C4 conditions. Prior to the cell culture, samples were ground with sandpaper to a final step of 1000. Then, the substrates were subjected to ultraviolet light for 30 min to reduce the contamination risk.

3.8.1. Cell culture.

For the cell culture, mouse preosteoblast MC3T3-E1 (subclone 14) cells (ATCC-American Type Culture Collection), passage 12, were cultured at 37 °C in modified alpha Minimum Essential Medium (α-MEM; Gibco, US) supplemented with 10 % Fetal Bovine Serum (FBS; Gibco, US), 1 % antibiotic-antimycotic solution composed of penicillin 10.000 units- streptomycin 10 mg/mL (Sigma-Aldrich) in a humidified 5 % CO_2 atmosphere.

After reaching the sub confluency, the cells were detached for 5 min in the CO_2 incubator at 37 °C using the enzyme trypsin, which is composed of 0.25 % trypsin-1 mM EDTA (Sigma-Aldrich). The enzyme was inactivated with α-MEM containing 10 % FBS. Cells suspensions were centrifuged at 1200 rpm, for 5 min at 4 °C. The supernatant was discarded, and the cell pellets were diluted in a new α-MEM/10% FBS medium.

3.8.2. Cell adhesion.

Samples were evaluated for cell adhesion, distribution and morphology using SEM (EVO-015, ZEISS, DE). Four samples of each alloy group (TH12Nb, TH40Nb and TH5Fe25Nb) were distributed in a 24-well plate. MC3T3-E1 cells were cultured at a density of 100 cells/mm^2 for 4, 24, 48 and 72 h.

After each period, samples were washed with Phosphate Buffered Salin solution (PBS; Gibco, US) to remove non-adhered cells. Then, samples were fixed by immersion in Karnovsky's solution containing 2.5% glutaraldehyde and 2% paraformaldehyde in 0.05 M sodium cacodylate buffer and 0.001 M calcium chloride, for 72 h. After fixation, the specimens were washed several times with cacodylate buffer 0.05 M and then, postfixed for 1 h with 1% osmium tetroxide in distilled water followed by extensive washing in distilled water to remove both the culture medium and buffer solution. Then, samples were sequentially dehydrated using ethanol gradient solutions (50, 60, 70, 80, 90, and 100%) for 10 min each, followed by drying. Finally, a thin gold coating was applied using a plasma sputtering system.

Five images at 45x magnification of each sample (20 images by each composition) were acquired for cell quantification.

3.8.3. Cell morphology and number.

Cell morphology and quantification was evaluated using a laser confocal fluorescent microscope (TCS SPE; Leica, Germany). For this purpose, three samples of each alloy group (TH12Nb, TH40Nb and TH5Fe25Nb) were used. The MC3T3-E1 cells were cultured at a density of 200 cells/ mm^2 for 4, 24, 48 and 72 h.

After culture time, the cells were fixed with using a solution of 2% paraformaldehyde in PBS for 20 min; then, samples were washed three times with PBS. Rhodamine phalloidin, a high-affinity F-actin probe, conjugated to the red-orange fluorescent dye, tetramethylrhodamine (TRITC), was used to label the actin cytoskeleton, as indicated by the supplier (Invitrogen™, US).

The samples were mounted face-up on glass slides and covered with rounded 13 mm coverslips. ProLong™ Diamond Antifade Mountant with DAPI (Invitrogen™) was used to counterstain nuclei in blue. The nuclei of cells were counted by Leica LAS X software.

3.8.4. Mineralisation assay.

Quantification and detection of the amount of mineralised calcium deposited in the extracellular matrix was performed by alizarin red staining. For the alizarin red assay, 0.050

mL of medium containing 50 cells/mm^2 (cultured as described procedure) was platted on the surface of substrates in 24-well plates, and 1.00 mL of medium was then added after 4 h of incubation. After 48 h, the cells were cultured in osteogenic medium containing 50 μg/mL acid ascorbic, 10 mM β-GP in α-MEM and 10% FBS.

The assay was performed in four replicates, on the different substrates, for 21 days. After this, the cells were washed with PBS three times and then fixed in 70% ethanol for 1 h at 4 °C. The cells were stained with 0.70 mL of alizarin red in ultrapure water for 10 min at room temperature. Then the cells were rinsed with ultrapure water, until the colour disappeared. Samples were observed by optical microscopy (Kodak GL 100 imaging system; Kodak Co., US).

Quantification method was obtained by addition of 280 μL of 10% (v/v) acetic acid solution to each well containing the substrate previously stained with alizarin red. The plate was shaken at room temperature for 30 min. After solubilisation, 100 μL of the extracted stain, from each substrate, were transferred to Eppendorf tubes and then 40 μL NH_4OH 10% was added to neutralise it. The coloured supernatant was put in a 96-well plate with a spectrophotometer (Synergy ™ Mx Monochromator-Based Multi-Mode Microplate Reader, BioTek Instruments Inc.) using a wavelength of 405 nm.

References

[1] C. Levoguer, "Using laser diffraction to measure particle size and distribution," *Met. Powder Rep.*, vol. 68, no. 3, pp. 15–18, 2013.

[2] C. Chirico, S. Tsipas, F. Toptan, and E. Gordo, "Development of Ti–Nb and Ti–Nb–Fe beta alloys from TiH2 powders," *Powder Metall.*, vol. 62, no. 1, pp. 44–53, 2019.

[3] H. Wang *et al.*, "Titanium and Titanium Alloy via Sintering of TiH2," *Key Eng. Mater.*, vol. 436, pp. 157–163, 2010.

[4] O. Ivasishin and V. Moxson, "Low-cost titanium hydride powder metallurgy," in *Titanium Powder Metallurgy*, Elsevier Inc., 2015, pp. 117–148.

[5] I. Paulin, Č. Donik, D. Mandrino, M. Vončina, and M. Jenko, "Surface characterization of titanium hydride powder," *Vacuum*, vol. 86, no. 6, pp. 608–613, 2012.

[6] H. Liu, P. He, J. C. Feng, and J. Cao, "Kinetic study on nonisothermal dehydrogenation of TiH2 powders," *Int. J. Hydrogen Energy*, vol. 34, pp. 3018–3025, 2009.

[7] Y. F. Yang and D. K. Mu, "Rapid dehydrogenation of TiH 2 and its effect on formation mechanism of TiC during self-propagation high-temperature synthesis from TiH 2 – C system," vol. 249, pp. 208–211, 2013.

[8] M. Roknian, A. Fattah-alhosseini, S. O. Gashti, and M. K. Keshavarz, "Study of the effect of ZnO nanoparticles addition to PEO coatings on pure titanium substrate: Microstructural analysis, antibacterial effect and corrosion behavior of coatings in Ringer's physiological solution," *J. Alloys Compd.*, vol. 740, pp. 330–345, 2018.

[9] X. Zhang *et al.*, "Characterization and property of bifunctional Zn-incorporated TiO2 micro-arc oxidation coatings: The influence of different Zn sources," *Ceram. Int.*, vol. 45, no. 16, pp. 19747–19756, 2019.

[10] D. Simeone, G. Baldinozzi, D. Gosset, S. Le Caer, and J. F. Bérar, "Grazing incidence X-ray diffraction for the study of polycrystalline layers," *Thin Solid Films*, vol. 530, pp. 9–13, 2013.

[11] C. Genzel, "X-ray residual stress analysis in thin films under grazing incidence - Basic aspects and applications," *Mater. Sci. Technol.*, vol. 21, no. 1, pp. 10–18, 2005.

[12] M. Birkholz, "Thin films and multilayers," *Int. Tables Crystalography*, vol. H, no. Chapter 5.4, pp. 581–600, 2019.

[13] "UNE-EN ISO 6507-1:2018 Metallic materials- Vickers hardness test- Part 1: Test method."

[14] W. C. Oliver, "Measurement of hardness and elastic modulus by instrumented indentation : Advances in understanding and refinements to methodology," 2004.

[15] C. Romero, F. Yang, and L. Bolzoni, "Fatigue and fracture properties of Ti alloys from powder-based processes – A review," *Int. J. Fatigue*, vol. 117, pp. 407–419, 2018.

[16] E. . Hearn, "Simple Stress and Strain," in *Mechanics of Materials 1: an introduction to the mechanism of elastic and plastic deformation of solids and structural components*, 3rd ed., Musselburgh: Butterwoth Heinemann, 1997, pp. 1–26.

[17] J. Ureña, E. Tabares, S. Tsipas, A. Jiménez-Morales, and E. Gordo, “Dry sliding wear behaviour of β-type Ti-Nb and Ti-Mo surfaces designed by diffusion treatments for biomedical applications,” *J. Mech. Behav. Biomed. Mater.*, vol. 91, pp. 335–344, 2019.

CHAPTER 4

Study of Titanium hydride decomposition

CHAPTER 4

4.1. Introduction.

The β-Ti alloys in this study were designed to be composed predominantly of β-Ti phase, as a strategy to reduce the elastic modulus of the Ti alloys; avoiding or preventing the stress shielding phenomenon. β-Ti alloys were produced by the addition of Nb and Fe as alloying elements and using titanium hydride (TiH_2) powder as Ti source. Three different compositions containing Ti-12Nb, Ti-40Nb and Ti-5Fe25Nb (in wt.%) were prepared in this work. [1]

The objective of this work is to identify the phases formed during the decomposition of TiH_2 as well as the effect of the addition of β-stabilising elements such as Fe and Nb on the decomposition of TiH_2, in order to be able to control the decomposition process and produce β-Ti alloys from TiH_2.

Understanding the thermal behaviour of TiH_2 is essential for the processing of Ti alloys. The use of TiH_2 offers advantages. Hydrogen elimination, during dehydrogenation, provides a H-rich atmosphere that protects Ti against oxidation. Besides, use of TiH_2 instead of Ti powder promotes sintering, achieving samples with higher densification compared to Ti samples consolidated under the same conditions. [1]–[3]

The dehydrogenation process was analysed considering two conditions. Firstly, using a constant high purity argon flow, which allows to follow the dehydrogenation process in-situ. Secondly, heating the samples in high vacuum conditions (VAC). The phase evolution in VAC was studied for temperatures from 400 °C to 1100 °C, which allows evaluating the dehydrogenation (at lower temperatures) and the alloying element diffusion process (at higher temperatures).

The study was performed controlling shrinkage, mass loss related to hydrogen released, and densification, as well as the evolution of the microstructure during the different stages of the process. The dehydrogenation evolution under argon flow and high vacuum conditions are compared and discussed in this chapter.[2]

---

[1] Both Fe and Nb employed in this section are referred to as Fe-2 and Nb-2 in Section 3.2

[2] The main part of the information compiled on this chapter is published in:
"Beta Titanium Alloys Produced from Titanium Hydride: Effect of Alloying Elements on Titanium Hydride Decomposition". **Chirico, C.**; Tsipas, S.A.; Wilczynski, P.; Gordo, E. doi.org/10.3390/met10050682

4.2. Thermodynamic design of alloy composition.

This work aims to reduce the Young's Modulus of the current Ti alloys employed as biomedical implants by developing β-Ti alloys processed by powder metallurgy route. The alloying elements must be a non-toxic and biocompatible β-stabiliser elements, which restricts the alternatives. It has been reported several times that elements such as Nb, Mo, Ta, Zr comply with these requirements, showing a wide solubility in BCC β-titanium [4]–[7].

It is well known that Nb is an isomorphous β stabiliser element for Ti due to the complete solubility of Nb in β-Ti phase. However, processing of Ti-Nb alloys is a challenge in both ingot and powder metallurgy (PM) routes. In the first case, high temperature is required due to the high melting point of Nb (2477 °C) that causes macro and micro-segregation of Nb [8], [9]. Whereas in PM processing, the low Nb diffusivity in Ti inhibits the development of homogeneous microstructures of Nb-rich Ti alloys. Therefore, high sintering temperature and long sintering times are required to promote the complete diffusion among Nb and Ti. [10], [11]

High Nb content is needed to obtain stable β-Ti phase at room temperature. Addition of large amounts of Nb implies increasing the weight of the alloy, due to its high density (8.57 g/cm^3); and raising the alloy cost since Nb is an expensive metal. Hence, it is desirable to develop β-Ti alloys based on low-cost alloying elements such as Fe, Cr, Mn and Sn that promote the β phase stabilisation with lower Nb amount, reducing the alloy cost [12], [13]. The new generation of β-Ti alloys with non-toxic and low-cost elements involves systems like Ti-Cr-Al, Ti-Mn, Ti-Cr-Sn-Zr, Ti-(Cr, Mn)-Sn, Ti-Sn-Cr and Ti-Mn-Fe. [14], [15]

Addition of small amounts of Fe has several advantages for Ti alloys processing [16], [17]: Fe promotes the β phase stabilisation allowing the decrease of the Nb content required; it improves the sinterability of Ti alloys since it accelerates mobility of Ti atoms by rapid Fe diffusion; Fe increases the Ti auto-diffusion coefficient [18], which could enhance the Nb diffusion process, promoting a homogeneous microstructure; and, finally, Fe is a low-cost material, considered non-toxic and biocompatible, so substituting Nb with Fe fraction can contribute to the cost reduction of the alloy. Both Fe and Nb are non-toxic and biocompatible β-stabilizer elements, so they can be promising alternatives to develop novel low elastic modulus Ti alloys [19].

For Ti-xNb alloys, two Nb additions were selected that allow obtaining: 1) a biphasic (α+β) microstructure, similar to that exhibited by Ti6Al4V alloy, commonly used in the manufacture of the hip implants; and 2) a microstructure composed mainly by β-Ti phase. It has been reported in the bibliography [4], [20], [21], that around 10-15 wt.% of Nb leads to a biphasic microstructure, with alpha phase as the dominant phase; while for Nb content above 35 wt.%, the Ti alloy becomes entirely β-Ti phase. Based on the literature, compositions containing Ti-12 wt.% Nb and Ti-40 wt.% Nb were considered as starting compositions for Ti-Nb system. **Figure 4.1a** shows the phase diagram obtained for Ti-xNb system and **Figure 4.1b** the Ti-5Fe-xNb system using Thermocalc © software.

This work attempts to evaluate the effect of 5 wt.% of Fe on Nb-Ti diffusion process. The addition of 5wt% Fe was selected based on previous studies developed in the research group [22], [23], which reveal that with a 5 wt.% of Fe addition, Fe remains well dissolved into the Ti matrix, and there is no formation of TiFe intermetallic. For Ti alloys containing 5 wt.% Fe, a strengthening effect was observed, as well as an increase of the β-Ti fraction compared to pure Ti alloy.

Composition for Ti-5Fe-xNb was chosen according to the fraction of the alpha and beta phase theoretically expected at 400 °C in the phase diagrams of the Ti-Nb and Ti-5Fe-Nb (**Figure 4.1**) obtained by thermodynamic simulation, with Thermocalc © software using Ti alloys database V3.1 (TTTI3).

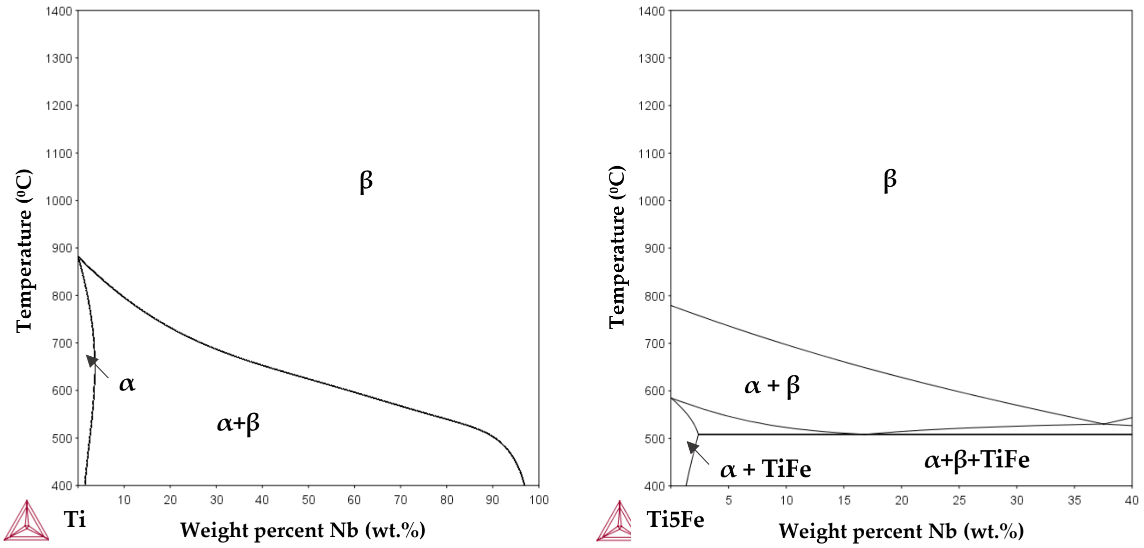

(a) **(b)**

Figure 4.1. Phase diagram for: a) Ti-xNb and b) Ti-5Fe-xNb system. Obtained by Thermocalc software using Ti alloys database V3.1 (TTTI3).

The aim is to obtain the highest β phase fraction, decreasing Nb weight percentage. First, the amount of β phase was determined for the starting compositions of Ti-12Nb and Ti-40Nb at 400 °C. Then, Ti-5Fe-Nb system was evaluated in order to determine the Nb amount needed to achieve a similar β-phase fraction to Ti-40Nb composition at the same temperature of 400 °C.

Table 4.1. summarises the phase fractions and beta transus temperature expected for each alloy, as predicted by Thermocalc ©. For Ti-40Nb, the maximum β phase fraction is 27% approximately, according to phase diagram results. Hence, the alloy that allows reaching a similar fraction of 25% of β phase is Ti-5Fe-25Nb. Moreover, a noticeable beta transus

temperature reduction with respect to unalloyed Ti can be observed, due to the Nb addition. Beta transus is reduced at least 100 ºC bellow for the alloy containing Ti-12Nb, and until 287 °C for alloy Ti-5Fe-25Nb.

Table 4.1. Estimated parameters for Ti-Nb and Ti-5Fe-Nb obtained by Thermocalc at 400 °C.

Samples	**Phase fraction (wt. %)**		**$\beta_{transus}$ (ºC)**
	α-Ti	**β-Ti**	
Ti-12Nb	93.8	6.2	775
Ti-40Nb	73.2	26.8	650
Ti-5Fe-25Nb	75.1	24.9	595

4.3. Thermal behaviour during titanium hydride decomposition.

4.3.1. Effect of alloying elements on thermal decomposition of titanium hydride.

Figure 4.2 shows the DTA results of the powder samples. For comparison proposes, an unalloyed TiH_2 curve has been plotted alongside the powder mixtures in all cases. **Table 4.2** summarises the temperatures of interest for each decomposition stage obtained from DTA tests. DTA curves exhibit a typical decomposition behaviour for TiH_2. Overall, for all samples and compositions, two reactions can be distinguished, represented by two intense and discernible endothermic peaks between 450-625 °C. The temperature of these peaks coincided with local maximums of hydride decomposition reaction and hydrogen release rate. The last stage observed, corresponding to a slight shoulder (marked with an arrow) around 630-870 °C, is associated with the third decomposition stage. Changes in the third stage were subtle since the amount of remaining hydrogen was very low to produce significant differences in this temperature range. Moreover, diffusion of the alloying elements (Nb and Fe) could occur close to this range of temperature. Hence, two processes might be taking place simultaneously, which could overlap.

According to literature, the whole TiH_2 decomposition takes place between 380-800 °C approximately [24], [25]. Reported data of accurate temperature of dehydrogenation stages, as well as the corresponding phase transformation, can differ. This is because there is a strong dependence on samples' characteristics such as the powder purity, samples mass, powder particle size, surface contamination, and experimental techniques employed, like heating rate, atmosphere, etc.

Liu et al. [26], Kennedy [27], and Ma et al. [28] proposed that dehydrogenation occurs with the following sequence (**Equation 4.1)**

$$\delta(TiH_2)\xrightarrow{\text{Stage I}}\delta(TiH_x)\xrightarrow{\text{Stage II}}\beta(Ti)_H\xrightarrow{\text{Stage III}}\beta(Ti)_H+\alpha(Ti)_H\xrightarrow{\text{Stage IV}}\alpha(Ti) \qquad \textbf{Equation 4.1}$$

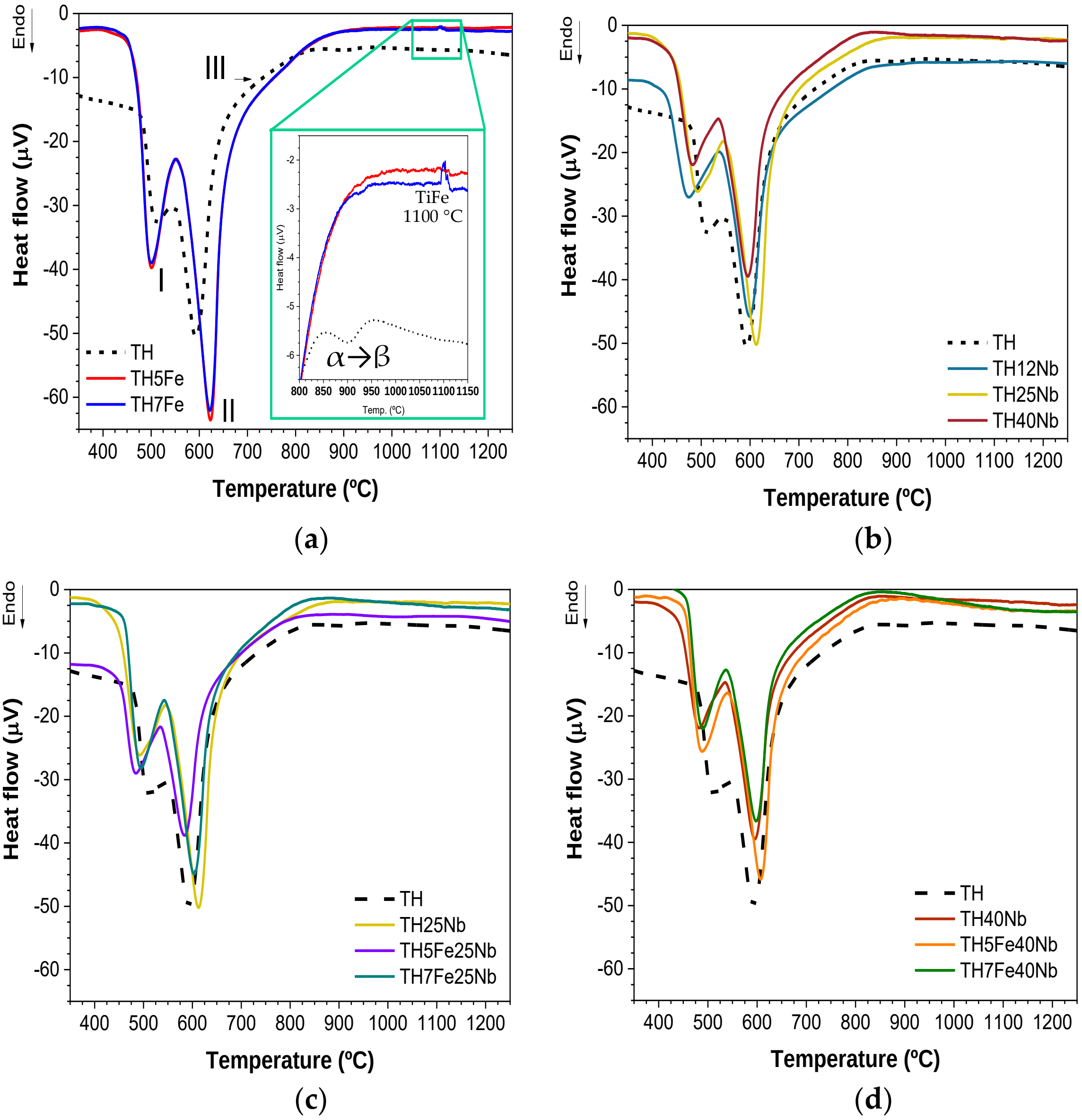

(**a**) (**b**)

(**c**) (**d**)

Figure 4.2. Comparison of differential thermal analysis (DTA) curves between TiH_2 and mixtures of powders under high purity argon atmosphere heated at 10 °C/min. (a) TH-Fe (5 and 7 wt. %); (b) TH-Nb (12, 25, 40 wt. %); (c) TH-Nb-Fe (25 wt. % Nb and 5, 7 wt. % Fe) and (d) TH-Nb-Fe (40 wt. % Nb and 5, 7 wt. % Fe).

In the beginning, hydrogen atoms are released and change their position randomly from tetrahedral to octahedral interstitials sites, but keeping the initial FCC structure of δ-TiH_2 (stage I). During stage II, as hydrogen is lost, the δ phase is gradually transformed to a β-Ti phase that is hydrogen-rich (β-Ti_H) with a BCC crystal structure. In stage III, hydrogen is continuously released from β-Ti_H, and α-Ti_H begins to form when the hydrogen amount is low enough. Overall, during stages II and III, the highest conversion of titanium hydride takes place, achieving up to 80% of dehydrogenation. These stages are usually quick and intense; they may occur, simultaneously, between 500-700 °C [26]. The phase transformation model is like a core-shell structure, where δ (TiH_x) constitutes the nucleus; the intermediate layer corresponds to β-Ti_H and external layer is α-Ti_H. Finally, complete α-Ti transformation occurs, which means that complete hydrogen elimination is produced in the last stage, but this stage is very dependent on the surface features. It has been reported that the formation of a slight oxide layer on the particles surface could hinder complete dehydrogenation [26], [29], [30].

Table 4.2. Transformation temperatures found during the dehydrogenation process analysed by differential thermal analysis (DTA).

Sample	Temperature (°C)					
	Stage I		Stage II		Stage III	
	Onset	Peak	Onset	Peak	Onset	Offset
TiH_2 (TH)	475	510	555	592	650	830
TH-5Fe	395	500	555	623	700	880
TH-7Fe	385	500	555	620	700	875
TH-12Nb	380	470	535	600	645	850
TH-25Nb	385	490	545	613	645	870
TH-40Nb	390	480	540	596	630	830
TH-5Fe25Nb	410	485	535	585	645	815
TH-7Fe25Nb	405	495	542	695	630	840
TH-5Fe40Nb	420	487	535	608	635	855
TH-7Fe40Nb	425	490	545	600	630	845

Several authors only agree on the first decomposition stage, where the progressive loss of hydrogen is produced, keeping the FCC structure. Another approach [31], [32] claims that the TiH_2 decomposition occurs through the δ (TiH_x) transformation to α-Ti on the particle surface. In this case, the phase structure changes from FCC to HCP.

The dehydrogenation process did not seem considerably modified by the addition of different amounts of Nb and Fe, either by elemental or combined addition, considering that for all samples, the three stages of the dehydrogenation process could be observed (**Figure 4.2**). However, the addition of alloying elements was found to accelerate the beginning of the reaction during the first stage: Both onset and peak temperatures were shifted up to 95 °C and 40 °C below the correspondent values for the unalloyed material. (**Table 4.2**); whereas the temperature of stage II was maintained similar to that of TiH_2 for all samples with a variation of ±25 °C. Finally, it can be seen that the dehydrogenation process for mixtures of powders finished at higher temperatures compared to pure TiH_2. This factor suggests that the alloying elements could act as a barrier to the removal of the remaining hydrogen. The last theoretical dehydrogenation reaction (stage IV), where the transformation (β_H + α_H) to α-Ti phase takes place, was not expected to happen for the alloyed samples due to the presence of a high quantity of beta-stabiliser elements incorporated, which reduce the beta transus temperature considerably with respect to unalloyed Ti (See **Table 4.1**).

On the other hand, as observed in **Figure 4.2**, a slight endothermic peak between 850-950 °C for TiH_2 can be seen, which corresponds to theoretical $\alpha \rightarrow \beta$ transformation (882 °C). No $\alpha \rightarrow \beta$ transformation was observed for samples of the Ti-Nb and Ti-5Fe-Nb systems. The $\alpha \rightarrow \beta$ transformation was expected to occur at lower temperatures due to Fe and Nb addition, as well as the possible remaining hydrogen. Hydrogen is frequently used in Ti alloys processing as a temporary alloying element for improving the workability of the alloy [33]. Therefore, the absence of this slight endothermic peak in all powders that contained Fe and Nb alloying elements could be attributed to the $\alpha \rightarrow \beta$ transformation taking place at lower temperatures and overlapping with the second stage of dehydrogenation process.

At higher temperatures, around 1090 °C, an exothermic reaction for TH-7Fe (detail in **Figure 4.2**a) was produced, which was associated with the formation of intermetallic TiFe [23]. In the case of TH-5Fe, there was no evidence of this reaction. This could indicate that 5 wt. % Fe was not enough to promote TiFe formation. During cooling, reverse reactions to those produced during heating were not observed, due to the irreversibility of Ti-Fe reaction, and the stability of the β phase.

4.3.2. Shrinkage evolution during the dehydrogenation process.

In order to understand the behaviour during TiH_2 decomposition and sintering of base Ti alloys, dilatometry experiments were carried out for all compositions. **Figure 4.3** plots the dilatometric curves. In all diagrams, a curve for pure TiH_2 is included as a reference. According to Wang et al. [30], densification behaviour of TiH_2 compounds is a consequence of two factors: (1) The volume change caused by the high density of dislocations and vacancies due to the dehydrogenation process, which increases diffusion rates. (2) The cleaning effect of the hydrogen atoms released which can remove a fraction of oxygen of the Ti surface and promote sintering densification. In this work, the effect of the addition of β-stabiliser elements, like Nb and Fe, on dehydrogenation and densification processes is evaluated.

Samples with a lower amount of alloying elements (TH-5Fe, TH-7Fe, and TH-12Nb) presented similar shrinkage to unalloyed TiH_2. As the content of alloying elements increased, shrinkage was considerably modified as compared to pure TiH_2.

In the beginning, all samples exhibited expansion up to 500 °C; this coincides with stage I of TiH_2 decomposition. This extension could be attributed to the increase of the lattice parameter of δ-TiH_x due to the thermal expansion coefficient change as the temperature increased, as well as to the lattice defects generated by hydrogen removal.

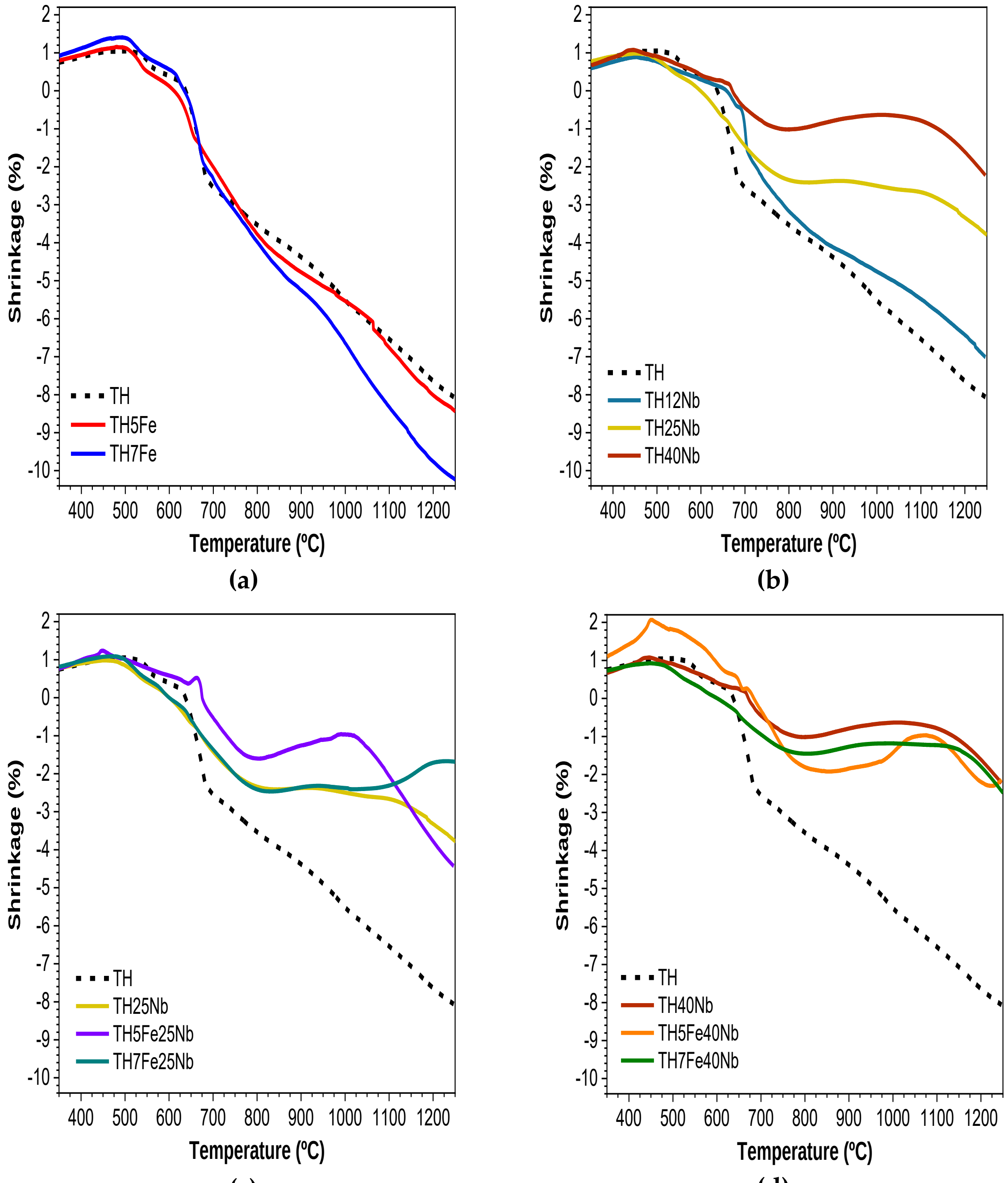

(a) **(b)**

(c) **(d)**

Figure 4.3. Dilatometric curves for compact powders. Analyses were performed under a high-purity argon atmosphere, heating at 10 °C/min. (a) TH-Fe (5 and 7 wt. %); (b) TH-Nb (12, 25, 40 wt. %); (c) TH-Nb-Fe (25 wt. % Nb and 5, 7 wt. % Fe) and (d) TH-Nb-Fe (40 wt. % Nb and 5, 7 wt. % Fe).

In **Figure 4.3a**, it can be seen that expansion was followed by a drastic increase of shrinkage rate up to 600 °C. This agrees with stage II of TiH_2 decomposition, which is the most intense step of the dehydrogenation process and produces a quick shrinkage of the samples due to the higher amount of hydrogen released. During this stage, the crystallographic structure changed from FCC (δ-TiH_x) to BCC (β-Ti_H), which also contributed to the change in volume due to solute atoms' rearrangement. Taking into account the diffraction patterns obtained from the International Centre for Diffraction Data (ICDD) database for δ-TiH_x (03-065-0934) and β-Ti (01-089-4913), which have lattice parameters of 4.450 Å and 3.283 Å, respectively, an approximate calculation of the shrinkage expected could be made. According to these lattice parameters and the number of atoms in the unit cell of each crystal structure, one-unit cell, FCC (δ-TiH_x) had a volume of 0.088 nm^3, and it was transformed into two-unit cells BCC (β-Ti), which exhibited a volume of 0.071 nm^3 (0.035 nm^3 each one). Hence, with a rough calculation, it could be estimated that this crystal structure changes involved shrinkage of around 20%.

Between 600 and 800 °C shrinkage occurred at a slower rate, since dehydrogenation was almost finished. Around 800 °C, a slight slope change could be observed, which suggests that sintering has started. From 800 °C onwards, the shrinkage observed could be related to the neck formation between Ti particles. Results indicate that Fe addition promotes sample densification since TH-7Fe showed higher contraction value than TH-5Fe and TiH_2. Samples TiH_2 and TH-5Fe reached a shrinkage of 8% and 8.5%, respectively, while 10.2% was achieved for sample TH-7Fe. This fact may have been caused because Fe increases self-diffusion coefficient of Ti, which enhances the sinterability [34]; furthermore, the small particle size of the Fe employed (Fe-2; D_{50} 3–4 μm), and its spherical morphology, improves filling of empty spaces between TiH_2 particles, promoting better sample densification. Globally, TH-7Fe sample exhibited 24% higher shirnkage than pure TiH_2 and 18% higher than sample TH-5Fe. The possibility of formation of TiFe with the addition of 7 wt. % should be taken into account since it could be undesirable due to its brittle nature.

Concerning the Nb addition effect, **Figure 4.3b** indicates that as the Nb amount increased, the percentage of shrinkage decreased, which was expected because as TiH_2 content decreases, the sample contraction is lower, too. The linear shrinkage values correspond to 7%, 3.8%, and 2.2% for TH-12Nb, TH-5Fe-25Nb, and TH-40Nb, respectively. Sample TH-12Nb exhibited similar behaviour to TiH_2, although a decrease of the shrinkage rate from 650 °C (after stage II) could be noted. For samples TH-25Nb and TH-40Nb, after the initial expansion observed (stage I), the shrinkage rate was more subtle than for TiH_2, which suggested that Nb could delay or inhibit the TiH_2 decomposition process. On the other hand, around 900 °C a shoulder could be observed, which became more evident as the Nb amount increased. This could be related to the diffusion process of Nb into the Ti lattice. It has been reported that the interdiffusion coefficient of Ti-Nb decreases over 2–4 orders of magnitude with an increase in the Nb amount [35], [36]. According to the Ti-Nb phase diagram, BCC-Nb and BCC-Ti are completely soluble over 900 °C; therefore, from this temperature onwards, diffusion processes were faster with the increase in temperature [6].

Figure 4.3c,d shows the influence of Fe addition on the alloys with higher Nb content (25 wt. % and 40 wt. %, respectively). These alloys suffered smaller shrinkage than unalloyed TiH_2, and the influence of Nb combined with Fe was not clear. An expansion of 0.6% was found at 1000 °C for sample TH-5Fe25Nb, whereas TH-7Fe25Nb reached an expansion of 0.8%, which was delayed until 1250 °C. For samples containing 40 wt. % of Nb, expansion of

1% was observed just for TH-5Fe40Nb around 1075 °C, while TH-7Fe40Nb showed shrinkage behaviour similar to TH-40Nb. Further tests are necessary in order to understand the effect of the simultaneous addition of Nb and Fe.

Despite the fact that the starting temperature of dehydrogenation stages is shifted with alloying elements addition, decomposition behaviour did not seem to be modified significantly for the rest of the stages with respect to respect to unalloyed TiH_2 (as shown in **Section 4.3.1**). The final sample densification was considerably affected by the incorporation of the alloying element since both Fe and Nb had different and opposite interactions with Ti particles (once TiH_2 was decomposed): while Fe promoted sinterability and therefore, final densification increased; Nb, owing to its large atomic size and poor diffusion rate, impeded the densification.

4.3.3. Comparison of mass loss during the dehydrogenation process under different environments.

Mass losses of samples tested under argon (TGA analysis) and in vacuum conditions (VAC, heat treatment in a tubular furnace) are shown in **Figure 4.4a,b,** respectively. In both cases, the mass loss percentage is in accordance with the TiH_2 fraction present in each composition. So, TiH_2 exhibited the highest mass loss of 3.9%, while, as the amount of alloying elements increased, mass loss decreased. Thereby, the most alloyed composition, TH-40Nb, showed the lowest mass loss of 2.5%.

Table 4.3 summarises the relative weight loss achieved in both environments, which was related to the total amount of hydrogen according to the initial TiH_2 powder in each mixture. It was noticeable that at low temperature, while the dehydrogenation process took place (up to 800 °C approximately), samples evaluated under vacuum condition reached higher weight loss compared to samples treated in argon flow.

Table 4.3. Relative hydrogen weight loss (%) for treated samples heated in Thermogravimetric analysis (TGA) and Vacuum treatments (VAC) test**.**

Samples	400 °C		500 °C		650 °C		800 °C		1100 °C	
	TGA	VAC	TGA	VAC	TGA	VAC	TGA	VAC	TGA	VAC
TiH_2 - (TH)	2.3	16.7	1.7	76.8	66.3	98.9	89.1	99.8	94.8	99.1
TH-5Fe	<1	14.9	9.9	74.7	57.1	90.6	87.8	97.4	97.7	98.1
TH-12Nb	5.9	18.4	9.5	84.0	58.7	97.3	83.8	97.7	89.9	98.1
TH-40Nb	<1	24.7	15.0	92.8	70.9	96.0	93.9	99.7	98.4	99.7
TH-5Fe25Nb	8.5	14.0	7.0	84.6	62.9	97.9	86.7	98.3	90.6	98.0

No observable mass loss was found at 400 °C in argon flow for all samples, while in high vacuum at least 14% of hydrogen loss for TH-5Fe25Nb was reached. At 650 °C, almost all hydrogen contained in the samples was released for VAC samples: Sample TH-5Fe reached hydrogen loss of 90.6% under vacuum, while with argon it reached 57.1%. Finally, from 800 °C onwards, mass loss became stable for vacuum samples while for samples in argon, hydrogen was still being released. The amount of hydrogen retained on the samples TH-5Fe, TH-12Nb, and TH-5Fe25Nb could be attributed to formation of a slight oxide layer on the particle surface, which interferes with complete degasification. The formation of this oxide layer was highly likely due to the inherent nature of Ti, and has been previously reported in the literature [26], [29]–[31].According to results, dehydrogenation occurs faster under vacuum than in argon flow; this is due to the fact that hydrogen released during the decomposition process is continuously removed when the samples are under vacuum.

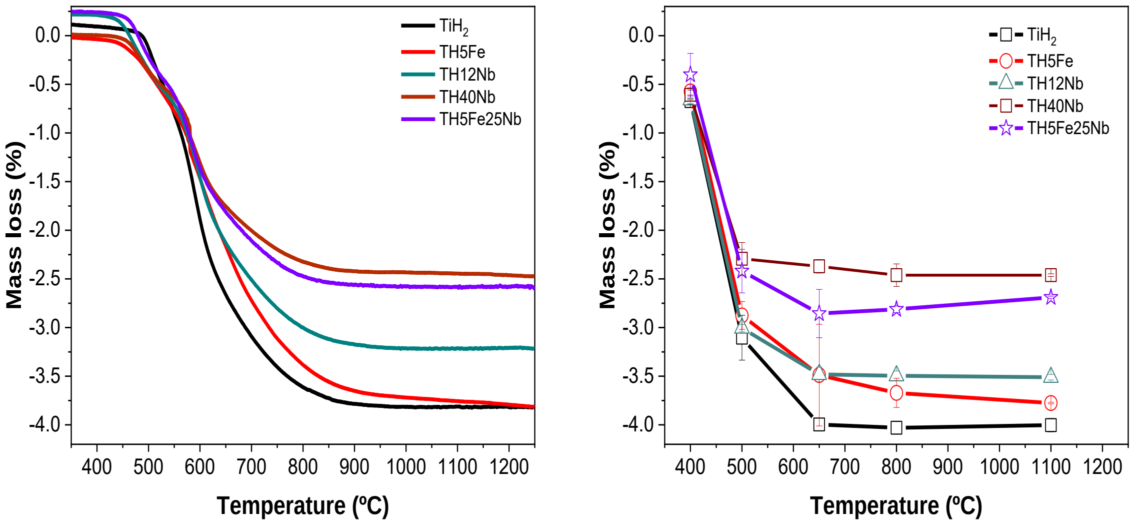

(a) (b)

Figure 4.4. Mass loss for the compositions prepared, obtained by **(a)** Thermogravimetric analysis (TGA) of mixtures of powders (samples measured under argon flow of 80 mL/min) and **(b)** Vacuum treatments (VAC) of compact samples (samples treated under high-vacuum conditions).

Moreover, the heating rate during dehydrogenation is an important aspect to consider. Many researchers have reported that a lower heating rate promotes an effective dehydrogenation process [26], [28]. Tests in argon flow were carried out with a heating rate of 10 °C /min, while in vacuum, a rate of 2 °C/min was employed. Hence, the sum of these observations suggests that both lower heating rate and high-vacuum sintering enhanced the dehydrogenation process, promoting an effective hydrogen elimination. In all cases, the addition of alloying elements did not hinder the achievement of full dehydrogenation, even when the starting and ending temperature of the reactions could be slightly shifted.

4.3.4. Microstructure evolution during the TiH_2 decomposition.

The microstructural evolution during the dehydrogenation process of TiH_2 and TiH_2 alloys heated from 400 to 1100 °C is explained below. **Figure 4.5**,**Figure 4.6**,**Figure 4.7**, **Figure 4.10** and **Figure 4.11** show the microstructures of the five compositions heat-treated at 400 ºC, 500 ºC, 650 ºC, 800 ºC and 100 ºC, respectively. .

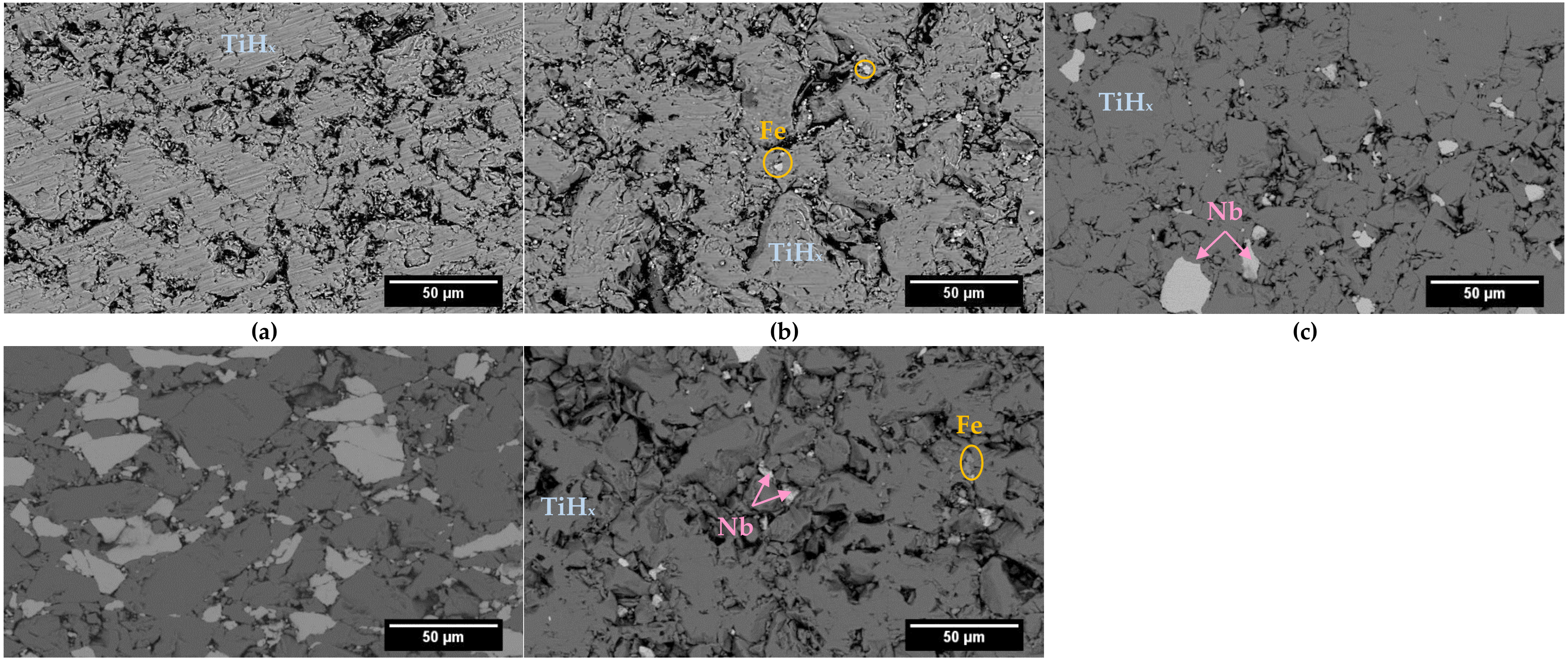

(a) (b) (c)

(d) (e)

Figure 4.5. Scanning Electron Microscopy images in backscattered electrons mode (BSE-SEM) for samples treated at 400 °C: **(a)** TiH_2 (TH); **(b)** TH-5Fe; **(c)** TH-12Nb; **(d)** TH-40Nb; and **(e)** TH-5Fe25Nb.

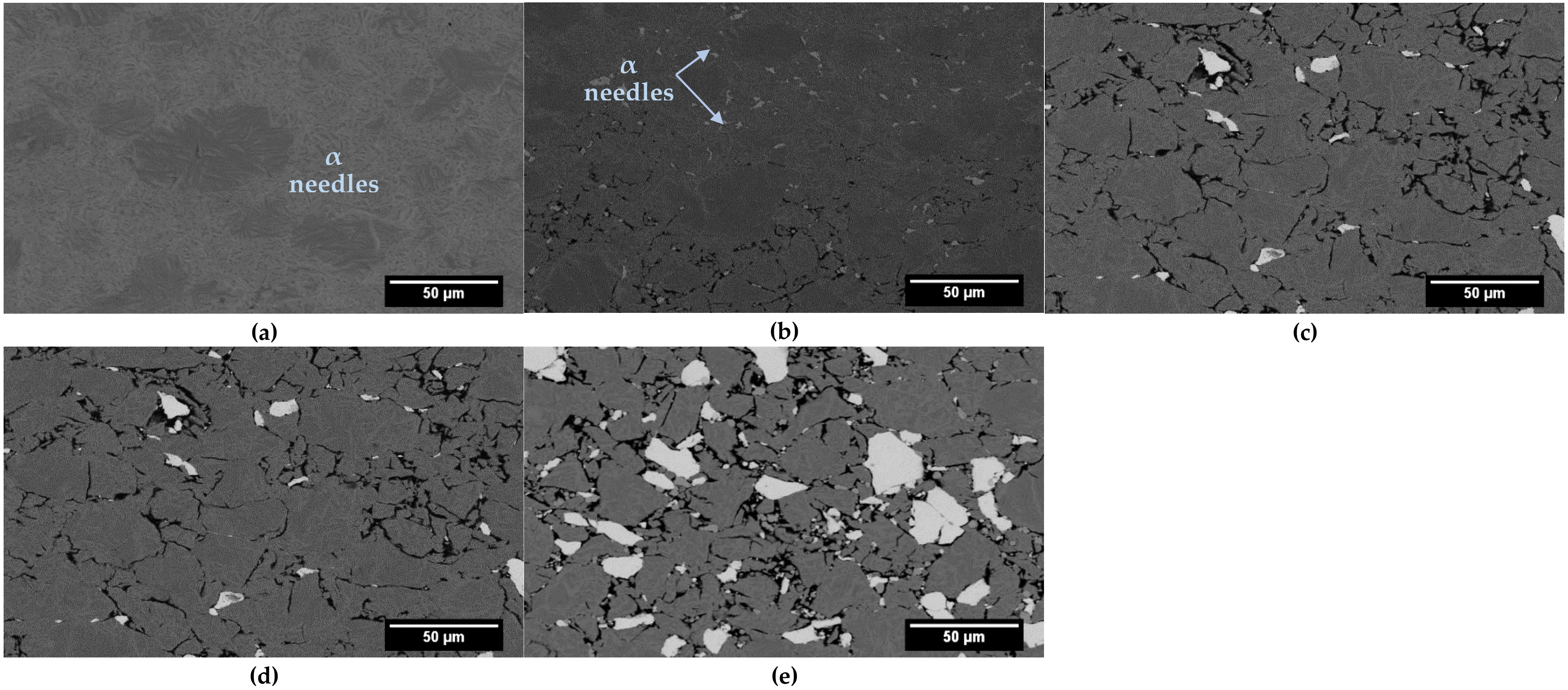

Figure 4.6. Scanning Electron Microscopy images in backscattered electrons mode (BSE-SEM) for samples treated at 500 °C: **(a)** TiH_2 (TH); **(b)** TH-5Fe; **(c)** TH-12Nb; **(d)** TH-40Nb; and **(e)** TH-5Fe25Nb.

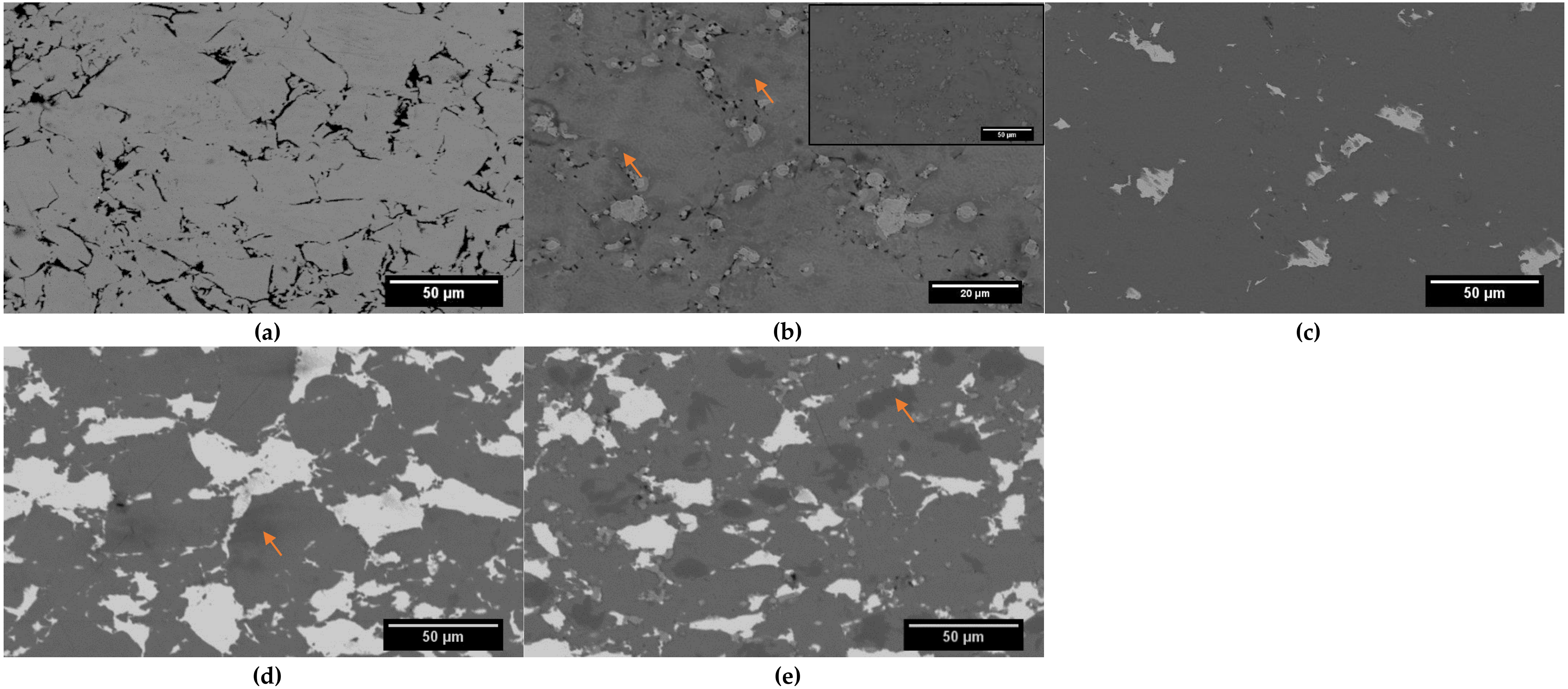

(a) (b) (c)

(d) (e)

Figure 4.7. Scanning Electron Microscopy images in backscattered electrons mode (BSE-SEM) for samples treated at 650 °C: **(a)** TiH_2 (TH); **(b)** TH-5Fe; **(c)** TH-12Nb; **(d)** TH-40Nb; and **(e)** TH-5Fe25Nb.

At 400 °C (**Figure 4.5**), no significant changes were found in the microstructure with respect to green compacts. The samples seem to be composed of titanium hydride particles, Nb, and Fe (for TH5Fe and TH5Fe25Nb). All samples maintain their original morphology induced by the pressing process. Due to the brittleness of titanium hydride, smaller broken particles can be seen filling the spaces in-between the bigger particles. According to the results reported in **Table 4.3**, samples at 400 °C achieved a weight loss between 14% and 25% of hydrogen, which suggests dehydrogenation had already started. This fact suggests that samples at 400 °C were composed of a nonstoichiometric titanium hydride, TiH_x, were x is referred to a fraction between 1 and 2.

At 500 °C (**Figure 4.6**), needle-like structures were found, forming from the outside towards the interior of the hydride particles. These needles could be associated with the first transformation of titanium hydride to α-Ti. Besides this, no interaction signs of alloying elements with titanium hydride were found, and particles seemed to be closer together than at 400 °C, which agrees with the dilatometric curves (**Figure 4.3**) that show initial shrinkage took place among 400-500 °C. Furthermore, samples heated up to 650 °C (**Figure 4.7**) show a drastic increase in densification. Shrinkage observed at 500 °C and 650 °C coincides with the linear shrinkage calculated for the samples heated under vacuum, as it can be seen in **Figure 4.8**, where there is a slight increase in contraction at 500 °C followed by a more pronounced shrinkage, reaching 4.5% for TiH_2 and TH-5Fe, 3.8% for TH-12Nb, 3% for TH-5Fe25Nb and 1.8% for TH-40Nb. Samples containing a higher amount of TiH_2 had higher contraction values as well. Hence, it can be confirmed that achieved densification was due to the dehydrogenation process.

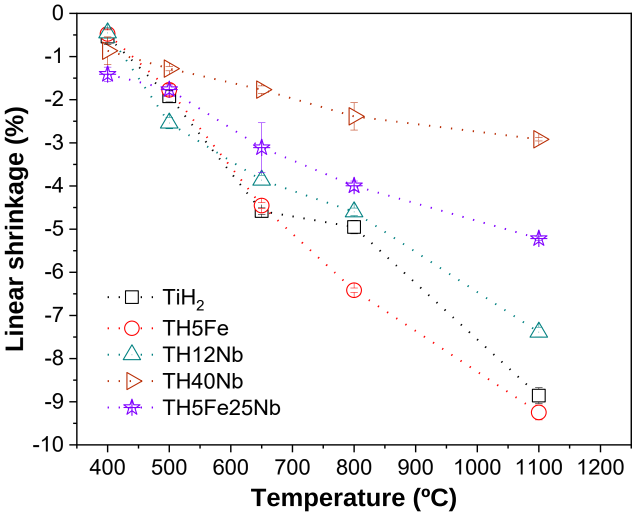

Figure 4.8. Linear shrinkage for samples heated under VAC conditions at different temperatures.

On the other hand, at 650 °C, alpha needles were no longer visible, suggesting that complete transformation took place during the dehydrogenation until all the structure of alloyed samples was composed of mainly α-Ti matrix with few H-rich regions (darkest spots indicated by orange arrows in **Figure 4.7**). Both densification and α-Ti transformation were expected since it has been reported that around 600-650 °C, most of the hydrogen is released, and samples are mainly composed of α-Ti [26].

The transformation from TiH_x to α-Ti phase was not in accordance with the mechanism previously proposed in Equation (1), in which, at this temperature (around 650 °C), the transformation from TiH_x to β-Ti was expected instead of transformation to α-Ti. In this case, alpha phase may appear during cooling since the heating of samples treated under vacuum conditions was stopped at specific temperatures and samples were cooled down for microstructural observation, also stopping the decomposition reaction. Hence, the β-phase obtained from the dehydrogenation process, according to the transformation process suggested, was reverted to α-Ti phase during cooling, which was not fast enough to maintain the β-phase microstructure.

In addition, it can be seen that the Fe particles were surrounded by a brighter ring that indicated that the diffusion processes between Fe and Ti had started. This effect is shown in detail for TH-5Fe in **Figure 4.9**. Fe diffusion in α-Ti is unlikely since the maximum solubility of Fe in α-Ti is lower than in β-Ti, 0.047 and 17 wt. %, respectively. Besides, it is known that diffusivities of Fe in β-Ti is around four orders of magnitude larger than in α-Ti [37]. So, β-Ti might have been stabilising around the Fe particles, even when the temperature was significantly lower than the β transus temperature expected (775 °C) according to Ti-Fe phase diagram for 5 wt. % of Fe (See **Table 4.1**).

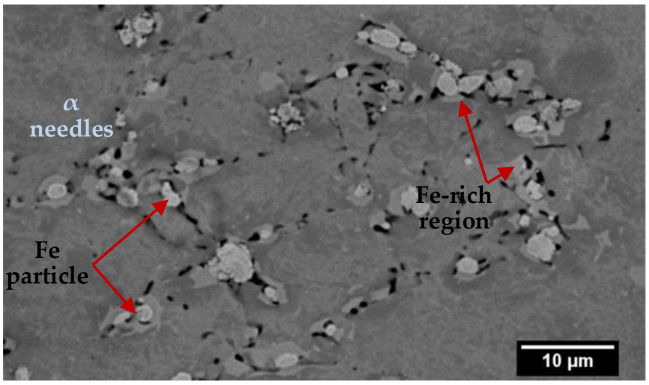

Figure 4.9. BSE-SEM image for TiH_2-5Fe heated up to 650 °C: Detail of Fe diffusion. Black spots correspond to pores.

This early β-Ti phase transformation could also be attributed to the presence of remaining hydrogen. Hydrogen is used as a temporary alloying element in the processing of Ti alloys since it can modify the phase composition, microstructure by controlled diffusion of other alloying elements in a hydrogen environment [33]. According to the Ti-H phase diagram, the β transus temperature was reduced from 882 °C for pure Ti to 300 °C for Ti alloy containing 39 at. % of hydrogen [38]. Hence, it is possible that a small amount of hydrogen could be enough to promote the β-phase stabilisation at lower temperatures.

Evidence of alpha needles could still be found for TH-5Fe (**Figure 4.9**), while no signs were found for TH-5Fe25Nb. This suggests that the presence of Nb could accelerate the dehydrogenation reactions allowing us to obtain a higher amount of β-Ti phase at the same temperature. This agrees with DTA results (**Figure 4.2** and **Table 4.2**), where a decrease in the peak temperature for samples containing Nb was observed.

Above 800 ° C, it can be considered that the remaining hydrogen content present in the samples at 650 °C was released, and the reaction $TiH_2 \rightarrow Ti + H_2 \uparrow$ was completed. **Figure 4.10** displays the microstructure obtained for samples treated at 800 °C.

In the case of pure TiH_2, the sample appears to be composed for a single α-Ti phase. On the other hand, TH-5Fe exhibits two different contrasts which correspond to two phases: the darker regions correspond to the α-Ti matrix, and the brighter ones related to (α+β)-Ti phase, which suggests Fe has been dissolved into Ti. The rest of the alloys (TH-12Nb, TH-40Nb and TH-5Fe25Nb) show evidence of neck formation between Ti particles and Ti-Nb particles (marked as A and B, respectively). In addition, in these alloys, three different zones can be distinguished: (1) Ti matrix mainly composed by α-Ti phase, identified by dark grey zone (Point C); (2) bright particles which correspond to Nb (Point D), and (3) light grey region, where the diffusion of Nb atoms into Ti matrix was taking place (Point E), hence, this zone would correspond to Nb-rich β-Ti phase. For sample TH-5Fe25Nb, this light grey region is also associated with the β-Ti phase formed by Fe diffusion.

It has been reported that complete Fe diffusion into Ti matrix occurs above 1080 °C for Ti-5 wt. % Fe; and almost no interaction between Ti-Fe particles was observed at 950 °C [18], [34], [39]. Besides, another study reported by Esteban et al. showed evidence of undissolved Fe particles at 900 °C for Ti alloy containing 7 wt.% Fe [22]. However, in this work, there were no signs of Fe particles at 800 °C; they had already been dissolved into Ti matrix. This could be related to hydrogen released from hydride powder having a cleansing effect on the particle surface, which not only allowed protecting Ti from getting oxygen but also increased the chemical activity of the Ti particles' surface, allowing a reduction of the temperature of the initiation of both sintering and diffusion processes [1], [40].

It was surprising that the porosity increased from 600 °C to 800 °C for alloyed samples. Nevertheless, this behaviour coincided with the expansion observed for alloyed samples in **Figure 4.3**. The expansion was more significant as a higher amount of alloying elements was incorporated. This could be associated with the formation of Kirkendall porosity, which is a result of the difference of intrinsic diffusion coefficient among the constituents of the alloy, forming a solid solution [41]. Kirkendall effect is a phenomenon of interdiffusion in substitutional alloys, where the difference on mass transfer involved in the interdiffusion process causes the diffusion couple (in this case Ti-Nb and Ti-Fe) to contract on one side and to swell the other side, inducing stress and could also generate porosity.

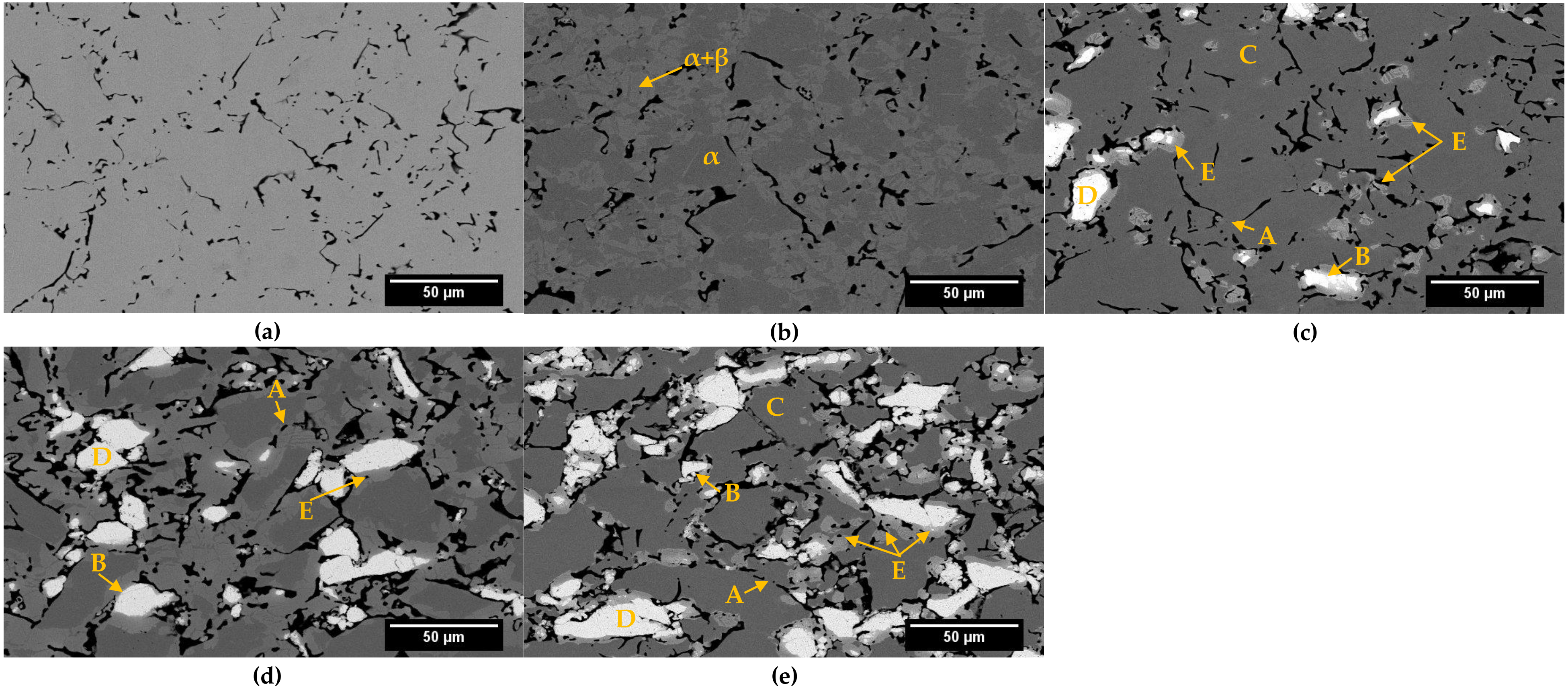

(a) (b) (c) (d) (e)

Figure 4.10. Scanning Electron Microscopy images in backscattered electrons mode (BSE-SEM) for samples treated at 800 °C: **(a)** TiH_2 (TH); **(b)** TH-5Fe; **(c)** TH-12Nb; **(d)** TH-40Nb; and **(e)** TH-5Fe25Nb

Interdiffusion processes depend strongly on the composition or amount of the alloying element. For Ti-Nb couple, the interdiffusion coefficient decreased 2 or 3 orders of magnitude as Nb content increased from 0 to 40 at. %. of Nb [6], [36]. Even though it has been reported that Fe increases the interdiffusion coefficient of Nb into Ti [42], self-diffusion of Ti seems to be controlling the diffusion during sintering. This might be explained due to the difference in melting points between the constituents Ti and Nb. Ti has a lower melting point than Nb; hence, Ti exhibits higher vacancy concentration and diffusion mobility, promoting the self-diffusion of Ti instead of the interdiffusion among Ti-Nb. Hence, high porosity around Nb particles can be observed. On the other hand, Kirkendall porosity could be formed by the diffusion couple Ti-Fe and/or Ti-Nb due to difference in diffusion rates. However, considering the low amount of Fe added with respect to Nb, it is more likely that the high porosity observed in the SEM images could be generated mainly by the Ti-Nb couple.

Microstructure for samples heated at 1100 °C is displayed in **Figure 4.11**. In general, the diffusion processes are activated and promoted as the temperature increases. Hence, for pure TiH_2 and TH-5Fe samples, a homogenous microstructure it can be seen, as was as a significant porosity reduction. TiH_2 sample is composed of a single α-Ti phases. The microstructure of TH-5Fe was found to be composed of primary alpha regions, and coarser biphasic (α+β) areas than those observed in samples at 800 °C due progress in the diffusion processesas temperature increases.

For samples containing Nb, significant changes in Nb diffusion were observed. Improvement on the neck growth between the Ti and Nb particles was seen, allowing a reduction of porosity compared to samples treated at 800 °C; however, a strong Kirkendall effect was maintained. Undissolved Nb particles surrounded by a diffusion region were found; so, Nb diffusion into Ti matrix was still taking place. This suggested that neither temperature nor sintering time (1100 °C, 5 min) were enough to complete both the diffusion of Nb and sintering of the alloy in order to achieve a higher amount of β-Ti phase, high densification and a homogeneous microstructure.

Sample TH-12Nb is composed of typical laminar (α+β) microstructure, where thin needles can be observed surrounding the undissolved Nb; which become coarser as they are further away from Nb particles. In contrast, isolated α-Ti needles in some areas of the samples were also observed for TH-40Nb and TH-5Fe25Nb, which could be associated with the incomplete Nb diffusion. Besides, microstructures suggest that Nb diffusion in TH-5Fe25Nb is better that than TH-40Nb; this fact could be related not only to the lower Nb content but to the fact that Fe contributes to improving sintering and diffusion in Ti alloys, since it increases the self-diffusion coefficient of Ti.

Microstructures of the obtained samples were compared with Ti-Nb samples produced by casting [21], [43]–[45]. The main difference between Ti-Nb alloys produced by

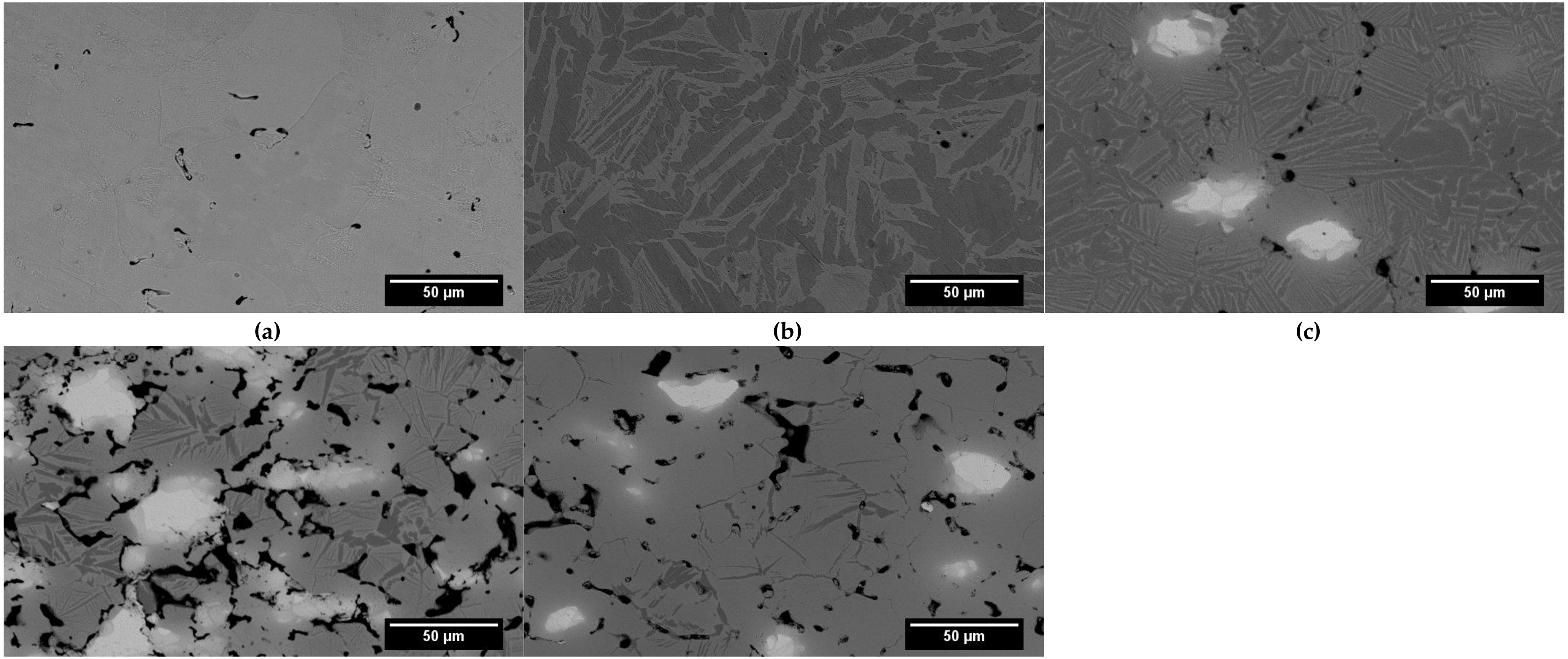

(a) **(b)** **(c)**

(d) **(e)**

Figure 4.11. Scanning Electron Microscopy images in backscattered electrons mode (BSE-SEM) for samples treated at 1100 °C: **(a)** TiH_2 (TH); **(b)** TH-5Fe; **(c)** TH-12Nb; **(d)** TH-40Nb; and **(e)** TH-5Fe25Nb.

casting and PM was that the β phase seems more homogeneous for PM alloys and α'' phase formed during cooling for cast-alloys was not observed in PM alloys. Since the microstructures obtained in this paper were not optimised in terms of complete sintering, it was difficult to assess the differences with fully sintered samples reported in the bibliography [13], [46], [47]. Nevertheless, similar findings were reported by Sharma et al. [48] and Hosnie et al. [49] for Ti-40 wt. % Nb alloy, processed from TiH_2 as starting powder produced by press and sinter process. Both cases highlight the incomplete Nb diffusion at temperatures between 1100 and 1200 °C, the presence of a diffusion zone with unreacted Nb particles surrounded by a β-Ti matrix, and some α-needles mainly located at the grain boundaries.

4.3.5. Effect of Fe and Nb alloying elements on phase evolution during dehydrogenation process.

Figure 4.12 shows the XRD patterns of the alloys after heat treatments from room temperature up to 1100 °C. Similar results were found between all compositions evaluated. At room temperature, as expected, TiH_2, Fe, and Nb were identified by XRD patterns. Diffraction patterns were obtained from the International Center for Diffraction Data (ICDD) database for FCC-TiH_2 (ICDD 03-065-0934), BCC-Nb (ICDD 01-089-5157) and BCC-Fe (ICDD 00-006-0696).

It is complicated to determine the exact sequence of hydrides formed during the entire dehydrogenation process, even employing high-temperature XRD analysis because this reaction is fast and takes place in a narrow interval of temperatures [32], [50]. However, the main stages of the process could be followed, as described below.

At 400 °C, FCC δ-TiH_2 was transformed into FCC-$TiH_{1.5}$ (ICDD 01-078-2216), which coincided with the first decomposition stage. For composition TH-40Nb, small peaks of TiH (ICDD 00-040-1244) were also identified; suggesting the hydrogen removal took place slightly faster than the other compositions evaluated.

Afterwards, as temperature increased (500 °C), part of $TiH_{1.5}$ was transformed into HCP-α-Ti phase (ICDD 01-089-4893). It can be observed that the peak intensity of $TiH_{1.5}$ was reduced, while peaks of α-Ti phase started to appear, which was confirmed by the needles found in the SEM images (**Figure 4.6**) that corresponded to α-Ti. Small peaks of TiH phase are still present in sample TH-40Nb.

Peaks of alpha phase at 500 °C did not agree with the transformation sequence proposed before (in **Equation 4.1**), which suggests that δ(TiH_x) is transformed to $\beta(Ti)_H$. However, this was attributed to the fact that these samples were analysed after cooling; thus, the fraction

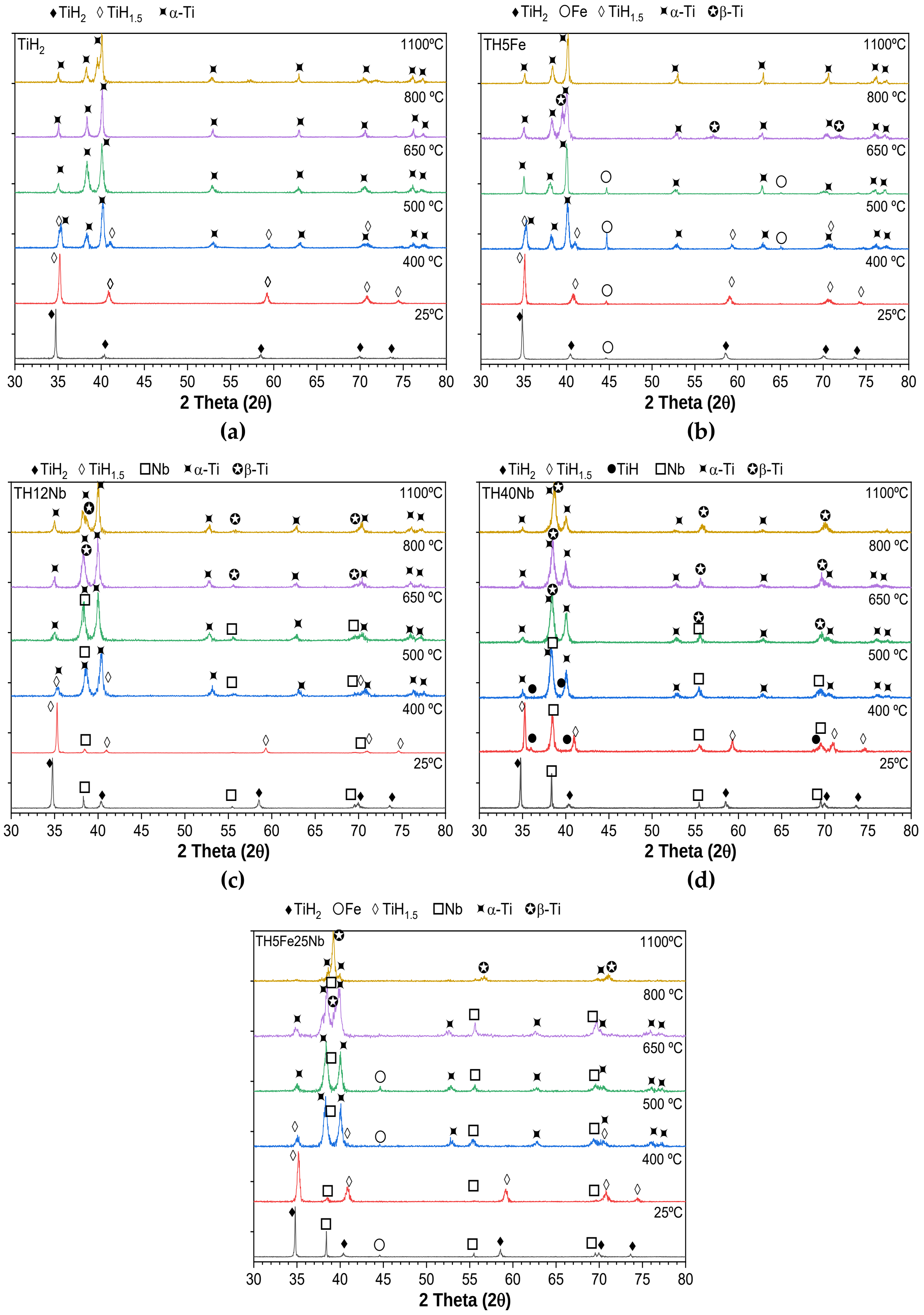

(a) (b) (c) (d) (e)

Figure 4.12. X-ray diffractograms showing the evolution of phases transformations as function of temperature from room temperature to 1100 °C by: (**a**) TiH_2 (TH); **(b)** TH-5Fe; **(c)** TH-12Nb; **(d)** TH-40Nb; and **(e)** TH-5Fe25Nb.

of beta transformation reached up to that stage was reverted to alpha phase during cooling, when FCC to HCP phase transformation occurs. It is essential to consider that the pattern diffraction obtained did not correspond to the phase transformation sequence since the high-temperature reaction was interrupted to perform the XRD measurement at room temperature. Hence, intermediate phases that were formed during dehydrogenation, at a specific interval of temperature, could have been reverted to another phase stable at a lower temperature.

At 650 °C, no signs of any kind of titanium hydride were observed. Samples are mainly composed of α-Ti phase and the alloying element. Alloy TH-40Nb shows peaks of β-Ti phase (ICDD 01-089-4913), due to its high Nb amount. This transformation coincides with the value of the $\beta_{transus}$ temperature of 650 ºC predicted for this alloy (**Table 4.1**).

As temperature increases to 800 °C, pure TiH_2 sample is composed of single α-Ti phase. Moreover, evidence of Fe peaks disappears for samples TH-5Fe and TH-5Fe25Nb. Diffractograms reveal that β-Ti phase starts to appear for all alloyed samples; which was expected since $\beta_{transus}$ temperature had been reached (**Table 4.1**). Both β-Ti phase formation and lack of Fe presence, were corroborated in the SEM images (**Figure 4.10**), where it could seen that Fe particles were completely dissolved into Ti matrix, and a diffusion zone denoted by brighter regions was observed, identified as β-Ti phase due to its high concentration of the alloying element.

Finally, TiH_2 and TH-5Fe, treated at 1100 °C, are mainly composed of α-Ti phase. The amount of Fe was not enough to stabilise a significant amount of β-Ti that could to be detected by XRD. Nevertheless, SEM images indicate that TH-5Fe has a biphasic microstructure with primary α-Ti and coarse (α+β) regions.

For the rest of the alloys, strong peaks corresponding to β-Ti phase were found. Even when Nb particles were observed in the SEM images, they were not found by XRD. This could be explained considering that the remaining undissolved Nb amount was lower than the detection limit. However, due to the incomplete Nb diffusion it was not possible to obtain only β-Ti phase. Small peaks of α-Ti phase were also identified for TH-5Fe25Nb, which could also be related to incomplete Nb diffusion. Therefore, it is necessary to increase both time and sintering temperature to promote the Nb diffusion and stabilise a higher content of β-Ti.

4.4. Partial conclusions.

From the results shown in this chapter, the following conclusions can be drawn:

1. Using thermal analysis (DTA, DIL), it is possible to follow the in-situ transformation during the whole dehydrogenation process and assess the effect of alloying elements. In contrast, for samples heated until a determined temperature and then cooled down (VAC), the dehydrogenation reactions were interrupted, and some phase transformations could not be identified since they were reverted during cooling. The following reactions were identified for unalloyed TiH_2 using conventional XRD:

$$\delta(TiH_2) \xrightarrow{400\ ^{0}C} \delta(TiH_{1.5}) \xrightarrow{550\ ^{0}C} \begin{array}{c}\delta(TiH_{1.5})\\+\\\alpha(Ti)\end{array} \xrightarrow{650\ ^{0}C} \alpha(Ti)$$

This **transformation sequence was modified with the addition of Fe and Nb as alloying elements**. The presence of these alloying elements reduced the beta transus temperature considerably. Hence, it is suggested that β → *α* reaction described in **Equation 4.1** did not occur. Once δ-TiH_x was transformed into β-Ti, this phase was maintained. It became more stable as temperature increased, and Fe and Nb diffusion was produced, which allowed stabilisation the β-Ti phase after cooling.

The following transformation sequence was proposed for alloyed TiH_2 with Fe and Nb during continuous heating:

$$\begin{array}{c}\delta(TiH_2)\\+\\Fe+Nb\end{array} \xrightarrow{400\ ^{0}C} \begin{array}{c}\delta(TiH_{1.5})\\+\\Fe+Nb\end{array} \xrightarrow{550\text{-}650\ ^{0}C} \begin{array}{c}\beta(Ti)_{H}+\beta(Ti)_{Fe\ rich}\\+\\Fe+Nb\end{array} \xrightarrow{800\text{-}1100\ ^{0}C} \begin{array}{c}\beta(Ti)_{H}+\\\beta(Ti)_{Fe\ rich}+\\\beta(Ti)_{Nb\ rich}+Nb\end{array}$$

2. **Fe was dissolved into Ti matrix at a lower temperature** than when using Ti powders as starting material. Hence, dehydrogenation allowed chemical activation of the particle surface, promoting an earlier diffusion of the alloying elements. The small amount of hydrogen retained on the last dehydrogenation stage could have promoted the **earlier diffusion** of elements that exhibited higher diffusivity in BCC-Ti than HCP-Ti.

3. Fe and Nb addition shifted the temperature of the initial and final stage of the dehydrogenation process with respect to unalloyed TiH_2.

On the one hand, Fe and Nb accelerated the beginning of the decomposition reaction, reducing the onset temperature of the first stage between 50–95 °C lower than TiH_2. On the other hand, Fe and Nb could act as a barrier to the removal of the remaining hydrogen content retained in the Ti phase, delaying the offset temperature of the third stage between 15-50 °C more than TiH_2.

No significant differences were detected for the intermediate stage (second stage), which was considered the main decomposition reaction.

4. The addition of alloying elements such as Fe and Nb, did not hinder the complete hydrogen elimination; however, they modified the decomposition process.

Addition of 7 wt.% of Fe promotes the sample densification compared to pure TiH_2 sample, while no significant differences were observed for 5 wt.% of Fe. In contrast, Nb acts as a barrier to densification during dehydrogenation. The higher Nb addition, the lower sample shrinkage. In samples with more than 12 wt.% of Nb, dehydrogenation is followed by an expansion caused by the Kirkendall effect, which also affects the final sample densification.

5. After dehydrogenation took place, the growth of initial β-Ti phase is promoted by **Fe dissolution at 650 °C,** which is below than the expected βtransus temperature; even when some unreacted Nb remains.

6. Large Nb particle size, as well as the large atomic size and poor diffusion rate, limited the densification; leading the formation of **Kirkendall porosity**.

References.

[1] I. M. Robertson and G. B. Schaffer, "Comparison of sintering of titanium and titanium hydride powders," *Powder Metall.*, vol. 53, no. 1, pp. 12–19, 2010.

[2] Z. Z. Fang *et al.*, "Powder metallurgy of titanium–past, present, and future," *Int. Mater. Rev.*, vol. 63, no. 7, pp. 407–459, 2018.

[3] C. Wang, Y. Zhang, S. Xiao, and Y. Chen, "Sintering Densification of Titanium Hydride Powders," *Mater. Manuf. Process.*, vol. 32, no. 5, pp. 517–522, 2017.

[4] Y. H. Hon, J. Y. Wang, and Y. N. Pan, "Composition/Phase Structure and Properties of Titanium-Niobium alloys," *Mater. Trans.*, vol. 44, no. 11, pp. 2384–2390, 2003.

[5] H. M. Silva, S. G. Schneider, and C. M. Neto, "Study of nontoxic aluminum and vanadium-free titanium alloys for biomedical applications," *Mater. Sci. Eng. C*, vol. 24, no. 5, pp. 679–682, 2004.

[6] L. Zhu *et al.*, "Measurement of interdiffusion and impurity diffusion coefficients in the bcc phase of the Ti--X (X = Cr, Hf, Mo, Nb, V, Zr) binary systems using diffusion multiples," *J. Mater. Sci.*, vol. 52, no. 6, pp. 3255–3268, 2017.

[7] P. Soma and P. Aloke, "Interdiffusion in Nb-Mo , Nb-Ti and Nb-Zr systems Interdiffusion in Nb-Mo , Nb-Ti and Nb-Zr systems," vol. 323–325, pp. 491–496, 2012.

[8] L. Zhang and L. Chen, "A Review on Biomedical Titanium Alloys: Recent Progress and Prospect," *Adv. Eng. Mater.*, 2019.

[9] M. Abdel-Hady Gepreel and M. Niinomi, "Biocompatibility of Ti-alloys for long-term implantation," *J. Mech. Behav. Biomed. Mater.*, vol. 20, pp. 407–415, 2013.

[10] D. Zhao, K. Chang, T. Ebel, H. Nie, R. Willumeit, and F. Pyczak, "Sintering behavior and mechanical properties of a metal injection molded Ti-Nb binary alloys as biomaterial," *J. Alloys Compd.*, vol. 640, pp. 393–400, 2015.

[11] R. Karre *et al.*, "Comparative study on Ti-Nb binary alloys fabricated through spark plasma sintering and conventional P/M routes for biomedical application," *Mater. Sci. Eng. C*, vol. 94, pp. 619–627, 2019.

[12] Y. Zhang, D. Sun, J. Cheng, J. Kit, H. Tsoi, and J. Chen, "Mechanical and biological properties of Ti –(0 – 25 wt %) Nb alloys for biomedical implants application," no. November 2019, pp. 119–127, 2020.

[13] A. Amigó, A. Vicente, C. R. M. Afonso, and V. Amigó, "Mechanical properties and the microstructure of β Ti-35Nb-10Ta-xFe alloys obtained by powder metallurgy for biomedical applications," *Metals (Basel).*, vol. 9, no. 1, 2019.

[14] M. Niinomi, Y. Liu, M. Nakai, H. Liu, and H. Li, "Biomedical titanium alloys with Young ' s moduli close to that of cortical bone," *Rege*, no. March, pp. 173–185, 2016.

[15] M. T. Mohammed, Z. a Khan, and A. N. Siddiquee, "Beta Titanium Alloys : The Lowest Elastic Modulus for Biomedical Applications : A Review," *Int. J. Chem. Nucl. Mater. Metall. Eng.*, vol. 8, no. 8, pp. 726–731, 2014.

[16] A. Biesiekierski, J. Lin, Y. Li, D. Ping, Y. Yamabe-Mitarai, and C. Wen, "Investigations

into Ti–(Nb,Ta)–Fe alloys for biomedical applications," *Acta Biomater.*, vol. 32, pp. 336–347, 2016.

[17] G. R. Bak, J. W. Won, H.-J. Choe, C. H. Park, and Y.-T. Hyuen, "Effect of iron content on β → α phase transformation behavior of Ti-5Al-xFe (x = 1, 2.5, 4) alloys during continuous cooling," *J. Mater. Res. Technol.*, vol. 8, no. 3, pp. 2887–2897, 2019.

[18] W. Wei, Y. Liu, K. Zhou, and B. Huang, "Effect of Fe addition on sintering behaviour of titanium powder," *Powder Metall.*, vol. 46, no. 3, pp. 246–250, 2003.

[19] S. Ehtemam-haghighi, K. G. Prashanth, H. Attar, A. K. Chaubey, G. H. Cao, and L. C. Zhang, "Evaluation of mechanical and wear properties of Ti \ \ 7Fe alloys designed for biomedical applications," *JMADE*, vol. 111, pp. 592–599, 2016.

[20] M. Bönisch *et al.*, "Composition-dependent magnitude of atomic shuffles in Ti-Nb martensites," *J. Appl. Crystallogr.*, vol. 47, pp. 1374–1379, 2014.

[21] C. M. Lee, C. P. Ju, and J. H. C. Lin, "Structure-property relationship of cast Ti-Nb alloys," *J. Oral Rehabil.*, vol. 29, pp. 314–322, 2002.

[22] P. G. Esteban, E. M. Ruiz-Navas, and E. Gordo, "Influence of Fe content and particle size the on the processing and mechanical properties of low-cost Ti-xFe alloys," *Mater. Sci. Eng. A*, vol. 527, no. 21–22, pp. 5664–5669, 2010.

[23] P. G. Esteban, L. Bolzoni, E. M. Ruiz-Navas, and E. Gordo, "PM processing and characterisation of Ti-7Fe low cost titanium alloys," *Powder Metall.*, vol. 54, no. 3, pp. 242–252, 2011.

[24] O. Ivasishin and V. Moxson, "Low-cost titanium hydride powder metallurgy," in *Titanium Powder Metallurgy*, Elsevier Inc., 2015, pp. 117–148.

[25] D. Lehmhus and G. Rausch, "Tailoring titanium hydride decomposition kinetics by annealing in various atmospheres," *Adv. Eng. Mater.*, vol. 6, no. 5, pp. 313–330, 2004.

[26] H. Liu, P. He, J. C. Feng, and J. Cao, "Kinetic study on nonisothermal dehydrogenation of TiH2 powders," *Int. J. Hydrogen Energy*, vol. 34, pp. 3018–3025, 2009.

[27] A. R. Kennedy and V. H. Lopez, "The decomposition behavior of as-received and soxidised TiH2 foaming-agent powder," *Mater. Sci. Eng. A*, vol. 357, pp. 258–263, 2003.

[28] M. Ma *et al.*, "Phase transformations of titanium hydride in thermal desorption process with different heating rates," *Int. Hydrog. Energy*, vol. 40, pp. 8926–8934, 2015.

[29] N. Peillon, J. B. Fruhauf, S. Gourdet, J. Feraille, S. Saunier, and C. Desrayaud, "Effect of TiH2 in the preparation of MMC Ti based with TiC reinforcement," *J. Alloys Compd.*, vol. 619, pp. 157–164, 2015.

[30] C. Wang, Y. Zhang, S. Xiao, and Y. Chen, "Sintering densification of titanium hydride powders," *Mater. Manuf. Process.*, vol. 32, no. 5, pp. 517–522, 2017.

[31] V. Bhosle, E. G. Baburaj, M. Miranova, and K. Salama, "Dehydrogenation of TiH2," *Mater. Sci. Eng. A*, vol. 356, pp. 190–199, 2003.

[32] C. Jiménez *et al.*, "Decomposition of TiH2 studied in situ by synchrotron X-ray and neutron diffraction," *Acta Mater.*, vol. 59, pp. 6318–6330, 2011.

[33] F. H. Froes, O. N. Senkov, and J. I. Qazi, "Hydrogen as a temporary alloying element in titanium alloys: Thermohydrogen processing," *Int. Mater. Rev.*, vol. 49, no. 3–4, pp.

227–245, 2004.

[34] Y. Liu, L. F. Chen, H. P. Tang, C. T. Liu, B. Liu, and B. Y. Huang, “Design of powder metallurgy titanium alloys and composites,” *Mater. Sci. Eng. A*, vol. 418, pp. 25–35, 2006.

[35] G. B. Gibbs, D. Graham, and D. H. Tomlin, “Diffusion in titanium and titanium—niobium alloys,” *Philos. Mag.*, vol. 8, no. 92, pp. 1269–1282, 1963.

[36] P. Soma and A. Paul, “Interdiffusion in Nb-Mo , Nb-Ti and Nb-Zr systems,” *Defect Diffus. Forum*, vol. 323–325, pp. 491–496, 2012.

[37] H. Nakajima and M. Koiwa, “Diffusion in Titanium,” *ISIJ Int.*, vol. 31, no. 8, pp. 757–766, 1991.

[38] K. Wang, X. Kong, J. Du, C. Li, Z. Li, and Z. Wu, “Thermodynamic description of the Ti-H system,” *CALPHAD Comput. Coupling Phase Diagrams Thermochem.*, vol. 34, no. 3, pp. 317–323, 2010.

[39] J. O’Flynn and S. F. Corbin, “The influence of iron powder size on pore formation , densification and shomogenisation during blended elemental sintering of Ti – 2 . 5Fe,” *J. Alloys Compd.*, vol. 618, pp. 437–448, 2015.

[40] O. M. Ivasishin, A. N. Demidik, and D. G. Savvakin, “Use of titanium hydride for the synthesis of titanium aluminides from powder materials,” *Powder Metall. Met. Ceram.*, vol. 38, no. 9–10, pp. 482–487, 1999.

[41] B. Pieraggi, “Diffusion and solid state reactions,” in *Developments in High Temperature Corrosion and Protection of Materials*, Woodhead P., W. Gao and L. Zhengwei, Eds. 2008, pp. 9–35.

[42] R. F. Peartt and D. H. Tomlin, “DIFFUSION OF ELEMENTS IN BETA-TITANIUM,” *Acta Metall.*, vol. 10, pp. 123–134, 1962.

[43] L. J. Xu, S. L. Xiao, J. Tian, Y. Y. Chen, and Y. D. Huang, “Microstructure and dry wear properties of Ti-Nb alloys for dental prostheses,” *Trans. Nonferrous Met. Soc. China (English Ed.*, vol. 19, pp. s639–s644, 2009.

[44] A. Cremasco, P. N. Andrade, R. J. Contieri, E. S. N. Lopes, C. R. M. Afonso, and R. Caram, “Correlations between aging heat treatment, ω phase precipitation and mechanical properties of a cast Ti-Nb alloy,” *Mater. Des.*, vol. 32, no. 4, pp. 2387–2390, 2011.

[45] M. Bönisch *et al.*, “Thermal stability and phase transformations of martensitic Ti-Nb alloys,” *Sci. Technol. Adv. Mater.*, vol. 14, no. 5, 2013.

[46] T. Ebel, T. Beißig, S. Ebner, X. Luo, A. B. Nagaram, and D. Zhao, “Reduction of the embrittlement effect of binder contamination in MIM processing of Ti alloys,” *Powder Metall.*, vol. 60, no. 3, pp. 157–166, 2017.

[47] D. Zhao *et al.*, “Microstructure and mechanical behavior of metal injection molded Ti-Nb binary alloys as biomedical material,” *J. Mech. Behav. Biomed. Mater.*, vol. 28, pp. 171–182, 2013.

[48] B. Sharma, S. K. Vajpai, and K. Ameyama, “Microstructure and properties of beta Ti–Nb alloy prepared by powder metallurgy route using titanium hydride powder,” *J.*

Alloys Compd., vol. 656, pp. 978–986, Jan. 2016.

[49] S. M. Hosnie, M. Yahaya, N. A. Haris, and I. Todd, "Fabrication of porous β-Type Ti-40Nb alloys incorporated with TiH2 via powder metallurgy processing route under reducing environment," *J. Mech. Eng.*, vol. 2, no. 2, pp. 99–112, 2017.

[50] D. V. Schur, S. Y. Zaginaichenko, V. M. Adejev, V. B. Voitovich, A. A. Lyashenko, and V. I. Trefilov, "Phase transformations in titanium hydrides," *Int. J. Hydrogen Energy*, vol. 21, no. 11-12 SPEC. ISS., pp. 1121–1124, 1996.

CHAPTER 5

Development of β-Titanium alloys

CHAPTER 5

5.1. Introduction.

This chapter describes the processing of three proposed Ti alloys (TH-12Nb, TH-40Nb and TH-5Fe25Nb) obtained by blending of elemental powders. Processing was optimised considering three aspects: (1) the influence of heating conditions that promote a complete and effective TiH_2 decomposition and transformation to Ti; (2) the sintering conditions (sintering time and temperature) to promote densification and improve Nb diffusion, contributing to the microstructure homogenisation and increasing the β-Ti phase fraction. (3) the influence of the characteristics of the starting powders, both Fe and Nb. The effects of processing parameters were evaluated by X-ray diffraction (XRD) and scanning electron microscopy (SEM). [1]

In addition to biocompatibility, low elastic modulus and high fatigue resistance are some of the most important properties that biomedical Ti alloys must exhibit. Due to the importance of these properties for the performance of this kind of material, they are analysed and discussed in this chapter. Young modulus was estimated by indentation method, considering the unloading behaviour, while three-point bending fatigue tests were used to evaluate the fatigue resistance. The mechanical characterisation was complemented with Vickers microhardness measurements and simple three-point bending tests.

The presence of precipitates found in some samples, especially at the grain boundaries, is related to decreasing mechanical properties and mechanical reliability, causing failure at a lower load than expected. Fractography analysis indicated that these precipitates affect mainly the performance of TH5Fe254Nb alloy composition. Hence, heat treatments were carried out to dissolve them to improve mechanical reliability and fatigue resistance.

To conclude this chapter, biological characterisation was included. For the three developed alloys, cell morphology, cell proliferation, and mineralisation were evaluated to validate their bioactivity for further processing stages.

---

[1] Part of the information compiled on this chapter is published in:
Chirico, C.; Tsipas, S.; Toptan, F; Gordo, E. "Development of Ti-Nb and Ti-Nb-Fe beta alloys from TiH_2 powders". Powder Metallurgy,2019, vol. 62, Nº 1, pp. 44-53. doi.org/10.1080/00325899.2018.1563953

5.2. Processing optimisation.

The previous chapter studied how the addition of Nb and Fe affects the titanium hydride decomposition process, and the sequence of phase transformations that occurred at different stages of the dehydrogenation process. Complementary, this section evaluates how the heating rate during titanium hydride decomposition affects the sample consolidation.

This section aims to optimise the processing conditions of Ti alloys produced using TiH_2 powder as Ti source. To achieve this, the temperature range in which the hydrogen removal is more intense (400-600 °C), obtained from the dehydrogenation study performed in **Chapter 4,** was considered as the starting point to design sintering cycles. The process optimisation was performed considering the following parameters: (1) varying the heating rate (continuous heating, isothermal heating at 500 °C and heating rate reduction between 450 °C and 650 °C); (2) varying the sintering time (between 2 and 4 h) and (3) varying the maximum sintering temperature (between 1200 °C and 1450 °C). **Figure 5.1**. displays the sintering cycles performed.

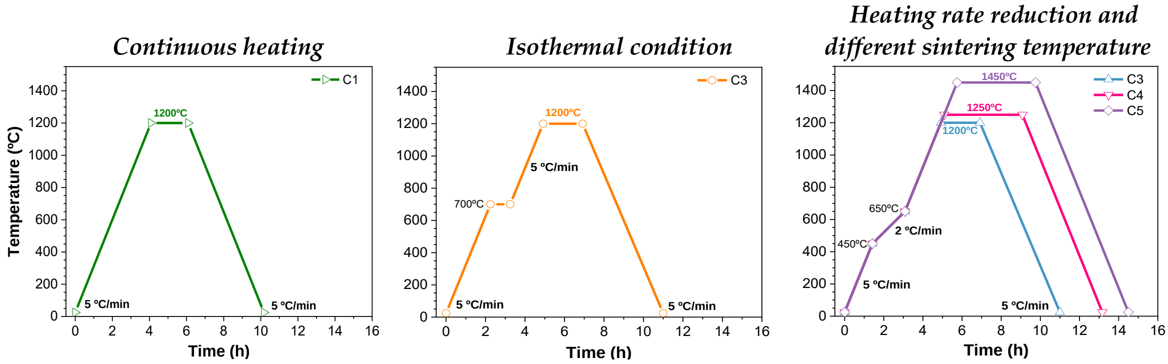

Figure 5.1. Sintering cycles carried out for the consolidation optimisation:
C1 (5 °C/min 1200 °C, 2 h); **C2** (5 °C/min 700 °C, 1 h- 5 °C/min 1200 °C, 2 h); **C3** (5 °C/min 450 °C-2 °C/min (450-650) °C- 5 °C/min 1200 °C, 2 h); **C4** (5 °C/min 450 °C→2 °C/min 650 °C→ 5 °C/min 1250 °C, 4 h); **C5** (5 °C/min 450 °C-2 °C/min (450-650) °C- 5 °C/min 1450 °C, 4 h).

The criteria for choosing the optimal sintering parameters were to achieve complete TiH_2 decomposition, high relative density (densification), and maximum diffusion of the alloying elements in order to promote a homogeneous microstructure and a high percentage of β-Ti phase.

Moreover, for this study, two kinds of Fe and Nb elemental powders were used (**See Section 3.2**), and the effect of the particle size of alloying powders was also considered. The type of powder employed for each sintering cycle is shown in **Table 3.5, Section 3.5.**

5.2.1. Effect of heating rate.

The influence of heating rate on the TiH_2 decomposition was studied for sintering cycles C1, C2 and C3; Fe and Nb powders labelled as (1) were employed. In these cycles, both sintering time and temperature were kept constant (1200 °C for 2 h), varying only the heating conditions during the TiH_2 decomposition process. The efficiency of the dehydrogenation process was evaluated by estimating hydrogen loss, which can be seen in **Figure 5.2**.

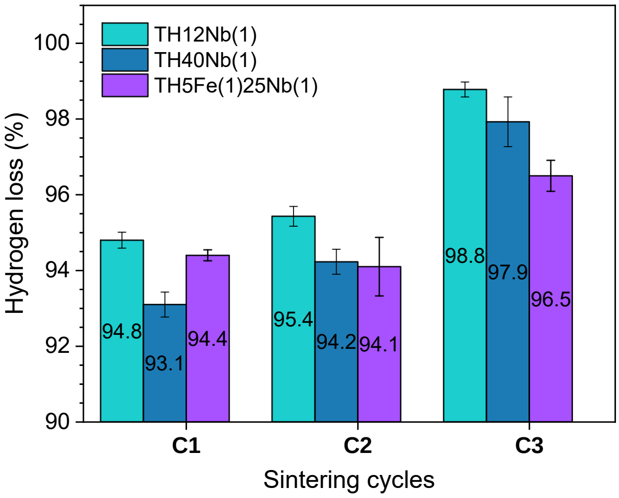

Figure 5.2. Hydrogen loss achieved for different sintering cycles, employing different heating conditions and same sintering temperature (1200 °C).

No appreciable differences in hydrogen loss were found between the sintering cycles carried out with continuous heating (C1) and the cycle with an isotherm at 700 °C for 1 h (C2), removing around 93% and 95% of the total hydrogen in both cases. However, it is noticeable that C3 provides the highest hydrogen loss for the three tested alloys by reducing the heating rate from 5 to 2 °C/min between 450 °C and 650 °C. This confirms the strong dependence of the heating rate on the dehydrogenation process [1]–[3] as studied by other authors. It has been reported that the dehydrogenation process tends to accelerate, reducing the critical temperatures of the different decomposition reactions, when the heating rate is reduced. [1], [2], [4], [5]

In **Chapter 4**, it was found by DTA analysis that the most important reactions of TiH_2 decomposition (from δ-TiH_x to β-Ti phase, stage II), where most of the TiH_2 is transformed, take place between 550 °C and 650 °C (**Table 4.2**). Additionally, the dehydrogenation study, under vacuum conditions, shows a drastic mass loss between 400 °C and 650 °C (**Figure 4.4**), and XRD results (**Figure 4.12**) show no evidence of titanium hydride phase above 650 °C. Therefore, these results suggest that the dehydrogenation process, performed under vacuum conditions, is almost completed above 650 °C.

In this chapter, the importance of controlling the heating rate (C3), while the most relevant changes involved in dehydrogenation occur is established. Reduced heating rate (from 5 °C/min to 2 °C/min between 450 °C to 650 °C) promotes a higher hydrogen removal and greater control of TiH_2 decomposition than that obtained with continuous heating up to sintering temperature (C1) or with isothermal at 700 °C followed by continuous heating (C2).

5.2.2. Effect of sintering cycles on sample densification.

The differences between the five sintering cycles employed to achieve optimal consolidation process in terms of densification, phases and homogeneity of microstructure are presented. For this study, samples were processed using different Fe and Nb powders, listed in **Table 3.1** (**Chapter 3**). The numbers (1) and (2) followed by the element in the composition, refer to the Nb and Fe powder type used. Bulk density values obtained for sintered samples are summarised in **Table 5.1**. As was expected, density increases as the Nb amount increases due to its higher density (8.57 g/cm^3) compared to pure Ti (4.51 g/cm^3).

Table 5.1. Bulk density achieved for sintered samples for each sintering cycle (g/cm^3).

Samples	TD	C1	C2	C3	C4	C5
TH-12Nb(1)	4.78	4.66±0.02	4.66±0.03	4.69±0.02	4.72±0.04	---
TH-12Nb(2)			---		4.67±0.05	4.73±0.07
TH-40Nb(1)	5.57	5.18±0.02	5.12±0.02	5.15±0.02	5.32±0.09	---
TH-40Nb(2)			---		5.20±0.04	5.33±0.08
TH-5Fe(1)25Nb(1)	5.24	4.92±0.03	4.83±0.04	4.87±0.09	4.93±0.03	---
TH-5Fe(2)25Nb(1)		---		5.06±0.02	5.19±0.04	
TH-5Fe(2)25Nb(2)			---		5.10±0.03	5.16±0.10

TD: Theoretical density, determined by the rule of mixtures.

(1) and (2) refer to the employed type of Fe and Nb powder, listed in **Table 3.5**.

For comparative purposes, **Figure 5.3** shows the relative density for each alloy for the corresponding sintering cycle. From these results, it is clear that the sintering cycles with heating rate reduction during the TiH_2 decomposition interval (C3, C4 and C5) provide the highest density values. This suggests that controlled dehydrogenation improves final densification. In contrast, sintering cycle C2 provides the lowest relative density values.

Alloy containing 12 wt.% Nb (**Figure 5.3**a) exhibits the highest relative density values, compared to the other alloys, regardless of the sintering cycle applied. It can be noted that TH12Nb alloy sintered under C3 shows higher relative density than C1 and C2, even though they were sintered at the same sintering temperature and holding time (1200 °C, 2 h). This is in accordance with the results of hydrogen loss (**Figure 5.2**), where C3 is the most effective cycle and enhances sintering. Hence, increasing sintering temperature (C4 and C5) increases density, achieving almost a full density material (around 99%).

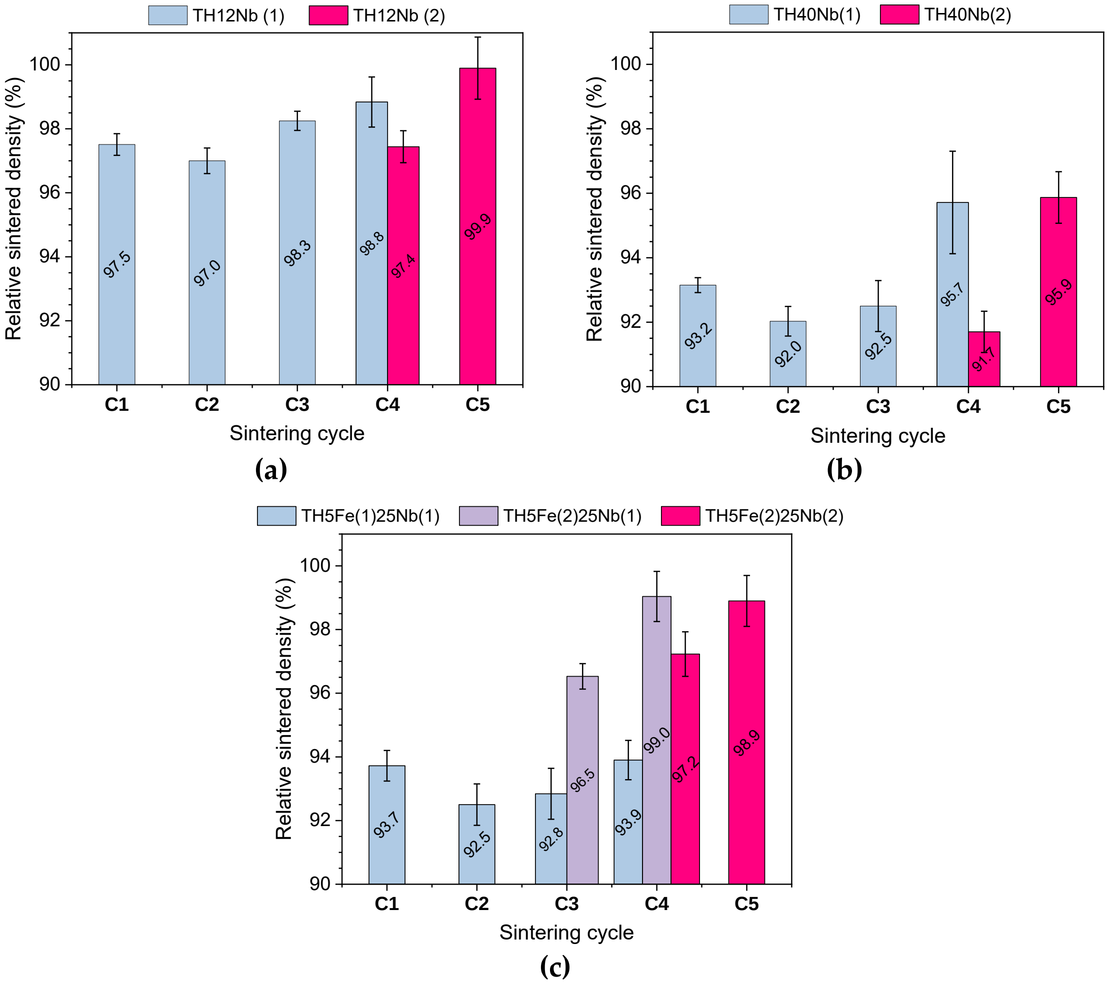

(a)

(b)

(c)

Figure 5.3. Relative density for sintered samples with different sintering cycles: a) TH12Nb; b) TH40Nb and c) TH5Fe25Nb.
(1) and (2) refer to the employed type of Fe and Nb powder, listed in **Table 3.5**.

The influence of controlled dehydrogenation is not so evident for compositions with higher Nb amount, since the alloying element diffusion becomes a critical factor in achieving higher densification. The alloying elements can act as a barrier, hindering the diffusion processes during sintering, being necessary higher sintering temperature and time to promote densification. Thus, for TH40Nb(1) and TH5Fe(1)25Nb(1) compositions, increasing the sintering temperature to 1250 °C and holding time for 4 h (C4) is required to achieve density values higher than 95% of the theoretical. Comparing the three alloys, Nb content has a clear influence on the final density achieved regardless of the sintering cycle employed, decreasing density when increases Nb content: TH12Nb > TH5Fe25Nb > TH40Nb.

These results coincide with several studies performed in Ti-Nb alloys that indicate that larger Nb addition is associated with lower densification [6], [7]. The influence of Nb content on porosity increase is related to the high melting point of Nb, which limits the densification process; and the significant difference in the diffusion rate between Ti and Nb, which may cause Kirkendall porosity and delay the diffusion of Nb into Ti matrix, reducing the sample densification [7]–[9]

According to Zhao et al.[10], the densification process of Ti-Nb alloys is dependant on the diffusion distance between Ti and Nb particles, which, in turn, is determined by the particle distribution of these elements in the sample and homogenisation, as well as the diffusion coefficients of possible couples in the Ti-Nb system at the consolidation temperature range. That includes the self-diffusion coefficient of Ti in β-Ti and α-Ti; the self-diffusion coefficient of Nb; diffusion coefficient of Ti in Nb, Nb into β-Ti and α-Ti. They stated that at 990 °C, densification is mainly governed by interactions between Ti particles, due to the fact that the self-diffusion coefficient of Ti in β-Ti is much higher than the interdiffusion coefficient of Nb into β-Ti. Hence, Nb diffusion into β-Ti is less favoured. Moreover, Nb particles act as diffusion barriers, because they hinder the contact between Ti particles, reducing the sample shrinkage.

At higher temperature (1156 °C), Nb particles start to dissolve into the β-Ti phase, then, the barrier effect of Nb particles is reduced. This promotes the diffusion between Ti particles, which increases the shrinkage and densification of the samples. Since the higher diffusivity of Nb into β-Ti matrix (~1200 °C → $3x10^{-12}$ m^2/s) compared to the diffusivity of Ti into Nb (~1200 °C → $1x10^{-18}$ m^2/s), the diffusion process between Ti and Nb occurs unidirectionally from Nb to Ti [11]. Moreover, due to the significant difference in melting point temperature between Nb (2477 °C) and Ti (1668 °C), the vacancy concentration towards the Ti-rich zone is higher than the vacancy concentration towards the Nb-rich side, also contributing to the higher diffusion toward Ti [12]. This unbalanced diffusion could produce Kirkendall porosity at the Nb/Ti interface. Above 1300 °C, complete homogenisation is obtained. Further shrinkage and pore elimination are attributed to the interdiffusion process in the Ti-Nb matrix. It must be noted that it has been reported that the interdiffusion coefficient between Ti-Nb, reduces as increases the Nb content in Ti-Nb alloys. It has been reported that the interdiffusion coefficient of Ti-Nb system reduces between 2 and 3 orders of magnitude in Ti-(0-40 at.%)Nb alloys. [12], [13]

Hence, it is reasonable to deduce that as Nb content increases, it increases the Nb particles amount. Thus/hence, there are a higher amount of Nb particles acting as a barrier, delaying/avoiding densification generated by sintering between Ti particles and the subsequent diffusion processes involved in sample densification. This explains that alloy containing 40 wt.% Nb shows the lowest values of relative density, reaching maximum values of 96% (**Figure 5.3**b) when sintering temperature was increased to 1450 °C. This is attributed to diffusion processes, typically are favoured at high temperature; consequently, densification is also enhanced. [13]

Regarding the effect of particle size of alloying powders in density, graphs in **Figure 5.3** contains results for two Nb and Fe powder, which characteristics can be found in **Table 3.1** (**Chapter 3**). The particle size of Fe-2 is smaller than Fe-1, and Nb-2 is bigger than Nb-1. In the case of Nb powder, although the D_{50} is not so different, the D_{90} value of Nb-2 is clearly higher, as can be seen in **Table 5.2**.

Table 5.2. Particle size distribution of Nb powders.

	D_{10}	D_{50}	D_{90}
Nb-1	4.4	13.7	30.3
Nb-2	5.1	21.5	52.2

The effect of Nb powder on sample densification can be observed for samples sintered with C4. TH40Nb(2) and TH12Nb(2) (using Nb-2) show lower relative density in comparison with those processed with Nb-1. Samples TH12Nb (2) reached a relative density value of about 97%, and TH40Nb(2) achieved 92%. In contrast, employing Nb-1, almost full density (99%) for TH12Nb(1) and 96% for TH40Nb(1) were achieved.

Both Ti-Nb alloys sintered with C5 and Nb-2 showed similar relative density values to those observed for C4 and Nb-1. In C5, the sintering temperature was increased to 1450 °C, favouring the diffusion process and, thus, promoting the densification of samples processed with Nb-2.

These densification results denote the strong influence of Nb particle size on sample densification. It is well known that powder metallurgy processing is significantly influenced by the starting powder features, like particle size, morphology, and impurities [14]. Although two Nb powders have irregular and sharp-edge morphology, they exhibit a slight difference in particle size distribution, as shown in **Table 5.2**. Nb-1 powder contains a higher fraction of fine particles than the Nb-2 powder. The coarser particles of Nb-2 are about 20 μm bigger than Nb-1. This difference in the particle size distribution of Nb powders determines the sample densification, probably because a larger particle size delays the diffusion process between the Ti-Nb couple.

For composition TH5Fe25Nb (**Figure 5.3**c), there are combined Fe and Nb particle size effects. Nb effect is similar to that observed in Ti-Nb alloys. Using the same Fe powder (Fe-2), TH5Fe25Nb alloys sintered under C4 show higher relative density for small Nb powder (Nb-1), reaching about 99%, while with coarse Nb powder (Nb-2), it decreases up to 97%.

Regarding the Fe particles size effect, it can be seen that for the same sintering cycle (C3 and C4) and using smaller Nb powder (Nb-1), samples with smaller Fe particle size (TH5Fe(2)Nb(1)) reached a higher relative density than samples with coarser Fe particle size (TH5Fe(1)Nb(1)), achieving an about 3.7% and 5.1% higher relative density for samples sintered with C3 and C4, respectively. This can be explained because the diffusion of Fe into Ti matrix occurs by an interstitial mechanism [15]. Smaller Fe particle size results in a higher specific surface area, favouring interdiffusion and, therefore, higher sample densification than larger particle size [16], [17]. The effect of Fe particle size is more remarkable than that of Nb powder. This is because the differences between Fe powders are greater than between Nb powders.

5.3. Microstructural characterisation.

The alloy with composition TH12Nb (**Figure 5.4** and **Figure 5.5**) shows a typical ($\alpha+\beta$) lamellar microstructure with alpha phase needles growing from the grain boundaries. Pores in this composition are mostly isolated and spherical; they are situated mainly on grain boundaries. This fact suggests samples reached the final stage of sintering, so, it is difficult to eliminate this kind of porosity since higher densification implies prolonged sintering cycles which might cause an undesirable increase in grain size [18]. Porosity is in accordance with the results shown in **Figure 5.3**a, where samples processed from Nb-1 and sintered with C1 and C2, exhibited a higher amount of porosity than C3 and C4.

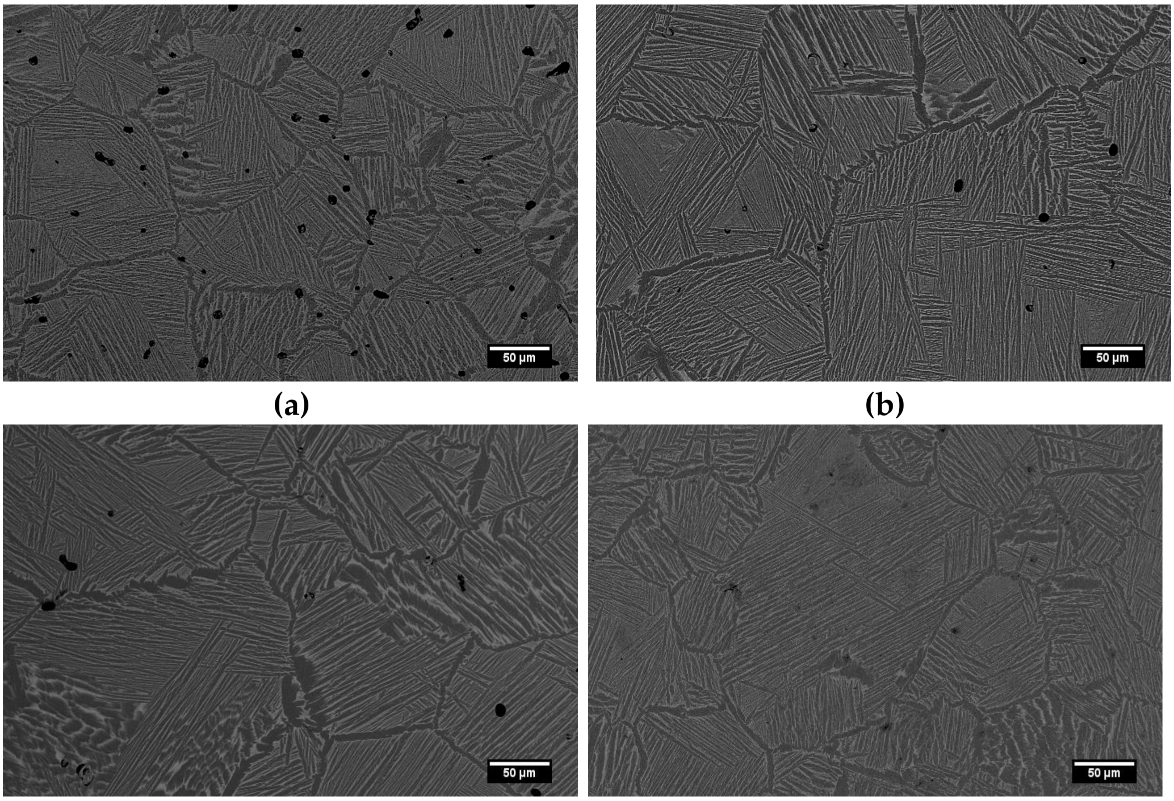

(a) (b)

(c) (d)

Figure 5.4. BSE-SEM images for sintered samples of TH12Nb alloy composition (using Nb-1 powder): a) Cycle 1 (C1); b) Cycle 2 (C2); c) Cycle 3 (C3); d) Cycle 4 (C4).

In contrast to these homogeneous microstructures, the image shown in **Figure 5.5a**, corresponding to samples produced using Nb-2 powder, presents a higher amount of porosity and incomplete diffusion of Nb, evidenced by the bright and diffuse Nb-rich area. This area corresponds to β phase, which explains the absence of alpha needles in the surroundings. Cycle 5 (C5), comprising higher sintering temperature, allowed to obtain dense and homogenous microstructure, with no evidence of undissolved Nb (**Figure 5.5b**). However, grain size growth is observed due to the sintering temperature increase. [18]

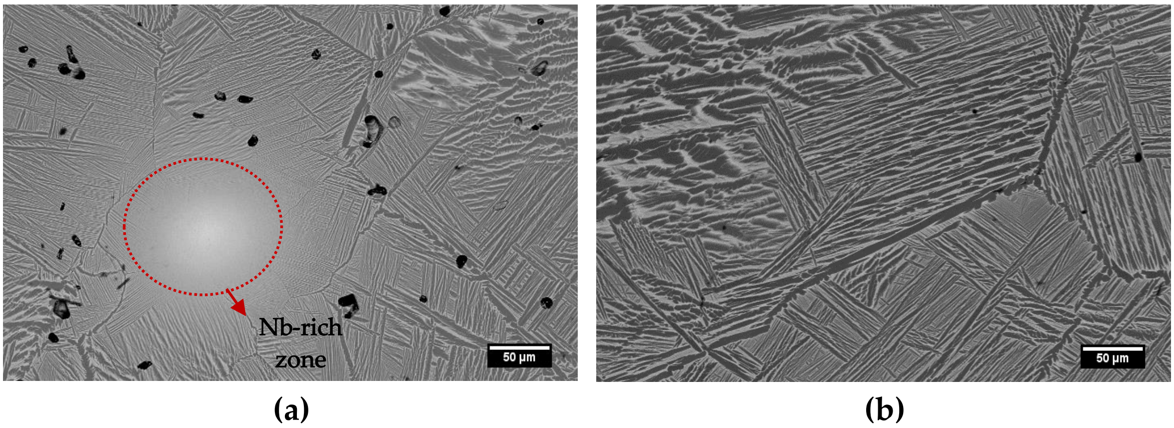

Figure 5.5. BSE-SEM images for sintered samples of TH12Nb composition (using Nb-2 powder): a) Cycle 4 (C4) and b) Cycle 5 (C5).

The microstructure of TH40Nb alloy composition obtained using Nb-1 and Nb-2 powder is shown in **Figure 5.6** and **Figure 5.7**, respectively. It can be seen that this composition has a predominantly β-Ti microstructure. In addition, titanium carbide (TiC) precipitates (identified with arrows) were found, preferably located at the grain boundaries, regardless of sintering conditions or kind of Nb powder. The bright spots correspond to Nb-rich areas where Nb remains undissolved. These heterogeneous zones seem to disappear for samples sintered at 1250 °C (C4) in samples processed with Nb-1. In contrast, undissolved Nb presence becomes more evident for TH40Nb composition obtained with Nb-2 powder under C4 conditions (**Figure 5.7a**), likely due to the larger Nb-2 particle size. Large bright spots can be seen, with almost unreacted Nb particles inside the Ti matrix and bright diffused areas corresponding to Nb-rich zones. This undesirable heterogeneous microstructure is improved when sintering runs under C5 cycle; the higher temperature allows to diffuse Nb particles and to obtain β-phase microstructures.

Concerning porosity, no significant differences were observed between C1, C2, C3 and C4 (Nb-1). Pores for TH40Nb composition are mainly elongated; there are few spherical pores situated at the grain boundaries. SEM images suggest that the final sintering stage has not yet been reached. Therefore, neither 1200 °C nor 1250 °C is high enough temperature to improve sample densification.

Samples TH40Nb sintered with C5 (Nb-2) show the most homogeneous microstructure without undissolved Nb. Like TH12Nb, sample TH40Nb shows lower porosity and grain size increase due to the sintering temperature rise.

To summarise, TH12Nb exhibits a more homogeneous microstructure, but it is a biphasic (α+β) alloy. In contrast, TH40Nb alloy presents β-Ti phase but shows heterogeneous Nb-rich zones due to undissolved particles and higher porosity. Particle size distribution of Nb powder has a significant effect on microstructure homogenisation. Samples processed with the smaller Nb powder (Nb-1) requires a lower sintering temperature to achieve a homogeneous microstructure. In contrast, those processed from coarser Nb powder (Nb-2) demand a higher sintering temperature to obtain a similar microstructure to those observed with the smaller Nb powder.

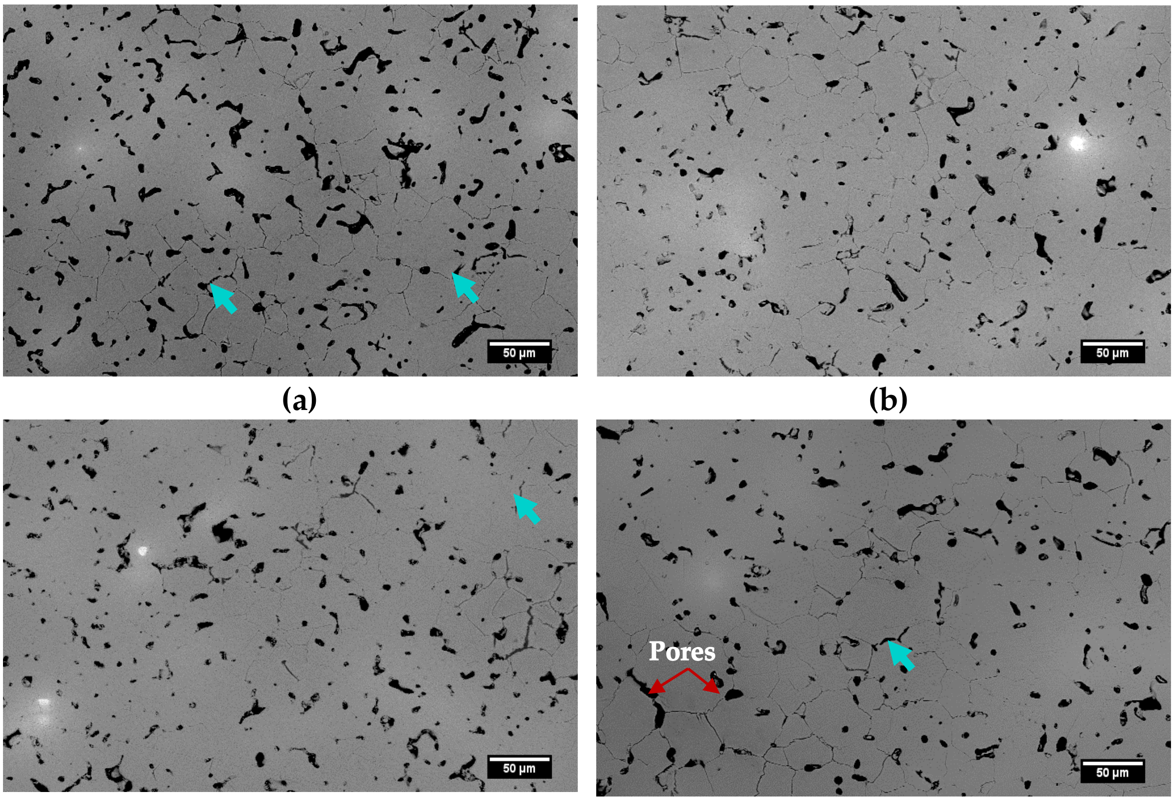

(a) (b) (c) (d)

Figure 5.6. BSE-SEM images for sintered samples of TH40Nb alloy composition (using Nb-1): a) Cycle 1 (C1); b) Cycle 2 (C2); c) Cycle 3 (C3); d) Cycle 4 (C4). Arrows indicate TiC precipitates.

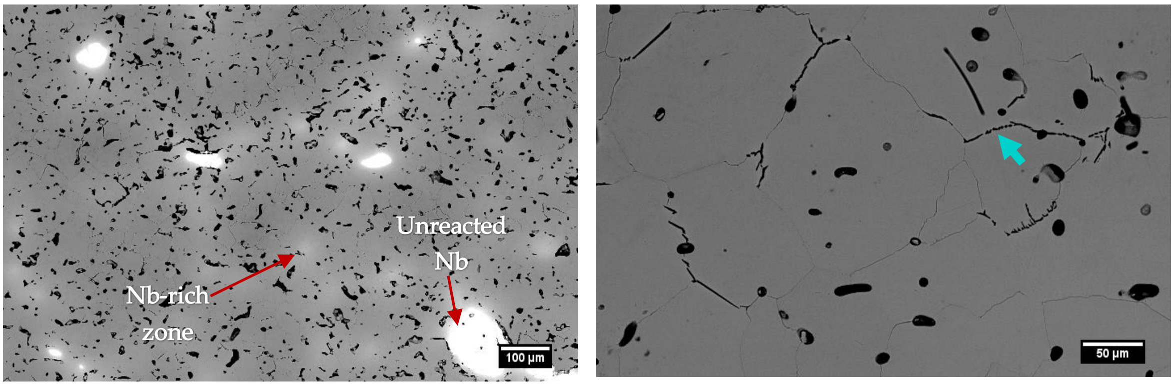

(a) (b)

Figure 5.7. BSE-SEM images for sintered samples of TH40Nb(2) alloy composition (using Nb-2 powder): a) Cycle 4 (C4); b) Cycle 5(C5). Arrows indicate TiC precipitates.

- *Effect of Fe powder on sample densification.*

Composition TH5Fe25Nb was studied using two kinds of Nb and Fe powders. **Figure 5.8** and **Figure 5.9** display the microstructures obtained for sintered samples using Nb-1 along with Fe-1 and Fe-2, respectively. **Figure 5.10** shows the microstructure achieved using Nb-2 and Fe-2 powders for C4 and C5.

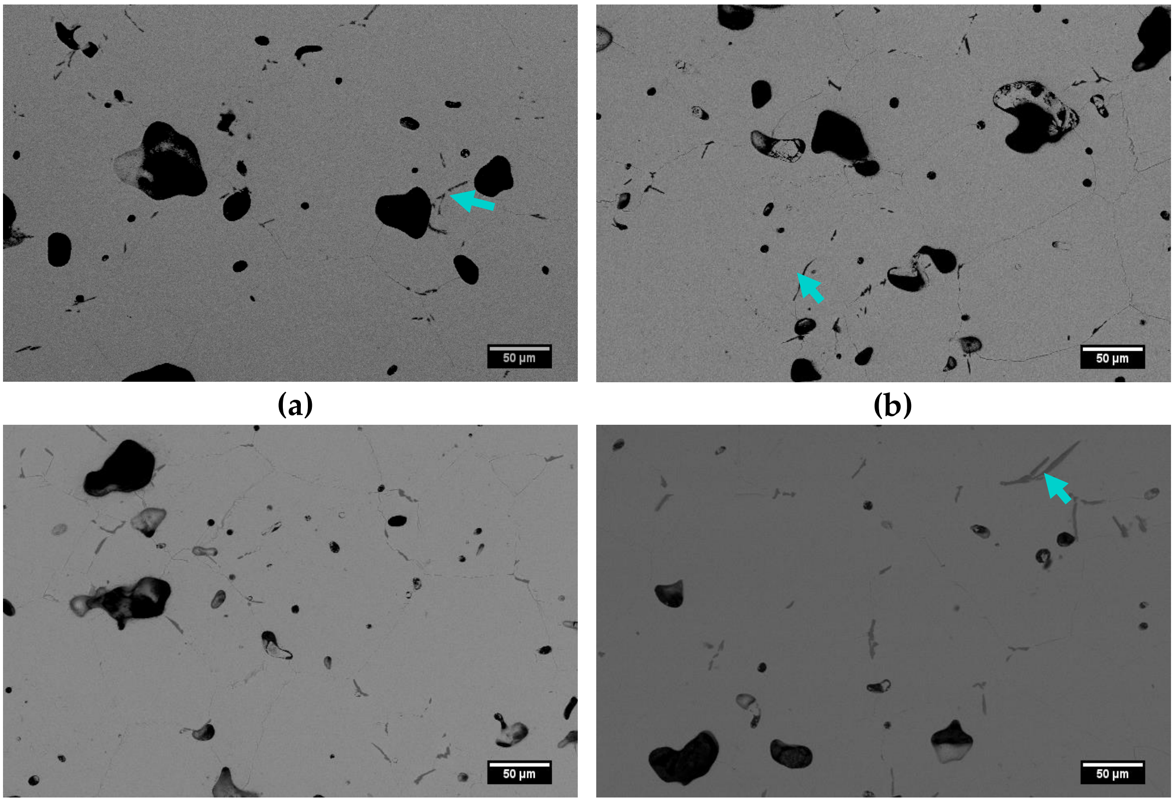

(a) (b)

(c) (d)

Figure 5.8. BSE-SEM images for sintered samples of TH5Fe25Nb alloy composition using Fe-1 and Nb-1: a) Cycle 1 (C1); b) Cycle 2 (C2); c) Cycle 3 (C3) and d) Cycle 4 (C4). Arrows indicate TiC precipitates.

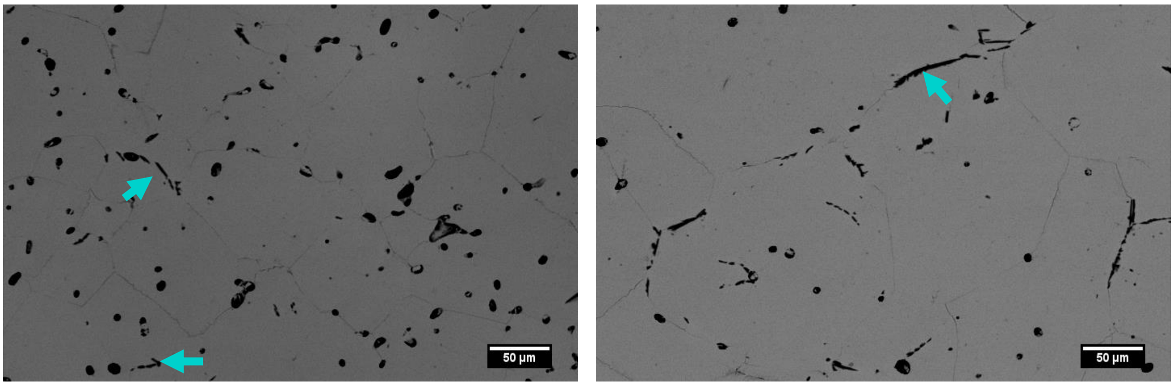

(a) (b)

Figure 5.9. BSE-SEM images for sintered samples of TH5Fe25Nb alloy composition (using Fe-2 and Nb-1 powders): a) Cycle 3 (C3) and b) Cycle 4 (C4). Arrows indicate TiC precipitates.

Regardless of the type of powder employed and sintering conditions, TH5Fe25Nb composition shows a mainly β-Ti microstructure and thin TiC precipitates, located at the grain boundaries (indicated with arrows in the corresponding images). Moreover, from these images, it can be seen that Fe addition favour the formation of a more homogeneous microstructure, as the bright Nb-rich spots that could be seen in TH40Nb composition are not present in any of the samples, except for sample processed with Fe-2 and Nb-2 consolidated under C4. This sample shows some bright diffuse zones (indicated in **Figure 5.10**a), suggesting incomplete Nb diffusion.

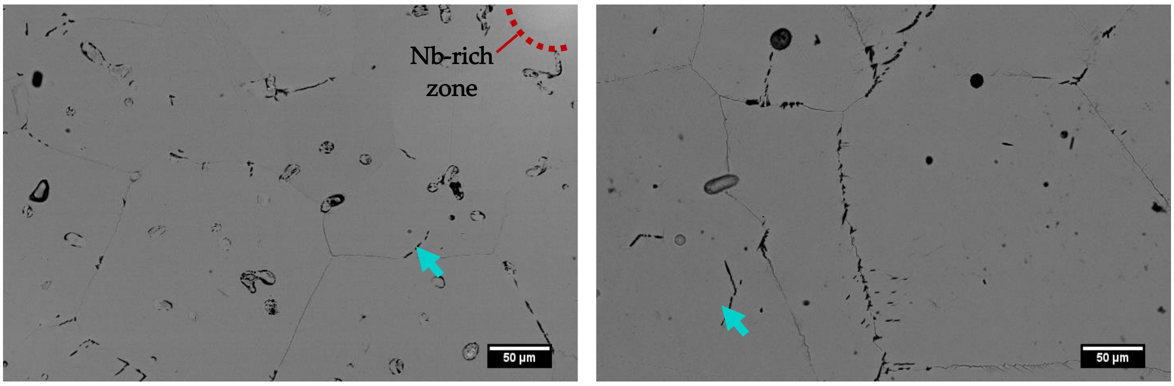

(a) **(b)**

Figure 5.10. BSE-SEM images for sintered samples of TH5Fe(2)25Nb(2) alloy composition (using Fe-2 and Nb-2 powders): a) Cycle 4 (C4); b) Cycle 5(C5). Arrows indicate TiC precipitates.

Several studies support that Fe is a fast diffusing alloying element, which improves the sinterability of Ti alloys; allowing higher densification and improving sample homogenisation [16], [19]–[21]. Similarly, for TH5Fe25Nb alloy composition, Fe addition plays an important role in promoting Nb diffusion, regardless of the particle size.

For both kinds of Fe, porosity seems to decrease for samples sintered at 1250 °C (C4). Nevertheless, final porosity and pore morphology are highly influenced by particle size and morphology of the employed Fe powder. Samples TH5Fe25Nb processed with coarser Fe (Fe-1) have higher amount of porosity than that obtained with smaller Fe (Fe-2) for C3 and C4. As shown in **Figure 5.8**, samples processed using Fe-1 exhibit pores up to 50 µm in length, which is considerably larger than pores achieved using Fe-2 (**Figure 5.9**), which reach a few microns in length. Samples with Fe-2 show more rounded pores, located inside the grains and at the grain boundaries, which suggest an advanced sintering stage.

Atoms mobility during sintering process might result in the appearance of vacancies, their coalescence resulting in the formation of large pores [17], [18]. The bonding between powder particles during sintering requires mass transport mechanisms in the interparticle contact zone. According to the model proposed by Kuczynski et al. [22], it is considered that volume diffusion or vacancies movement is the most dominant transport mechanism in the sintering process. The transport mechanism depends on the particle surface, activation energies of powder particles and the number of particles to diffuse [18]. Also, during the sintering of a couple of components, like Ti-Fe, with different self-diffusion coefficients, vacancies precipitate on the side of the faster-diffusing element that means, through the Fe side, forming empty channels/pores; and, atoms migrate towards the Ti side [22]. Besides, since the Fe diffusion coefficient into Ti is more than two orders of magnitude than the Ti diffusion coefficient into Fe [23], [24]; thus, there is an unbalanced diffusion rate during sintering between Ti and Fe. Unbalanced diffusion may lead to the formation of Kirkendall porosity, explaining the porosity observed in sintered TH5Fe25Nb alloys, especially in those processed with coarser Fe particle size (**Figure 5.8**). It has been reported that the atomic diffusion processes are favoured for finer powders since the contact area is higher [18]. Moreover, it has been reported that more spherical powders provide better control of particle packing and favour densification [25]. Both samples contain the same Fe amount (mass percentage); however, the number of particles for smaller Fe is higher than the coarser Fe, which increases the contact regions; hence a better sinterability for Fe-2 is expected. The diffusion surface is smaller as Fe particle size increases, as it is the case of Fe-1, which may delay the diffusion process during sintering, compared to smaller Fe (Fe-2) powder. This affects the size and amount of the final porosity.

From the sintering study, it can be concluded that the particle size of raw powders influences sample homogenisation. Samples obtained from smaller particles size (both Nb and Fe) require lower sintering temperature to achieve complete homogenisation and relative high densification. In comparison, alloys from coarser particles size demand higher sintering temperature and longer holding time to promote the diffusion process and reach suitable homogenisation. Concerning sintering temperature, the three alloys developed in this work present the highest densification values and better homogenisation as increases the sintering temperature. However, the apparent increase of grain size is notorious, as the sintering temperature increases from 1250 °C to 1450 °C, which could negatively affect mechanical behaviour.

- ***Formation of titanium carbides (TiC) precipitates.***

As mentioned above, samples TH40Nb and TH5Fe25Nb present titanium carbides (TiC) precipitates located at the grain boundary for all sintering cycles and kinds of powders employed. The formation of TiC will be discussed, considering the carbon content measured for samples sintered under C5 (**Table 5.3**).

Table 5.3. Measurement of carbon content for samples sintered under C5 conditions.

Composition	C (wt.%)
TH12Nb	0.069 ± 0.007
TH40Nb	0.053 ± 0.011
TH5Fe25Nb	0.042 ± 0.005

To understand the formation of these TiC precipitates, it is essential to know the interaction between Ti and C and how it changes with alloying elements. **Figure 5.11** shows the Ti-C phase diagram. It can be seen that the solubility limit in α-Ti is higher than for β-Ti, being 0.37 wt.% and 0.08 wt.%, respectively. Above the solubility limit, the Ti matrix cannot dissolve the extra carbon, and TiC precipitates as a secondary phase.

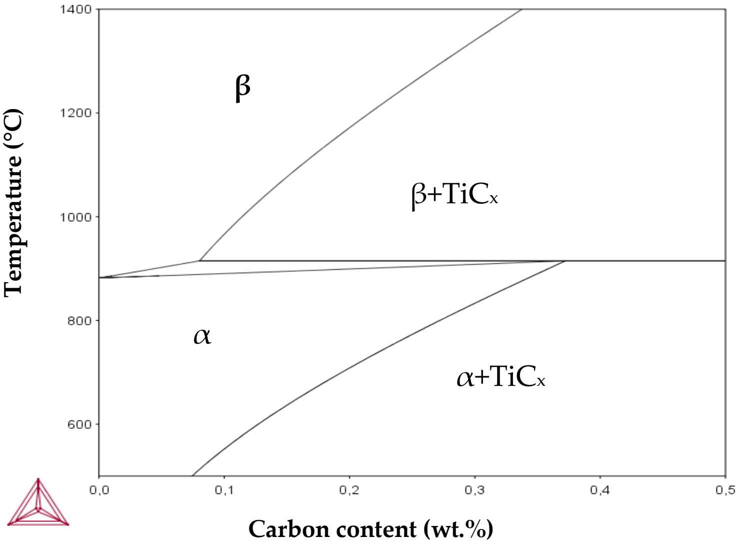

Figure 5.11. Ti-C phase diagram obtained with Thermocalc Software using the Ti alloys database V3.1 (TTTI3).

Moreover, it has been stated that Nb addition may reduce the solubility limit of carbon into Ti [26], [27]. In addition, the addition of Cr, Mo, Mn, and Fe may also lead to a decrease of carbon solubility in Ti alloys; whereas Co, V, and Ta can increase the carbon solubility in Ti alloys [28].

Figure 5.12 shows the phase diagram for the Ti-xNb-C system, where x corresponds to 12, 25, and 40 wt.%. As it can be noted, the solubility limit of carbon in β-Ti highly decreases as the Nb content increases, reaching 0.03 wt.%, 0.01 wt.% and 0.005 wt.% for 12, 25, and 40 wt.% of Nb, respectively. Furthermore, carbon solubility increases with increasing temperature, reaching 0.31% in Ti-12Nb, 0.25% in Ti-25Nb and 0.18% in Ti-40Nb, at the sintering temperature of 1450 °C. The solubility limit of carbon on the biphasic (α+β) region also decreases.

In the Ti5Fe25Nb-C system (**Figure 5.13**), the reduction of carbon solubility is even more severe than Ti-xNb-C. The carbon solubility limit in β-Ti is hugely low (about 0.001 wt.%). Carbon solubility increases as increasing temperature, reaching up to 0.16 wt.% at the sintering temperature. This value is similar to that predicted for the Ti-40Nb-C alloy Hence, it seems that the effect of carbon solubility reduction is intensified by combining Fe and Nb elements in TH5Fe25Nb, even though the total content of alloying elements be lower than 40 wt.%.

All compositions have carbon content (**Table 5.3**) lower than the solubility limit at the sintering temperature. Consequently, TiC precipitates would be not expected at this temperature. Based on phase diagrams (**Figure 5.12** and **Figure 5.13**), all carbon in sintered alloys should be in an interstitial solid solution with β-Ti phase for three processed alloys. Nevertheless, for TH40Nb and TH5Fe25Nb alloys, this not happen since several titanium carbides precipitates were observed in SEM images. Hence, it is reasonable to deduce that titanium carbide precipitates are formed during cooling. Considering the carbon content in sintered samples is expected TiC precipitate below 970 °C in TH-12Nb, 1075 °C in TH-40Nb and TH5Fe25Nb. These points are indicated with (★) in **Figure 5.12**b and **Figure 5.13**b.

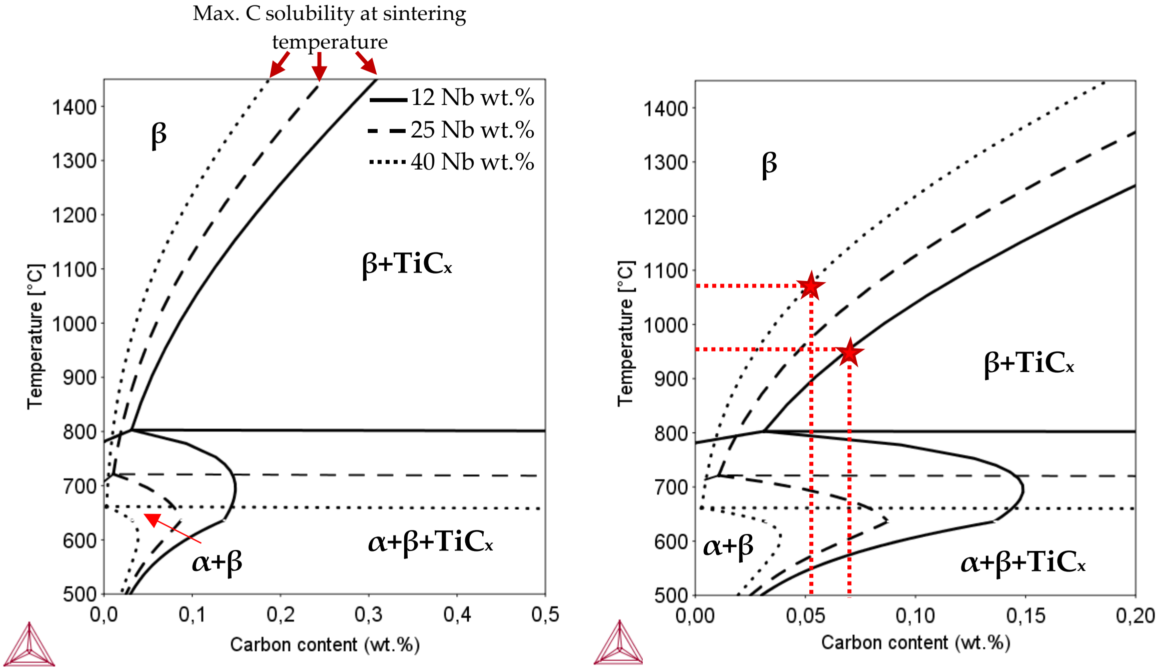

(a) **(b)**

Figure 5.12. Phase diagram of Ti-xNb-C alloys obtained by Thermocalc software for different Nb additions (x=12, 25, 40 wt.%) using the using Ti alloys database V3.1 (TTTI3). a) Carbon concentration up to 0.5 wt.% and b) Detail of Ti-xNb-C phase diagram until 0.2 wt.% of carbon.
★ Indicates the expected point to TiC formation during cooling.

In the case of TH12Nb alloys, the carbon solubility range in the biphasic (α+β) field is considerably higher than that in Ti-40Nb wt.% and Ti-5Fe-25Nb alloys. It is 0.15 wt.% for Ti-12Nb, 0.04 wt.% in Ti-40Nb and 0.012 wt.% in Ti-5Fe-25Nb. Then, it is possible that for TH12Nb alloy, as the carbon content is lower than carbon solubility in (α+β) region (**Figure 5.12**b), carbon has dissolved into α-Ti phase due to the greater carbon solubility in this phase compared to that in β-Ti phase. On the contrary, as TH5Fe25Nb and TH40Nb present a carbon content above the lower carbon solubility in the (α+β) region, TiC precipitation is produced since the Ti matrix cannot dissolve the carbon excess.

Despite the TiC presence in TH40Nb and TH5Fe25Nb compositions, the three alloys processed in this work, have a carbon content within maximum permissible in the standard ASTM F136, established for Ti-6Al-4V alloy for surgical implant applications (0.08 wt.%) [29]. However, even if the carbon content meets the requirements, the TiC precipitates could affect the mechanical behaviour of alloys, increasing the elastic modulus and reducing ductility.

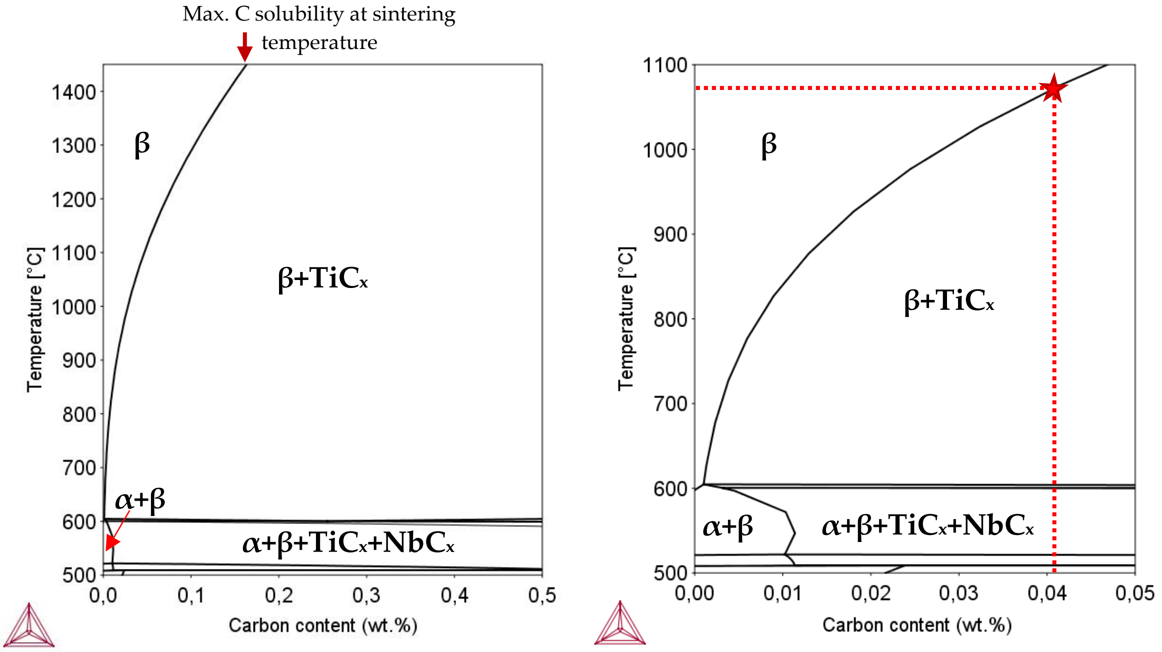

(a) (b)

Figure 5.13. Phase diagram of Ti-5Fe-25Nb-C predicted with Thermocalc software, using Ti alloys database V3.1 (TTTI3). a) Phase diagram with carbon concentration up to 0.5 wt.% and b) Detail of the left side diagram (a) up to 0.05 wt.% of carbon.

★ Indicates the expected point to TiC formation during cooling.

5.3.1. Phase identification by X-ray diffraction (XRD).

Considering the results obtained so far, the coarser Fe powder (Fe-1) and sintering cycles C1 and C2 were discarded, since they did exhibit a more porous and less homogeneous microstructure. The next results presented in this section correspond to samples produced using sintering cycles C3, C4 and C5.

Figure 5.14 displays the XRD patterns for each composition, sintered with different cycles (C3, C4 and C5). The phases identified by XRD are in accordance with the phases observed by SEM (**Figure 5.4-Figure 5.10**).

It can be seen that TH12Nb is composed of (α+β)-Ti phase, coinciding with pattern diffraction of α-Ti (ICDD 01-089-3073) and β-Ti (ICDD 01-089-4913). Also, it can be seen that the samples TH40Nb and TH5Fe25Nb are composed mainly of β-Ti phase. However, a small peak corresponding to the main reference peak of α-Ti phase was also identified in the diffraction pattern of TH5Fe25Nb sintered with C5. No evidence of TiC was found for TH40Nb and TH5Fe25Nb; which indicate that TiC amount is not enough to be detected by XRD.

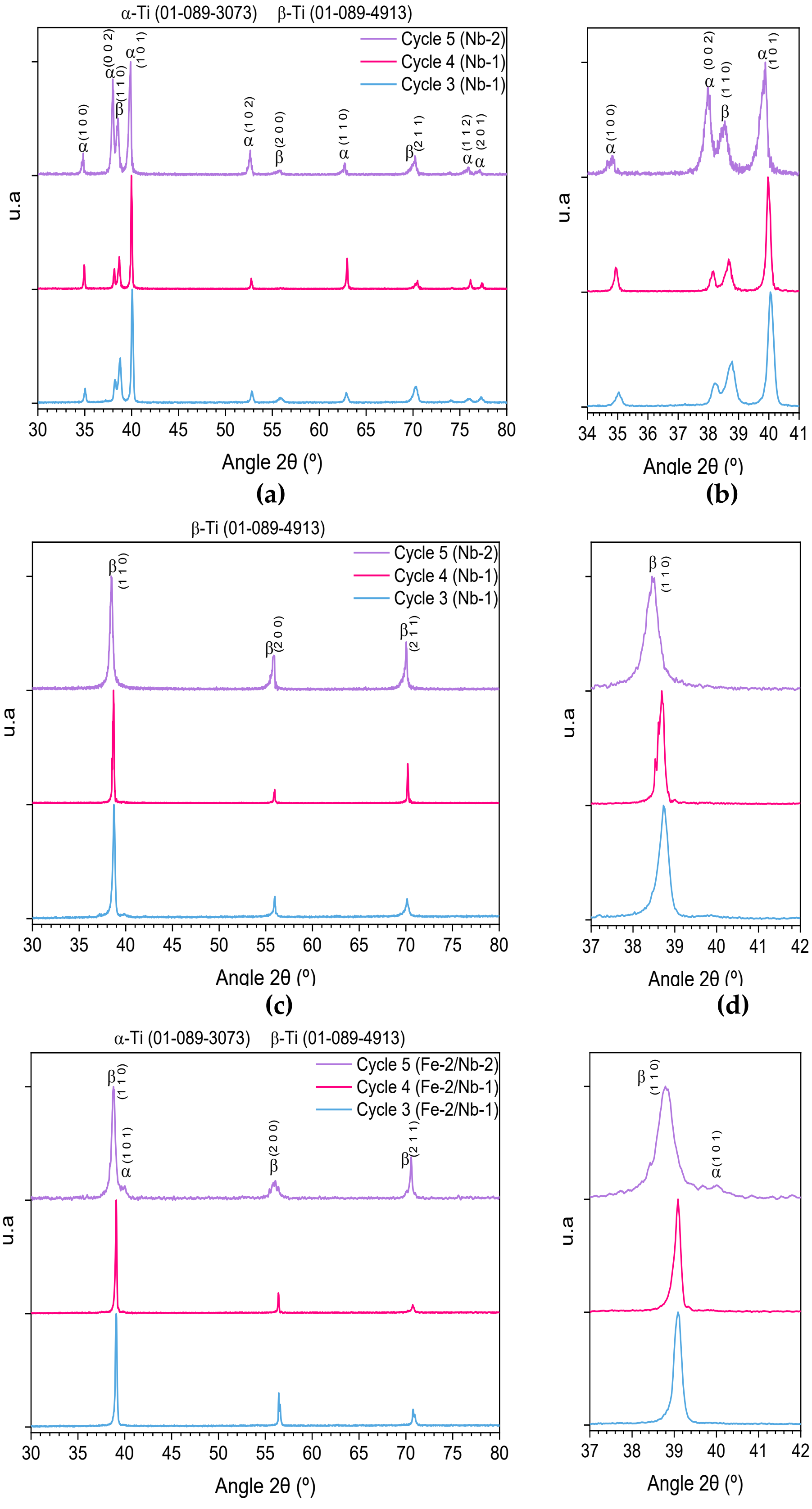

(a) (b) (c) (d) (e) (f)

Figure 5.14. XRD diffraction patterns employing different sintering cycles and kind of Nb powder: (a-b) TH12Nb; (c-d) TH40Nb and (e-f) TH5Fe25Nb.
Images b, d and f correspond to details of each diffractogram to the corresponding composition.

Although the phases identified for all sintering cycles are the same for each composition, some subtle changes were detected as sintering temperature increases. These changes are shown in more detail in **Figure 5.14**.b, d and f for TH12Nb, TH40Nb and TH5Fe25Nb, respectively. **Table 5.4** shows the angle diffraction of the principal peak, corresponding to the plane (1 1 0) of β-Ti phase obtained for the three processed alloys, sintered with cycles 3, 4 and 5.

Table 5.4. Diffraction angles of plane (1 1 0) of β-Ti phase for sintered samples with different sintering cycles.

	TH12Nb	**TH40Nb**	**TH5Fe25Nb**
Cycle 3	38.75	38.74	39.08
Cycle 4	38.67	38.70	39.09
Cycle 5	38.53	38.47	38.80

In general, for the three compositions, it is observed that the main peak is shifted to the left, towards smaller diffraction angles, as the sintering temperature increases. The peak position on XRD measurements provides information about crystallographic features such as lattice parameter, unit cell dimensions, crystalline system, identification of crystalline phases and semi-quantitative analysis [30]. Besides, it has been reported, that the presence of multiple elements with different atomic size and energy levels, produces lattice distortions, which can be identified by shifting the reference peaks position compared to the lattice of the pure element [31].

Both pure β-Ti and Nb have the same crystal structure BCC, and close diffraction angles (38.759° and 38.507°, respectively). The incorporation of alloying element into Ti network produces lattice distortions which supposes a peak displacement toward greater or lower diffraction angles, depending on the solute atom size [32], [33].

The atomic radius of Nb is higher than that of Ti (207 and 147 pm, respectively). Hence, when a solute Nb atom replaces a Ti atom, the volume cell increases by the size differences. Besides, close to each solute atom (Nb), the atoms are not sited at the regular positions of the pure lattice. This produces local distortions that expand the lattice, varying the diffraction angles, explaining the displacement observed for the plane (110) toward lower diffraction angle for samples TH12Nb and TH40Nb. Since in an alloy formed by solid solution, such as Ti-Nb alloys, it is expected that diffraction angle occurs at intermediate angles, between pure β-Ti and Nb [32], [34].

It is noted that this displacement is more pronounced for higher sintering temperatures. This fact could be ascribed to as the diffusion process is enhanced/favoured at high temperature. Then, if a higher amount of Nb diffuses into the Ti matrix, it is achieved higher homogenisation and lattice distortions, producing the shifting of angle diffraction toward Nb.

In contrast, for TH5Fe25Nb alloy, the main peak of the β-Ti phase is located at a greater angle than Ti-Nb alloys (**Table 5.4**). This is because Fe has a smaller atomic radius (0.126 nm) than Ti (0.147 nm) and Nb (0.206 nm), so when Fe diffuse into Ti, and forms a solid solution, lattice parameter of β-Ti decreases, moving the peak to higher angle diffraction [35]. As indicated in **Table 5.4**, the diffraction angle of the main peak decreases for TH5Fe25Nb sintered under C5 conditions

These results can be related to the strong β-stabilising effect of Fe in β-Ti over Nb. As seen in **Chapter 4**, Fe particles fully dissolve into Ti matrix below 800 °C. At that temperature, the Nb diffusion just begins. A hypothesis could be that at low sintering temperature (C3 and C4), β-Ti phase is governed by Fe diffusion and lesser extent, by Nb partial diffusion. Then the distortions in the network cause the peak to be at a greater angle. While at a higher sintering temperature, diffusion between Nb and Ti is promoted, producing lattice parameter expansion, and therefore the displacement of the main peak toward lower angle diffraction. This displacement is less than that observed in Ti-Nb alloys since the effect of Fe (shrinkage), and Nb (expansion) is combined.

Finally, samples sintered with C5 show a broader peak of the β-Ti phase; this supports the conclusion that higher phase homogenization was achieved for C5 compared to C4 and C3.

5.4. Mechanical characterisation.

5.4.1. Microhardness.

Vickers microhardness measurements for samples sintered with different sintering cycles are displayed in **Figure 5.15**. The hardness results were analyzed considering porosity, grain size (qualitative) and oxygen content (presented in **Table 5.5**), due to their great influence on mechanical properties. High porosity and grain size reduce hardness, while high oxygen concentration is associated with a hardness increase [36], [37]. Ç

From **Figure 5.15**, it can be seen that TH5Fe25Nb composition presents the higher hardness values for all sintering cycles. It has been stated that Fe addition has a solid-solution strengthening effect in Ti alloys, which may explain the higher hardness values observed in TH5Fe25Nb respect to the other Ti-Nb alloys [38], [39].

The lowest hardness values were obtained for TH40Nb, for all sintering cycles. Regardless of the sintering cycle employed, TH40Nb composition reached higher porosity than TH12Nb and TH5Fe25Nb (at least 4% more porosity). Greater porosity could explain the low hardness values observed for TH40Nb. Similarly, samples sintered with C3 present the lowest hardness values, which is also associated with the higher porosity achieved with this sintering condition.

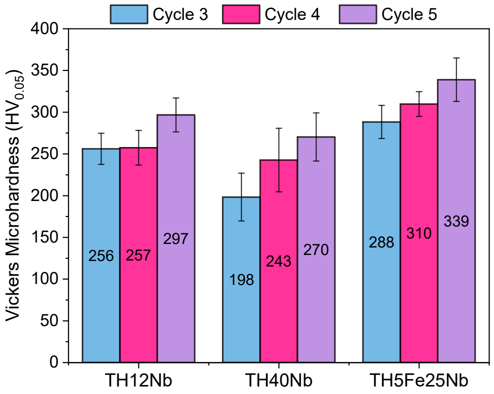

Figure 5.15. Vickers microhardness measurements for sintered samples with different sintering cycles (C3, C4 and C5).

Table 5.5. Oxygen content for sintered samples under C4 and C5 (wt. %).

Sintering cycle	TH12Nb	TH40Nb	TH5Fe25Nb
C3	0.497 ± 0.006	0.574 ± 0.039	0.477 ± 0.012
C4	0.403 ± 0.004	0.437 ± 0.056	0.503 ± 0.008
C5	0.790 ± 0.022	0.592 ± 0.025	0.633 ± 0.026

Hardening of an alloy can be reached by grain size refining that increases the grain boundaries and dislocations density. Precipitation of secondary phases, carbides or oxide particles can also have a hardening effect [40], [41]. Based on this, it was expected higher hardness for samples sintered with C3 and C4 (with smaller grain size). On the contrary, the three alloys sintered with C5 exhibit the highest hardness values, despite having significant grain size growth compared to grain size observed for C3 and C4. According to **Table 5.4**, samples sintered with C5 present higher oxygen content for all compositions, reaching about 0.8% and 0.6% for TH12Nb, and TH40Nb and TH5Fe25Nb, respectively. Greater oxygen content obtained with C5 can lead to hardening with respect to the other sintering cycles. [42], [43]

Current results suggest that grain size have no significant effect on hardness for the studied alloys. Hardness seems to be mainly affected by porosity and oxygen content. Achieving higher hardness values is favourable to improve wear properties.

5.4.2 Elastic modulus.

Elastic modulus is of the most important mechanical properties to consider for the biomaterial design. For biomedical applications, low elastic modulus alloys should be employed, in order to avoid the stress-shielding phenomenon, since it is associated with long-term bone resorption, compromising the bone-implant fixation. [43]–[45]

Young's modulus measurements, obtained for samples sintered using C4 and C5 cycles, are shown in **Figure 5.16**, where it is clear that no significant differences were found. This confirms that grain size does not affect the resulting elastic modulus, which is influenced by alloy composition. As was expected, higher Nb content reduces the sample stiffness. Hence, the composition containing 40 wt.% of Nb reached the lowest Young's modulus values, achieving about 64±12 GPa and 73±12 GPa, respectively, for C4 and C5. Besides, the porosity of TH40Nb (about 4% for both sintering cycles) may also contribute to reducing the elastic modulus.

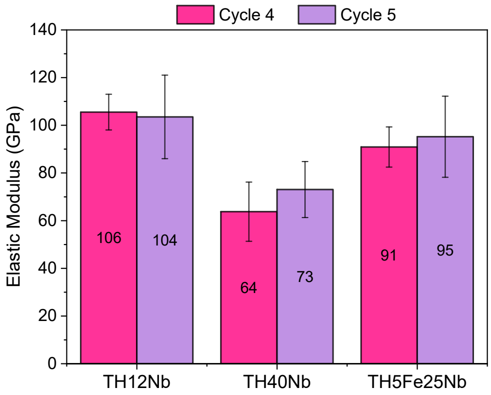

Figure 5.16. Young's modulus values for sintered samples under different sintering cycles (C4 and C5).

Despite the clear microstructure differences observed by SEM images for samples TH12Nb (α+β) and TH5Fe25Nb (mainly β), sample TH12Nb has elastic modulus values slightly higher than that obtained for TH5Fe25Nb composition. Sample TH12Nb reached elastic modulus of 106±8 GPa and 104±17 GPa, for C4 and C5 respectively; while TH5Fe25Nb achieved 91±8 GPa and 95±14 GPa, for C4 and C5 respectively. Biphasic (α+β)-Ti alloys, typically, exhibit higher Young's modulus and yield strength than β-Ti alloys [44], [46]. The α-Ti phase has an HCP structure that is more brittle since BCC structure possesses more active slip systems than HCP structure [43], [47]. Nevertheless, no significant differences in elastic modulus were found for these compositions.

Mechanical properties of Ti alloys are strongly influenced by processing route, thermal treatments and other material features, such as interstitial elements or total porosity. In particular, the elastic modulus of β-Ti alloys is powerfully influenced by the crystal orientation; hence, the crystallographic texture should be controlled by processing to reduce the elastic modulus. All this makes the comparison of some properties with reported data difficult. Nevertheless, alloys processed by powder metallurgy usually have no crystallographic texture.

Different Young modulus values have been reported for alloys with similar composition, obtained with different processing routes. It should be noted that many of the Ti-Nb alloys showing elastic modulus lower than the bone usually have high porosity. For instance, Hosnie et al. reported elastic modulus of 17 GPa for Ti-40Nb alloy with 55% of porosity [48]; while Abdi et al. stated elastic modulus of 62 GPa, for the same composition, processed by melting [49]. Moreover, alloys of the Ti-Nb-Fe system like Ti-12Nb-5Fe alloy produced by cold crucible levitation melting reaches 90 GPa [50]. Besides, it has been reported for Ti-25Nb-3Fe, obtained by casting, had an elastic modulus of 65 GPa [51]; while cast-quenched Ti-27Nb-7Fe alloy exhibited 115 GPa. The differences among these alloys, with similar composition, is attributed to the hardening effect by martensitic transformation of β to α'' phase produced by fast cooling [52]. The formation of brittle phases such as α', α'' or ω, should be controlled to prevent rising of elastic modulus values.

The three compositions processed in this work present similar elastic modulus values to those reported in the bibliography, which are lower than the current Ti-6Al-4V and Ti-6Al-7Nb alloys, that reaches about 114 GPa [50]. Hence, the processed alloys could be a suitable alternative for biomedical Ti alloys, since they are composed of non-toxic and non-allergic alloying elements, achieving an elastic modulus decrease as well.

5.4.3. **Fatigue behaviour.**

Fatigue resistance is a key property of implant materials since, during their lifetime, hip implants continuously must withstand cyclic loads, which could cause plastic deformation in stress concentration sites or heterogeneous zones [53], [54]. Then, evaluate fatigue behaviour is especially important to confirm the feasibility and reliability of the alloy as implant material. In this section, fatigue behaviour was evaluated for the three Ti alloys sintered under condition C5.

With the aim to establish the initial load for the fatigue tests, static three-point bending tests were conducted to measure the maximum flexural strength (transverse rupture strength, TRS). Representative results for each alloy are shown in **Figure 5.17**. It can be seen that TRS reaches values of 1790 MPa, 1570 MPa and 1350 MPa for TH12Nb, TH5Fe25Nb and TH40Nb, respectively. The strain values are 9.3% for TH12Nb, 5.4% for TH40Nb, and 4.4% for TH5Fe25Nb. The low strength of TH40Nb may be attributed to lower relative density reported in **Figure 5.3**.

The TRS values obtained are comparable to those Ti-Nb alloys reported elsewhere. Lee et al. [55] evaluated the mechanical properties of cast processed binary Ti-Nb alloys containing Nb up to 35 wt.%. They reported that TRS decreases with the Nb content increasing, achieving 1700 MPa, 1650 MPa and 1400 MPa for 10 wt.%, 25 wt.%, and 35 wt.% of Nb. Despite the difference in porosity between samples processed by cast and PM, values reported by Lee et al. [55] are close to the reported in **Figure 5.17**. Processed samples exhibit higher TRS compared to other PM alloys. Ti15Nb3Fe and Ti15Nb3Cr alloys sintered at 1280 °C for 2 h, reached TRS of 700 MPa and 1400 MPa, respectively[56]. Eren et al. reported a TRS of 1200 MPa for Ti16Nb alloy [57]. The relative higher porosity of these samples (about 4%) may explain the low TRS values.

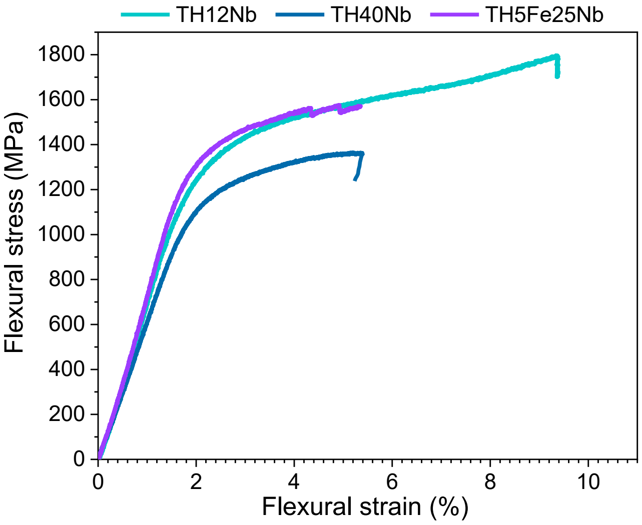

	TRS* (MPa)	σ_y (MPa)
TH12Nb	1790	1290
TH40Nb	1350	1120
TH5Fe25Nb	1570	1360

TRS: Transverse resistance strength.

Figure 5.17. Flexural stress-strain obtained for TH12Nb, TH40Nb and TH5Fe25Nb alloys.

β-Ti alloys have lower elastic modulus than (α+β) alloys. Moreover, owing to their BCC crystal structure, they are also recognised to exhibit higher ductility [58]. Then, the lower values of both strength and strain obtained for β-type alloys was unexpected.

It is well known that porosity has negative effects on mechanical properties. Pores diminish the effective cross-section of the sample, thereby, reduce the material fraction that must resist the applied load. Pores act as stress concentration sites for cracks nucleation, decreasing both ductility and strength [59]. Additionally, interstitial elements (O and N) have a solid-solution hardening effect in Ti alloys. Then, these elements strengthen the alloy but decrease ductility. [60]

TH12Nb and TH5Fe25Nb alloys have higher relative density values (**Figure 5.3**) and higher oxygen content (**Table 5.5**) than TH40Nb alloy. This may explain the higher TRS values achieved for TH12Nb and TH5Fe25Nb samples, but no the differences in ductility. Considering that TH5Fe25Nb presents a similar relative density and lower oxygen content (0.63 wt.% O) than TH12Nb (0.79 wt.% O), higher ductility would be expected for

TH5Fe25Nb. However, this does not occur. TH12Nb presents more than twice the elongation than the sample TH5Fe25Nb. Comparing both β-Ti alloys, there is almost no influence of porosity on the ductility of TH40Nb and TH5Fe25Nb. Even though TH40Nb presents a porosity of about 4% and TH5Fe25Nb achieve about 1%, TH40Nb show slight higher elongation than TH5Fe25Nb. These results suggest that there are different/additional factors to porosity and oxygen content affecting the mechanical behaviour of the alloys.

TiC precipitates increase the strength of Ti and its alloys by precipitation strengthening mechanism but also reduce the alloy ductility significantly. As seen in **Section 5.3**, higher Nb addition reduces the carbon solubility in Ti alloys, favouring the TiC precipitates formation. Hence, TH40Nb and TH5Fe25Nb are more likely to form TiC than TH12Nb. Indeed TiC precipitates were no observed in SEM images for TH12Nb composition, which explains the better flexural behaviour.

It is reasonable to deduce that the lower mechanical properties for TH40Nb and TH5Fe25Nb could be related to the presence of TiC precipitates instead of porosity. These results coincide with results reported by Zhao et al. [7]. They found higher detrimental effects on the ductility of Ti-Nb alloys caused by TiC precipitates than those produced by porosity.

To further understand why the ductility is reduced, the fracture surfaces of the three Ti alloys, after the static flexural test were examined and are shown in **Figure 5.18**. The fracture morphology of TH12Nb exhibits mainly dimple rupture, indicative of a ductile fracture; while TH40Nb shows significant interconnected porosity, which is related to ductility loss. Besides, dimples and cleavage facets are observed, suggesting a ductile-fragile fracture. In contrast, TH5Fe25Nb sample presents marked fragile and intergranular fracture features, where grains can be easily distinguished. Propagated cracks, among grains, are also observed. TH40Nb and TH5Fe25Nb show more signs of brittle fracture, which could be attributed to the detrimental effects generated by the presence of TiC.

After the static flexural test, it was selected 400 MPa as the starting load for the fatigues tests, which corresponds to around 30-35% of the yield strength of each alloy. The Stress-Number of cycles (S-N) diagrams summarising the fatigue data acquired (R= 0.1) are displayed in **Figure 5.19**.

Sample TH12Nb, showing an (α+β) microstructure, achieved the highest fatigue limit at high-cycle fatigue life, reaching about 368 MPa. In contrast, composition TH40Nb and TH5Fe25Nb, mainly composed of β-Ti phase, reached 321 MPa and 338 MPa, respectively. Moreover, it can be seen a higher data dispersion in the fatigue behaviour for samples TH40Nb and TH5Fe25Nb. For instance, some specimens of TH40Nb tested at 360 and 375 MPa shows lower fatigue life than that obtained for samples tested at 400 MPa, while others

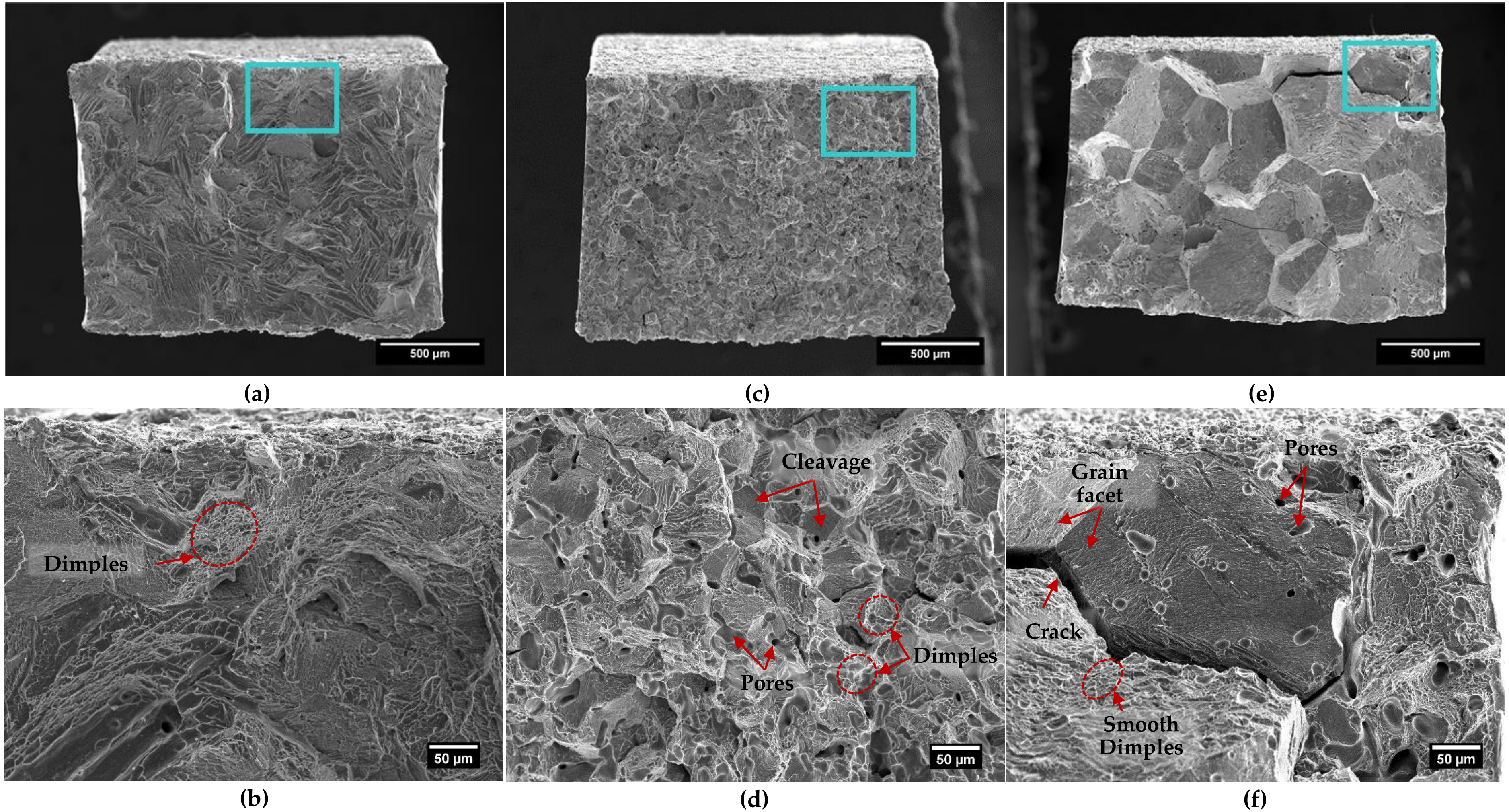

Figure 5.18. SE-SEM images showing fracture surface after three-point flexural tests for: (a-b) TH12Nb;(c-d) TH40Nb and (e-f) TH5Fe25Nb.

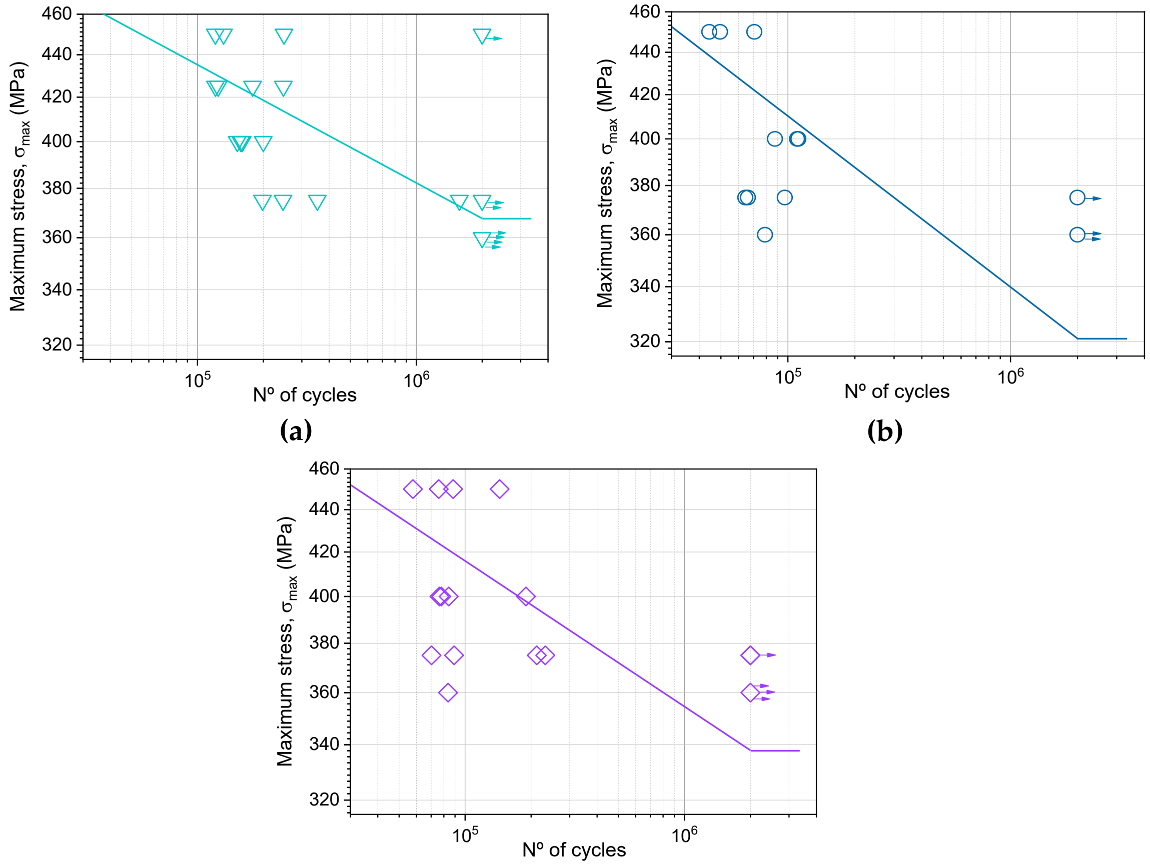

(a) **(b)**

(c)

Figure 5.19. S-N curves after three-point bending fatigue test for a) TH12Nb; TH40Nb and c) TH5Fe25Nb. Arrows indicate that run-out condition at 2x10⁶ cycles was achieved.

reach the run-out condition. This may be attributed to TiC precipitates, which are usually associated with the detriment of mechanical properties and the loss of reliability. TiC increases brittleness which may produce unexpected failure at lower loads. For TH40Nb alloy composition, the higher porosity, compared to TH12Nb and TH5Fe25Nb, can also decrease the fatigue limit.

The fracture surface was examined to better understand the fatigue failure mechanisms, and images are shown in **Figure 5.20**. For the three alloys, fatigue cracks initiation occurs in the upper sample section, where there is the highest stress concentration. Typical fatigue striations were observed for TH40Nb and TH5Fe25Nb samples (indicated with "I" in **Figure 5.20**).

Fatigue crack initiation is usually associated with defects such as inclusions, segregation, precipitates, pores or microstructural heterogeneities, which act as potential crack nucleation sites [61]. In evaluated samples, pores at the nucleation zone were observed, especially for TH40Nb sample, where different sizes of closed and interconnected pores were found. This could explain the lower fatigue properties for this composition.

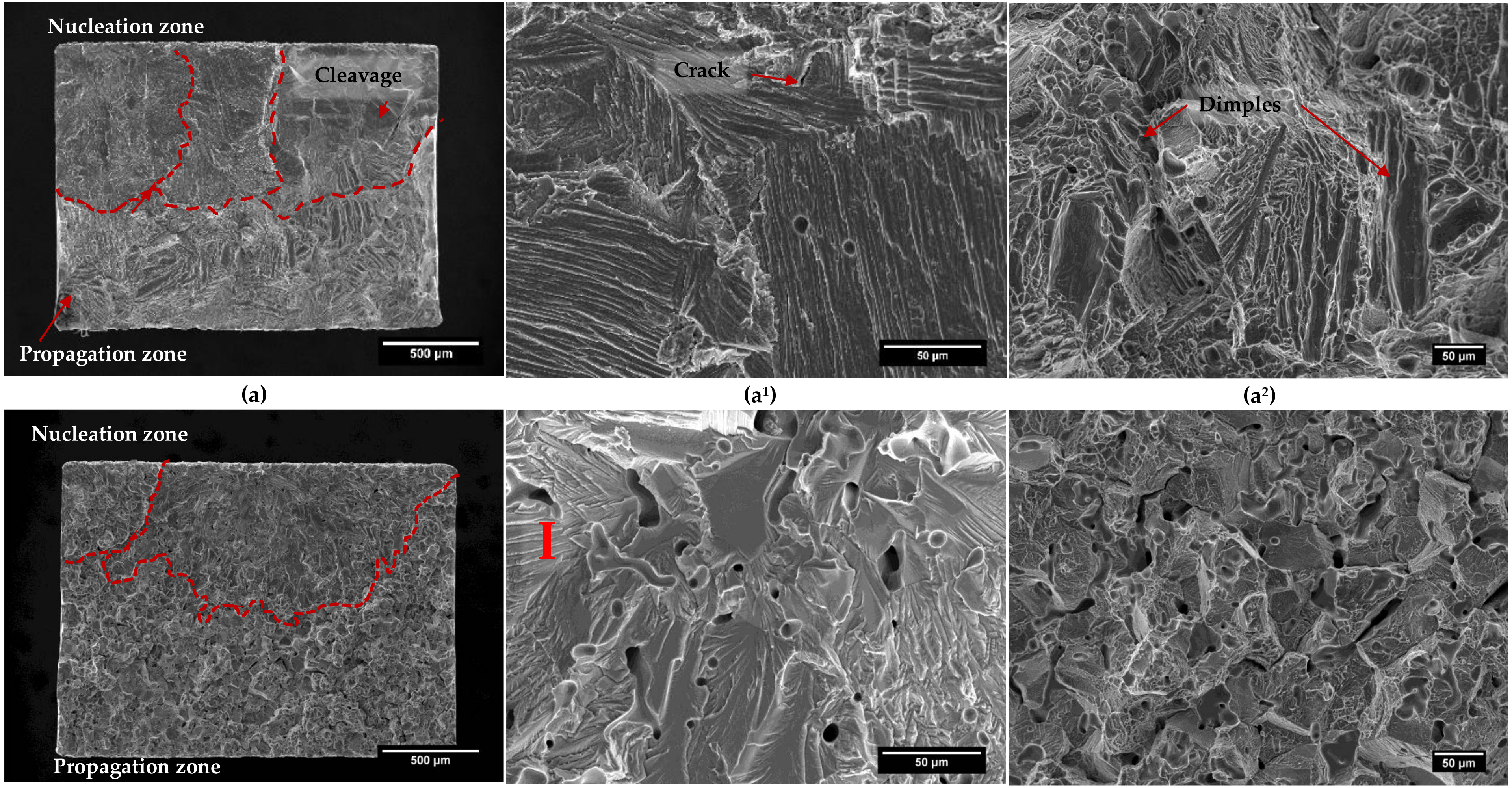

(a) **(a¹)** **(a²)**

(b) **(b¹)** **(b²)**

Figure 5.20. SEM images of fracture surface after three-point flexural fatigue test for samples tested at σ_{max} = 400 MPa. a) TH12Nb (N_f = 200.077 cycles); b) TH40Nb (N_f = 109.990 cycles) and c) TH5Fe25Nb (N_f = 189.499 cycles) after failure in high-cycle fatigue life region.

[1] Detail of nucleation zone; [2] Detail of propagation zone.

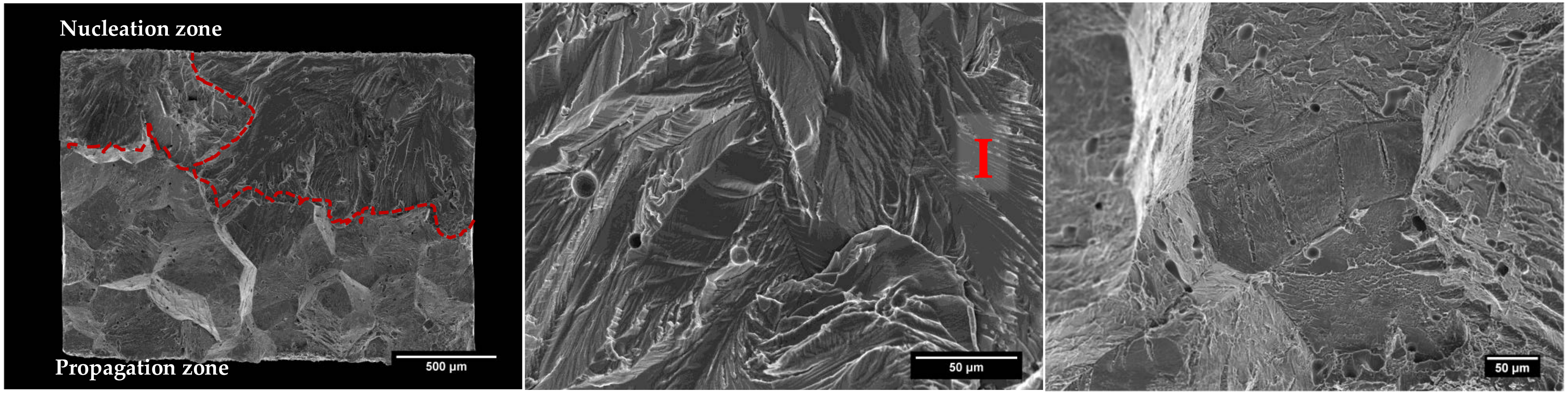

(c) **(b^1)** **(c^2)**

(Continuation) Figure 5.20. SEM images of fracture surface after three-point flexural fatigue test for samples tested at σ_{max} = 400 MPa. a) TH12Nb (N_f = 200.077 cycles); b) TH40Nb (N_f = 109.990 cycles) and c) TH5Fe25Nb (N_f = 189.499 cycles) after failure in high-cycle fatigue life region.

^{1} Detail of nucleation zone; ^{2} Detail of propagation zone.

Moreover, small cracks near the top surface were observed in TH12Nb sample. It has been reported that cleavage facets at the nucleation zone could be formed by easy crack propagation parallel to the local lamellar interface; in biphasic (α+β)-Ti alloys [62]. This agrees with the cleavage facets revealing parallel lines observed in **Figure 5.20a**^{1}), which correspond to the α/β lamellae that appear to be oriented towards the propagation direction.

Fast crack propagation region or catastrophic failure zone is similar to the fracture surface described in **Figure 5.20**. After nucleation region, TH12Nb exhibits a ductile fracture by the presence of dimples; for TH40Nb, evidence of dimples and cleavage facets indicated a ductile-brittle fracture, and severe intergranular fracture can be seen for TH5Fe25Nb sample.

Despite the fact that no TiC precipitates were detected at the nucleation zone for TH40Nb and TH5Fe25Nb samples; they seem to have a significant influence on the crack propagation zone. In **Figure 5.21**, empty rough areas of detached particles can be seen. EDX analysis indicates an increase of carbon content inside them, which suggest that they correspond to TiC particles. Hence, TiC embrittled the material, facilitating the crack propagation and intergranular fracture.

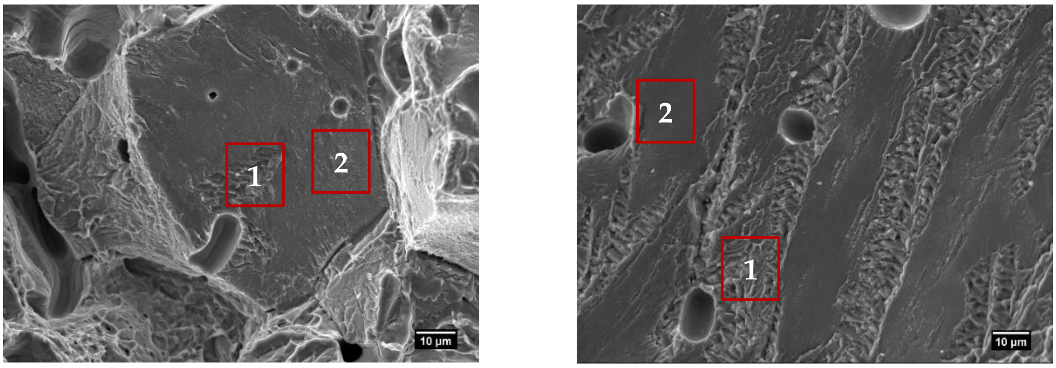

	Ti	Nb	C
A1	66.8	33.2	✓
A2	59.7	40.3	ND

ND: No detected

(a)

	Ti	Nb	Fe	C
A1	84	14	2	✓
A2	71.6	23.9	4.5	ND

ND: No detected

(b)

Figure 5.21. Detail of the propagation zone of the fracture surface with EDX analysis of interesting points attached of a) TH40Nb and b) TH5Fe25Nb.

The fatigue resistance obtained for the three alloys studied in this work is within the range reported for Ti6Al4V alloys, processed by cold pressing and vacuum sintered. It varies from 200 to 400 MPa for samples with density from 95% to 99% [63].

Nevertheless, the grain size, porosity, and high amount of TiC precipitates play an important role in degrading the mechanical properties of TH40Nb and TH5Fe25Nb alloys. Although they show high flexural strength, both their ductility and fatigue resistance are affected by these factors. Therefore, to improve the reliability and mechanical properties, performing heat treatments that help to refine the microstructure and dissolve the precipitates, would be appropriate.

It has been stated that the fatigue performance of titanium alloy depends on microstructures, which can be modified by heat treatments or thermomechanical treatments [53], [63]. Akahori et al. reported an increase in fatigue resistance for Ti-29Nb-13Ta-4.6Zr alloy, with β microstructure, from 380 to 680 MPa with an aging treatment at 450 °C for 72 h [64]. Similarly, Ti-24Nb-4Zr-7.6Sn alloy show fatigue resistance enhancing from 250 to 425 MPa after aging treatment at 400 °C for 4 h [65]. This improvement is attributed to the formation of fine α phase precipitates inside the β grains, that provide more resistance to fatigue crack initiation and hence, increase the fatigue strength [46], [63], [65]. Nevertheless, α precipitates may increase the elastic modulus, which is undesirable for biomedical Ti alloys. Thus, heat treatments should be carefully performed in order to avoid an increase of the elastic modulus. [66]

5.5. Study of TiC dissolution to improve the fatigue life in β-Ti alloys.

Mechanical properties such as Young's Modulus and fatigue resistance, are critical for Ti alloys employed in the biomedical field. Fatigue behaviour is especially important to confirm the reliability as metallic biomaterials. Titanium alloys show a wide range of mechanical properties according to the microstructures obtained, either by chemical modification, through the addition of α or β-stabilizers elements, heat treatments or thermo-mechanical processes. On the other hand, mechanical properties are also influenced by grain size, porosity, precipitates inside the matrix.

Due to the significant differences in hardness, elastic modulus, and electrochemical properties of TiC precipitates and the β-Ti matrix, the formation of titanium carbide (TiC), especially along the grain boundaries, has detrimental effects on the mechanical properties, fatigue behaviour, ductility and corrosion resistance; while Young's modulus increases [67]. Presence of this kind of carbides decreases the mechanical reliability of the alloy, because cracks could nucleate from TiC, and quickly propagate producing a premature failure, as seen in the previous section (**Section Fatigue** behaviour.). This section reports on the attempts carried out to improve the microstructural features of TH5Fe25Nb alloy by heat treatments to dissolve the TiC precipitates or reduce their size in order to enhance their mechanical properties for future works.

5.5.1. Design of heat treatments and microstructure evolution.

Heat treatments (HT) were proposed based on the Ti-5Fe-25Nb-C phase diagram (**Figure 5.13**); these are summarised in **Figure 5.22**. TiC dissolution was evaluated by heating the samples up to two stability regions of the phase diagram: 1) above the β-transus, heating up to 1300 °C and 1100 °C, where β phase is expected; and, 2) below β-transus, heating up to 900 °C, where β+TiC is expected. Note that carbon content of 0.04 wt.%, in Ti5Fe25Nb alloy, modifies the β-transus temperature from 540 °C to 1075 °C.

In addition, an ageing treatment at 650 °C was conducted to dissolve the TiC precipitates from the biphasic α+β region, considering that carbon solubility is higher in the α-Ti phase than in β-Ti phase. Ageing also leads to obtain α phase precipitates which, depending on their morphology, may enhance the fatigue resistance.

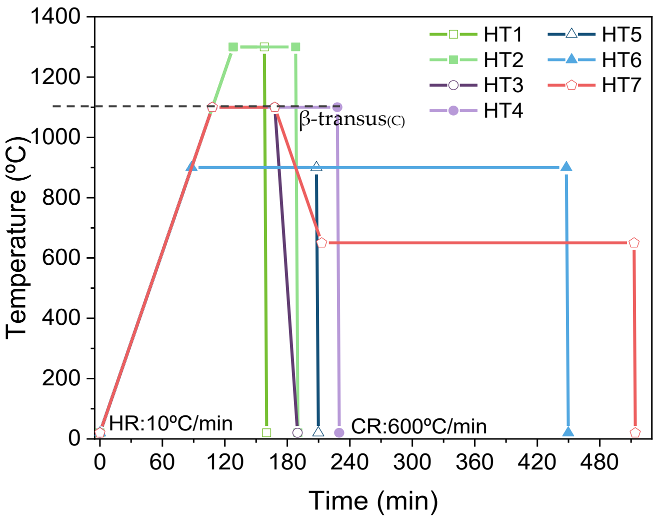

Figure 5.22. Conditions of heat treatments performed for composition TH5Fe25Nb.
HR: Heating rate.   CR: Cooling rate.

The microstructure of the as-sintered TH5Fe25Nb sample is displayed in **Figure 5.23.** Representative microstructures obtained after heat treatments are shown in **Figure 5.24, 5.25** and **5.27**. It can be seen that as-sintered TH5Fe25Nb exhibits elongated carbides, which are located both at the grain boundaries and inside the grain (**Figure 5.23**).

An entirely different carbide distribution can be seen for samples treated at 1300 °C and 1100 °C (HT1, HT2, HT3 and HT4) (**Figure 5.24**) compared to as-sintered sample,. Carbides become smaller than as-sintered samples. Furthermore, they are uniformly distributed and seem to precipitate preferentially inside the β grains instead of grain boundaries. The only significant difference HT1, HT2, HT3 and HT4 seem to be that carbide size is slightly reduced when increasing the holding time from 0.5 to 1h, for HT1 and HT2; although this effect does not happen from 1 to 2 h, for HT3 and HT4.

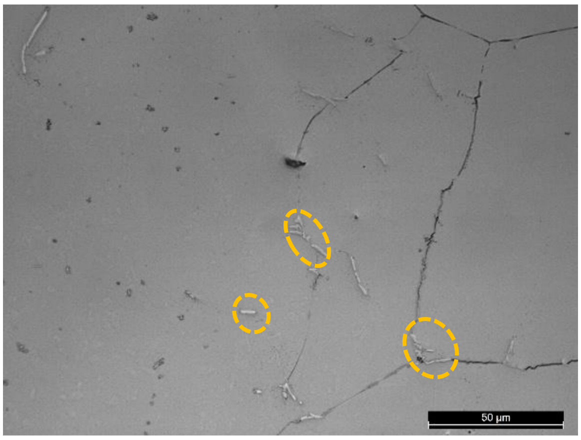

Figure 5.23. Optical microscopy images of as-sintered TH5Fe25Nb alloy. Circles indicate TiC precipitates.

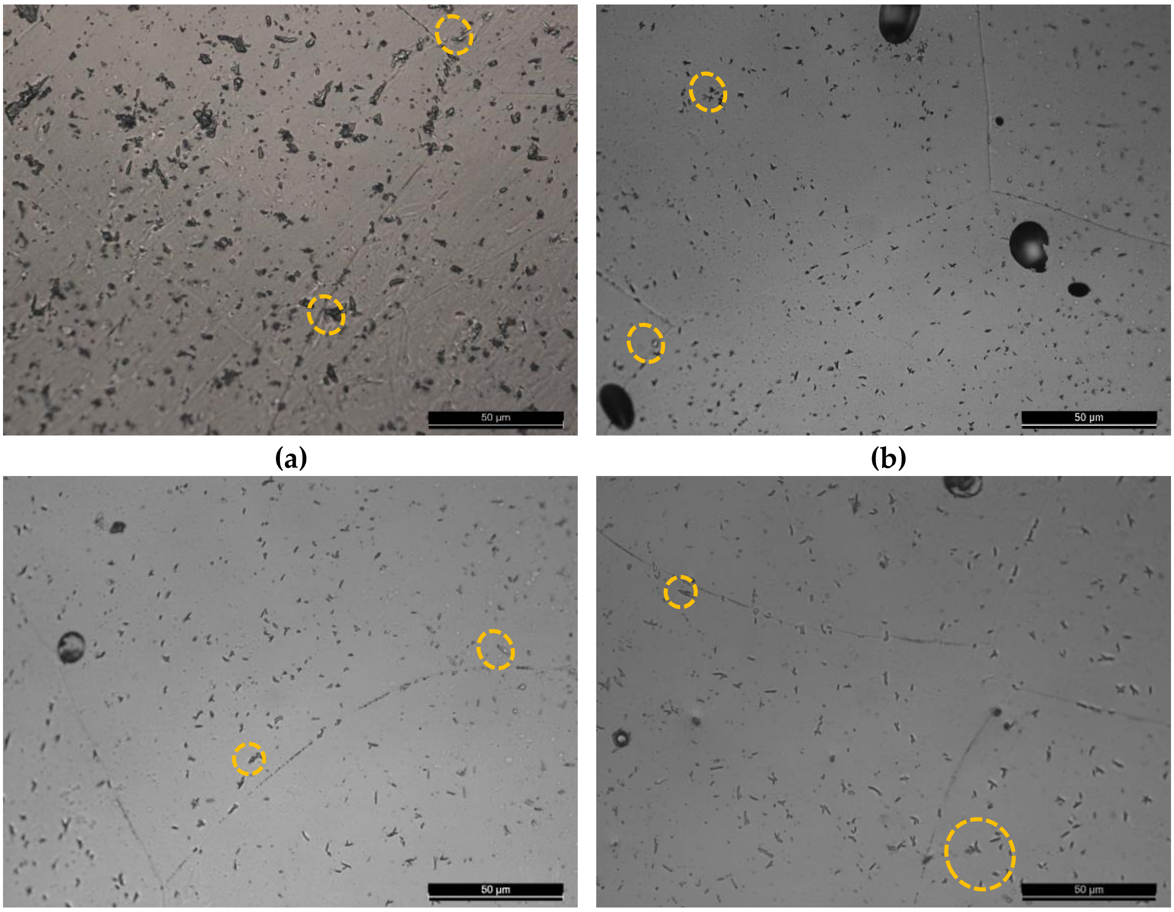

(a) (b)

(c) (d)

Figure 5.24. Optical microscopy images of representative microstructures for TH5Fe25Nb alloy with different treatments conducted above beta transus. a) HT1 (1300 °C-0.5 h); b) HT2 (1300 °C-1 h); c) HT3 (1100 °C-1h); d) HT4 (1100 °C-2 h. Circles indicate TiC precipitates.

The phase diagram of Ti5Fe25Nb-C (**Figure 5.13**) indicates that carbon solubility in the β phase increases as temperature increases, reaching a maximum of 0.046 wt.% and 0.1wt.% at 1100 °C and 1300 °C, respectively. These contents are higher than the total carbon content measured in as-sintered TH5Fe25Nb (0.04 wt.%, reported in **Table 5.3**). Therefore, at 1100 °C and 1300 °C, total carbon may dissolve fast in the β phase, based on the fact that it presents higher diffusivity in β than in α phase [68]. Hence, carbides are likely formed during cooling. The fact that similar microstructural features observed for HTs conducted at 1100 °C and 1300 °C (HT 1-4), could be attributed to the fact that cooling was conducted from the same stability region.

It has been reported that during the first stage of carbide precipitation, when cooling by water quenching from temperature over than β-transus, these start to form preferentially at grain boundaries, and then, with some delay, smaller carbides are formed inside the grain [68], [69]. However, this is not precisely the case in this study since the carbides preferentially precipitate in the interior of the grain. It is possible that the high cooling rate (600 °C/min), as well as the small samples size used for HTs 1-4, may produce a freezing-like effect of the microstructure with the carbides dissolved in β phase, hindering the nucleation at grain boundaries.

When the treatment temperature decreases to 900 °C (HT5 and HT6) (**Figure 5.25**), segmented carbides can be seen, which preferably precipitate along the grain boundaries. Images suggest that carbides obtained with HT6 are smaller than those with HT5. Thus, it appears that longer holding time reduces the carbide size. A carbide size reduction might positively affect fatigue properties since the contact area between grain boundary and precipitates is reduced.

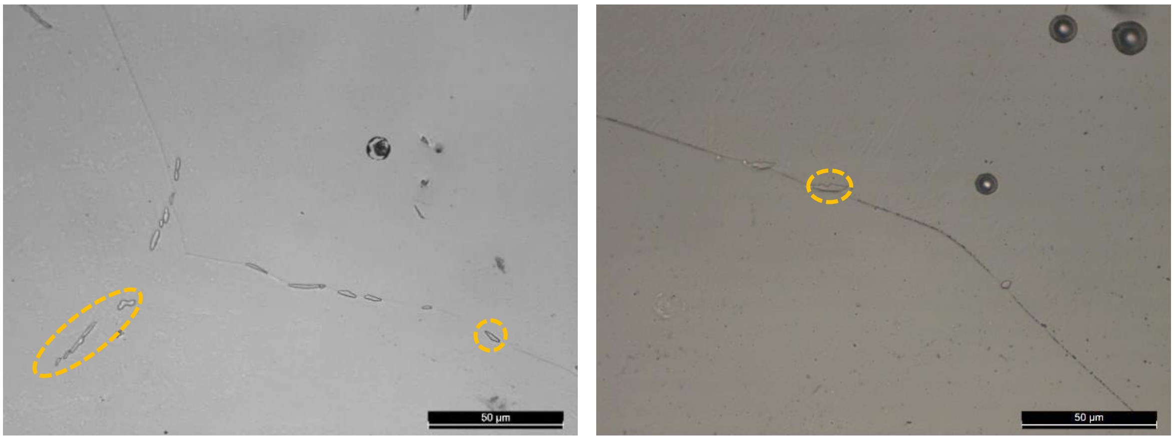

(a) **(b)**

Figure 5.25. Optical microscopy images of representative microstructures for TH5Fe25Nb alloy with heat treatments performed below beta transus at 900 °C. a) HT5 (900 °C-2 h); b) HT6 (900 °C-6 h). Circles indicate TiC precipitates.

Luo et al. [69] propose an anomalous fast dissolution process via short-circuit diffusion in the high-temperature range; when the temperature is below β-transus but above the maximum carbon solubility in (α+β) phase (about 650 °C), which is the temperature at which HT5 and HT6 was conducted, according to the phase diagrams. At the same time, α-Ti is formed since carbon enters into the α phase, stabilising it. To confirm if precipitates correspond to α-phase, EDX mapping was performed to evaluate the element distribution around precipitates (**Figure 5.26**) for samples with HT6. Mapping reveals high contrast for carbon and low contrast for both β-stabiliser elements (Fe and Nb). This suggests that precipitates, in fact, correspond to carbides and not to α phase. Based on previous studies of similar heat treatments conducted in Ti-22Nb alloy, if precipitates were of α phase, some small Nb amount would be detected inside them; since, at this temperature, the Nb diffusivity is too low to move out of α phase. [70]. Hence, it can be concluded that, despite what has been previously reported in the literature, no alpha phase precipitates were found, and carbides precipitate preferentially in grain boundaries and also inside the grain for HT5 and HT6.

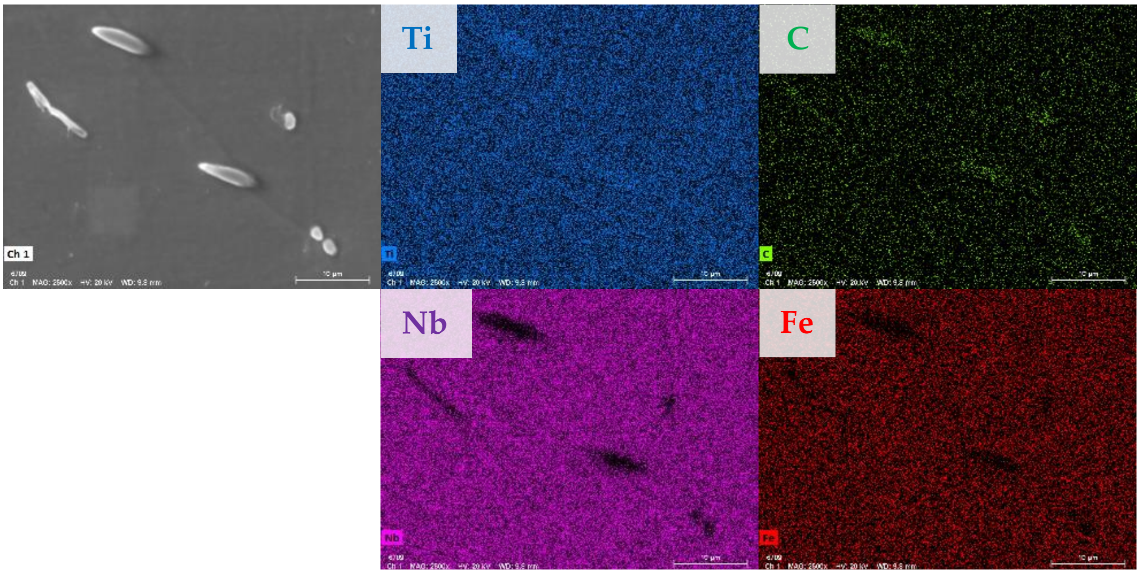

Figure 5.26. EDX mapping of TH5Fe25Nb treated with HT6 showing precipitates located at the grain boundary.

Aged TH5Fe25Nb sample with HT7 (**Figure 5.27**) shows a thin plate-like secondary phase corresponding to the α phase, that is located both along grain boundaries and inside the grain. Carbides seem smaller than those observed for as-sintered sample. It can be seen that α phase grows from carbide precipitates, which act as α nucleation sites. This could also contribute to carbide size reduction. EDX mapping (**Figure 5.28**) shows diffused carbon contrast around the carbides, which supports the hypothesis that carbon migrates from carbide particles to the matrix, forming the flake-like α-phase enriched in carbon.

According to the phase diagram (**Figure 5.13**) and previous studies [68], [70], ageing at low temperature causes the precipitation of α phase, which is consistent with the microstructures examined. This could have two advantages. First, carbides can be dissolved by α phase stabilisation and then, these α precipitates can enhance the mechanical properties.

From these results, it would be interesting to evaluate the fatigue behaviour of samples treated with HT6 and HT7. Samples treated with HT6, present a large fraction of carbides dissolved, and those that remain are much smaller than the as-sintered sample.

Samples treated with HT7, exhibit uniformly distributed fine α phase precipitates, nucleating from the carbides; which implies a hardening effect.

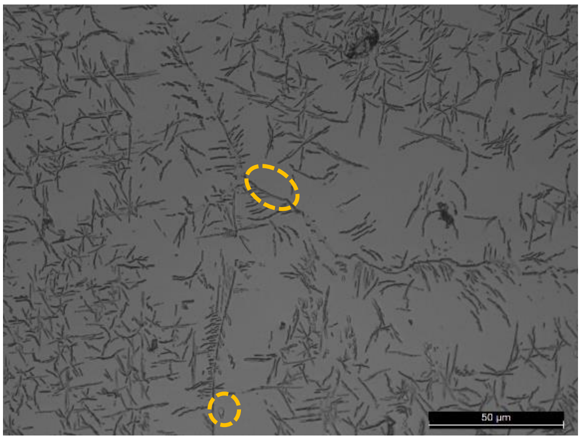

Figure 5.27. Optical microscopy images of representative microstructures for TH5Fe25Nb alloy after aging treatment (HT7: 1100 °C-1 h + 650 °C-5 h). Circles indicate TiC precipitates.

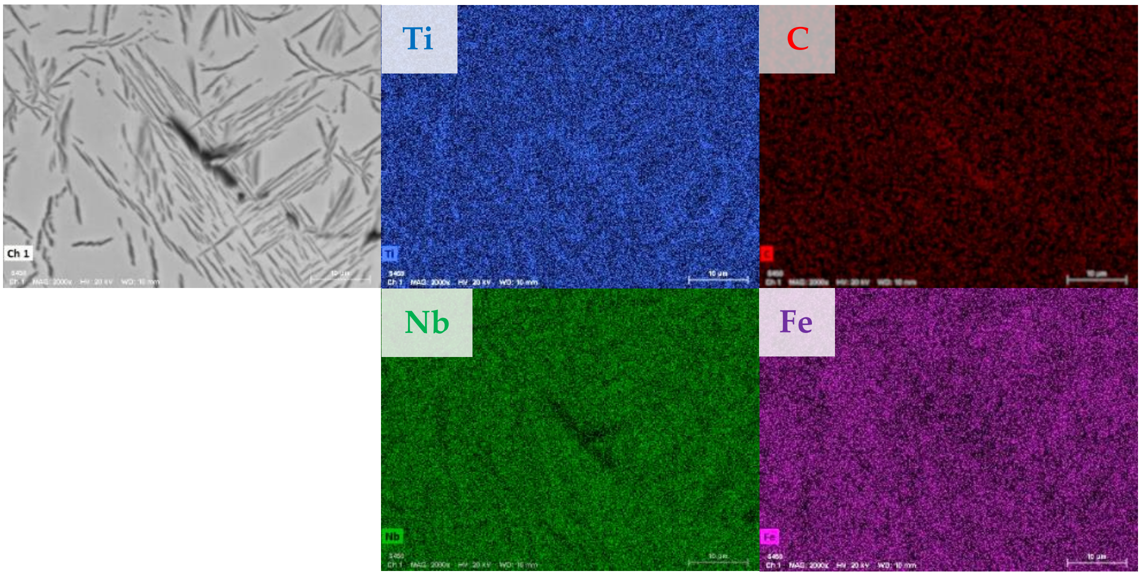

Figure 5.28. EDX mapping of TH5Fe25Nb treated with HT7 showing carbide precipitates acting as alpha nucleation sites.

These treatments can be an alternative to improve the mechanical properties of TH5Fe25Nb. Nevertheless, these microstructures must be further analysed to better understand the carbide dissolution mechanism and identify other possible brittle phases like α', α'' or ω, usually formed by fast cooling.

5.6. Evaluation of biological response.

This section summarises the biocompatible behaviour of the three compositions (TH12Nb, TH40Nb and TH5Fe25Nb), sintered with sintering cycle cycle 4.

These materials were analysed to determine the biocompatibility and cellular viability of each substrate to validate them as an alternative biomaterial, prior to proceeding with the subsequent stages of surface modification. It is considered that the results obtained or observed trends, can be extrapolated for sintered samples with C5 since there are no significant microstructural changes between C4 and C5 conditions.

For this characterisation, cell adhesion, cell morphology, cellular number of preosteoblasts and mineralisation was assessed and discussed.

5.6.1. Cell adhesion, morphology and proliferation.

Figure 5.29 presents the representative SEM images of the evaluation of adhesion and morphology of MC3T3-E1 cells on surfaces of the three Ti alloys groups for periods of 4, 24, 48 and 72 h.

Overall, it can be seen that cells number tend to increase with time for all evaluated compositions. Moreover, cells show a normal morphology, spread through well-developed lamellipodia and filopodia, which may favour the cellular process. Filopodia and lamellipodia are thin membrane protrusions located at the cells ends, which act as an antenna for cells inspecting the surrounding environment. Furthermore, these membranes are enriched in actin protein. Hence, they are involved in several cellular processes like wound healing, adhesion to extracellular matrix, cell motility, cell division and cytokinesis, cell signalling, as well as, cell junctions maintenance and cell shape. [71]–[73].

At 4 h of contact, groups show a different number of attached cells. Groups TH5Fe25Nb and TH40Nb present a higher number of cells attached, showing good dispersion; while TH12Nb shows isolated cells clusters. At 24 h, a remarkable increase of cells number is observed, especially for TH12Nb alloy.

For other periods (48 and 72 h), in general, cells show a similar aspect, rounded or ovoid morphology with cytoplasmatic extensions in all groups. Also, images suggest an increase in cell proliferation compared to initial periods (4 and 24 h). After 72 hours, the adhered cells can be seen in detail (indicated with arrows in **Figure 5.29**). Cell adhesion and spreading depend on the topographic features. It is generally considered that longer cell morphology, showing wide filopodia and large lamellipodia, is preferred to enhance/promote osteoblastic cell maturation [74]. In three substrates, cells show a flattened appearance and are communicated by cytoplasmic extensions. Despite the roughness differences between the surfaces, similar cell adhesion was observed.

Complimentarily, the cell attachment, morphology and cell quantification on each composition group, after cell culture for 4, 24, 48, and 72 h were also analysed by confocal microscopy (**Figure 5.30**). This technique allows to evaluate the coverage area of the cells with the cytoplasmatic membrane (marked with red) and quantify/recognise the living cells, after culture time, by the cell nuclei presence (marked with blue). Note that for this analysis, cells number seeded onto the substrates was increased to 200 cell/mm^2.

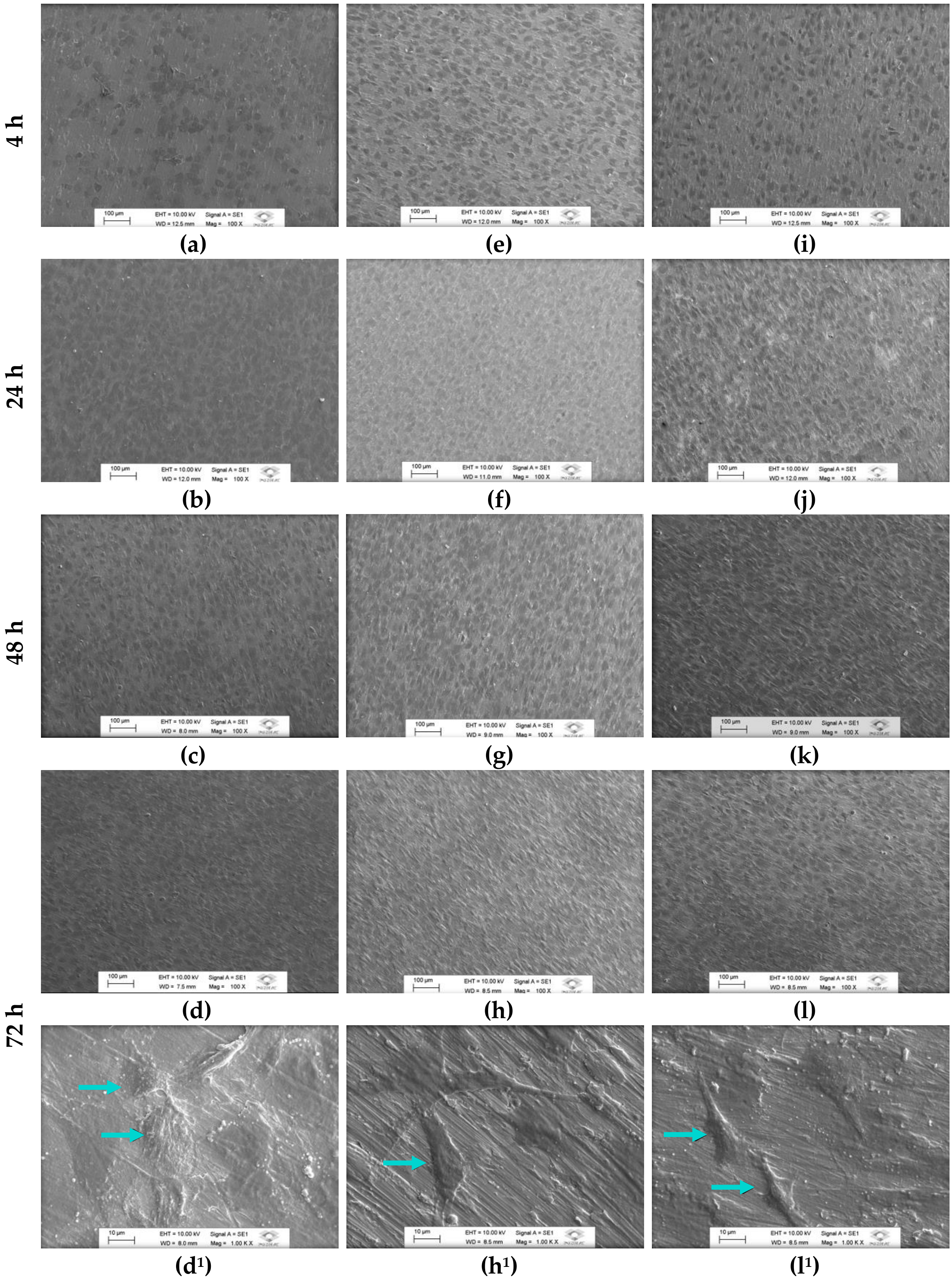

Figure 5.29. Morphology of MC3T3-E1 cells on surfaces after 4, 24, 48 and 72 h of adhesion for all groups: (a, b, c, d) TH12Nb; (d, e, f,g) TH40Nb and (I, j, k, l) TH5Fe25Nb.
[1] Detail at higher magnification showing adhered cells (indicated with arrows)

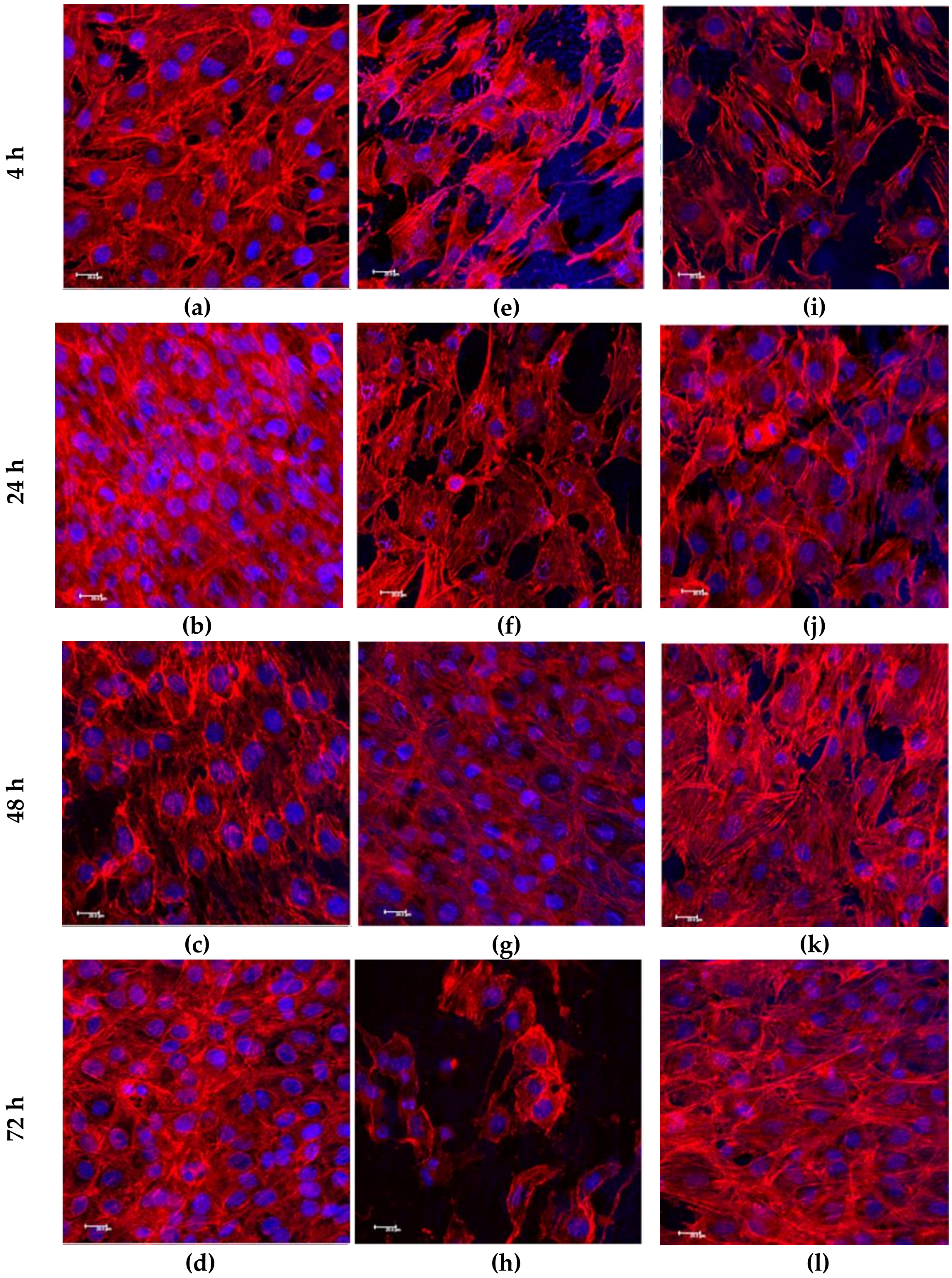

Figure 5.30. Confocal images showing the cellular morphological changes and proliferation at 4, 24, 48 and 72 h for all compositions: (a, b, c, d) TH12Nb; (d, e, f,g) TH40Nb and (I, j, k, l) TH5Fe25Nb. Scale bar: 20 μm.

Figure 5.30 suggest that cell proliferation occurs for all composition. Proliferation can be qualitatively evaluated by the number of blue labelled cell nuclei. The red actin filaments show the cellular morphology, which was initially spread and flat, with strong stress fibres. Later, the cells became less flat, with fewer and thinner actin filaments, suggestive of a cuboid phase. Cuboidal morphology is a feature of differentiated osteoblasts. [75]–[77]

Cell quantification is shown in **Figure 5.31**. Overall, it can be seen that MC3T3 preosteoblasts increase in number with time in all groups, except in TH40Nb composition. For this composition (TH40Nb), there is and increase between 4 to 48 h, but a significant decrease at 72 h is observed, showing 40% fewer cells.

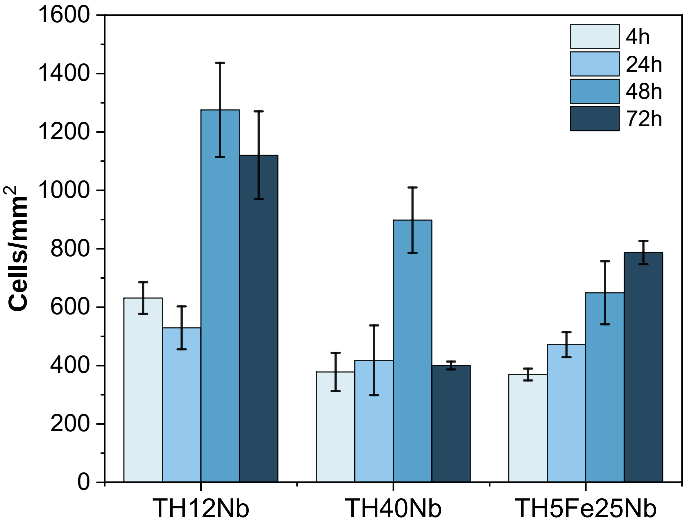

Figure 5.31. Average of cell quantification per area (cells/mm^2) on all Ti alloys after 4, 24, 48 and 72 h.

In contrast, the composition containing 12 wt.% of Nb presents the highest number of cells, followed by TH5Fe25Nb, and finally TH40Nb. It has been reported that cell growth is highly influenced by sample roughness or topography. It is considered greater roughness values favour cell adhesion and proliferation [78], [79]. In general, higher roughness can involve an increase of bonding strength between the bone and implant; which would improve the implant fixation [80].

For these compositions, the roughness effect is no evident. Samples with higher proliferation (TH12Nb and TH5Fe25Nb) show similar roughness values (Ra: 0.12 μm), whereas TH40Nb with the lowest proliferation exhibits higher roughness (Ra: 0.25 μm). Differences in roughness values can be attributed to different mechanical features for each alloy, even though the surface preparation was conducted following the same procedure for all samples.

According to what is reported in the bibliography, Nb is an element with high biocompatibility; it is not expected that an alloy rich in Nb, such as TH40Nb, presents a lower preosteoblasts proliferation. Results show good biocompatibility for all tested alloys, which is comparable to that of Ti6Al4V. Better cell behaviour was observed when in contact with TH12Nb, followed by TH5Fe25Nb.

5.6.2. Mineralisation assay.

The mineralization process was evaluated by determining the Ca^{2+} levels of the supernatants, obtained after 21 days of cell culture, onto the Ti alloys surfaces, through absorbance measurements.

Figure 5.32a shows the calcium deposition, illustrated by alizarin red S (ARS) on the surfaces after 21 days of culture. Alizarin red S staining is a standard method to determine calcium deposition of osteoblastic cell culture in vitro [81]–[83]. ARS dyes the mineralised zones in the surface of dark red colour, denoting calcium specific mineralised zones. It can be seen that the degree of mineralisation was non-uniform, especially for TH40Nb and TH5Fe25Nb, since brighter zones like motes, were found. However, most samples surface was red stained. Besides, it seems that the red colour is more intense for TH12Nb, indicating higher mineralisation for this composition.

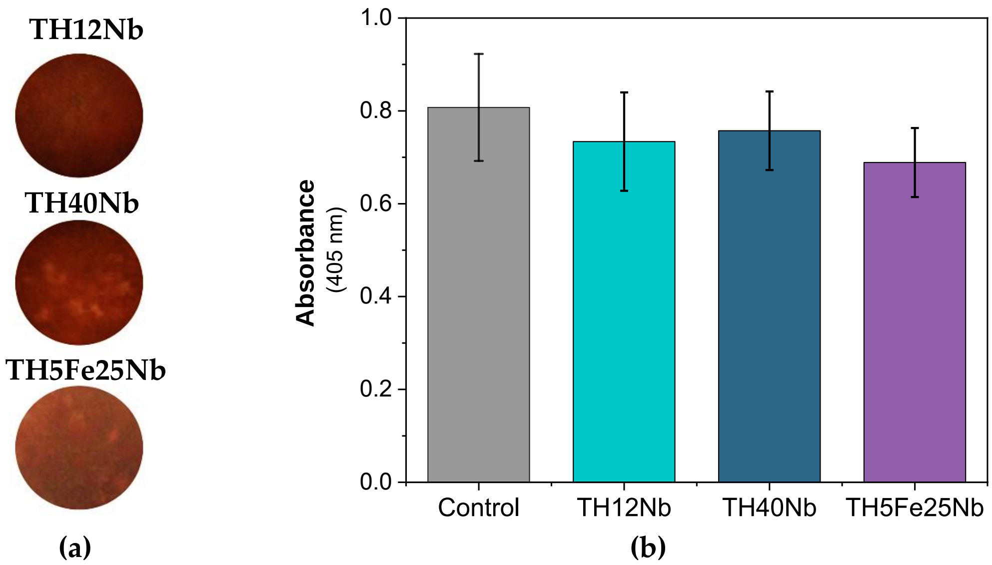

Figure 5.32. Mineralisation results of all Ti alloys, after MCT3-E1 osteoblasts cell culture for 21 days. a) Images of calcium deposited (Optical microscopy), and b) Amount of mineralised calcium deposited on the surface.

Figure 5.32b displays the absorbance measurement related to mineralisation quantification. Commercial Ti-6Al-4V alloy was used as a control sample. After 21 days, the cells cultured onto Ti surfaces showed a large calcium amount. The three alloys, developed in this work, exhibit a similar deposited mineral amount, but slightly lower than the control. Nevertheless, these results are promising, since the evaluated alloys show mineralisation similar to the control sample, but are composed of toxic-free elements, related to diseases or adverse effects harmful to the body.

Moreover, the results obtained are similar, even superior, compared to other β- type Ti alloys reported in the bibliography [84], [85]. All tested samples evidence extracellular matrix mineralisation after 21 days. Also, the novel Ti alloys, show good cell proliferation and biocompatibility. All this suggests that these surfaces could be a suitable implant material that helps accelerate the osteogenic differentiation of MC3T3-E1 cells. Hence, these substrates are considered appropriate for future modification steps.

5.7. Partial conclusions.

From the results shown in this chapter, the following conclusions can be drawn:

1. Heating rate reduction from 5 °C/min to 2 °C/min, between 450 and 650 °C, where the main dehydrogenation reaction from δ-TiH_x to β-Ti takes place, ensures the highest hydride decomposition. Therefore, using a sintering cycle (C3) with reduced heating rate and controlled dehydrogenation, seems to enhance the sample densification, compared to samples sintered at the same sintering temperature (cycles C1 and C2).

2. Sample TH12Nb shows an (α+β) lamellar microstructure for all sintering cycles, whereas TH40Nb and TH5Fe25Nb show a predominantly β-phase microstructure. The most homogeneous microstructures were obtained with sintering cycles C4 and C5 (higher sintering temperatures).

3. **Fe improves the Nb diffusion**, and final homogeneous microstructure is obtained for TH5Fe25Nb alloy. Final porosity is determined by the particle size of Fe employed. Coarse Fe particle size (Fe-1) causes larger closed pores, while finer Fe (Fe-2) enhances the sinterability, decreasing amount and size of pores.

4. Nb diffusion is very susceptible to the **particle size** distribution of the starting powder. In either case, high temperatures are required to promote adequate diffusion. Employing fine Nb powder (Nb-1), and at least 1250 °C, is required; while with coarser Nb (Nb-2), it is necessary to increase the sintering temperature to 1450 °C to achieve a homogeneous microstructure.

5. Nb addition leads to a decrease of the carbon solubility limit in the Ti matrix. Hence, **increasing Nb content promotes carbides precipitation**.

6. **Young's modulus values** achieved for TH40Nb and TH5Fe25Nb (73±12 GPa and 95±14 GPa, respectively) are lower compared to TH12Nb (104±17 GPa) and other typical (α+β) alloys, but higher than that of the cortical bone; which reach about 10-30 GPa.

7. **Fatigue resistance** is lower for samples with higher Nb content, reaching values of 368 MPa, 321 MPa and 338 MPa at $2x10^6$ cycles for TH12Nb, TH5Fe25Nb and TH40Nb, respectively. Moreover, yield strength, elongation/ductility and mechanical reliability are also lower for alloys with higher Nb amount (TH40Nb and TH5Fe25Nb). Fractography analysis revealed that carbide precipitates, along with porosity, are the main factors contributing to a decrease in mechanical properties.

8. **Heat treatments (HT)** conducted at 1300 °C and 1100 °C (from the β stability field) show smaller precipitates, uniformly distributed inside the β-grains. HTs performed at 900 °C (from the β+TiC stability field) cause a carbide dissolution via short circuit diffusion, significantly reducing the amount of carbides in the matrix.

Ageing treatment favours the formation of thin plate-like α-phase precipitates, where carbides act as α-nucleation sites. This reduces the size of carbides and could involve improvements in the fatigue behaviour of TH5Fe25Nb alloy.

9. Regarding **biological characterisation**, after 72 h of culture, all alloys show signs of good cell adhesion and cuboidal morphology typical of differentiated osteoblasts. Moreover, overall, the three alloys present good cell proliferation and present satisfactory mineralisation results. All this suggests that surfaces could be a good implant material that helps accelerate the osteogenic differentiation of MC3T3-E1 cells.

References.

[1] H. Liu, P. He, J. C. Feng, and J. Cao, "Kinetic study on nonisothermal dehydrogenation of TiH2 powders," *Int. J. Hydrogen Energy*, vol. 34, pp. 3018–3025, 2009.

[2] M. Ma *et al.*, "Phase transformations of titanium hydride in thermal desorption process with different heating rates," *Int. J. Hydrogen Energy*, vol. 40, pp. 8926–8934, 2015.

[3] N. Peillon, J. B. Fruhauf, S. Gourdet, J. Feraille, S. Saunier, and C. Desrayaud, "Effect of TiH2 in the preparation of MMC Ti based with TiC reinforcement," *J. Alloys Compd.*, vol. 619, pp. 157–164, 2015.

[4] H. R. Z. Sandim, B. V. Morante, and P. A. Suzuki, "Kinetics of thermal decomposition of titanium hydride powder using in situ High-temperature X-ray Diffraction (HTXRD)," *Mater. Res.*, vol. 8, no. 3, pp. 293–297, 2005.

[5] V. Bhosle, E. G. Baburaj, M. Miranova, and K. Salama, "Dehydrogenation of TiH2," *Mater. Sci. Eng. A*, vol. 356, no. 1–2, pp. 190–199, 2003.

[6] R. Karre, B. Kumar, A. Rajendran, and J. Nivedhitha, "Comparative study on Ti-Nb binary alloys fabricated through spark plasma sintering and conventional P / M routes for biomedical application," *Mater. Sci. Eng. C*, vol. 94, pp. 619–627, 2019.

[7] D. Zhao *et al.*, "Microstructure and mechanical behavior of metal injection molded Ti-Nb binary alloys as biomedical material," *J. Mech. Behav. Biomed. Mater.*, vol. 28, pp. 171–182, 2013.

[8] K. A. Nazari, A. Nouri, and T. Hilditch, "Mechanical properties and microstructure of powder metallurgy Ti – xNb – yMo alloys for implant materials," *JMADE*, vol. 88, pp. 1164–1174, 2015.

[9] R. Karre *et al.*, "Comparative study on Ti-Nb binary alloys fabricated through spark plasma sintering and conventional P/M routes for biomedical application," *Mater. Sci. Eng. C*, vol. 94, pp. 619–627, 2019.

[10] D. Zhao, K. Chang, T. Ebel, H. Nie, R. Willumeit, and F. Pyczak, "Sintering behavior and mechanical properties of a metal injection molded Ti-Nb binary alloys as biomaterial," *J. Alloys Compd.*, vol. 640, pp. 393–400, 2015.

[11] Y. Liu, T. Pan, L. Zhang, D. Yu, and Y. Ge, "Kinetic modeling of diffusion mobilities in bcc Ti-Nb alloys," *J. Alloys Compd.*, vol. 476, pp. 429–435, 2009.

[12] P. Soma and A. Paul, "Interdiffusion in Nb-Mo , Nb-Ti and Nb-Zr systems," *Defect Diffus. Forum*, vol. 323–325, pp. 491–496, 2012.

[13] L. Zhu *et al.*, "Measurement of interdiffusion and impurity diffusion coefficients in the bcc phase of the Ti – X (X 5 Cr , Hf , Mo , Nb , V , Zr) binary systems using diffusion multiples," *J. Mater. Sci.*, vol. 52, no. 6, pp. 3255–3268, 2017.

[14] K. S. Narasimhan and M. O. H. Amuda, "Powder Characterization," *Ref. Modul. Mater. Sci. Mater. Eng.*, 2017.

[15] H. Nakajima and M. Koiwa, "Diffusion in Titanium," *ISIJ Int.*, vol. 31, no. 8, pp. 757–

766, 1991.

[16] W. Wei, Y. Liu, K. Zhou, and B. Huang, “Effect of Fe addition on sintering behaviour of titanium powder,” *Powder Metall.*, vol. 46, no. 3, pp. 246–250, 2003.

[17] O. M. Ivasishin, V. Bondarchuk, and D. G. Savvakin, “Diffusion during Powder Metallurgy Synthesis of Titanium Alloys,” *Defect Diffus. Forum*, vol. 277, pp. 177–185, 2008.

[18] F. Thümmler and W. Thomma, “The sintering process,” *Metall. Rev.*, vol. 115, pp. 69–108, 1967.

[19] A. Carman, L. C. Zhang, O. M. Ivasishin, D. G. Savvakin, M. V Matviychuk, and E. V Pereloma, “Role of alloying elements in microstructure evolution and alloying elements behaviour during sintering of a near- ◎ titanium alloy,” *Mater. Sci. Eng. A*, vol. 528, no. 3, pp. 1686–1693, 2011.

[20] D. G. Savvakin, A. Carman, O. M. Ivasishin, M. V. Matviychuk, A. A. Gazder, and E. V. Pereloma, “Effect of iron content on sintering behavior of Ti-V-Fe-Al near-β titanium alloy,” *Metall. Mater. Trans. A Phys. Metall. Mater. Sci.*, vol. 43, no. 2, pp. 716–723, 2012.

[21] P. G. Esteban, L. Bolzoni, E. Ruiz-Navas, and E. Gordo, “PM processing and characterisation of Ti – 7Fe low-cost titanium alloys-,” *Powder Metall.*, vol. 53, no. 3, pp. 242–252, 2011.

[22] G. C. Kuczynski, “Model Experiments and the Theory of Sintering,” in *Sintering Key Papers*, S. Shigeyuki and Y. Moriyoshi, Eds. Londond, 1990, pp. 502–509.

[23] R. F. Peart, “Effect of Pressure on the Diffusion of Fe in Ti and Ti+10%Fe,” *Phys. Status Solidi*, vol. 20, pp. 545–550, 1967.

[24] P. Klugkist and C. Herzig, “Tracer diffusion of titanium in α-iron,” *Phys. Status Solidi*, vol. 148, pp. 413–421, 1995.

[25] S. Eddine, M. Letenneur, C. Alex, and V. Brailovski, “Influence of particle morphology and size distribution on the powder flowability and laser powder bed fusion manufacturability of Ti-6Al-4V alloy,” *Addit. Manuf.*, vol. 31, no. August 2019, p. 100929, 2020.

[26] D. Zhao, T. Ebel, M. Yan, and M. Qian, “Trace Carbon in Biomedical Beta-Titanium Alloys : Recent Progress,” *J. Mater.*, vol. 67, no. 10, pp. 2236–2243, 2015.

[27] W. Weng, A. Biesiekierski, Y. Li, and C. Wen, “Effects of selected metallic and interstitial elements on the microstructure and mechanical properties of beta titanium alloys for orthopedic applications,” *Materialia*, vol. 6, 2019.

[28] Z. Q. Chen, Y. G. Li, and M. H. Loretto, “Role of alloying elements in microstructures of beta titanium alloys with carbon additions.,” *Mater. Sci. Technol.*, vol. 19, pp. 1391–1398, 2003.

[29] M. Kaur and K. Singh, “Review on titanium and titanium based alloys as biomaterials for orthopaedic applications,” *Mater. Sci. Eng. C*, vol. 102, pp. 844–862, 2019.

[30] J. R. Severino Martins and C. R. Grandini, “Structural characterization of Ti-15Mo alloy used as biomaterial by Rietveld method Rietveld method,” *J. Appl. Phys.*, vol.

111, pp. 083535-(1-8), 2012.

[31] M. Wen, C. Wen, P. Hodgson, and Y. Li, "Fabrication of Ti-Nb-Ag alloy via powder metallurgy for biomedical applications," *Mater. Des.*, vol. 56, pp. 629–634, 2014.

[32] V. A. Lubarda, "On the effective lattice parameter of binary alloys," *Mech. Mater.*, vol. 35, no. 1–2, pp. 53–68, 2003.

[33] M. Komarasamy *et al.*, "A novel method to enhance CSL fraction, tensile properties and work hardening in complex concentrated alloys-Lattice distortion effect," *Mater. Sci. Eng. A*, vol. 736, pp. 383–391, 2018.

[34] Y. Y. Li, L. M. Zou, C. Yang, Y. H. Li, and L. J. Li, "Ultrafine-grained Ti-based composites with high strength and low modulus fabricated by spark plasma sintering," *Mater. Sci. Eng. A*, vol. 560, pp. 857–861, 2013.

[35] É. S. Najar Lopes, C. A. Fernandes Salvador, D. R. Andrade, A. Cremasco, K. Niitsu Campo, and R. Caram, "Microstructure, Mechanical Properties, and Electrochemical Behavior of Ti-Nb-Fe Alloys Applied as Biomaterials," *Metall. Mater. Trans. A*, vol. 47A, pp. 3213–3226, 2016.

[36] J. Oh *et al.*, "Grain Refinement and Hardness Increase of Titanium via Trace Element Addition," vol. 51, no. 11, pp. 2009–2012, 2012.

[37] I. Sen, S. Tamirisakandala, D. B. Miracle, and U. Ramamurty, "Microstructural effects on the mechanical behavior of B-modified Ti – 6Al – 4V alloys," vol. 55, pp. 4983–4993, 2007.

[38] H. Hsu, S. Hsu, and S. Wu, "Structure and mechanical properties of as-cast Ti – 5Nb – x Fe alloys," *Mater. Charact.*, vol. 61, no. 9, pp. 851–858, 2010.

[39] P. G. Esteban, L. Bolzoni, E. M. Ruiz-Navas, and E. Gordo, "PM processing and characterisation of Ti-7Fe low cost titanium alloys," *Powder Metall.*, vol. 54, no. 3, pp. 242–252, 2011.

[40] N. Popova *et al.*, "Grain size effect on yield strength of titanium alloy implanted with aluminum ions Grain Size Effect o n Yield Strength o f Titanium Alloy Implanted with Aluminum Ions," vol. 050002, no. January 2016, 2018.

[41] B. Zhang *et al.*, "Enhanced mechanical properties in β-Ti alloy aged from recrystallized ultrafine β grains," *Mater. Des.*, vol. 195, 2020.

[42] E. Baril, L. P. Lefebvre, and Y. Thomas, "Interstitial elements in titanium powder metallurgy: sources and control," *Powder Metall.*, vol. 54, no. 3, pp. 183–187, 2011.

[43] R. Prakash Kolli and A. Devaraj, "A Review of Metastable Beta Titanium Alloys," *Metals (Basel).*, vol. 506, no. 8, 2018.

[44] S. Guo, Q. Meng, X. Zhao, Q. Wei, and H. Xu, "Design and fabrication of a metastable β-type titanium alloy with ultralow elastic modulus and high strength.," *Sci. Rep.*, vol. 5, 2015.

[45] M. Niinomi, Y. Liu, M. Nakai, H. Liu, and H. Li, "Biomedical titanium alloys with Young ′ s moduli close to that of cortical bone," *Rege*, no. March, pp. 173–185, 2016.

[46] M. T. Mohammed, Z. a Khan, and A. N. Siddiquee, "Beta Titanium Alloys : The Lowest Elastic Modulus for Biomedical Applications : A Review," *Int. J. Chem. Nucl.*

Mater. Metall. Eng., vol. 8, no. 8, pp. 726–731, 2014.

[47] K. S. Krishnan and R. S. Mishra, “Titanium Alloys,” in *Metallurgy and Design of Alloys with Hierarchical Microstructures*, K. S. Krishnan and R. S. Mishra, Eds. E, 2017, pp. 177–288.

[48] S. M. Hosnie, M. Yahaya, N. A. Haris, and I. Todd, “Fabrication of porous β-Type Ti-40Nb alloys incorporated with TiH2 via powder metallurgy processing route under reducing environment,” *J. Mech. Eng.*, vol. 2, no. 2, pp. 99–112, 2017.

[49] S. Abdi, M. S. Khoshkhoo, O. Shuleshova, M. Bönisch, and M. Calin, “Effect of Nb addition on microstructure evolution and nanomechanical properties of a glass-forming Ti-Zr-Si alloy,” *Intermetallics*, vol. 46, pp. 156–163, 2014.

[50] J. M. Cordeiro and V. A. R. Barao, “Is there scientific evidence favoring the substitution of commercially pure titanium with titanium alloys for the manufacture of dental implants?,” *Mater. Sci. Eng. C*, vol. 71, pp. 1201–1215, 2016.

[51] J. M. Chaves, O. Florêncio, P. S. Silva, P. W. B. Marques, and C. R. M. Afonso, “Influence of phase transformations on dynamical elastic modulus and anelasticity of beta Ti-Nb-Fe alloys for biomedical applications,” *J. Mech. Behav. Biomed. Mater.*, vol. 46, pp. 184–196, 2015.

[52] C. D. Rabadia *et al.*, “High-strength β stabilized Ti-Nb-Fe-Cr alloys with large plasticity.,” *Mater. Sci. Eng. A*, vol. 732, pp. 368–377, 2018.

[53] M. Niinomi, “Fatigue performance and cyto-toxicity of low rigidity titanium alloy, Ti-29Nb-13Ta-4.6Zr,” *Biomaterials*, vol. 24, pp. 2673–2683, 2003.

[54] M. Abdel-Hady Gepreel and M. Niinomi, “Biocompatibility of Ti-alloys for long-term implantation,” *J. Mech. Behav. Biomed. Mater.*, vol. 20, pp. 407–415, 2013.

[55] C. M. Lee, C. P. Ju, and J. H. C. Lin, “Structure-property relationship of cast Ti-Nb alloys,” *J. Oral Rehabil.*, vol. 29, pp. 314–322, 2002.

[56] A. Amigó *et al.*, “Microstructural characterisation of Ti-Nb-(Fe-Cr) alloys obtained by powder metallurgy,” *Powder Metall.*, vol. 57, no. 5, pp. 316–319, 2014.

[57] Y. Eren, A. Gökçe, F. Findik, H. Ozkan, and İ. Osman, “Mechanical properties and electrochemical behavior of porous Ti-Nb biomaterials,” *J. Mech. Behav. Biomed. Mater.*, vol. 87, pp. 59–67, 2018.

[58] F. H. Froes and H. B. Bomberger, “The Beta Titanium Alloys,” *J. Met.*, no. July, pp. 28–37, 1985.

[59] O. M. Ferri, T. Ebel, and R. Bormann, “Influence of surface quality and porosity on fatigue behaviour of Ti-6Al-4V components processed by MIM,” *Mater. Sci. Eng. A*, vol. 527, pp. 1800–1805, 2010.

[60] Y. L. Hao, M. Niinomi, D. Kuroda, K. Fukunaga, Y. L. Zhou, and R. Yang, “Aging Response of the Young’ s Modulus and Mechanical Properties of Ti-29Nb-13Ta-4 . 6Zr for Biomedical Applications,” *Metall. Mater. Trans. A*, vol. 34A, no. April, pp. 1007–1012, 2003.

[61] J. Belan, L. Kuchariková, E. Tillová, M. Chalupová, and D. Rozumek, “Three-Point Bending Fatigue Test of TiAl6V4 Titanium Alloy at Room Temperature,” *Adv. Mater.*

Sci. Eng., vol. 2019, 2019.

[62] K. Tokaji, M. Kamakura, Y. Ishiizumi, and N. Hasegawa, "Fatigue behaviour and fracture mechanism of a rolled AZ31 magnesium alloy," vol. 26, pp. 1217–1224, 2004.

[63] F. Cao and K. S. Ravi Chandran, "Fatigue Performance of Powder Metallurgy (PM) Ti-6Al-4V Alloy: A Critical Analysis of Current Fatigue Data and Metallurgical Approaches for Improving Fatigue Strength," *JOM*, vol. 68, no. 3, pp. 735–746, 2016.

[64] T. Akahori, M. Niinomi, H. Fukui, M. Ogawa, and H. Toda, "Improvement in fatigue characteristics of newly developed beta type titanium alloy for biomedical applications by thermo-mechanical treatments," *Mater. Sci. Eng. C*, vol. 25, no. 3, pp. 248–254, 2005.

[65] S. . Li, T. . Cui, Y. . Hao, and R. Yang, "Fatigue properties of a metastable β-type titanium alloy with reversible phase transformation," *Acta Biomater.*, vol. 4, pp. 305–317, 2008.

[66] M. Niinomi, M. Nakai, and J. Hieda, "Development of new metallic alloys for biomedical applications," *Acta Biomater.*, vol. 8, pp. 3888–3903, 2012.

[67] Y. F. Yang and D. K. Mu, "Rapid dehydrogenation of TiH 2 and its effect on formation mechanism of TiC during self-propagation high-temperature synthesis from TiH 2 – C system," vol. 249, pp. 208–211, 2013.

[68] S. Z. Zhang, M. M. Li, and R. Yang, "Mechanism and kinetics of carbide dissolution in near alpha Ti-5.6Al-4.8Sn-2Zr-1Mo-0.35Si-0.7Nd titanium alloy," *Mater. Charact.*, vol. 62, pp. 1151–1157, 2011.

[69] X. Luo, T. Ebel, F. Pyczak, W. Limberg, and Y. Lin, "Carbide evolution and its potential reduction methods in Ti-22Nb based alloys prepared by metal injection moulding," *Mater. Lett.*, vol. 193, pp. 295–298, 2017.

[70] T. Ebel, T. Beißig, S. Ebner, X. Luo, A. B. Nagaram, and D. Zhao, "Reduction of the embrittlement effect of binder contamination in MIM processing of Ti alloys," *Powder Metall.*, vol. 60, no. 3, pp. 157–166, 2017.

[71] P. K. Mattila and P. Lappalainen, "Filopodia: Molecular architecture and cellular functions," *Nat. Rev. Mol. Cell Biol.*, vol. 9, no. 6, pp. 446–454, 2008.

[72] J. Albuschies and V. Vogel, "The role of filopodia in the recognition of nanotopographies," *Sci. Rep.*, vol. 3, 2013.

[73] M. Nemethova, S. Auinger, and J. V. Small, "Building the actin cytoskeleton: Filopodia contribute to the construction of contractile bundles in the lamella," *J. Cell Biol.*, vol. 180, no. 6, pp. 1233–1244, 2008.

[74] M. Salido, J. I. Vilches, J. L. Gutiérrez, and J. Vilches, "Actin cytoskeletal organization in human osteoblasts grown on different dental titanium implant surfaces," *Histol. ans Histopathol.*, vol. 22, pp. 1355–1364, 2007.

[75] J. A. Gallagher, R. Gundle, and J. N. Beresford, "Isolation and Culture of Bone-Forming Cells (Osteoblasts) from Human Bone," in *Methods in Molecular Medicine Human Cell Culture Protocols*, G. . Jones, Ed. New Jersey: Humana Press Inc, 2003, pp. 233–262.

[76] R. Florencio-Silva, G. Rodrigues da Silva, E. Sasso-Cerri, M. Simoes, and P. Cerri, "Biology of Bone Tissue: Structure, fuction, and factors that influence bone cells.," *Biomed Res. Int.*, vol. 2015, 2015.

[77] A. Rutkovskiy, K.-O. Stensløkken, and I. J. Vaage, "Osteoblast Differentiation at a Glance," *Med. Sci. Monit. Basic Res.*, vol. 22, pp. 95–106, 2016.

[78] A. Cimpean *et al.*, "Osteoblast cell behavior on the new beta-type Ti – 25Ta – 25Nb alloy," *Mater. Sci. Eng. C*, vol. 32, no. 6, pp. 1554–1563, 2012.

[79] G. Kara and G. Purcek, "Mechanical properties and cell proliferation response of borided biomedical titanium alloys with different crystalline structures," *Surf. Coat. Technol.*, vol. 397, 2020.

[80] J. Xu *et al.*, "Potential Use of Porous Titanium-Niobium Alloy in Orthopedic Implants: Preparation and Experimental Study of Its Biocompatibility In Vitro," *PLoS One*, vol. 8, no. 11, 2013.

[81] L. R. Chaudhary, A. M. Hofmeister, and K. A. Hruska, "Differential growth factor control of bone formation through osteoprogenitor differentiation," *Bone*, vol. 34, no. 3, pp. 402–411, 2004.

[82] C. A. Gregory, W. G. Gunn, A. Peister, and D. J. Prockop, "An Alizarin red-based assay of mineralization by adherent cells in culture: Comparison with cetylpyridinium chloride extraction," *Anal. Biochem.*, vol. 329, no. 1, pp. 77–84, 2004.

[83] S. An, Y. Gao, J. Ling, X. Wei, and Y. Xiao, "Calcium ions promote osteogenic differentiation and mineralization of human dental pulp cells: Implications for pulp capping materials," *J. Mater. Sci. Mater. Med.*, vol. 23, no. 3, pp. 789–795, 2012.

[84] R. Ion *et al.*, "In vitro bio-functional performances of the novel superelastic beta-type Ti-23Nb-0.7Ta-2Zr-0.5N alloy," *Mater. Sci. Eng. C*, vol. 35, no. 1, pp. 411–419, 2014.

[85] B. D. Choi *et al.*, "Secretory leukocyte protease inhibitor promotes differentiation and mineralization of MC3T3-E1 preosteoblasts on a titanium surface," *Mol. Med. Rep.*, vol. 14, no. 2, pp. 1241–1246, 2016.

CHAPTER 6

Improving wear behaviour of β-Titanium alloys

CHAPTER 6

6.1. Introduction.

High wear is one of the main problems related to hip implants, limiting long-term durability [1], [2]. As a result of wear, metal ions and wear debris are released, which may damage the cell tissue, having local and systemic effects [3]–[5]. Additionally, the continuous release of wear debris may affect the fixation causing implant loosening and thus, ultimately leading to implant replacement [6], [7]. The development of new Ti alloys with improved wear and tribocorrosion resistance is needed to avoid adverse biological effects and early implant failure.

Surface engineering techniques have been employed to enhance wear resistance since, usually, harder alloys exhibit better wear resistance [8]–[10]. Oxidation, carburising and nitriding are within the most popular thermochemical treatments employed to enhance the surface properties of Ti and its alloys [11]. Nitride coatings are considered a good candidate, since they show high adhesion to the metal substrate and present good wear and corrosion resistance. Nitriding treatment involves interactions between nitrogen and the metal surface in order to produce a hard external layer composed of TiN and Ti_2N phases that protects Ti substrate [12]–[15]. Due to inward nitrogen diffusion, nitrogen dissolves into the Ti matrix, forming internal nitride precipitates beneath the compound layer. The high nitrogen solubility in α-Ti leads to the formation of α-Ti(N) solid solution, which has a hardening effect on the substrate, producing a hardness gradient in the diffusion zone. Hardness values decrease from the surface inward due to the decrease in nitrogen concentration. [16], [17]

Alternatively, the development of titanium matrix composite (TMC) incorporating hard particles such as TiC, TiB_2, SiC and TiN, have also been studied to improve wear resistance owing to the significant hardness increasing. [18]–[21]. An appropriate reinforcement compound should have good interfacial bonding between the metal matrix and reinforcement, avoiding the formation of reaction products at the interface. In addition, it should exhibit high thermodynamic stability in the Ti matrix at the sintering temperature, high hardness, and a low difference in thermal expansion coefficient to avoid residual thermal stress generation, which might compromise mechanical properties [22], [23]. TiB_2 and TiN could be candidates to produce TMC for biomedical applications since they comply with reinforcement requirements and show similar cytotoxicity to CP-Ti.[24], [25]. One of the disadvantages of TMC is that they tend to increase the elastic modulus, which is unfavourable for implant materials. [26]

In this chapter, β-Ti alloys (TH40Nb and TH5Fe25Nb) are modified using two different routes: (1) development of titanium matrix composites by incorporation of 5 vol.% of ceramic particles and (2) nitriding surface treatments using different substrates. **Figure 6.1** summarises the routes followed; the samples processed indicating the nomenclature used from now onward for each sample.

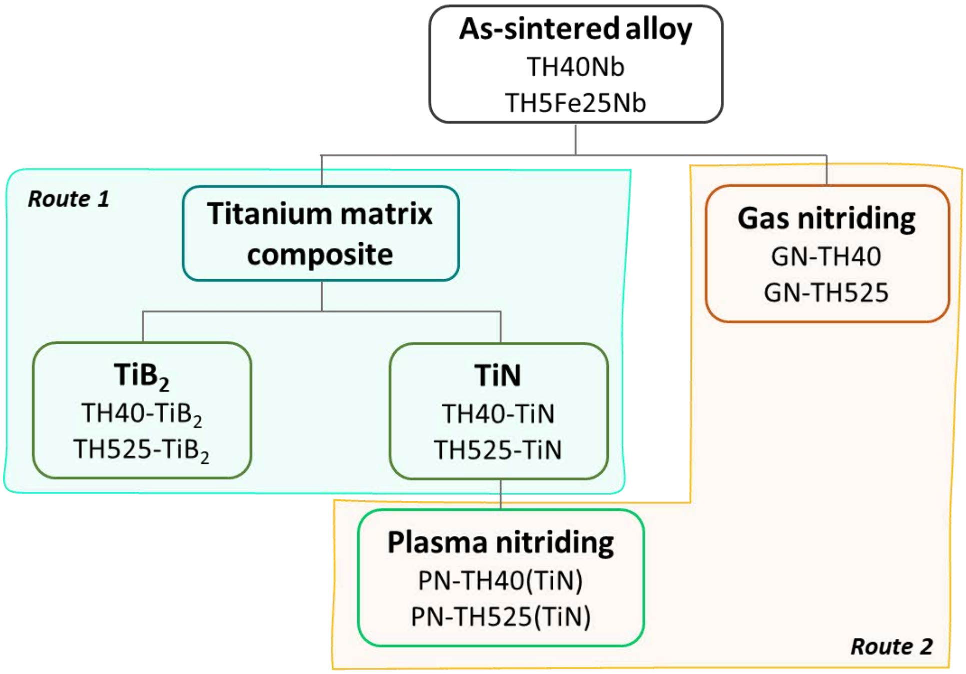

Figure 6.1. Schematic of the modified β-Ti alloys and nomenclature used for each sample.

This chapter describes the microstructural features obtained for all processed samples. Mechanical properties (hardness and elastic modulus) are also analysed considering the microstructures. Finally, wear resistance was evaluated by dry sliding tests against an alumina ball, applying 10 N and 20 N load.

6.2. β-Titanium matrix composite materials by addition of ceramic reinforcement.

6.2.1. TiB_2 reinforced β-Ti composite.

To facilitate the comparison between TiB_2 and TiN reinforced and unreinforced alloys, the microstructures of the base alloys (TH40Nb and TH5Fe25Nb) are shown in **Figure 6.2**. To summarise, both base alloys exhibit a predominantly β-Ti microstructure with elongated and thinner TiC precipitates (dark phase), which are preferentially located at the grain boundaries. Additionally, TH5Fe25Nb composition has smaller amount of porosity than TH40Nb. Details of the employed processing condition to obtain the composites are given in **Section 3.6.1.**

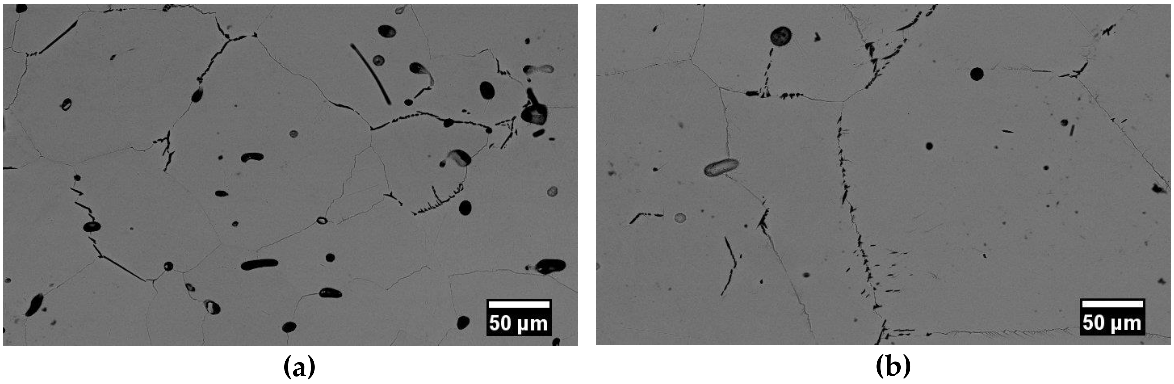

Figure 6.2. BSE-SEM images for unreinforced sintered β-Ti alloys. a) TH40Nb and b) TH5Fe25Nb.

Microstructures for TiB_2 reinforced alloys are shown in **Figure 6.3**. It can be seen that TiB_2 addition has totally modified the microstructure. For the TH40-TiB_2 sample (**Figure 6.3**a,b), the following features are observed: the β-Ti matrix (indicated with A) and several precipitates (labelled as B) that appear to form agglomerates in some areas, leaving part of the matrix unreinforced. These agglomerates indicate a poor dispersion of TiB_2 particles, generating heterogeneities that may affect the mechanical reliability of the alloy due to a non-uniform distribution of the in-situ reinforcements formed in the matrix. Moreover, a dark phase (indicated with C) is observed located mainly at the grain boundaries for this composition. In contrast, the TH525-TiB_2 composition (**Figure 6.3**c,d) presents a bright phase corresponding to the β-Ti matrix (A), small and thin precipitates (B), which are almost imperceptible at low magnification, and darker areas (C) were also observed, but they are uniformly distributed in the matrix. In general, the bright phase (A) is alloying elements riched, the darkest phase (C) is mainly Ti composed, whereas grey precipitates (B) are boron-rich.

Both TiB_2 reinforced alloys show a significant decrease in grain size compared to the untreated alloys.TH525-TiB_2 exhibits a more refined and less porous microstructure than TH40-TiB_2 composition. This refinement effect was expected since it has been claimed repeatedly in the bibliography even when low TiB_2 content is used. [27]–[29]

Titanium boride precipitates can be formed by different solid-state reactions, indicated in **Table 6.1**. Even though reactions (2-4) have lower Gibbs free energy than reaction (1), they cannot spontaneously occur, since boron is not available as ion in the lattice to react with Ti or TiB. Moreover, it has been reported that reaction (1) is the most favourable reaction when there is a Ti excess, and the boron content in the reaction zone is less than 18 wt.% [22], [30]. Hence, it is reasonable to deduce that, in this case, precipitates are formed in the β-Ti matrix by reaction of the TiB_2 particles with Ti particles to form the thermodynamically stable TiB through the matrix following the reaction (1). The TiB grows as pristine single-crystal whiskers in the matrix. TiB whiskers have a preferential growth along [010] direction that occurs by the one-way diffusion of boron atoms, favoured by the strong B-B bonds in the [010] direction. Hence, the precipitate grows faster in the longitudinal direction than in the transverse direction, leading to the formation of precipitate with a characteristic whisker or needle-like morphology. [22]

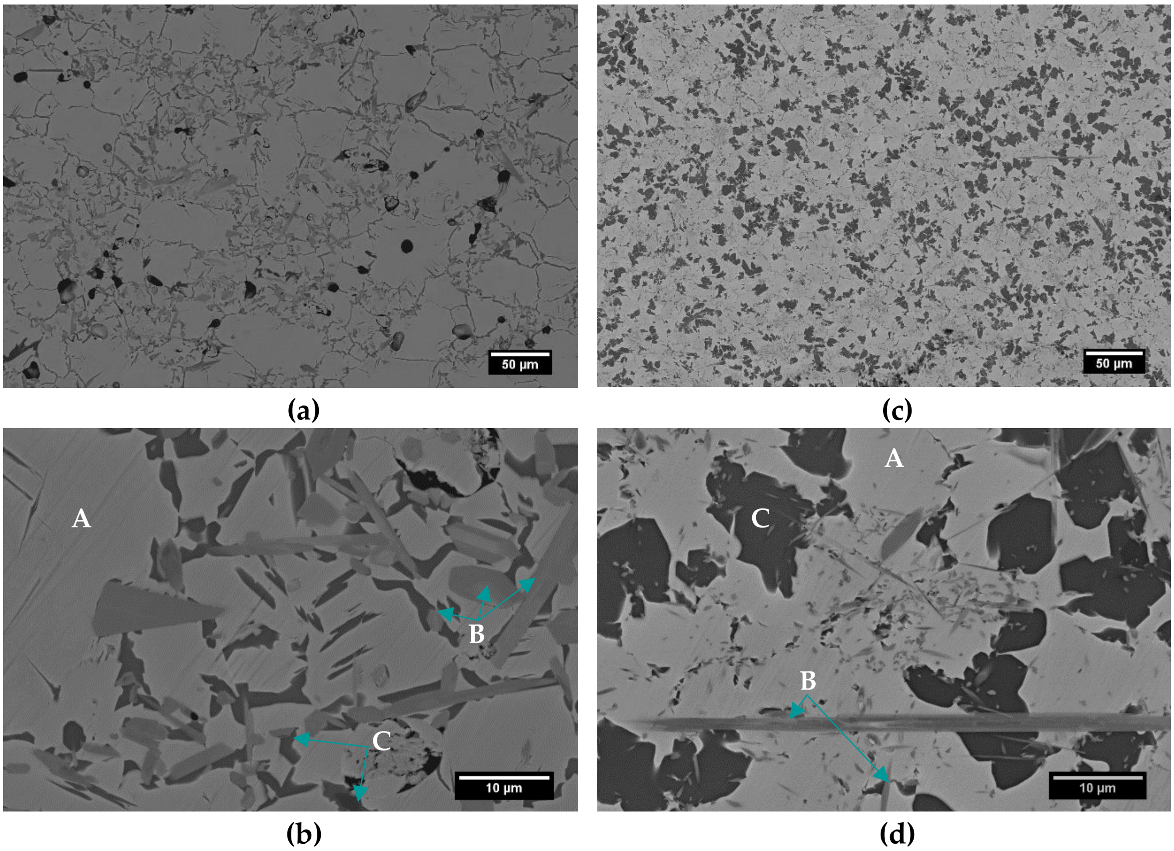

Figure 6.3. BSE-SEM images for reinforced β-Ti alloys with 5 vol.% of TiB_2. (a-b) TH40- TiB_2 and (c-d) TH525-TiB_2.
A is indicating β-Ti matrix, B boride precipitates and C dark phase.

Table 6.1. Gibbs free energy of formation of different titanium borides calculated at the sintering temperature (1400 °C) using Thermocalc software.

	Reaction	**ΔG (J) at 1400 °C**
(1)	$Ti + TiB_2 \rightarrow 2TiB$	-26.455
(2)	$TiB + B \rightarrow TiB_2$	-97.640
(3)	$Ti + B \rightarrow TiB$	-150.549
(4)	$Ti + 2B \rightarrow TiB_2$	-248.191

Different morphology of precipitates is observed in **Figure 6.3**c,d. This is due to the whisker orientation during metallographic observation; the elongated whiskers correspond to the longitudinal/transversal section, while those with prismatic-like morphology correspond to the whisker cross-section. Furthermore, precipitates exhibit different colour contrasts, suggesting a mixture of titanium a niobium boride was obtained. Considering that NbB and TiB show high mutual solubility, the presence of a mixed boride is not surprising.

XRD patterns displayed in **Figure 6.4** confirms the phases detected by SEM. It can be distinguished β-Ti phase (ICDD 01-089-4913) corresponding to the matrix, and TiB (ICDD 01-073-2148) and NbB (ICDD 01-089-2309). No evidence of TiB_2 phase was detected, suggesting a complete transformation of TiB_2 powder into TiB. A shift is observed in the peaks corresponding to the β-Ti matrix. In both alloys, these peaks are shifted to the left, to smaller angles than for pure β-Ti. This fact is attributed to lattice distortions caused due to the incorporation of alloying elements into the Ti lattice. TH40Nb composition has a higher alloying element content than TH5Fe25Nb, which explains the greater displacement in the TH40Nb sample. This behaviour was also observed before the addition of ceramic particles. This suggests that the TiB_2 addition does not impair the matrix stability of both alloys.

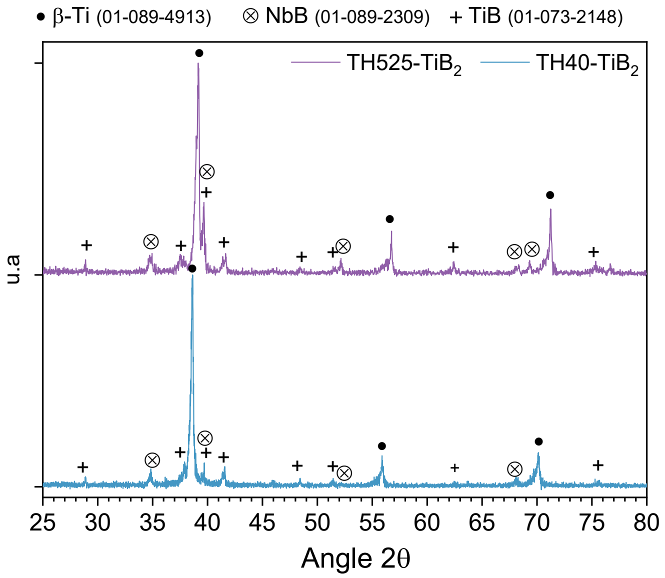

Figure 6.4. X-ray patterns diffraction of TMC alloys with 5 vol.% of TiB_2.

Due to the complex microstructure, a more detailed analysis was performed. EDS line scan measurement was done in order to evaluate the composition changes within a precipitate, and it is shown in **Figure 6.5**a. Complementary, to evaluate how the composition of the different phases identified varies, elemental compositional mapping was conducted (**Figure 6.5**b).

Contrasting both results, four regions can be identified: region 1 corresponding to the surrounding β-Ti matrix, region 2 and 3 correspond to the precipitates and, region 4 corresponds to the dark phase. Concerning the boride precipitate, it can see that the central part of the boride is enriched in Nb, whose composition is 25 at.% Nb, 30 at.% Ti and 45 at.% B; while the outer part presents about 17 at.% Nb and a higher Ti content, which decreases or increases as it approaches or moves away from the Nb-rich section, respectively. Ti content varies from 57 to 35 at.%. The dark phase (region 4, identified with letter C in **Figure 6.3**) is mainly composed of Ti; a drastic decrease in both B and Nb can be observed in this region. This can be better seen in the mapping, where the Nb or B presence in the darker phase is not highlighted. EDS measurements performed in similar regions for both alloys corroborate this finding, namely, that this phase is a Ti-rich phase, containing about 95 at.% Ti. A similar Ti-rich phase was reported in TiB_2 reinforced TiFeMo alloys processed by vacuum sintering, spark plasma sintering and hot isostatic pressing. No details about the formation mechanism of this phase are given in this work [31]. It is possible that this Ti-rich zone is a result of Nb depletion (depletion zone) due to the formation of mixed Ti-Nb mixed borides

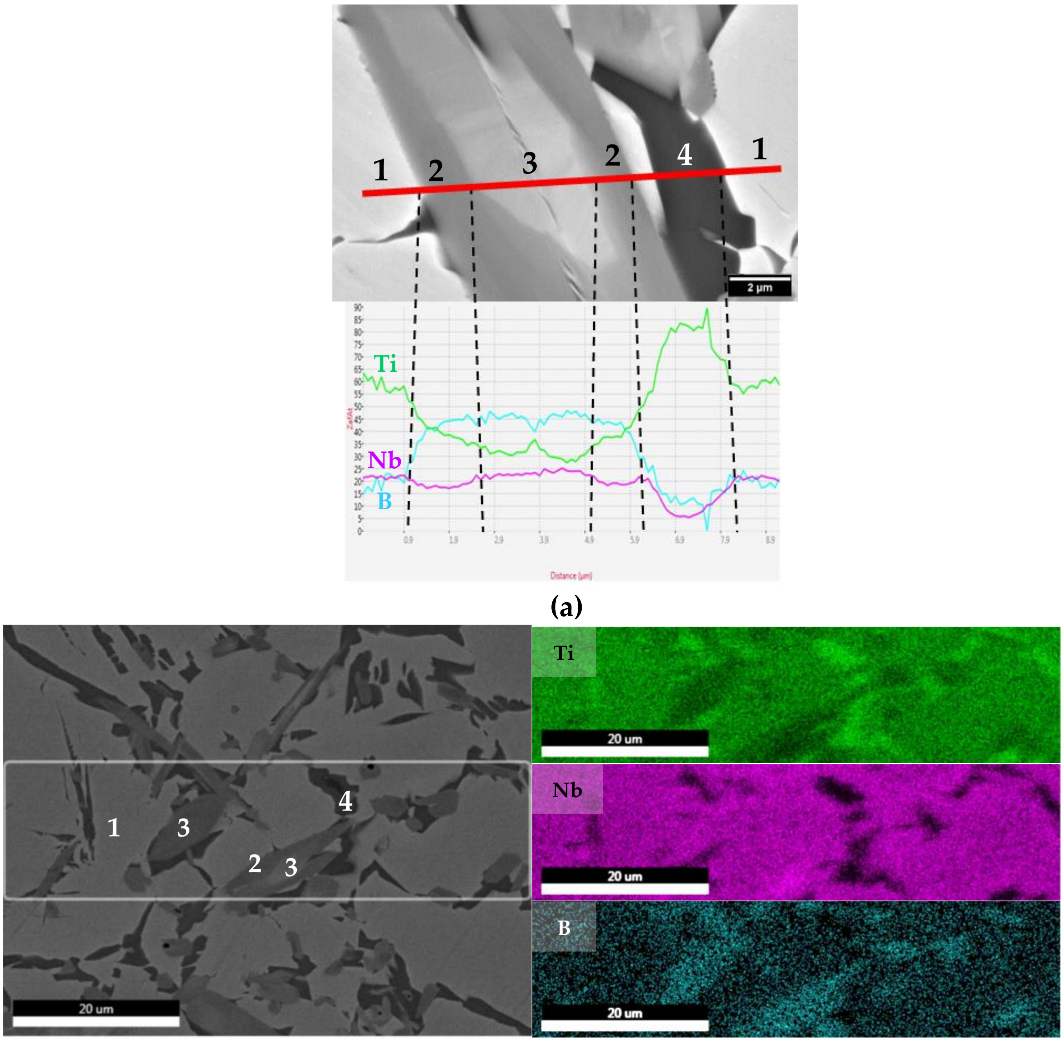

(a)

(b)

Figure 6.5. Detail of the composition of the precipitates in TH40-TiB_2 sample. a) EDS line scan (composition is indicated in at.%) and b) Compositional mapping.

To further evaluate the morphology of the precipitates, samples were deeply etched with Kroll's reagent in order to remove the β-Ti matrix and reveal the morphology and distribution of whiskers (**Figure 6.6**).

Whiskers surface is well defined and faceted. Both alloys exhibit whiskers with random orientation; nevertheless, significant differences are observed between both alloys concerning the distribution, amount and size of the whiskers reinforcements, despite the fact that the TiB_2 volume fraction added to both compositions is the same (5 vol.%). Many of the reinforcements formed in TH40-TiB$_2$ exhibit a hexagonal cross-section, while in TH525-TiB$_2$, they have flatter edges.

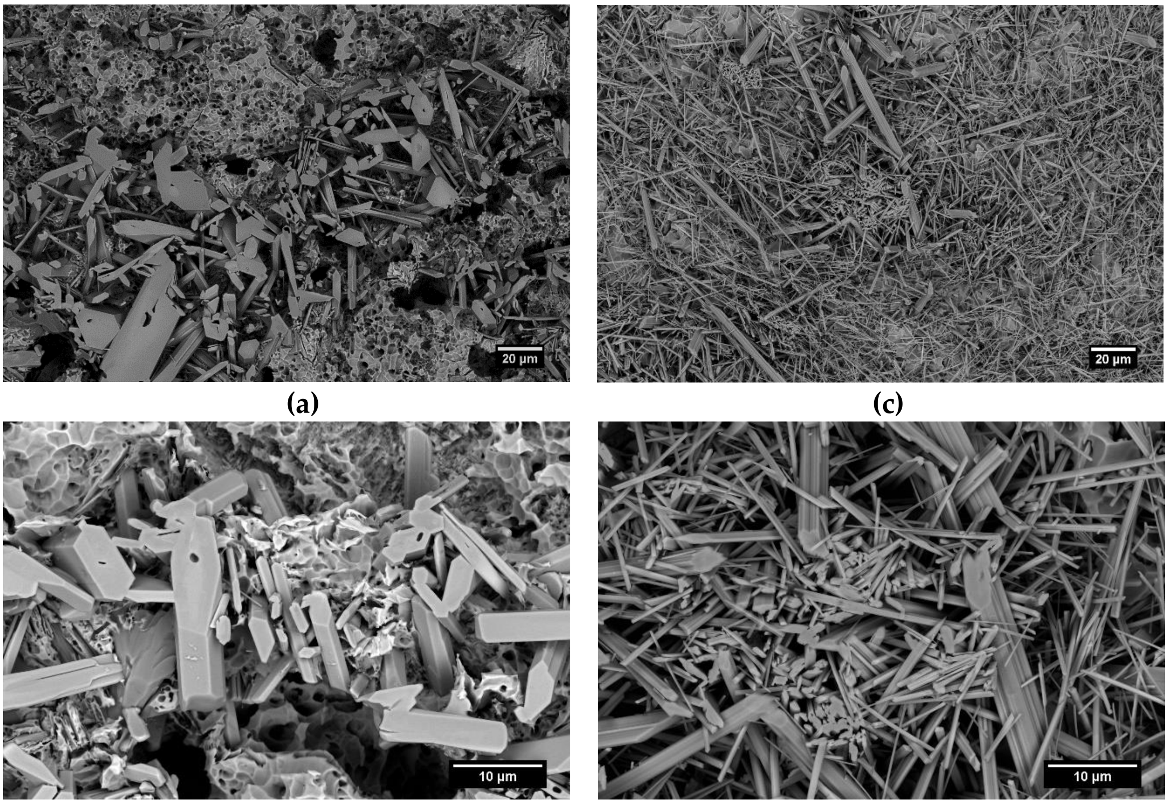

(a) (c)

(b) (d)

Figure 6.6. BSE-SEM images for reinforced β-Ti alloys with 5 vol.% of TiB$_2$ after deep etching. (a-b) TH40- TiB$_2$ and (c-d) TH525-TiB$_2$

It is noticeable that precipitates in the TH40-TiB$_2$ samples appear to be coarser and seem to be a lower quantity than those observed in TH525-TiB$_2$. TiB whiskers of TH525-TiB appear to be dense, while some of the whiskers in TH40-TiB$_2$ samples show some internal porosity, as shown in **Figure 6.6a,b**. Similar behaviour has been reported for TiB whiskers obtained by solidification, where a shrinkage produced during TiB transformation generates hollow cores [32]. The TiB formed in the TH40-TiB$_2$ sample does not seem to be well integrated into the matrix and tends to form clusters composed of bigger precipitates. In contrast, the reinforcements in TH525-TiB$_2$ are better distributed throughout the β matrix and appear to be embedded into the matrix, which could be favourable to improve the mechanical properties of the material.

The clustered whiskers formed in TH40-TiB$_2$ could be attributed to two reasons: (1) a poor dispersion of TiB$_2$ particles and (2) few contact points between Ti and TiB$_2$ particles. It has been reported that for high TiB$_2$ volume fractions in Ti-TiB$_2$ composites, the TiB whiskers tend to group, generating a kind of monolithic form, coarsening the precipitate [33]. This reasoning can be applied to the TH40Nb sample, to the areas where the agglomerates of the TiB$_2$ particles are found, which may explain the whiskers' size difference.

On the other hand, the volume fraction of Nb particles in TH40-TiB_2 is higher than TH525-TiB_2 (25 vol.% and 14 vol.%, respectively). Hence, the amount of Ti-TiB_2 particle contacts is reduced, which increases the dependence on Ti backward diffusion, across the Nb particles, into TiB_2 regions to form TiB [34]. It has been found that the reduction of Ti-TiB_2 contacts favours the formation of coarser and shorter precipitates [28], [32]. While in TH525-TiB_2, the nucleation of new whiskers is favoured more than their thickening, resulting in a high density of thin and interconnected precipitates.

The morphology and relative proportions of precipitates formed during the *in-situ* reaction in the composite material are influenced by many factors. Some of them are: (1) boron diffusion through TiB to lead to whisker growth, (2) the starting fraction of Ti and TiB_2 particles, (3) the powder packing and (4) the location of powder particles in the starting mixtures. Intimate contact between Ti and TiB_2 particles is desired to promote a homogeneous distribution of the reinforcements.

It is considered that the use of TiH_2 powder as Ti source does no affect the precipitation and growth mechanisms of TiB, due to the fact that it has been demonstrated that TiB starts to form in the temperature range of 800-1100 °C, that means, when the dehydrogenation process is almost completed [35]–[39]. Although dehydrogenation should not affect the formation of precipitates, the microstructural changes produced after TiH_2 transformation could affect. Within this temperature range (800-1100 °C), Kirkendall porosity is generated, especially for the TH40Nb sample (**See Chapter 4**), due to the diffusion of Nb particles in the Ti matrix. This could modify the arrangement of the TiB_2 particles, altering the contact points between the Ti and TiB_2 particles. This is just a hypothesis; more detailed studies are needed to confirm it. The processing of this type of samples is complex to analyse since many simultaneous processes take place simultaneously, such as dehydrogenation, phase transformation from α-Ti to β-Ti, diffusion of the alloying elements and, their incorporation into the precipitates formed *in-situ*, as well as sample densification. All this makes it difficult to follow each process and how it can affect the rest.

6.2.2. TiN reinforced β-Ti composite.

The microstructures of TiN reinforced samples are displayed in **Figure 6.7.** Two well-differentiated phases can be identified, where the bright zones correspond to the β-Ti matrix and the dark regions correspond to reinforcement particles of TiN. No evidence of interface defects was found, which implies good interfacial bonding between matrix and reinforcement.

Both TiN reinforced alloys showed a similar volume fraction of the ceramic reinforcement, measured using the Image J software, reaching about 34.6% and 36.6% for TH40-TiN and TH525-TiN, respectively. Although both alloys have a similar reinforcement volume fraction, images suggest a different distribution of this phase. TH525-TiN seems to exhibit a better distribution of reinforcement particles through the β-Ti matrix, whereas in TH40-TiN, agglomerates or clusters of reinforcement particles can be seen. The volume fraction of reinforcement is surprising, since it appears that there is a significant increase, considering the initial powder mixtures contains just 5 vol.% TiN. This suggests there are several reactions between the matrix and particle reinforcements taking place during sintering.

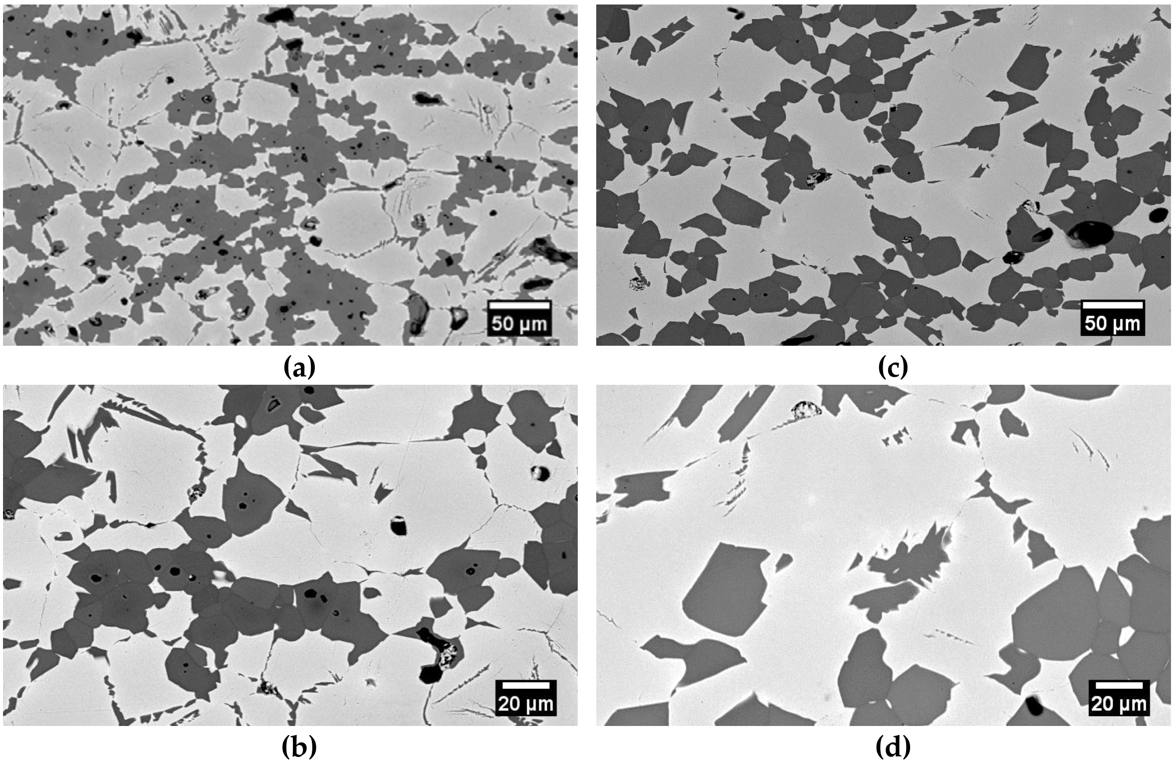

(a) **(c)**

(b) **(d)**

Figure 6.7. BSE-SEM images for reinforced β-Ti alloys with 5 vol.% of TiN. (a-b) TH40-TiN and (c-d) TH525-TiN

XRD results (**Figure 6.8**) coincide with the observed in SEM images. Two phases were identified. The most intense peaks correspond to the β-Ti matrix, whereas the minority phase, corresponding to the reinforcements, coincides with the $TiN_{0.3}$ phase with HCP crystal structure (ICDD 00-041-1352). This nitride composition is in agreement with the EDS measurements (**Table 6.2**), where reinforcements exhibit a reduction of the stoichiometric nitrogen amount of the TiN compound, showing about 25-30 at.% of N. EDS indicates that the Nb of the matrix migrated toward nitride to form a mixed Ti/Nb nitride. The Nb concentration in the nitride is higher for the alloy with a higher Nb amount. The average detected amount was 6 and 4 at.% of Nb for TH40-TiN and TH525-TiN, respectively.

Furthermore, it was found that both β-Ti matrices become slightly enriched in alloying elements (Nb and Fe) compared to their starting compositions. This leads to the assumption that Ti diffuses out to the matrix to react with nitrogen from the reinforcement particles and to further form new nitrides. Depending on nitrogen content, this could produce a solid-solution strengthening effect as nitrogen content increases, which would imply further enhancement of the mechanical properties. [16], [42], [43][40], [41].

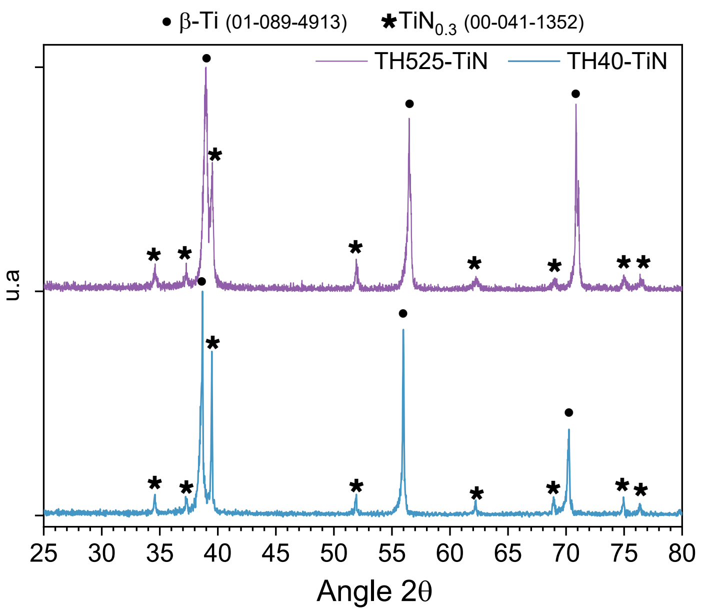

Figure 6.8. X-ray patterns diffraction of TMC samples with 5 vol.% of TiN.

Table 6.2. EDS measurements conducted in interest zones of TiN reinforced alloys expressed in atomic per cent.

	TH40-TiN		**TH525-TiN**	
at. %	**Matrix**	**Reinforcement**	**Matrix**	**Reinforcement**
Ti	70.0 (54.5)*	66.3 (77.5)	75.4 (64.1)	70.3 (82.3)
Nb	30.0 (45.4)	5.7 (13.0)	17.6 (29.0)	3.9 (8.8)
Fe	---	---	7.0 (6.9)	--
N	---	28.0 (9.5)	--	25.8 (8.9)

* Amount in () indicates the composition in weight per cent.

The fact that the ceramic phase fraction has increased from 5 vol.% (incorporated in the mixture of powders) to 35 vol.% (measured by Image J), suggests that dissolution processes have occurred between the matrix, alloying elements and TiN particles, which allows the growth of reinforcement phase. A hypothesis could be that this growth could be produced by the Nb incorporation into the Ti matrix. This could explain the higher Nb content detected in the TH40-TiN reinforcements (**Table 6.2**). In the TH40-TiN case, the nitride particles are agglomerated, which leaves some pores between them. While in TH525-TiN, the nitrides are more dispersed. Nitrides do not contain Fe, because it is completely dissolved in the Ti matrix. Therefore, it is possible that Fe could limit the Nb dissolution into nitride particles, explaining the lower Nb content in the TH525-TiN reinforcements than those of TH40-TiN.

Considering EDS and XRD results, it can be concluded that there was nitrogen lost during sintering, which changes the nitride stoichiometry from the starting TiN to $TiN_{0.3}$ phase. It has been reported that nitrogen loss is a common problem observed in vacuum-sintering of cermets or composite materials containing Ti(C, N) and TiN [44], [45]. During vacuum-sintering, part of the nitrogen is removed; this released gas can be trapped between the particles, generating internal porosity, as shown in **Figure 6.7b**. Internal porosity seems to be more noticeable for TH40-TiN alloy than TH525-TiN. Internal porosity can also be formed due to incomplete nitride-nitride sintering by the coalescence of initial TiN particles, which leaves some pores between them and the Ti matrix.

TiN reinforcements are bigger than the raw TiN powder (1-3 μm), suggesting that the re-precipitation process could occur during sintering. Even though nitrogen loss was observed for both alloys, obtaining the same reinforcement phase $TiN_{0.3}$, images suggest that TH525-TiN sample exhibits less coalescence among TiN particles, which results in a more homogeneous phase and bigger reinforcement size compared to TH40-TiN composition.

It is well known that Fe addition improves the sinterability of Ti alloys and increases the self-diffusion coefficient of Ti, which may enhance the diffusivity of the other elements [18]. Fe addition likely affects the diffusion process during sintering, promoting the sample homogenisation, whereas Nb may act as a diffusion barrier. Hence, this may explain the better sinterability observed in the TH525-TiN sample compared to TH40-TiN.

To summarise, reinforced Ti alloys present completely different microstructural features for both reinforcement compounds, TiN and TiB_2. TiB_2 and TiN addition seems to reduce the grain size of the samples (**Figure 6.2**). This is because ceramic particles prevent grain growth causing a grain size refinement effect [46], [47].

TiB_2 composite samples exhibit a wide variety of whisker-like precipitates (in terms of size, distribution and chemical composition) as reinforcement phase. The TiB precipitates morphology varies depending on the alloy composition. Processing of in-situ TiB reinforced alloys is a more complex process than the processing of TiN reinforced alloys. The formation mechanisms of TiB whiskers are still not entirely understood, so the processing of TiB_2 reinforced alloy should be further investigated, in order to achieve a controlled and homogeneous microstructure. In contrast, TiN reinforced alloys show similar particulate reinforcements for both treated alloys. TiN reinforced materials are more homogeneous than TiB reinforced materials, which could contribute to achieving more uniform and improved properties.

6.3. Development coating by nitriding treatment.

6.3.1. Gas nitriding treatment.

Figure 6.9 shows the microstructure obtained after gas nitriding (GN) treatment of both TH40 and TH525 alloys. The microstructure of nitrided samples is altered by nitriding temperature, gas purity, and the kind of Ti alloy treated (α, α+β or β). Alloying elements play a key role in the final microstructure; they can alter the diffusion front of nitrogen, since the diffusivity and solubility of nitrogen in each element may vary. Moreover, it is considered that both nitride layer thickness and diffusion region increase with increasing nitriding temperature [48]

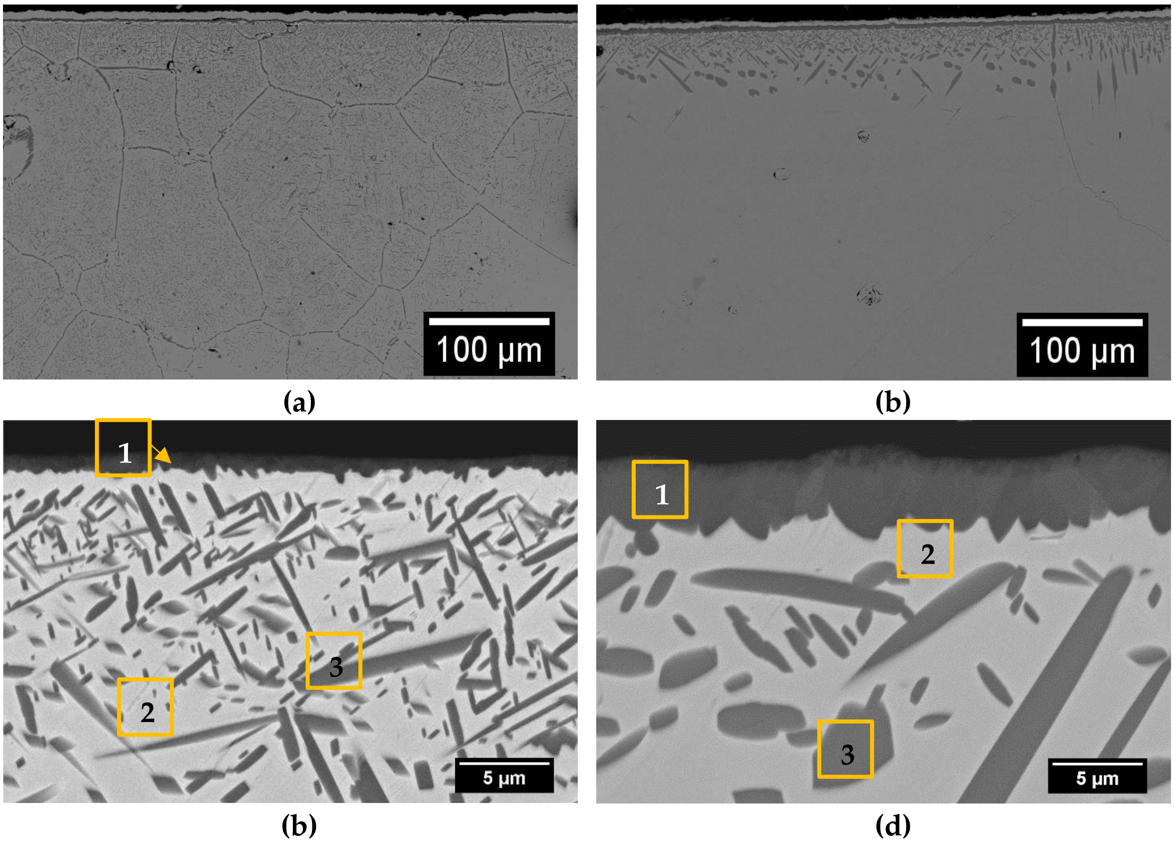

Figure 6.9. BSE-SEM images for nitrided samples: (a-b) GN-TH40 and (c-d) GN-TH525.

Even though gas nitriding treatments were conducted under the same conditions, it can be observed that nitriding results in different microstructural features for the two compositions evaluated. Several morphologies of precipitates, as well as evident differences in the depth of the diffusion zone, can be seen in **Figure 6.9.** Simplifying the microstructure, it can see that it is composed of the following phases: 1) The coating layer, 2) β-Ti matrix and, 3) Internal nitrogen-rich precipitates.

Concerning the coating layer, both alloys show a continuous and homogeneous nitride layer, covering the whole sample surface. Both samples exhibited a golden yellow colour, typical of titanium nitride. This layer seems to be compact and well adhered to the substrate. The thickness of the nitride layer was higher for sample GN-TH525 than GH-TH40, reaching around 3.35 ± 0.61 µm and 1.17 ± 0.41 µm, respectively.

A small Nb amount in the coating was detected by EDS measurement. The results for GN-TH40 were 49.7 at.% Ti, 44.7 at.% N and 5.5 at.% Nb, while for GN-TH525, they were 44.9 at.% Ti, 53.9 at.% N and 1.2 at.% Nb. TiN is the most thermodynamically stable nitride of the Ti-Nb-N system, for this compositional range and temperature. Nevertheless, pure TiN is not usually found in this kind of system, since the compounds δ-TiN and δ-NbN present complete solid solubility between them. Therefore, for a wide compositional range of Ti-Nb alloys, Nb tends to migrate to form a nitride. As a result, a Ti-rich nitride phase with some Nb amount (δ-(Ti, Nb)N) will be the nitride in equilibrium with the metallic phase. GN-TH40 has higher Nb content than GN-TH525; hence, a higher amount of Nb in the coating was expected.[49]

The Nb amount strongly influences the final microstructure. Samples with higher Nb content (GN-TH40) show small nitrogen-rich precipitates in almost the whole cross-section (about 2.5 mm), and precipitates at the grain boundaries are also observed. On the other hand, samples with lower Nb content (GN-TH525) achieved a significantly lower diffusion zone depth, reaching up to 6.5 μm in thickness. Nitrogen-rich precipitates for this sample are coarser and seem to have a preferential orientation relationship with the β-Ti matrix, as the precipitate gets bigger [50]. The decrease in precipitates size coincides with the findings reported by Buscaglia et al. They found that the precipitates, formed by nitriding of several Ti-Nb alloys, become thinner and smaller as Nb content increases. This is mainly attributed to the nucleation frequency that changes orders of magnitude as the alloy composition changes [49], [50]. The alloying element addition affects the nitrogen solubility and nitrogen transport mechanisms; and, therefore, affects the nitrogen interactions with the different elements of the alloy.[16], [51]

Figure 6.10 shows diffraction patterns obtained from the top surface of both alloys before and after nitriding. The presence of peaks corresponding to the β-Ti phase of the matrix indicates that the phases detected correspond to both the nitride coating and internal precipitates. The phases identified for both alloys were β-Ti (ICDD 01-089-4913), α-Ti (ICDD 01-089-4893), TiN (ICDD 03-065-0414) with FCC crystal structure, Nb_2N (ICDD 00-039-1398) with HCP crystal structure, and HCP $TiN_{0.3}$ (ICDD 00-041-1352).

An interesting observation in the β-Ti matrix can be made by comparing the TH40Nb and GN-TH40 XRD results. For untreated TH40Nb alloy, the most intense peak of β-Ti phase is located at 38.47°, whereas after gas nitriding treatment, the β phase was decomposed into two phases (**Figure 6.10**b): an intense peak at 38.40° corresponds to Nb (ICDD 01-089-4760), and a small peak at 38.75°, corresponding to the β-Ti phase was found. This finding may be attributed to a Nb enrichment of the β phase near the surface, where the highest amount of nitride is present. During nitriding, there is an active diffusion of the alloying elements from the most nitrogen-rich part (i.e., near the surface), towards the interior of the sample. Hence, a redistribution of alloying elements between the external nitride coating layer, the matrix and the nitrogen-rich diffusion area occurs. β-stabiliser elements enrich the β phase due to the preferential Ti segregation into the nitrogen-rich precipitates and nitride coating layer. The Ti segregation toward nitrogen-rich phases leaves the matrix depleted in Ti and enriched in Nb. [50]

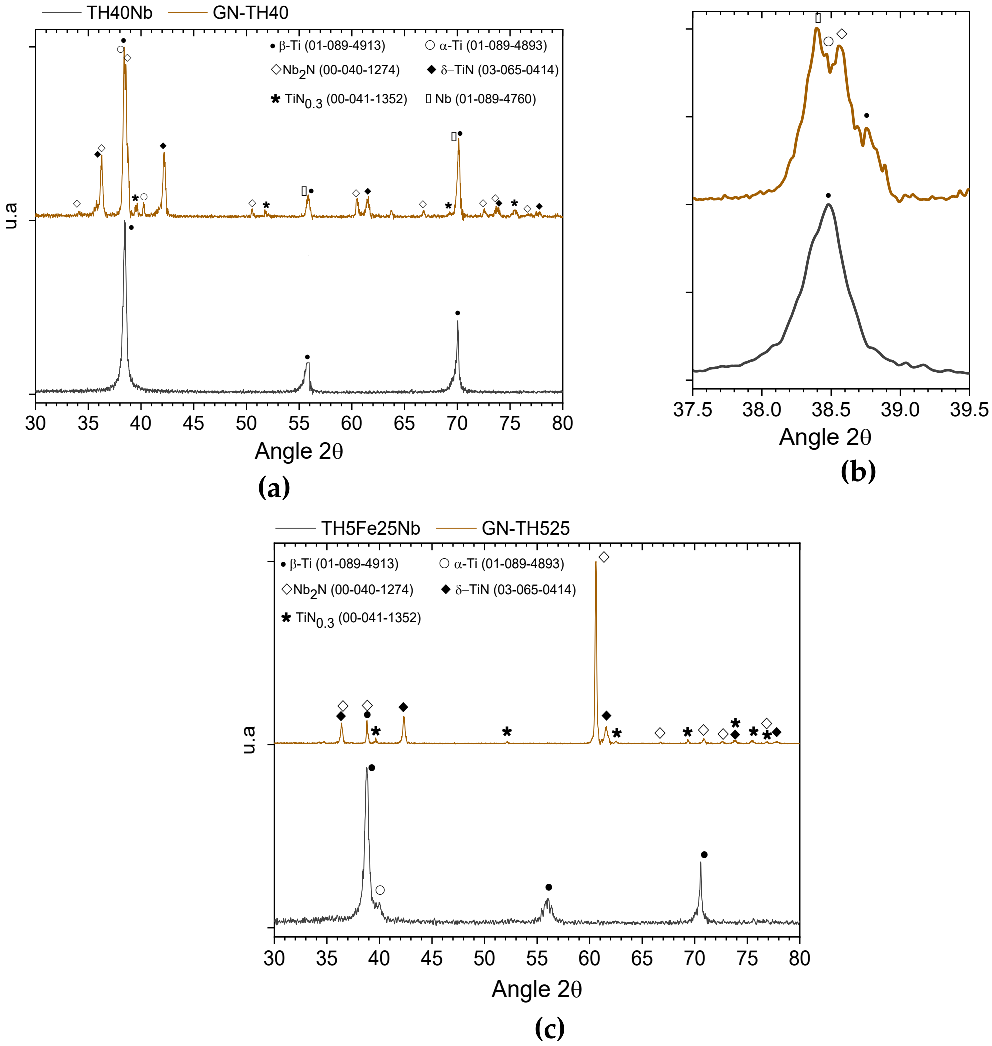

(a)

(b)

(c)

Figure 6.10. X-ray diffraction of the top surface of untreated and gas nitrided β-Ti alloys. (a-b) TH40Nb alloy; and c) TH5Fe25Nb alloy.

EDS measurements of both alloys performed at different depths support this fact (**Table 6.3**). In the centre of the sample, where no nitrogen-rich precipitates were found (GN-TH525 case), or they are very thin precipitates present (GN-TH40 case), the matrix composition is similar to the theoretical composition. In contrast, close to the surface, where the nitride coating layer and a high number of nitrogen-rich precipitates are present, the matrix has about 16-13 at.% less Ti than the starting composition, and Nb and Nb/Fe enrichment.

Table 6.3. EDS measurements (in atomic per cent) of the metal matrix at different depth of the coating layer for gas nitrided samples.

	GN-TH40			GN-TH525		
	Starting composition	Close to surface	Centre	Starting composition	Close to surface	Centre
Ti	74.4 (60.0)	58.8	75.1	80.3 (70.0)	67.4	79.5
Nb	25.6 (40.0)	41.2	24.9	14.8 (25)	23.6	17.2
Fe	---	---	---	4.9 (5.0)	9.0	4.3

*() indicate the composition in weight per cent.

The lower intensity of the β-Ti phase observed in GN-TH525 compared to that in GN-TH40 could be attributed to the higher thickness of the coating layer of GN-TH525. The high intensity of the Nb_2N peak (around 60°) and the weak intensity of TiN peaks was unexpected since this does not coincide with EDS analysis, in which it was determined that the coating layer is mainly composed of TiN.

This mismatch is because conventional XRD measurement, in some cases, is not suitable for characterising thin films since it generally produces a weak signal from the coating and an intense signal from the substrate. Grazing incidence X-Ray diffraction (GIXRD) reduces the penetration depth of the X-ray beam, minimising the substrate contribution, which is useful when studying thin films [52]. Hence, GIXRD measurements were conducted to better understand which phases correspond to the nitride coating layer and which correspond to the internal nitrogen-rich precipitates. Results are shown in **Figure 6.11**.

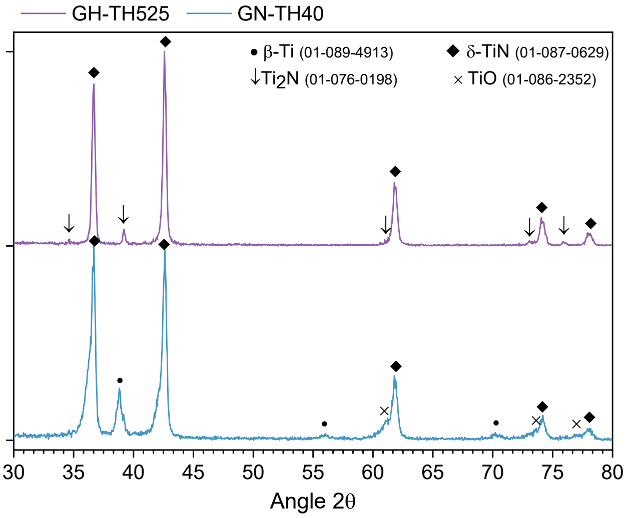

Figure 6.11. X-ray pattern diffraction with grazing incidence of 1° of gas nitrided samples.

According to GIXRD results, the coating layer of GN-TH525 samples is composed of Ti_2N and δ-TiN, while in GN-TH40, it is composed of δ-TiN. In addition, small peaks of TiO (ICDD 01-086-2352) were also detected in GN-TH40, indicating contamination problems during treatment due to the high Ti affinity with interstitials elements [53]. TH5Fe25Nb alloy contains a higher Ti amount than TH40Nb; so TH5Fe25Nb should have more risk of contamination. However, TH5Fe25Nb does not present titanium oxides.

Having confirmed the coating phases, it can be concluded that internal precipitates are a combination of Nb_2N, $TiN_{0.3}$ and α-Ti; the latter enriched in nitrogen (α-Ti(N)).

The formation of precipitates mainly depends on the concentration and solubility of nitrogen. It is expected that nitrogen concentration decreases throughout the sample at greater depth. Since the GN-TH40 sample shows precipitates along the whole cross-section, it is interesting to evaluate how these precipitates vary at different depths. For this, XRD measurements were conducted at 100 and 500 µm of depth (**Figure 6.12**).

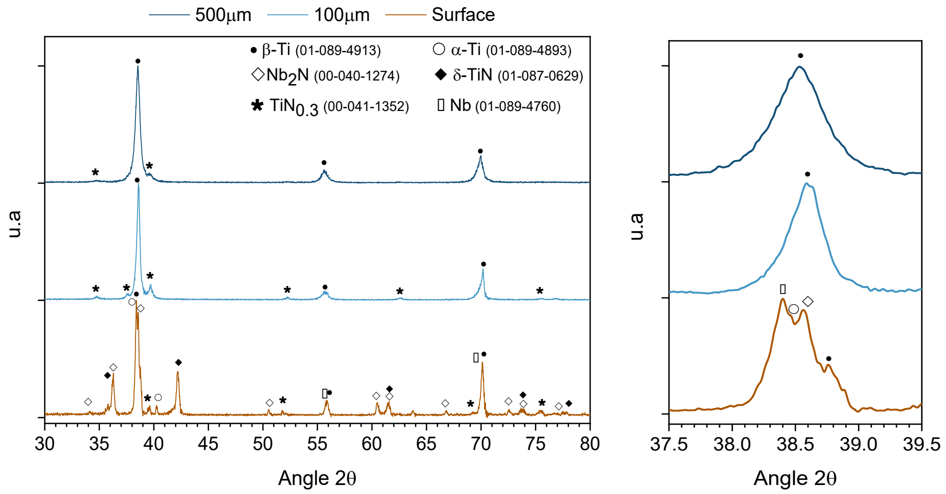

(a) **(b)**

Figure 6.12. X-ray pattern diffraction of GN-TH40 samples at different depth.

Although the same phases were detected ($TiN_{0.3}$ and β-Ti) at both depths, the peaks intensity is different. It can be seen that the intensity of the $TiN_{0.3}$ phase is lower at 500 µm than at 100 µm. This is attributed to the fact that as the depth increases, the amount of precipitates decreases, and they become smaller and more separated from each other, which reduces the contribution of this phase. Furthermore, as depth increases, the β-Ti phase is recovered, obtaining a single peak corresponding to this phase. This confirms that the matrix becomes Ti depleted near the surface due to a great concentration of nitrides precipitates, while it keeps stable moving away from the surface, where both size and amount of nitrogen-rich precipitates is reduced.

The Nb_2N phase was only detected in conventional XRD measurements made on as-nitrided surfaces (**Figure 6.10**). This suggests that Nb_2N precipitates are found close to the nitride coating layer, at a relatively shallow depth. The increase in the Nb concentration in the matrix (**Table 6.3**) due to Ti depletion just beneath the coating layer, together with the nitrogen-rich environment, may favour the formation of Nb_2N precipitates. At greater depths, these precipitates do not form since the Nb content decreases. The formation of $TiN_{0.3}$ and α-Ti precipitates mainly depends on the concentration and solubility of nitrogen. In gas nitriding treatment, nitrogen concentration decreases throughout the sample at greater depths. Internal nitrogen-rich precipitates through the whole cross-section of GN-TH40 highlight the strong dependence of alloying elements on the nitrogen diffusion and nitrogen diffusivity in the Ti matrix (α and β phase). Alloying elements may act as a barrier to nitrogen diffusion. In the case of low-diffuser elements such as Nb, this effect could be intensified. Hence, it is reasonable to deduce that the higher Nb content, the slower the nitrogen diffusion. Based on this, it would be expected that nitrogen diffusion and dissolution throughout the matrix is limited in GN-TH40 alloy, due to the high amount of Nb-rich zones, that may act as nitrogen pin sites. Hence, when nitrogen concentration reaches locally the critical value, above 34 N at.%, TiN_x precipitates are formed. On the contrary, since GN-TH525 has lower Nb amount, nitrogen can dissolve throughout the whole Ti matrix, before reaching the critical nitrogen concentration, avoiding the formation of precipitates.

Nitriding of Ti alloys is a complex process because it involves several simultaneous reactions at the interface between the gas and metal and within the substrate and with different elements. Nitriding can be summarised as follows: nitrogen diffuses from the sample surface inward, it dissolves into β-matrix to form a solid solution with nitrogen. The solid-solution is quickly transformed into α-Ti phase due to the low nitrogen solubility limit in β-Ti phase (6.2 at.%/2.1 wt.%). The resulting α-Ti phase is also nitrogen-rich (α-Ti(N)), forming a solid solution. The α phase is preferentially formed at the grain boundary of the β-Ti phase and tends to grow into the substrate with a needle-like morphology. When nitrogen concentration exceeds the nitrogen solubility limit in α-Ti(N), it is gradually transformed into different nitrides, depending on the surrounding matrix composition by a reaction-diffusion process. Later, when nitrogen concentration becomes high enough, different reactions occur on the surface to form the coating layer composed of TiN/Ti_2N or TiN phase by a reaction-diffusion process [11], [50], [54], [55]. The region where nitrogen diffuses is known as a gas-saturated area, where improvement in mechanical properties is expected due to solid solution strengthening effect.

6.3.2. Plasma nitriding.

Figure 6.13 displays the cross-section of TiN reinforced alloys coated by plasma nitriding (PN-TH40(TiN) and PN-TH525(TiN)). After treatment, both alloys become golden, confirming the formation of the titanium nitride layer. Both alloys show similar coating thickness, reaching about 1 µm. Coating layer seems compact, dense and uniform; however, some cracks and voids can be seen at the interface coating/alloy.

Small voids could be formed due to irregularities in the sample surface (**Figure 6.13c,f**). Since samples are composed of two phases (metal matrix and ceramic particles) with different hardness, so some residual stresses between TiN particles and the metal matrix could be generated during polishing (previous to plasma nitriding), affecting the adhesion of these areas. Cracks are preferentially formed above reinforcement particles, suggesting poor adhesion between the coating layer and the substrate.

Thermal expansion coefficients (CTE) of ceramics are usually lower than metals. At room temperature, TiN and Ti have a CTE of 9.4×10^{-6}/K and 8.6×10^{-6}/K [22], respectively; as temperature increases, the CTE difference between these materials becomes higher, reaching about 9.5×10^{-6}/K [56] and 11×10^{-6}/K [57], respectively (at 400 °C). The thermal expansion mismatch between coating and the two substrate phases causes thermal stresses leading to coating cracking at the interface [58]. Internal cracks compromise the coating adhesion and reduce its mechanical reliability, which is undesirable. Cracks are not generated in gas nitrided samples because the TiN coating is composed of a single β-Ti phase instead of β-Ti phase matrix and TiN particles.

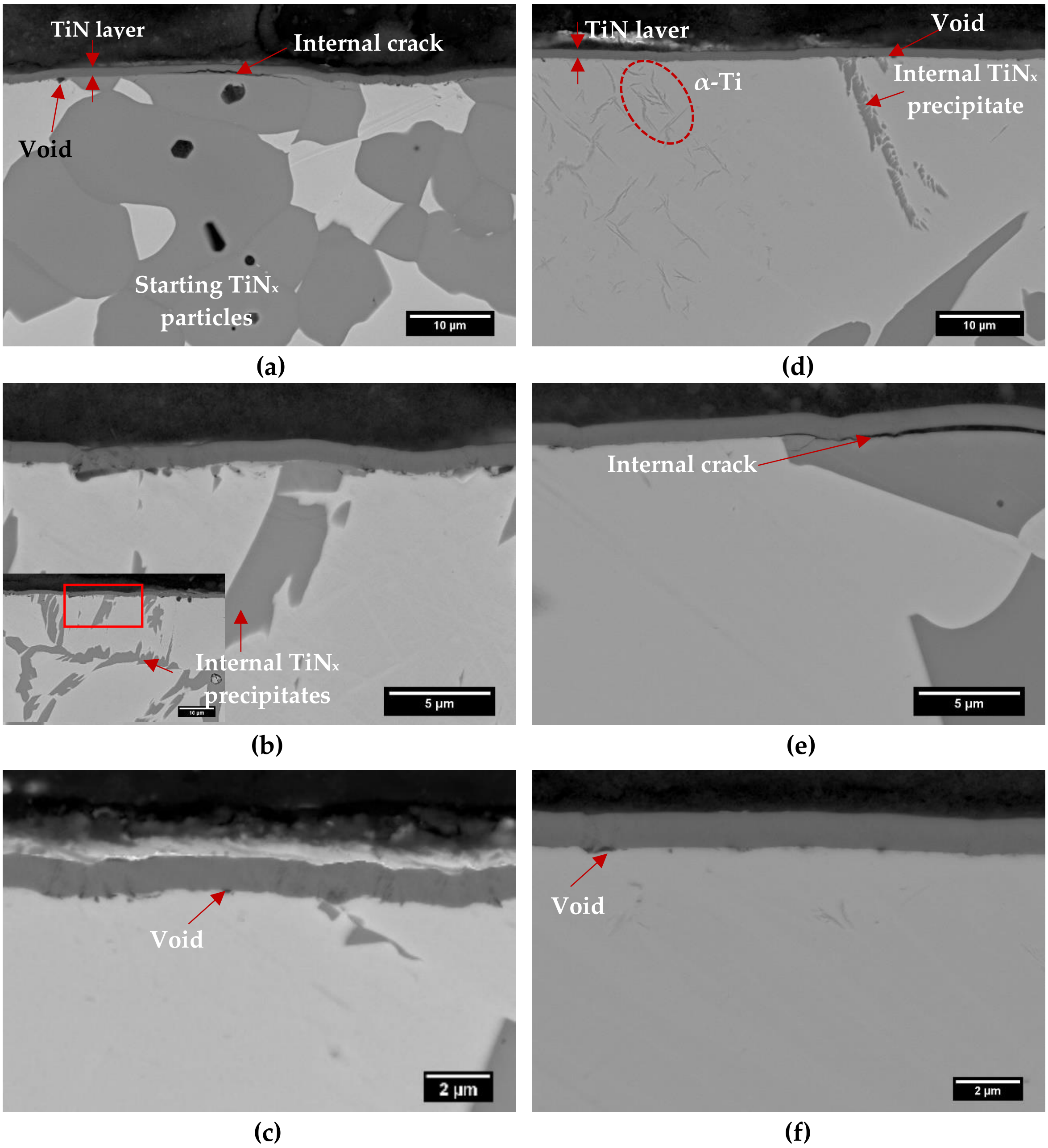

Figure 6.13. BSE-SEM images of the cross-section of TH40-TiN and TH525-TiN alloys after plasma nitriding treatment. (a-c) PN-TH40-TiN and (c-d) PN-TH525-TiN.

Unlike gas nitriding treatment, no significant precipitates were found below the TiN coating. This could be related to the fact that plasma nitriding was conducted at 400 ºC, which is lower than the temperature employed in gas nitriding. At this temperature, inward nitrogen diffusion is limited. Some nitrogen may diffuse into the substrate, forming a solid solution, initially with β-Ti, and then, as nitrogen content increases, forming α-Ti. It has been reported that nitrogen enrichment in the diffusion zone due to solid solution results in a hardness gradient. The higher the nitrogen content, the higher the hardness obtained.

A phase with fine plume-like morphology was observed in PN-TH525(TiN) (**Figure 6.13d**), which may correspond to nucleation sites of the α-Ti phase. Similar morphology was observed in TH5Fe25Nb after ageing, where dissolved titanium carbides acted as α phase nucleation sites (**See Section 5.5.1**). This phase was not found in PN-TH40(TiN).

EDS measurements indicate matrix composition, just below the coating, is 66.2% Ti, 24.8% Nb and 9.0% N for PN-TH40(TiN) sample; whereas for PN-TH525(TiN), it was 64.7% Ti, 13.4% Nb, 7.1% Fe and 14.7% N. Compositions are expressed in atomic per cent. PN-TH525(TiN) presents a higher nitrogen content than PN-TH40(TiN). Higher nitrogen concentration suggests a higher solubility in the PN-TH525(TiN) matrix, explaining the plume-like α phase formation (**Figure 6.13d**). A greater hardness increasing would be expected for PN-TH525(TiN) as compared to PN-TH40(TiN) due to the higher nitrogen content dissolved into the matrix.

Even though there is nitrogen in the matrix, no internal nitrogen-rich precipitates will be formed if nitrogen concentration is not high enough to form a nitride. TiN particles act as a barrier, since nitrogen diffusivity into TiN is several orders of magnitude lower than that of nitrogen into Ti. Hence, it is reasonable to consider that areas occupied by reinforcement particles further limit nitrogen diffusion, impeding thus the formation of large internal nitrogen-rich precipitates.

Although the nitrogen diffusion is slow, there are regions with enough nitrogen concentration, where some internal precipitates beneath the coating layer are formed, as shown in **Figure 6.13.** Large and fragmented precipitates that grow from the TiN layer toward the matrix can be seen. The chemical composition of these precipitates was determined by EDS analysis. Results show a nitrogen content in the range of 28-24 at.%. For both alloys, the N/Ti atomic ratio was about 0.3, suggesting that precipitates correspond to the $TiN_{0.3}$ phase.

XRD patterns diffraction of the sample surface before and after plasma nitriding treatment are shown in **Figure 6.14**. The phases identified are: the β-Ti corresponding to the matrix; $TiN_{0.3}$ corresponding to the ceramic reinforcement and internal nitrogen-rich precipitates; and δ-TiN corresponding to the coating layer. α-Ti phase was not detected in PN-TH525(TiN) samples, which suggests only a small amount of α-Ti, below XRD detection limit, was formed.

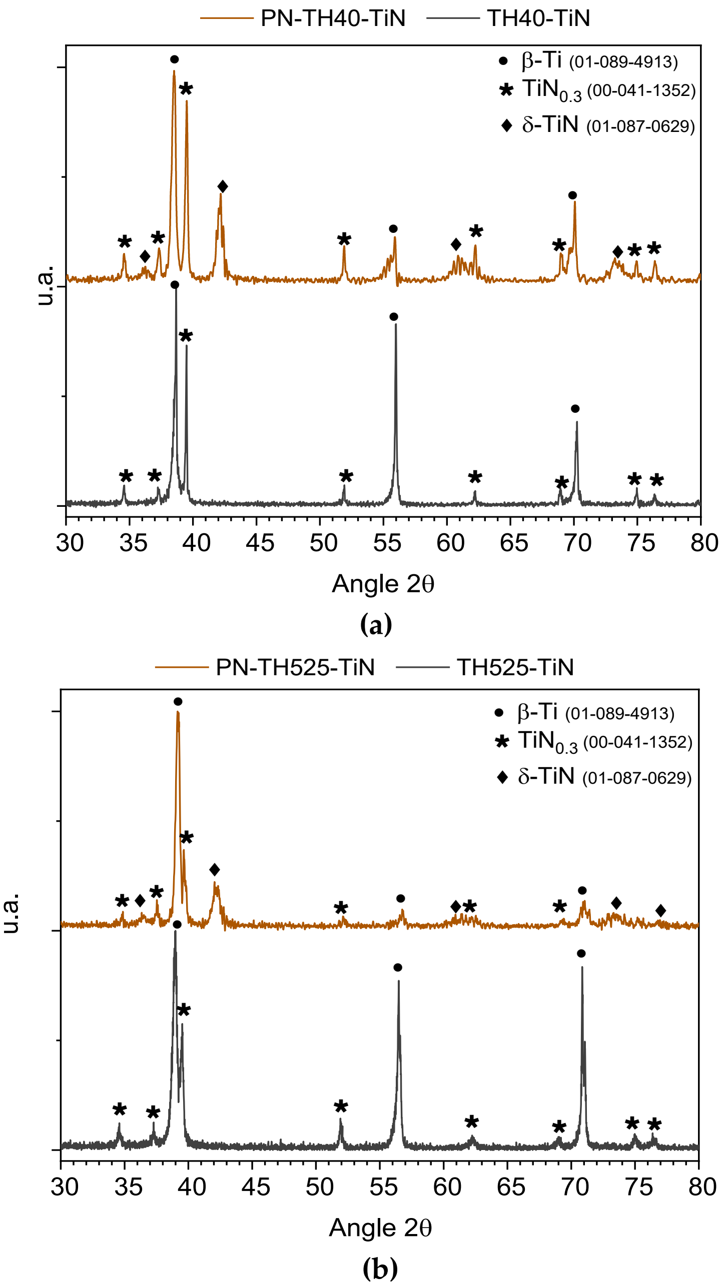

Figure 6.14. X-ray pattern diffraction of the top surface of untreated and plasma nitrided (PN) β-Ti alloys: a) TH40-TiN alloy and b) TH525-TiN alloy.

Gas nitrided samples exhibit a thicker and well-adhered TiN coating layer, compared to the coating obtained by plasma nitriding. The secondary reinforcement phase affects the coating adhesion with the substrate, forming cracks due to differences in the coefficient of thermal expansion of TiN and metal matrix. In contrast, gas nitrided samples, being composed of a single beta-Ti phase, do not present cracks at the coating/substrate interface. On the other hand, the influence of temperature treatment on the diffusion zone can be highlighted. As temperature decreases, nitrogen diffusion decreases, and consequently, the diffusion zone also decreases. This may imply a limited strengthening effect. In this regard, as plasma nitriding was performed at lower temperature (400 °C) than gas nitriding (900 °C), a shorter diffusion zone and lower hardening effect can be expected. Considering the diffusion zone and coating adhesion, TiN coatings obtained by gas nitriding treatment seem more suitable for improving wear properties.

6.4. Mechanical behaviour.

Elastic modulus is one of the main mechanical properties to be considered during the design of implant material [59]. For biomedical applications, low elastic modulus alloys should be employed in order to avoid the stress-shielding phenomenon, which is associated with bone resorption around the implant [3], [10]. Hip implants are also susceptible to wear. Low wear resistance leads to release wear debris or metallic ions that may result in the implant loosening. In addition, wear debris can cause several adverse reactions in the tissues where they are accumulated. They could produce damage of cell tissue, inflammation, hypersensitivity, toxicity or carcinogenicity, requiring the implant replacement. [3], [5], [10]

High hardness alloys tend to have better wear behaviour. Improvement in hardness and a decrease in elastic modulus would enhance the lifetime of implants [14], [60]. Hence, these properties are determined in this section in order to assess the viability of these materials as implant materials, since they are helpful parameters to predict the service life of a component.

6.4.1. Vickers microhardness.

Hardness measurements were conducted in the cross-section of all processed alloys. For both types of nitrided samples, the surface hardness was measured in order to evaluate the hardness of the TiN coating layer. For the uncoated substrates and the reinforced samples, it is considered that materials are isotropic, and there are no differences between hardness values of the surface and cross-section. Vickers microhardness measurements for all samples are displayed in **Figure 6.15**.

It can be seen that all samples of the Ti-Nb-Fe system achieve higher hardness values than samples of the Ti-Nb system. This fact could be attributed to Fe addition having a strengthening effect in Ti alloys, enhancing the mechanical properties [61], [62], and to the higher apparent porosity observed in all samples with 40% Nb.

Reinforced titanium alloys show higher hardness than base alloys. TiN addition has a similar effect in both compositions. Hardness increases by about 40% for TH40-TiN and 35% for TH525-TiN compared to unreinforced alloys. In contrast, different effects are observed in TiB_2 reinforced alloys. TH40-TiB_2 composition shows a slight hardness increase (about 8%) with respect to the base alloy, whereas TH524-TiB_2 presents hardness values 56% higher than the untreated sample.

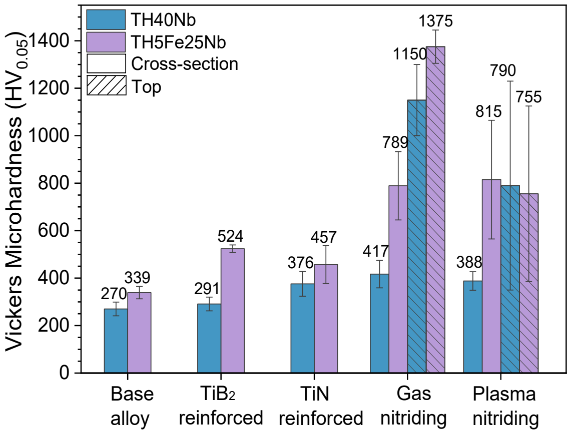

Figure 6.15. Vickers microhardness measurements of modified and untreated β-Ti alloys (TH40Nb and TH5Fe25Nb).

The relative low hardness increase of TH40-TiB_2 sample could be associated with the higher porosity, as well as the poor dispersion of TiB precipitates, which were formed in isolated regions, leaving unreinforced matrix areas. Hence, no significant hardness improvement is obtained. In contrast, the hardness improvement in the TH525-TiB_2 sample could be related to a high number density of fine whiskers observed in **Figure 6.6c**. It has been reported that fine and uniform distributed TiB whiskers enhance the mechanical properties [63]. Additionally, precipitates are embedded within the matrix, offering a better reinforcement effect.

Microstructural features influence the mechanical properties of the materials. Uniform and controlled microstructure is required to obtain improved mechanical properties. Although TiB_2 addition enhances hardness, it is highly affected by the size and distribution of whiskers. TiB_2 reinforcement was discarded for the next characterisation steps since it was considered that further experimental work would be necessary in order to obtain a controlled final microstructure, morphology and distribution of the precipitates formed in the *in-situ* reaction.

Diffusion surface treatments, such as gas and plasma nitriding, improve the substrate properties by the formation of a hard layer that acts as a barrier and protects the substrate. Additionally, as it was mentioned before, inward nitrogen diffusion toward the substrate occurs during these treatments. Thus, the matrix below coating becomes enriched in nitrogen, forming a solid solution. Initially, the solid solution is composed of β-Ti(N), and then, as nitrogen content increases, α-Ti(N) is formed. Finally, if the nitrogen content is high enough, nitride precipitates are formed. Solid solution and internal precipitates have a hardening effect on the nitrided substrate. Hence, hardness improvements depend on nitrogen diffusion toward the metal matrix. It is expected that for a deep diffusion zone, a higher matrix fraction will harden, increasing the bulk material hardness.

Figure 6.15 reveals that both nitrided samples show higher hardness than the respective untreated substrates. In addition, the hardness increase is greater for gas nitrided samples than for plasma nitrided samples. GN-TH40 and GN-TH525 show hardness values 54% and 133% higher than untreated TH40Nb and TH5Fe25Nb alloys, respectively. This suggests that the larger $TiN_{0.3}/\alpha$-Ti(N) needle-like precipitates below the GN-TH525 coating are more effective in increasing the hardness than the smaller precipitates found in GN-TH40.

In contrast, PN-TH40(TiN) and PN-TH525(TiN) achieved an increase of 3% and 78% higher than untreated TH40-TiN and TH525-TiN, respectively. The nitrogen amount measured in PN-TH40(TiN) matrix (about 9 at.% N) suggests that a solid solution α-Ti(N) was formed. Nevertheless, it is possible that the diffusion zone is too small to enhance the hardness significantly, because most of the matrix remains unaltered by nitrogen diffusion. Therefore, after the plasma nitriding treatment, the matrix is similar to untreated TH40-TiN, and it shows similar hardness values. In contrast, the nitrogen content in the PN-TH525(TiN) matrix is higher than PN-TH40(TiN), reaching about 15 at.% N. It can be deduced that the higher solid solution fraction, and the deeper diffusion zone formed in PN-TH525(TiN), increases the hardness of the substrate.

Nitriding treatment is highly influenced by nitrogen diffusion and hence by temperature. Plasma nitriding was conducted at a lower temperature (400 °C) than gas nitriding (900 °C). Several authors have reported higher hardness values for nitrided Ti alloys with increases in the nitriding temperature [16], [64]. Usually, a higher nitriding temperature promotes formation of a thicker coating layer and diffusion processes that allow solid solution strengthening and internal precipitates formation. Hence, the lower hardness increase of plasma nitrided samples compared to gas nitrided samples could be attributed to the smaller thickness and fewer precipitates due to the lower nitriding temperature of plasma nitriding treatment. Low temperature limits nitrogen diffusion into the substrate, reducing the diffusion zone and solid solution formation.

Regarding the coating hardness, it can be seen that GN-TH525 presents higher values than GN-TH40 (1375 HV and 1150 HV, respectively). This could be attributed to the thicker coating layer of GN-TH525 compared to GN-TH40. It has been reported that the Ti_2N phase has higher hardness than TiN. GN-TH525 coating is composed of a mixture of Ti_2N/TiN, while GN-TH40 is formed only by the TiN phase (**Figure 6.11**). Hence, both coating thickness and coating phases may explain the greater improvement in hardness of GN-TH525.

PN-TH40(TiN) and PN-TH525(TiN) samples show similar coating hardness, reaching about 790 HV and 755 HV, respectively. Similar coating hardness was expected since both samples show similar coating thickness (1 μm) and chemical composition, being mainly composed of δ-TiN phase.

It is noticeable that plasma nitrided coatings hardness is much lower than those obtained for gas nitrided. Nevertheless, a high standard deviation is observed in plasma nitrided coating, which reduces the average hardness value. The maximum hardness values of plasma nitrided coatings are closer to those of gas nitrided coatings. The high standard deviation may be attributed to internal cracks and voids found between coating layer and substrate. Regions with cracks become weak, while regions without cracks result are harder, which produces variability in hardness measurements.

Internal defects on the coating layer should be avoided in order to guarantee homogeneous mechanical properties. Internal cracks or defects reduce the coating adhesion and could favour the coating fracture and further detachment, leaving the substrate exposed against wear. In addition, if the coating layer breaks, coating debris are released, acting as a third body, accelerating the wear damage mechanisms. Plasma nitriding treatment of TiN reinforced alloys should be deeper studied, attempting to obtain free-defect coatings that improve wear resistance.

Given the hardness results, it can be concluded that both types of nitrided samples exhibited better overall wear behaviour than both types of reinforced alloys. The cross-section and surface hardness of reinforced alloys is homogeneous in all directions, since the reinforcement is homogeneously distributed within the metal matrix, On the contrary, nitrided samples present considerably higher surface hardness, more than twice than the cross-section hardness. The harder surface of nitrided samples, introduces additional advantages over reinforced alloys, concerning wear. Nitrided samples have a continuous TiN layer covering the whole sample surface, protecting the substrate against wear. In contrast, reinforced alloys present discontinuous reinforcements embedded into the matrix, so part of the metal matrix is left exposed: Ti matrix has lower hardness and, consequently, lower wear resistance than the ceramic phase; hence, it is reasonable to that expect nitrided samples will exhibit improved properties compared to reinforced alloys

6.4.2. .Elastic modulus.

Elastic modulus measurements of all processed samples are displayed in **Figure 6.16.** It can be seen that, TiN reinforced alloys present the highest elastic modulus values, reaching 114 GPa for TH40-TiN and 150 GPa for TH525-TiN. These values are even higher than those reported for pure CP-Ti (100 GPa) and the current Ti6Al4V (112 GPa) and Ti6Al7Nb (110 GPa) alloys [10]. Therefore, they are not suitable to be employed as implant materials.

On the contrary, gas nitrided and untreated alloys present the lowest elastic modulus values. Despite the significant differences in hardness, the elastic modulus does not seem to be affected, reaching values similar to the untreated alloys. This finding is consistent with results reported by Bèdouin et al. [65]. They found that elastic modulus of Ti-27 at.% Nb (Ti-42 wt.% Nb) alloy is not affected by gas nitriding treatment, despite the increase in substrate hardness. Improvement in hardness, keeping low the elastic modulus, is desirable for biomedical applications. Hence, gas nitriding of both β-Ti alloys could be a good alternative for developing implant materials.

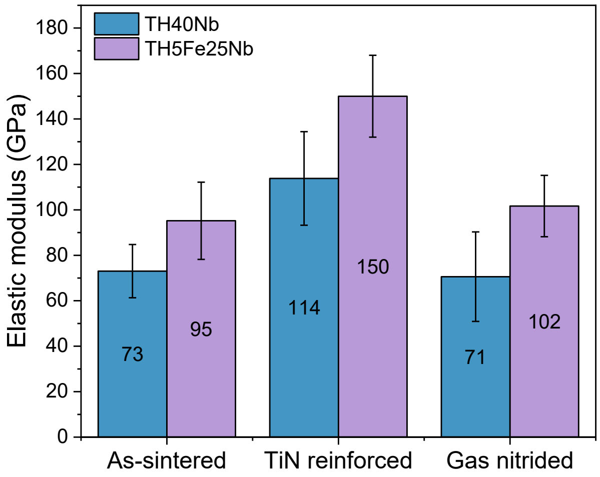

Figure 6.16. Elastic modulus values of untreated β-Ti alloys, TiN reinforced alloys and gas nitrided samples.

Samples containing 40% Nb exhibit lower elastic modulus values (around 70 GPa) than samples with 25% Nb and 5% Fe (about 100 GPa). This may be related to a higher amount of β-stabiliser that contributes to a greater reduction of elastic modulus [66]. Even though lower elastic modulus than Ti6Al4V and Ti6Al7Nb was achieved for the processed alloys, it is still higher than the bone; therefore, these materials should continue to be studied in order to reduce the elastic modulus further.

6.5. Wear behaviour

In this work, the wear resistance of both untreated β-Ti alloys (TH40Nb and TH5Fe25Nb) was evaluated, and compared to TiN reinforced alloys and samples subjected to gas nitriding. Wear resistance improvement was evaluated in terms of coefficient of friction (COF) evolution during the wear test, microstructure, wear track profile, and wear rate.

The evolution of the coefficient of friction (COF) for all samples during the dry sliding wear test at 10 N and 20 N is reported in **Figure 6.17**. All samples evaluated at 20 N exhibit slightly higher COF values than those observed for samples tested at 10 N.

For both load conditions, no measurable differences in friction between the substrates and the TiN reinforced alloys were found. Nevertheless, results suggest that TiN reinforced alloys achieve slight lower COF values compared to substrates. This reduction seems to be higher for TH525-TiN than for TH40-TiN sample. COF values of TiN reinforced samples increases progressively, especially at the beginning of the test, probably due to the fracture of the reinforcement particles, generating a third body, which is undesirable since it may favour the abrasive wear mechanism and the wear debris release into the body.

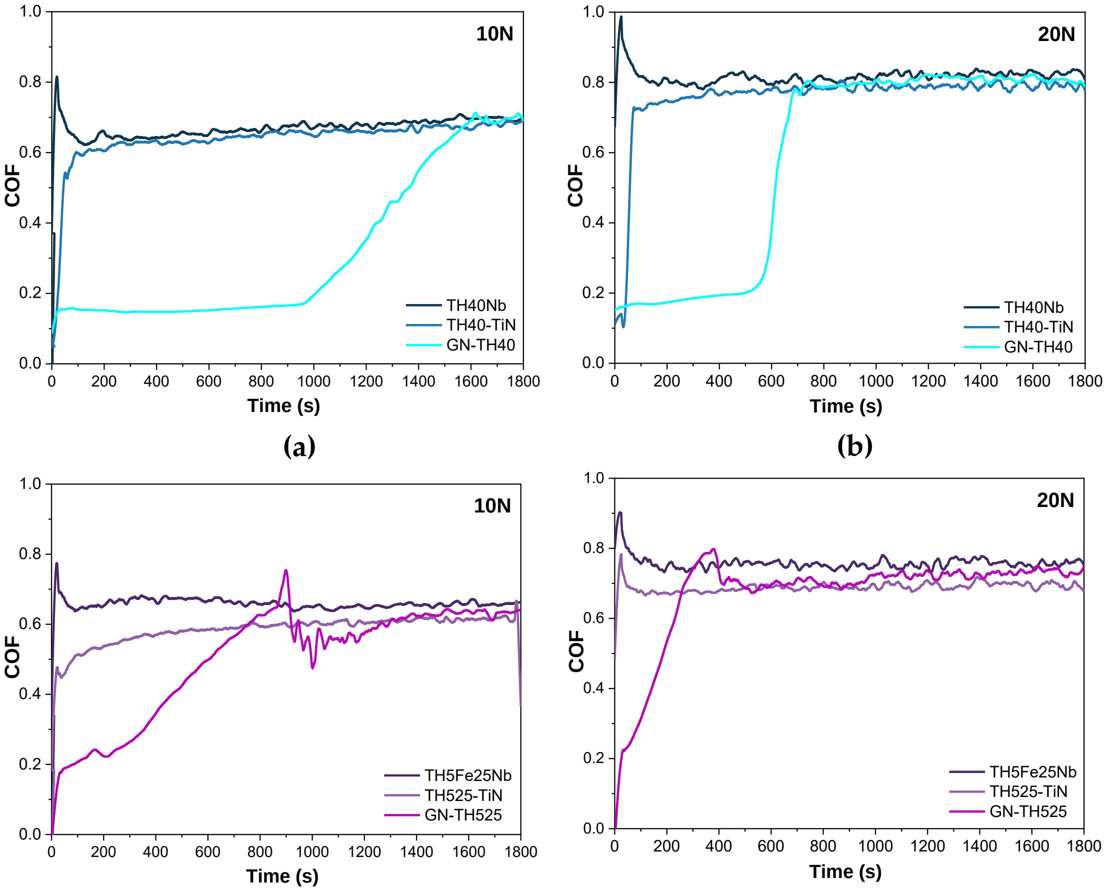

(a) (b)

(c) (d)

Figure 6.17. Coefficient of friction for as-sintered and modified β-Ti alloys: a) TH40Nb tested at 10 N, b) TH40Nb tested at 20N, c) TH5Fe25Nb tested at 10 N and d) TH5Fe25Nb tested at 20N.

COF values of gas nitrided samples were much lower than untreated alloys, suggesting the hard TiN coating protects the material, reducing the friction value. COF progressively increases over time, suggesting TiN layer is gradually damaged. Finally, COF reaches similar values to untreated alloys, indicating that the protective layer was removed, leaving the substrate surface exposed.

Initially, GN-TH40 samples exhibit COF of 0.15. This keeps relatively constant until around 950 s for 10 N and 500 s for 20 N. Then, COF shows a drastic increase related to the loss or damage of the TiN coating layer. COF increases up to 0.70 at around 1500 s, and up to 0.80 around 650 s, for samples evaluated at 10 N and 20 N, respectively. After this point, the external layer is lost, and samples exhibit similar COF to the substrates.

For GN-TH525, COF increases continuously from 0.2 until it reaches a maximum of 0.75 around 900 s, for samples tested at 10 N; and 0.80 after 400 s, for samples tested at 20 N.

Then, COF decreases until it reaches a similar COF to the base alloy. The oscillations of COF after the TiN layer is lost could be due to debris fragments of coating detached during the test, which increase the friction, acting as a third body. Subsequently, rearrangement of debris particles may take place, reducing and stabilising the COF.

So far, it can be concluded that the TiN layer kept adhered for a longer time in samples tested at 10 N than at 20 N, and in samples GN-TH40 than in GN-TH525. Despite the fact that, GN-TH525 has a thicker TiN layer (3 μm) than GN-TH40 (1 μm) and shows higher hardness (both on the surface and cross-section) than GN-TH40 (**Figure 6.15**), the coating layer was removed before for GN-TH525. TiN layer of GN-TH525 sample has high hardness; hence, it could be more brittle than that of GN-TH40, which may provoke the coating fracture or breakage. In addition, wear resistance could be influenced by internal precipitates and new phases formed after nitriding treatment **(Figure 6.9**) rather than the thickness of the nitrided layer [14], [67].

The morphology of the worn surface, together with the wear track profiles obtained after sliding tests at 10 N and 20 N for Ti-Nb and Ti-Fe-Nb alloys, is shown in **Figure 6.18** and **Figure 6.19**, respectively. Yellow dotted lines indicate the wear track width. Complementary, **Table 6.4** displays the width average of the wear tracks measured for all samples tested at both loads.

Table 6.4. Width of wear tracks obtained after dry sliding test at 10 and 20 N load.

	Width (mm)	
Sample	**10 N**	**20 N**
TH40Nb	2.03 ± 0.08	2.64 ± 0.02
TH40-TiN	2.12 ± 0.07	2.63 ± 0.20
GN-TH40	1.04 ± 0.05	2.49 ± 0.10
TH5Fe25Nb	1.96 ± 0.08	2.47 ± 0.06
TH525-TiN	1.63 ± 0.09	2.29 ± 0.20
GN-TH525	1.62 ± 0.02	2.21 ± 0.20

From the general view of the wear tracks, wider and deeper tracks with greater signs of wear damage can be observed for samples tested at 20 N compared to those tested at 10 N. This was expected, since higher load usually implies an increase in the wear damage level [68]. On the other hand, the modified alloys, either by addition of TiN particles or by gas nitriding treatment, show a reduction in wear tack width, compared to the untreated substrates, except for TH40-TiN samples. TH40-TiN wear tracks present similar width (even higher) values and greater depth than the base alloy (TH40Nb), suggesting a greater wear level. Hence, TiN addition does not seem to considerably increase the wear resistance for TH40Nb alloy. In contrast, TH525-TiN shows a width and depth reduction compared to TH5Fe25Nb, indicating better wear resistance than the substrate and TH40-TiN alloy.

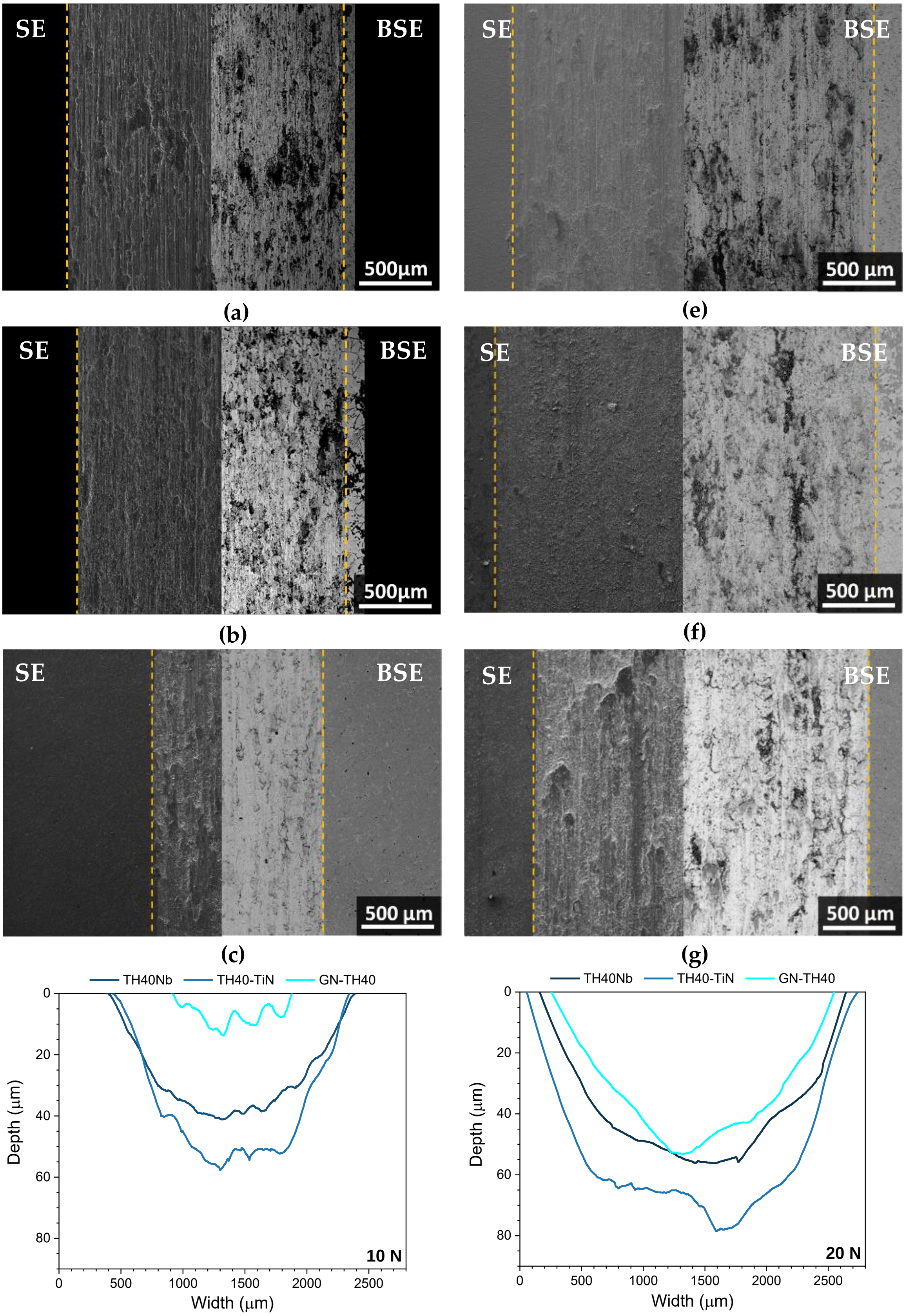

(a) (e) (b) (f) (c) (g) (d) (h)

Figure 6.18. SE-BSE SEM images of the wear tracks of TH40Nb alloys after dry sliding tests at 10 N (a-c) and 20 N (e-g) for: (a,e) As-sintered TH40Nb; (b,f) TH40-TiN; (c,g) GN-TH40. (d,h) Wear tracks profile measured with a profilometer.

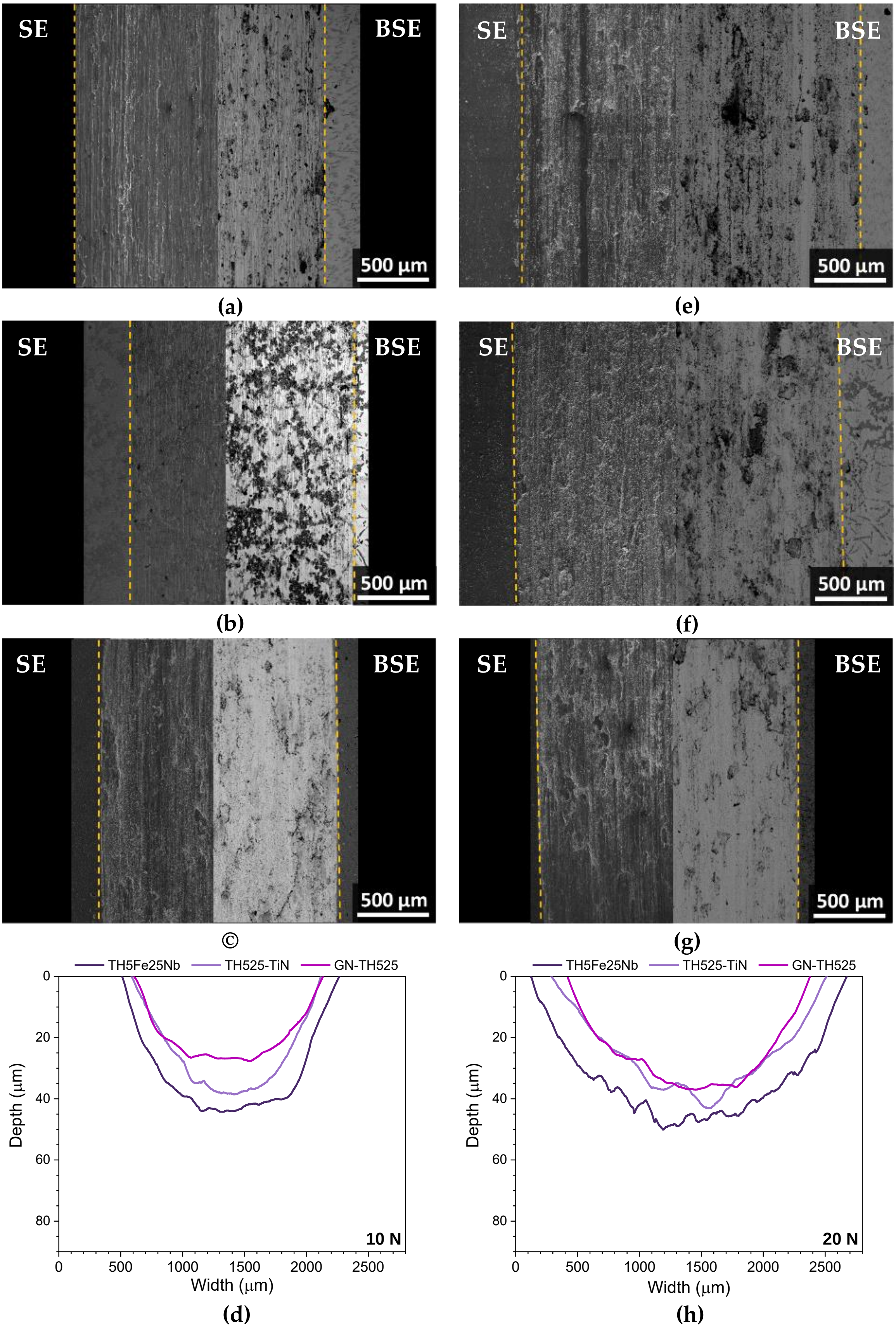

(a) (e)

(b) (f)

© (g)

(d) (h)

Figure 6.19. SE-BSE SEM images of the wear tracks of TH5Fe25Nb alloys after dry sliding tests at 10 N (a-c) and 20 N (e-g) for: (a,e) As-sintered TH5Fe25Nb; (b,f) TH525-TiN; (c,g) GN-TH525 and (d,h) Wear tracks profile measured with a profilometer.

Gas nitrided samples exhibit the narrowest wear tracks. GN-TH40 tested at 10 N presents a wear track width with values around 1.04 mm, while GN-TH525 reached about 1.62 mm, which corresponds to a reduction of 50% and 15%, respectively, compared to untreated alloys. For nitrided samples evaluated at 20 N, width reduction is also observed, but it is lower than that obtained at 10 N, achieving a reduction of around 5% and 7% for GN-TH40 and GN-TH525, respectively.

Regarding the depth of wear track of gas nitride alloys, samples evaluated at 10 N load reach a maximum depth of 10 μm for GN-TH40 (**Figure 6.18d**) and 25 μm for GN-TH525 (**Figure 6.19d**); while under more severe conditions (20 N), samples show a maximum depth of 30 μm for GN-TH525 (**Figure 6.19h**) and 50 μm for GN-TH40 (**Figure 6.18h**). Considering the microstructure of gas nitrided samples (**Figure 6.20**), it can be observed that the wear track depth does not exceed the diffusion zone of GN-TH525, affected by nitriding treatment, where there are large and coarse internal precipitates. These precipitates seem to slow down the wear advance, reducing the track depth more efficiently than GN-TH40 sample, which presents a high number density of small precipitates distributed in the β matrix. This agrees with results reported by Chan et al. [14]. They attribute the wear behaviour enhancement of laser gas alloyed with nitrogen Ti-35.3Nb-7.3Zr-5.7Ta alloy to the internal nitrogen-rich precipitates.

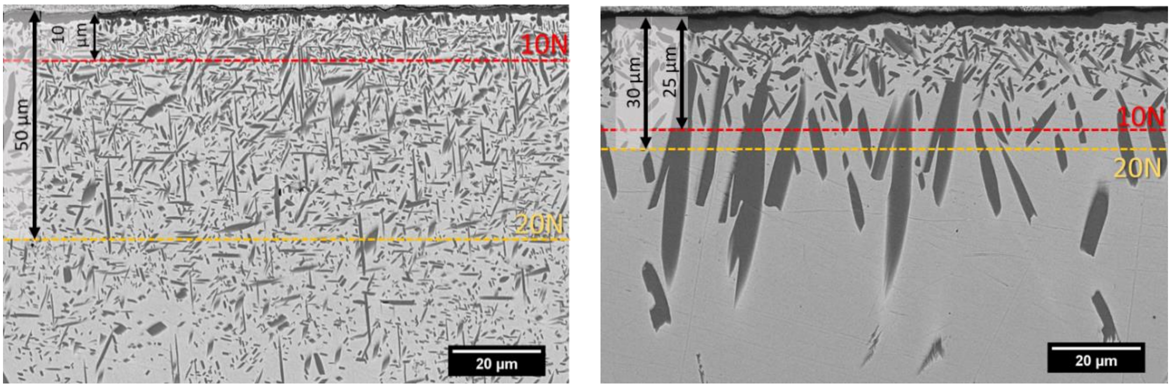

(a) **(b)**

Figure 6.20. SEM cross-section images of gas nitrided simples indicating the maximum depth of the wear tracks achieved at 10 N and 20 N. a) GN-TH40 and b) GN-TH525.

In order to know the mechanisms that govern the wear behaviour of the evaluated samples, wear tracks details of Ti-Nb and Ti-Fe-Nb alloys are displayed in **Figure 6.21** and **Figure 6.22,** respectively. SEM images suggest lower wear damage for gas nitrided samples, followed by TiN reinforced alloys, and finally, untreated samples. The relative higher wear debris amount generated in samples evaluated at 20 N indicates a higher wear damage level than at 10 N. Wear debris corresponds to, in part, broken TiN particles (from either the coating layer or the TiN reinforced matrix) and a mix of hardened particles of the loose oxide

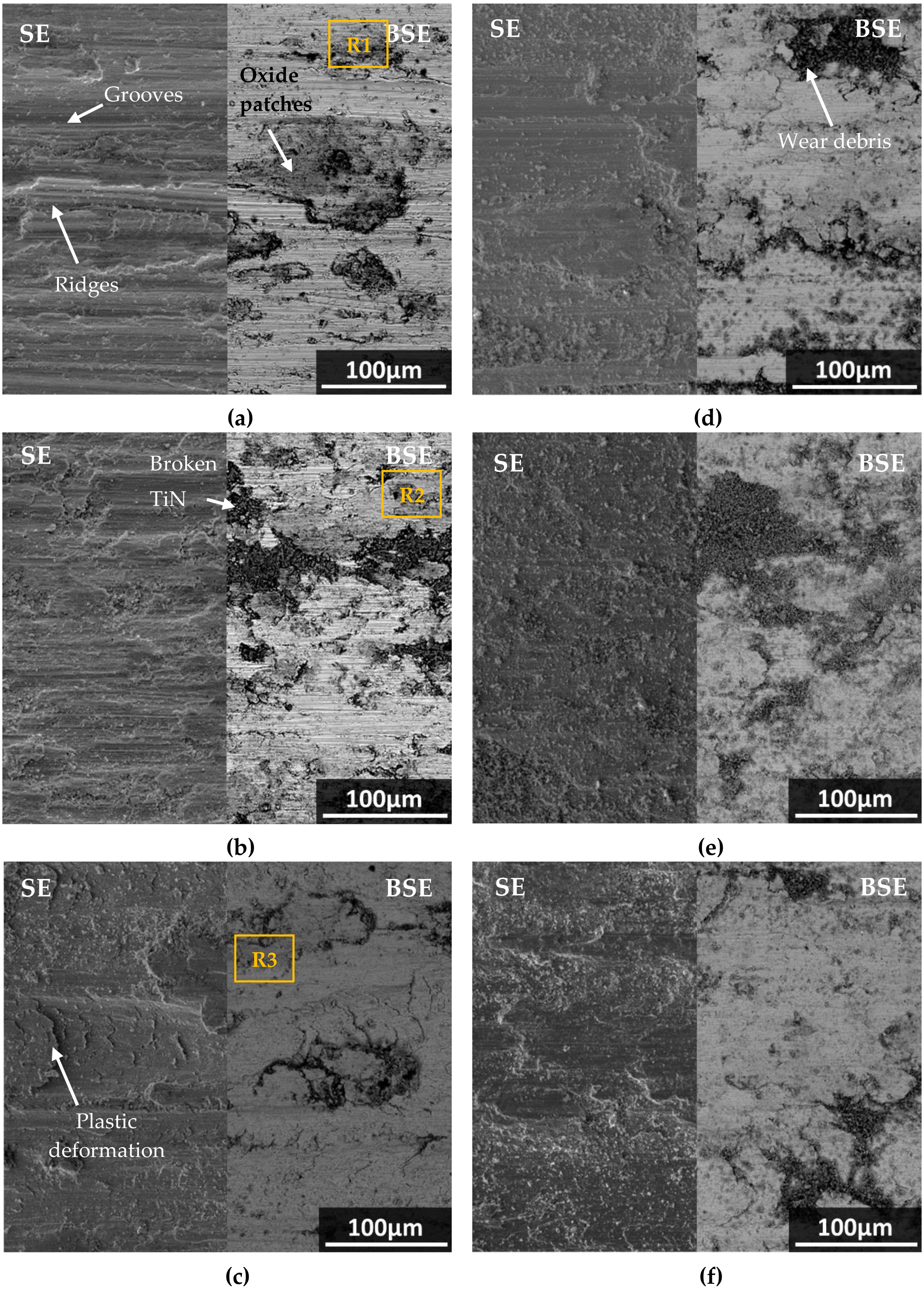

(a) (d) (b) (e) (c) (f)

Figure 6.21. SE-BSE SEM images of details of the worn surfaces of Ti-Nb alloys after dry sliding wear test (a-c) at 10 N load, (d-f) at 20 N load. (a, d) Untreated TH40Nb; (b, e) TH40-TiN and (c, f) GN-TH40.

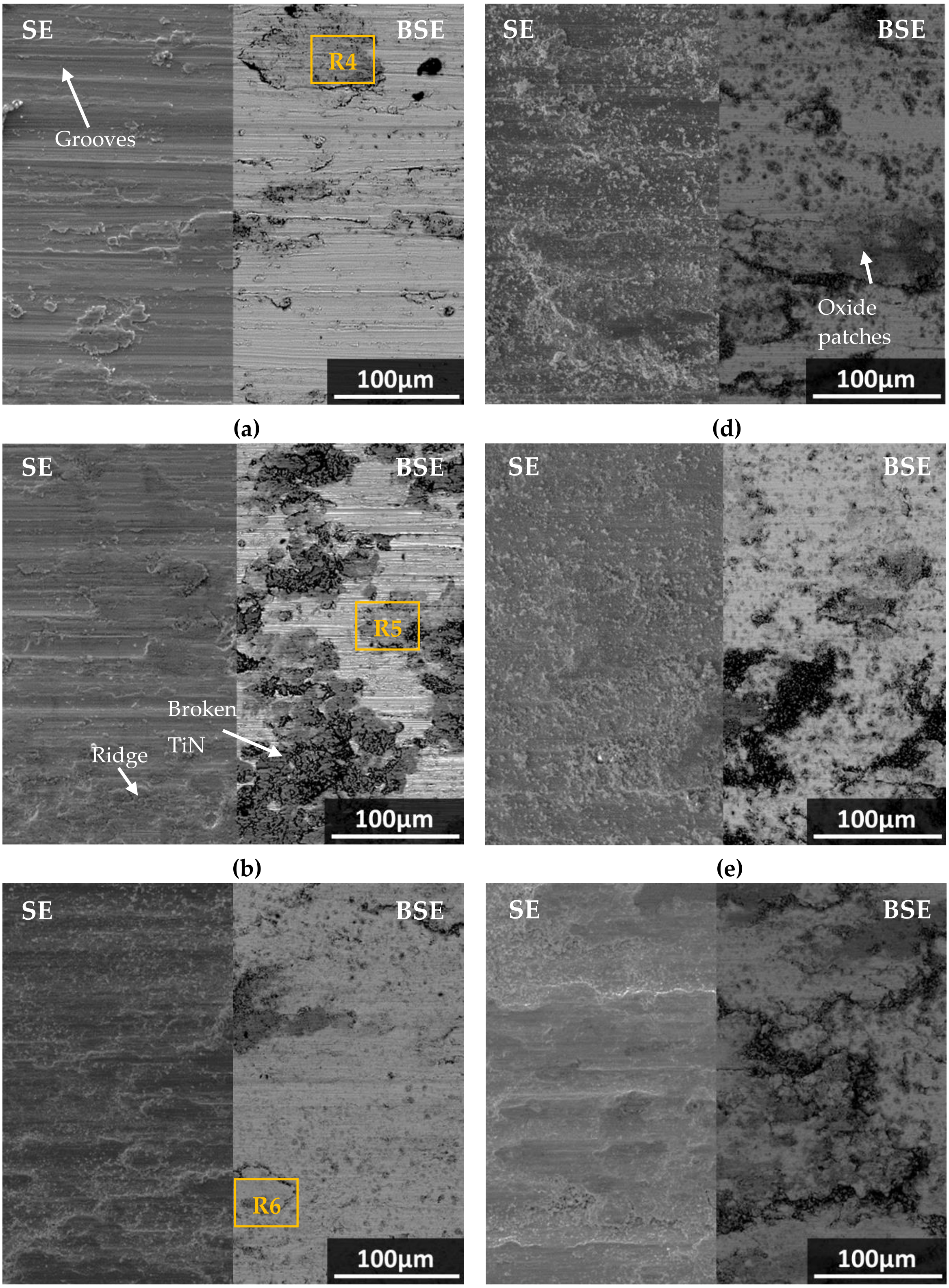

(a) (d)

(b) (e)

(c) (f)

Figure 6.22. SE-BSE SEM images of details of the worn surfaces of Ti-Nb alloys after dry sliding wear test (a-c) at 10 N load, (d-f) at 20 N load. (a, d) Untreated TH40Nb; (b, e) TH40-TiN and (c, f) GN-TH40.

debris and base material alloy. They act as a third body and may favour abrasive wear, which affects the tribological properties.

In general, a mix of wear damage mechanisms was observed for all tested samples. Parallel grooves along the sliding direction, produced from the continuous crushing and ploughing by the counter material, confirm abrasive wear mechanism. Darker zones of the wear tracks (indicated by a yellow square in **Figure 6.21** and **Figure 6.22**) were analysed by EDS analysis (**Table 6.5**). Results reveal the presence of Al and O due to the transfer from the counter material, forming oxide patches, which is a sign of adhesive wear. All modified alloys present a lower amount of Al content than untreated alloys.

Table 6.5. EDS measurement of indicated zones of the worn surface of samples tested at 10 N load. Composition expressed in weight per cent (wt.%)

		Composition (wt.%)					
Sample	**Region**	**Ti**	**Nb**	**Al**	**O**	**N**	**Fe**
TH40Nb	R1	46.8	35.3	7.2	10.7	---	---
TH40-TiN	R2	53.2	27.0	4.1	6.9	8.9	---
GN-TH40	R3	48.4	40.2	1.8	2.3	7.3	---
TH5Fe25Nb	R4	56.8	23.5	6.7	8.7	---	4.3
TH525-TiN	R5	59.3	22.9	2.3	5.4	5.3	4.7
GN-TH525	R6	61.4	22.5	1.6	2.1	8.4	3.8

Besides, worn surfaces show signs of plastic deformation and ridges along the sliding direction due to the accumulation of removed material and wear debris. Ridges could modify the contact areas during sliding because of material deposition on the surface.

Untreated TH40Nb presents deeper grooves than untreated TH5Fe25Nb, which exhibits smother wear grooves. This suggests higher abrasive wear. The bigger ridges observed in TH40Nb denote that a larger material fraction was released, then it was accumulated, becoming entrapped by squashing in these areas. Images suggest that there are more dark regions, corresponding to oxide patches, in TH40Nb, denoting higher adhesive wear. Although both untreated alloys show the same wear mechanism signs, they seem more severe for TH40Nb. The lower damage level of TH5Fe25Nb may be related to its lower porosity, and its higher hardness (339 HV) compared to TH40Nb (270 HV), which results in wear resistance improvement.

Similar behaviour was observed in TiN reinforced alloys. At 10 N, sample TH40-TiN shows deeper grooves than TH525-TiN. Additionally, it appears that there is a higher amount of wear particles in the TH40-TiN samples, which corresponds to broken TiN particles. Reinforcement particles present a higher hardness than the β-Ti matrix, which could facilitate their fracture. In addition, as seen in **Figure 6.7**, reinforcements in the TH40-TiN sample present internal porosity and are worse consolidated than in the case of the TH525-TiN samples. This could weaken TiN particles, and they may break more easily and begin to act as a third body. Titanium nitride has high hardness so that the broken particles may accelerate abrasive wear. This might explain the increase in both width and depth of TH40-TiN wear tracks compared to the substrate TH40Nb.

On the contrary, in TH525-TiN, as the reinforcement is better consolidated and integrated into the matrix, appears to be more resistant. The softer ridges observed in TH525-TiN confirm that a less material was removed from the surface, suggesting better reinforcement resistance than in TH40-TiN, which has more pronounced ridges. Once the metal matrix is removed from the surface, TiN reinforcements are exposed; although they also break, they protect the matrix during sliding since they appear to remain more compact or adhered to the surface. As the particles are not released, they do not accelerate wear, hence a smoother worn surface is observed compared to the TH40-TiN sample, as well as a reduction in the wear track profile depth as compared to the substrate TH5Fe25Nb.

The surface of gas nitrided samples was the least affected. Plastic deformation, tearing, and flakes covering the worn surface, especially for GN-TH40 at 10 N, are observed. This morphology of the worn surface suggests adhesive wear. At 10 N, more severe wear damage was observed for GN-TH525 alloy. This could be related to the fact that the TiN coating layer was removed after 900 s in GNTH525, while in GN-TH40, removal occurs after 1500 s (**Figure 6.17**). Therfore, the substrate was exposed to wear for a longer time, increasing wear damage. Moreover, G GN-TH525 has a coarser TiN layer; hence, a higher amount of TiN fragments is detached once the coating layer is removed, which might also contribute to increasing wear damage.

Additionally, EDS analysis of GN-TH40 sample at 10 N (**Table 6.5**) reveals a decrease of Al amount, which suggests less transfer of material from the alumina ball; and an increase of the Nb content, which could be attributed to the formation of a Nb_2O_5 passive layer. Low Al content was also detected in GN-TH525, suggesting lower transfer of material than for untreated alloys; however, EDS analysis does not confirm the presence of this passive layer. It has been reported that Nb_2O_5 passive layer enhances the wear resistance since it has a lubricant effect, is more stable, and repassivates quicker than titanium oxides. [10], [69]

Although at 20 N, GN-TH525 shows a narrower and less deep wear track than GN-TH40, and the TiN coating layer kept adhered to the substrate for a shorter time (around 400 s for GN-TH525 and 650 s for GN-TH40, **Figure 6.17**), the GN-TH525 worn surface seems more affected. This may be related to the higher amount of TiN fragments coming from the coating that generates a greater residual stress relief, as can be observed in (**Figure 6.22f**). However, since the GN-TH525 substrate has a considerably higher hardness (789 HV) than GN-TH40 (417 HV), better wear resistance and shallower wear profile is expected and. On the other hand, the passive layer may likely have formed in GN-TH40, and when it reached a critical thickness, it may become unstable and break, forming new wear debris that aggravates the wear.

To sum up, a combination of abrasive and adhesive wear seems to be the wear mechanism in untreated alloys. Abrasive wear is the predominant mechanism in TiN reinforced alloys, while gas nitride samples are dominated by adhesive wear. The wear mechanisms at 20 N are similar to those at 10 N but present more severe damage due to a higher amount of wear debris detached from the surface, which acts as a third body, accelerating wear.

The wear rate values after dry sliding wear tests are presented in **Figure 6.23**. In agreement with the previous results, samples tested at 20 N show a higher wear rate than samples tested at 10 N. Furthermore, alloys with Ti-Nb-Fe matrix, both untreated, nitride and reinforced, present a lower wear rate than the Ti-Nb matrix alloys system, except for GN-TH40. This is attributed to the higher hardness and lower porosity of the Ti-Fe-Nb alloys, which plays an important role to enhance the wear behaviour.

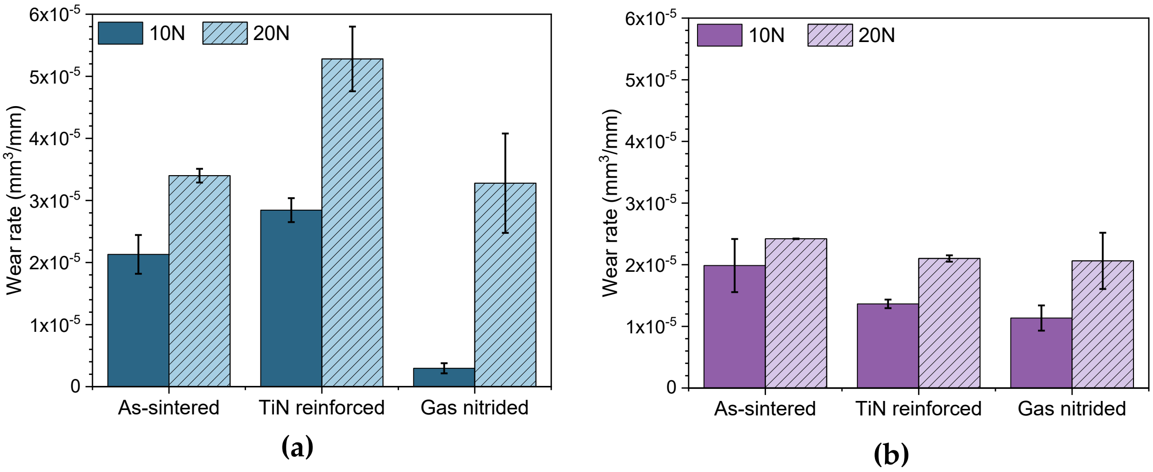

Figure 6.23. Wear rate after dry sliding wear tests performed at 10 N and 20 N for untreated and modified β-Ti alloys (TiN reinforced and Gas nitrided). a) TH40Nb alloys and b) TH5Fe25Nb alloys.

TH40-TiN samples show a higher wear rate for both load conditions compared to untreated TH40Nb alloys, achieving about 33% and 53% higher wear at 10 N and 20 N, respectively. On the contrary, GN-TH40 exhibits the lowest wear rate with a reduction of around 86% compared to TH40Nb at 10 N. At 20 N, there is a wear rate reduction, but it is much lower, reaching about 4% less than untreated alloy at the same condition.

For alloys of the Ti-Fe-Nb system, gas nitrided samples show the highest wear rate reduction, followed by TiN reinforced samples. The wear rate is reduced for both load conditions; nevertheless, this reduction is more pronounced for samples evaluated at 10 N than at 20 N. GN-TH525 samples exhibit a wear rate reduction of 43% and 15% for 10 N and 20 N with respect to untreated alloys, while TH525-TiN alloy reaches about 31% at 10 N and 15% at 20 N.

6.6. Partial conclusions

From the results shown in this chapter, the main conclusions can be summarised as follow:

Processing of reinforced β-Ti matrix composites and Coating

1. TiN and TiB_2 reinforced alloys show a completely different microstructure. TiB whiskers and $TiN_{0.3}$ particulates are the obtained reinforcement phases in each case. Reinforced TH5Fe25Nb alloys exhibited a more homogeneous microstructure than reinforced TH40Nb.

2. **Gas nitriding** treatment of base alloys results in a **homogeneous, continuous and dense nitride layer.** The thickness of this layer was1.17 ± 0.41 μm for GN-TH40 and 3.35 ± 0.61 μm for GN-TH525. Nitride layer of GN-TH525 sample is composed of a mix Ti_2N and TiN, whereas for GN-TH40, it is composed of TiN. Small Nb amount was detected in the coating layer due to the mutual solubility of titanium and niobium nitride.

Nb content influences on **morphology and distribution of precipitate**s formed during nitriding treatments. Lower Nb (25 wt.%) addition results in coarser and larger needle-like precipitates, corresponding to α-Ti(N)/$TiN_{0.3}$ phase. For a higher Nb amount (40 wt.%), the number density of precipitates increases, becoming thinner and smaller with a deeper diffusion zone. This is related to changes in the nucleation mechanisms produced by increasing Nb. Ti segregation beneath the coating layer leaves the matrix region enriched in Nb, ultimately leading to the formation of Nb_2N precipitates.

3. **Plasma nitriding** of TiN reinforced alloys provides a continuous TiN layer of about 1 μm in thickness for both compositions. Nevertheless, the coating layer presents internal cracks generated by thermal expansion mismatch between matrix and reinforcement, which compromise the coating adhesion.

Mechanical properties:

1. **All modified alloys present higher hardness** compared to untreated samples. The hardness increase was higher for samples of Ti-Fe-Nb system than for the Ti-Nb system. TH525-TiB_2 and TH525-TiN reach values 54% and 35% higher than untreated samples, respectively. While, GN-TH525 show increase of 132% compared to the base alloy, and PN-TH525(TiN) shows increases by about 78% compared to untreated TH525-TiN alloy.

2. Gas nitriding treatment provides higher hardness increase than plasma nitriding, since gas nitriding involves higher interaction between nitrogen and substrate, promoting the solid solution strengthening and internal precipitates formation, and hence, higher hardness.

3. TiN reinforced alloys present the highest elastic modulus values, reaching 114 GPa for TH40-TiN and 150 GPa for TH525-TiN. In contrast, gas nitrided samples, despite achieved an improved hardness, show elastic modulus values similar to untreated alloys, racing about 71 MPa for GN-TH40 and 102 MPa for GN-TH525. The balance between high hardness and low young modulus suggest gas nitriding treatment could be a promising alternative to enhance the wear resistance of biomedical Ti alloys.

Wear resistance:

1. Samples of **Ti-Nb-Fe system show better wear resistance** than samples of Ti-Nb system. This is attributed to the strengthening effect of Fe, higher hardness and lower porosity of Ti-5Fe-25Nb alloys compared to Ti-40Nb.

2. Untreated samples show signs of **adhesive and abrasive wear mechanism**. Abrasive wear is the predominant mechanism in TiN reinforced alloys, while gas nitride samples are dominated by adhesive wear. More severe wear damage was observed in samples tested at 20 N than at 10 N due to the higher wear debris amount.

3. The addition of TiN particles reduces the wear rate of TH525-TiN alloys, showing 31% (at 10 N) and 13% (at 20 N) lower than TH5Fe25Nb base alloy. In contrast, wear rate increases for TH40-TiN composition between 33% (at 10 N) and 55% (at 20 N) higher than untreated TH40Nb. This suggests wear resistance of TiN reinforced alloys is strongly influenced by the consolidation characteristics and homogeneity of the reinforcement phase within the matrix.

4. **Gas nitriding treatment allows enhancing wear resistance** of the two studied Ti alloys at both load conditions. At 10 N, wear rate was 86% and 43 % lower than untreated alloys for GN-TH40 and GN-TH525, respectively. At 20 N, lower wear rate reduction was obtained than at 10 N, achieving about 4% and 15 % lower than untreated samples, for GN-TH40 and GN-TH525, respectively.

References

[1] OECD, "Health at a Glance 2011: OECD Indicators," *OECD Publ.*, 2011.

[2] K. . Sipek, M. . Lyvers, and M. . Mathew, "Failure Causes in Total Hip Replacements: A Review.," *Austin J. Orthop. Rheumatol.*, vol. 5, no. 1, 2018.

[3] M. Abdel-Hady Gepreel and M. Niinomi, "Biocompatibility of Ti-alloys for long-term implantation," *J. Mech. Behav. Biomed. Mater.*, vol. 20, pp. 407–415, 2013.

[4] Q. Chen and G. A. Thouas, "Metallic implant biomaterials," *Mater. Sci. Eng. R Reports*, vol. 87, pp. 1–57, 2015.

[5] M. Kaur and K. Singh, "Review on titanium and titanium based alloys as biomaterials for orthopaedic applications," *Mater. Sci. Eng. C*, vol. 102, pp. 844–862, 2019.

[6] M. Long and H. J. Rack, "Titanium alloys in total joint replacement- a materials science perspective," *Biomaterials*, vol. 19, pp. 1621–1639, 1998.

[7] M. B. Nasab, M. R. and Hassan, and B. Bin Sahari, "Metallic Biomaterials of Knee and Hip-A Review," *Trends Biomater. Artif. Organs*, vol. 24, no. 2, pp. 69–82, 2010.

[8] H. Mohseni, P. Nandwana, A. Tsoi, R. Banerjee, and T. W. Scharf, "In situ nitrided titanium alloys: Microstructural evolution during solidification and wear," *Acta Mater.*, vol. 83, pp. 61–74, 2015.

[9] W. Qu, X. Sun, B. Yuan, K. Li, and Z. Wang, "Tribological behaviour of biomedical Ti – Zr-based shape memory alloys," *Rare Met.*, vol. 36, no. 6, pp. 478–484, 2017.

[10] M. Geetha, A. K. Singh, R. Asokamani, and A. K. Gogia, "Ti based biomaterials, the ultimate choice for orthopaedic implants- A review.," *Prog. Mater. Sci.*, vol. 54, no. 3, pp. 397–425, 2009.

[11] A. Zhecheva, W. Sha, S. Malinov, and A. Long, "Enhancing the microstructure and properties of titanium alloys through nitriding and other surface engineering methods," *Surf. Coatings Technol.*, vol. 200, no. 7, pp. 2192–2207, 2005.

[12] F. Yildiz, A. F. Yetim, A. Alsaran, and A. Çelik, "Plasma nitriding behavior of Ti6Al4V orthopedic alloy," *Surf. Coatings Technol.*, vol. 202, no. 11, pp. 2471–2476, 2008.

[13] J. Kang *et al.*, "Tribological behavior of titanium alloy treated by nitriding and surface texturing composite technology," *Materials (Basel).*, vol. 12, no. 2, 2019.

[14] C. W. Chan *et al.*, "Enhancement of wear and corrosion resistance of beta titanium alloy by laser gas alloying with nitrogen," *Appl. Surf. Sci.*, vol. 367, pp. 80–90, 2016.

[15] X. Liu, P. K. Chu, and C. Ding, "Surface modification of titanium, titanium alloys, and related materials for biomedical applications," *Mater. Sci. Eng. R*, vol. 47, pp. 49–121, 2005.

[16] H. Spies, B. Reinhold, K. Wilsdorf, H. Spies, B. Reinhold, and K. Wilsdorf, "Gas nitriding-Process control and nitriding non-ferrous alloys," *Surf. Eng.*, vol. 17, no. 1, pp. 41–54, 2001.

[17] Z. D. Cui, S. L. Zhu, H. C. Man, and X. J. Yang, "Microstructure and wear performance of gradient Ti/TiN metal matrix composite coating synthesized using a gas nitriding

technology," *Surf. Coatings Technol.*, vol. 190, no. 2–3, pp. 309–313, 2005.

[18] V. V. Dabhade, T. R. R. Mohan, and P. Ramakrishnan, "Sintering behavior of titanium-titanium nitride nanocomposite powders," *J. Alloys Compd.*, vol. 453, no. 1–2, pp. 215–221, 2008.

[19] J. I. Silva, A. C. Alves, A. M. Pinto, F. S. Silva, and F. Toptan, "Dry sliding wear behaviour of Ti-TiB-TiNx in-situ composite synthesised by reactive hot pressing," *Int. J. Surf. Sci. Eng.*, vol. 10, no. 4, pp. 317–329, 2016.

[20] I. Y. Kim, B. J. Choi, Y. J. Kim, and Y. Z. Lee, "Friction and wear behavior of titanium matrix (TiB + TiC) composites," *Wear*, vol. 271, no. 9–10, pp. 1962–1965, 2011.

[21] S. C. Tjong and Y. Mai, "Processing-structure-property aspects of particulate- and whisker-reinforced titanium matrix composites," *Compos. Sci. Technol.*, vol. 68, pp. 583–601, 2008.

[22] K. S. Ravi Chandran, K. B. Panda, and S. S. Sahay, "TiBw-reinforced Ti composites: Processing, properties, application prospects, and research needs," *Jom*, vol. 56, no. 5, pp. 42–48, 2004.

[23] T. Saito, "The automotive application of discontinuously reinforced TiB-Ti composites," *Jom*, vol. 56, no. 5, pp. 33–36, 2004.

[24] M. Das, K. Bhattacharya, S. A. Dittrick, and C. Mandal, "In situ synthesized TiB-TiN reinforced Ti6Al4V alloy composite coatings: Microstructure, tribological and in-vitro biocompatibility," *J. Mech. Behav. Biomed. Mater.*, vol. 29, pp. 259–271, 2014.

[25] S. Kundu, M. Hussain, V. Kumar, S. Kumar, and A. K. Das, "Direct metal laser sintering of TiN reinforced Ti6Al4V alloy based metal matrix composite: Fabrication and characterization," *Int. J. Adv. Manuf. Technol.*, vol. 97, no. 5–8, pp. 2635–2646, 2018.

[26] M. E. Maja, O. E. Falodun, B. A. Obadele, S. R. Oke, and P. A. Olubambi, "Nanoindentation studies on TiN nanoceramic reinforced Ti–6Al–4V matrix composite," *Ceram. Int.*, vol. 44, no. 4, pp. 4419–4425, 2018.

[27] Y. Dong, Y. Li, T. Ebel, and M. Yan, "Cost-affordable, high-performance Ti-TiB composite for selective laser melting additive manufacturing," *J. Mater. Res.*, vol. 35, no. 15, pp. 1922–1935, 2020.

[28] A. Sabahi Namini and M. Azadbeh, "Microstructural characterisation and mechanical properties of spark plasma-sintered TiB2-reinforced titanium matrix composite," *Powder Metall.*, vol. 60, no. 1, pp. 22–32, 2017.

[29] Y. F. Yang, M. Yan, S. D. Luo, G. B. Schaffer, and M. Quian, "Modification of the α-Ti laths to near equiaxed α-Ti grains in as-sintered titanium and titanium alloys by a small addition of boron," *J. Alloys Compd.*, vol. 579, pp. 553–557, 2013.

[30] K. Morsi and V. V. Patel, "Processing and properties of titanium-titanium boride (TiBw) matrix composites - A review," *J. Mater. Sci.*, vol. 42, no. 6, pp. 2037–2047, 2007.

[31] M. Selva Kumar, P. Chandrasekar, P. Chandramohan, and M. Mohanraj, "Characterisation of titanium-titanium boride composites processed by powder metallurgy techniques," *Mater. Charact.*, vol. 73, pp. 43–51, 2012.

[32] S. S. Sahay, K. S. Ravichandran, R. Atri, B. Chen, and J. Rubin, "Evolution of

microstructure and phases in in situ processed Ti-TiB composites containing high volume fractions of TiB whiskers," *J. Mater. Res.*, vol. 14, no. 11, pp. 4214–4223, 1999.

[33] K. B. Panda and K. S. Ravi Chandran, "Titanium-titanium boride (Ti-TiB) functionally graded materials through reaction sintering: Synthesis, microstructure, and properties," *Metall. Mater. Trans. A Phys. Metall. Mater. Sci.*, vol. 34 A, no. 9, pp. 1993–2003, 2003.

[34] K. B. Panda and K. S. Ravi Chandran, "Synthesis of ductile titanium-titanium boride (Ti-TiB) composites with a beta-titanium matrix: The nature of TiB formation and composite properties," *Metall. Mater. Trans. A Phys. Metall. Mater. Sci.*, vol. 34 A, no. 6, pp. 1371–1385, 2003.

[35] H. Attar *et al.*, "Comparative study of microstructures and mechanical properties of in situ Ti-TiB composites produced by selective laser melting, powder metallurgy, and casting technologies," *J. Mater. Res.*, vol. 29, no. 17, pp. 1941–1950, 2014.

[36] H. Feng, D. Jia, and Y. Zhou, "Spark plasma sintering reaction synthesized TiB reinforced titanium matrix composites," *Compos. Part A*, vol. 36, pp. 558–563, 2005.

[37] A. Mohammadzadeh, M. Azadbeh, H. Danninger, and A. Sabahi, "Ti-TiB2 composites consolidated by spark plasma sintering: Reaction mechanism, characteristics of in-situ formed phases and densification behavior," *Mater. Chem. Phys.*, vol. 242, 2020.

[38] C. Chirico, S. A. Tsipas, P. Wilczynski, and E. Gordo, "Beta titanium alloys produced from titanium hydride: Effect of alloying elements on titanium hydride decomposition," *Metals (Basel).*, vol. 10, no. 5, 2020.

[39] H. Singh, M. Hayat, Z. He, V. K. Peterson, R. Das, and P. Cao, "In situ neutron diffraction observations of Ti-TiB composites," *Compos. Part A*, vol. 124, 2019.

[40] R. P. Elliott, "Diffusion in Titanium and Titanium Alloys," p. 58, 1962.

[41] H. Nakajima and M. Koiwa, "Diffusion in Titanium," *ISIJ Int.*, vol. 31, no. 8, pp. 757–766, 1991.

[42] O. E. Falodun, B. A. Obadele, S. R. Oke, M. E. Maja, and P. A. Olubambi, "Effect of sintering parameters on densification and microstructural evolution of nano-sized titanium nitride reinforced titanium alloys," *J. Alloys Compd.*, vol. 736, pp. 202–210, 2018.

[43] A. Kamat, S. Copley, A. Segall, and J. Todd, "Laser-Sustained Plasma (LSP) Nitriding of Titanium: A Review," *Coatings*, vol. 283, no. 9, pp. 1–22, 2019.

[44] M. de Nicolás, H. Besharatloo, P. Alvaredo, J. J. Roa, L. Llanes, and E. Gordo, "Design of alternative binders for hard materials," *Int. J. Refract. Met. Hard Mater.*, vol. 87, no. October 2019, p. 105089, 2020.

[45] J. Garcia and W. Lengauer, "Quantitative mass spectrometry of decarburisation and denitridation of cemented carbonitrides during sintering," *Mikrochim. Acta*, vol. 136, no. 1–2, pp. 83–89, 2001.

[46] L. Zhao, C. Cui, S. Liu, L. Zhao, and N. Li, "Microstructure and mechanical properties of TC4 alloy modified and reinforced by TiB+TiN/Ti inoculants ribbons," *Mater. Sci. Eng. A*, vol. 663, pp. 8–16, 2016.

[47] Y. Liu, L. F. Chen, H. P. Tang, C. T. Liu, B. Liu, and B. Y. Huang, "Design of powder metallurgy titanium alloys and composites," *Mater. Sci. Eng. A*, vol. 418, pp. 25–35, 2006.

[48] I. N. Pogrelyuk, "On the problem of intensification of nitriding of titanium alloys," *Met. Sci. Heat Treat.*, vol. 41, no. 5–6, pp. 242–245, 1999.

[49] W. Mayr, W. Lengauer, V. Buscaglia, J. Bauer, M. Bohn, and M. Fialin, "Nitridation of Ti_Nb alloys and solid-state properties of δ(Ti,Nb)N," *J. Alloys Compd.*, vol. 262–263, pp. 521–528, 1997.

[50] V. Buscaglia, A. Martinelli, R. Musenich, W. Mayr, and W. Lengauer, "High-temperature nitridation of Nb-Ti alloys in nitrogen," *J. Alloys Compd.*, vol. 283, no. 1–2, pp. 241–259, 1999.

[51] F. Siyahjani, E. Atar, and H. Cimenoglu, "Structural changes on the surface of alloy Ti6Al7Nb under gas nitriding," *Met. Sci. Heat Treat.*, vol. 58, no. 3–4, pp. 170–174, 2016.

[52] D. Simeone, G. Baldinozzi, D. Gosset, S. Le Caer, and J. F. Bérar, "Grazing incidence X-ray diffraction for the study of polycrystalline layers," *Thin Solid Films*, vol. 530, pp. 9–13, 2013.

[53] E. Baril, L. P. Lefebvre, and Y. Thomas, "Interstitial elements in titanium powder metallurgy: sources and control," *Powder Metall.*, vol. 54, no. 3, pp. 183–187, 2011.

[54] M. A. Hussein, A. M. Kumar, and B. S. Yilbas, "Laser Nitriding of the Newly Developed Ti-20Nb-13Zr at .% Biomaterial Alloy to Enhance Its Mechanical and Corrosion Properties in Simulated Body Fluid," *J. Mater. Eng. Perform.*, vol. 26, no. 11, pp. 5553–5562, 2017.

[55] I. Pohrelyuk and V. Fedirko, "Chemico-Thermal Treatment of Titanium Alloys-Nitriding," in *Titanium Alloys-Towards Achieving Enhanced Properties for Diversified Applications*, A. K. M. Nurul Amin, Ed. London: IntenchOpen, 2012, pp. 141–174.

[56] M. Bartosik *et al.*, "Thermal expansion of Ti-Al-N and Cr-Al-N coatings," *Scr. Mater.*, vol. 127, no. September, pp. 182–185, 2017.

[57] P. Hidnert, "Thermal expansion of titanium," *J. Res. Natl. Bur. Stand. (1934).*, vol. 30, pp. 101–105, 1943.

[58] M. B. Uday, M. N. Ahmad-Fauzi, A. M. Noor, and S. Rajoo, "Current Issues and Problems in the Joining of Ceramic to Metal," in *Joining Technologies*, Mahadzir Ishak, Ed. London: IntenchOpen, 2016, pp. 159–193.

[59] Y. Li, C. Yang, H. Zhao, S. Qu, X. Li, and Y. Li, "New Developments of Ti-Based Alloys for Biomedical Applications," pp. 1709–1800, 2014.

[60] S. Kaur, K. Ghadirinejad, and R. H. Oskouei, "An overview on the tribological performance of titanium alloys with surface modifications for biomedical applications," *Lubricants*, vol. 7, no. 8, 2019.

[61] P. G. Esteban, E. M. Ruiz-Navas, and E. Gordo, "Influence of Fe content and particle size the on the processing and mechanical properties of low-cost Ti-xFe alloys," *Mater. Sci. Eng. A*, vol. 527, no. 21–22, pp. 5664–5669, 2010.

[62] S. Ehtemam-Haghighi, Y. Liu, G. Cao, and L. C. Zhang, "Phase transition,

microstructural evolution and mechanical properties of Ti-Nb-Fe alloys induced by Fe addition," *Mater. Des.*, vol. 97, pp. 279–286, 2016.

[63] S. Gorsse and D. B. Miracle, "Mechanical properties of Ti-6Al-4V/TiB composites with randomly oriented and aligned TiB reinforcements," *Acta Chir. Orthop. Traumatol. Cech.*, vol. 51, pp. 2427–2442, 2003.

[64] A. Zhecheva, S. Malinov, and W. Sha, "Titanium alloys after surface gas nitriding," *Surf. Coatings Technol.*, vol. 201, no. 6, pp. 2467–2474, 2006.

[65] Y. Bédouin *et al.*, "Enhancement of the biocompatibility by surface nitriding of a low-modulus titanium alloy for dental implant applications," *J. Biomed. Mater. Res. - Part B Appl. Biomater.*, vol. 107, no. 5, pp. 1483–1490, 2019.

[66] S. Ehtemam-Haghighi, G. Cao, and L.-C. Zhang, "Nanoindentation study of mechanical properties of Ti based alloys with Fe and Ta additions," *J. Alloys Compd.*, vol. 692, pp. 892–897, 2017.

[67] D. M. Gordin, A. Guillou, I. Thibon, M. Bohn, D. Ansel, and T. Gloriant, "Duplex nitriding treatment of a beta-metastable Ti94Mo6 alloy for biomedical applications," *J. Alloy. Compd. A*, vol. 457, pp. 384–388, 2008.

[68] J. Zhang and A. T. Alpast, "Transition between mild and severe wear in aluminium alloys," *Acta Mater.*, vol. 45, no. 2, pp. 513–528, 1997.

[69] S. Bahl, S. Suwas, and K. Chatterjee, "Comprehensive review on alloy design, processing, and performance of β Titanium alloys as biomedical materials," *Int. Mater. Rev.*, 2020.

CHAPTER 7

Surface treatment for bioactivity enhancement

CHAPTER 7

7.1. Introduction.

Titanium is the most biocompatible metal; nevertheless, it is a bioinert material, so, it lacks bioactivity. This limits the fixation between the bone and the implant as it cannot lead to bone growth around the implant. Surface modification techniques are employed to modify the interaction of Ti, and its alloys, with surrounding bone tissues enhancing their bioactivity and promoting osseointegration.

A wide variety of surface treatments can be performed to biofunctionalise the implant surface. These include ion implantation [1], [2], sol-gel method [3], [4], thermal spraying [5], [6], chemical vapour deposition [7], [8], physical vapour deposition [9], [10], and micro-arc oxidation (MAO) [11]–[14]. Among these surface treatments, MAO is one of the most attractive methods. It is a low-cost electrochemical treatment that does not need expensive equipment, offers the possibility to coat complex shape, the coating obtained presents excellent adhesion with the substrate, and leads to incorporate bioactive elements from the electrolyte bath [15], [16]. Furthermore, it has been reported bio-functionalised MAO surfaces improve osseointegration and promote *in vivo* bone growth. [17]

MAO treatment allows to maintain the starting alloy properties and provides a multiscale porous and rough coating composed mainly of TiO_2. Porous coatings showing moderated roughness favour the biological response, providing a more natural environment for cell attachment, enhancing cell migration and proliferation [15], [18], [19]. Besides, the MAO coating increases the corrosion and wear resistance of the components. [20], [21]

In this chapter, a MAO treatment is proposed in order to obtain a bioactive coating rich in calcium (Ca), phosphorus (P) and zinc (Zn), using an electrolyte frequently employed in the bibliography [22]–[25]. The electrolyte is composed of 0.35 M of calcium acetate and 0.02 M of β-glycerophosphate disodium salt and different concentrations of ZnO NPs (4, 6 and 12 g/L), as Zn source.

The MAO treatment was carried out for TiN reinforced alloys (TH40-TiN and TH525-TiN, described in **Section 6.2.2**). From now on, these samples will be referred to as MAO-TH40(TiN) and MAO-TH525(TiN), respectively.

This work presents a brief analysis of the electrical response of treated samples during the MAO treatment in order to understand the growth mechanisms of the oxide layer.

It is also evaluated how ZnO NPs affect the porous surface morphology and how these NPs are incorporated into the coating. In addition, the Ca/P ratio, Zn amount and anatase and rutile presence are determined to evaluate the potential use of MAO treatment to provide bioactivity to the β-Ti alloys developed in this work.

7.2. Growth of coating obtained by micro-arc oxidation (MAO) treatment.

The growth mechanisms of coatings can be evaluated by studying the current evolution during the MAO coating process. Representative current-time curves for all coated samples are shown in **Figure 7.1**. The MAO process was performed at 300 V, using electrolytes containing different concentrations of ZnO nanoparticles (NPs) (as described in **Section 3.6.3**).

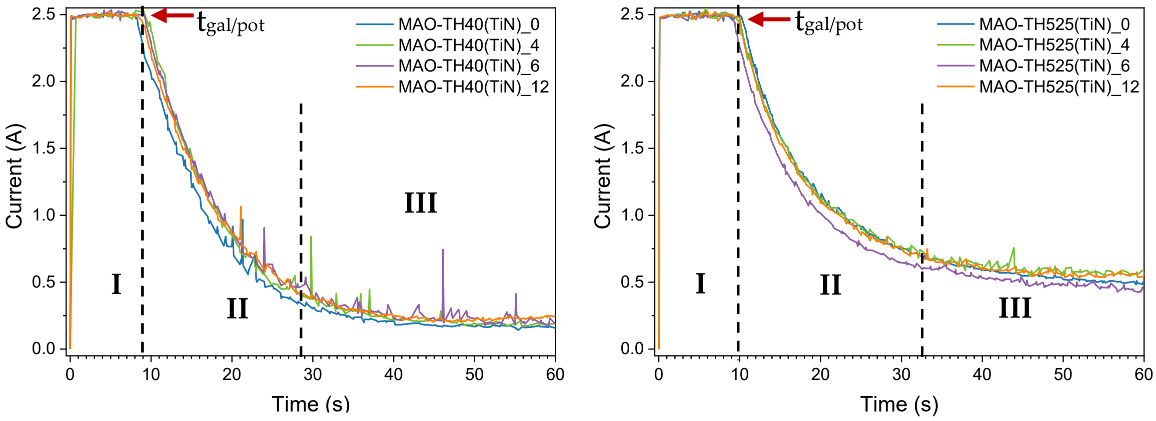

(a) **(b)**

Figure 7.1. Representative current-time curves during MAO process at 300 V, employing electrolytes with different ZnO nanoparticles concentration for: a) MAO-TH40(TiN) and b) MAO-TH525(TiN) alloys. 0, 4, 6 and 12 indicate the ZnO NPs concentration in g/L.

Both substrates exhibit similar current evolution curves, where the three different regions that are typically observed in anodic treatments can be distinguished. First, current increases drastically up to 2.5 A, which corresponds to the limiting current, and then it remains constant (Stage I). Next, in stage II, the current falls exponentially when the maximum working voltage (300 V) is reached. This point is known as $t_{gal/pot}$, which is identified as the point where the current is no longer constant and starts to decrease. $t_{gal/pot}$ indicates anodic regime changes from galvanostatic to potentiostatic control; subsequently, the voltage becomes constant while the current continues to decrease [22]. It can be seen in **Figure 7.1** that all samples exhibit similar $t_{gal/pot}$, around 9-10 s. Finally, in stage III, the current tends to stabilise until the end of the treatment, reaching about 0.25 A and 0.5 A, for MAO-TH40(TiN) and MAO-TH525(TiN) compositions, respectively. This difference in the final current for the two substrates could be attributed to a thicker or more porous anodic layer was formed for MAO-TH40(TiN) samples, making it more insulating, and limiting the current flow through the oxide layer. Current fluctuations observed during MAO treatment are associated with micro-arc discharge. It can be seen that spark density or current fluctuation is higher for MAO-TH40(TiN) samples than MAO-TH525(TiN), whose curves seem smoother. Spark discharges lead to pore formation and thickening of the anodic layer; hence, higher thickness and porosity are expected for anodised MAO-TH40(TiN) samples. This could explain the differences in the final current.

The processes that take place are described below, using a schematic representation of the processes that occur in the different stages of the MAO treatment (**Figure 7.2**).

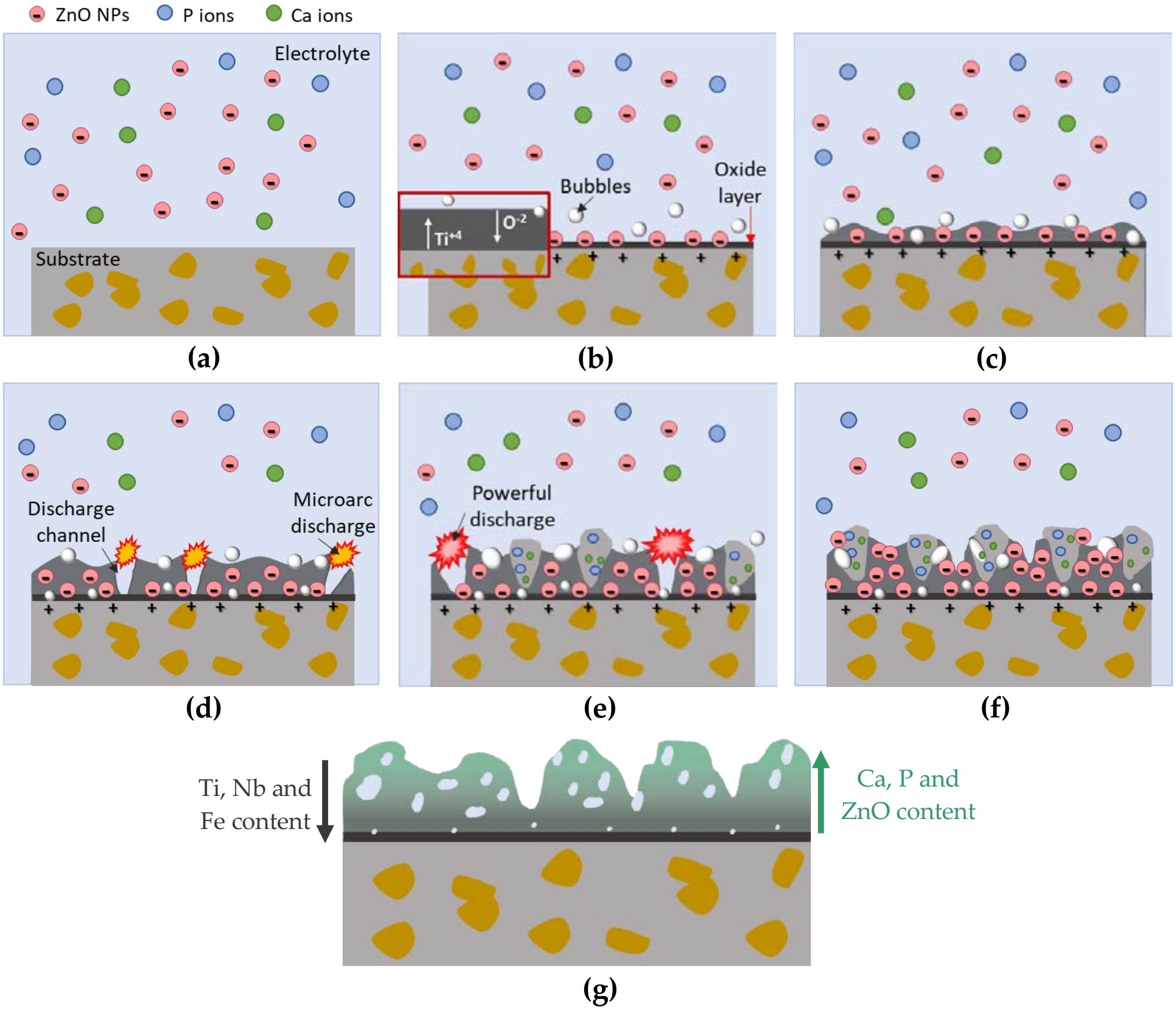

Figure 7.2. Schematic representation of different stages of the MAO process. a) Starting condition, b) Passive oxide film formation and NPs adsorption by electrophoretic effect, c) Bubbles generation, d) Beginning of micro-arc discharges, e) Growing of oxide layer and incorporation of bioactive elements, f) Final condition and g) Representative schematic of elements distribution into the coating layer.

In stage I, a compact and uniform thin passive oxide layer is formed at the surface. This oxide layer is produced by O^{-2} ions migration toward the sample surface and Ti^{+4} ions migration outward (**Figure 7.2**b) [26], [27]. The oxide layer acts as a barrier to the electrical current flow. As this oxide layer grows, its resistivity increases; therefore, according to the

Ohm law, the voltage must also increase to maintain the current flow [28]. Simultaneously, gas generation and small oxygen bubbles are produced as voltage increases [29]. These bubbles may get trapped in the metal/oxide interface (**Figure 7.2**c); as the anodising stages progress, these become larger, promoting the formation of larger pores [26].

Additionally, in the early stage of the anodic treatment conducted in electrolytes containing ZnO NPs, part of these NPs get trapped in the oxide layer formed before the dielectric breakdown voltage is reached [11], [30] (**Figure 7.2**c). It has been demonstrated that the ZnO NPs have a negative surface charge showing negative zeta potential values in contact with similar electrolyte to that used in this work [31]. Hence, these particles become attracted/adsorbed by electrophoretic effect into the sample surface, which exhibits a positive charge (**Figure 7.2b**) [11].

When the oxide film reaches a critical thickness value, dielectric breakdown of the passive film occurs, producing micro-arc discharges in vulnerable zones, also called spark discharge, favouring the growth and densification in these specific areas (**Figure 7.2**d) [32]. During these discharges, the temperature rises significantly, producing the melting in localised regions of the oxide film, allowing the incorporation of Ca, P and ZnO, present in the electrolyte. Besides, the fast melting-solidification process produces thermal stresses that could generate internal cracks. [20], [33]

As layer oxide grows, powerful and longer discharges are produced, generating more discharge channels (**Figure 7.2**e) and promoting the incorporation of a higher amount of electrolyte elements into the coating. Moreover, above the breakdown voltage, the gas evolution increases, and thus, bigger and interconnected pores are formed (**Figure 7.2**f).

The final MAO coating shows a concentration gradient from the sample surface to the outmost surface, in contact with the electrolyte (**Figure 7.2**g). The concentration of the elements that constitute the base alloy is reduced from the sample surface towards the top. In contrast, the concentration of the elements in the electrolyte bath increased from the sample surface outward. [14]

Concerning the role of NPs addition in anodic treatments, many authors agree that NPs addition such as Al_2O_3, ZrO_2, ZnO, etc. improve the coating properties; enhancing the corrosion and tribocorrosion resistance and biological behaviour, providing antibacterial properties or promoting cell adhesion and proliferation [19], [20], [34]. Nevertheless, there is much controversy regarding the influence of NPs addition on the electrical response of MAO process. Li et al. [35] assure that ZrO_2 NPs addition promotes a fast-growth of the anodic layer, reaching higher final potential. Similar results were reported by Wang et al. [36] incorporating Al_2O_3 NPs. In contrast, Lee et al.[37] reported no significant differences in voltage evolution during MAO process, adding ZrO_2 and TiO_2 NPs. On the other hand, Shokoulfar et al. [21] stated that no considerable differences on neither current evolution, breakdown voltage, nor coating thickness were detected after addition of SiC, TiO_2 and Al_2O_3

NPs. From **Figure 7.1**, it can be deduced there are no variations in the oxidation behaviour, concerning current evolution and final current when ZnO NPs are incorporated.

MAO coatings are strongly depended on external factors such as electrical parameters (current density, voltage or treatment time) and internal factors like chemical composition, pH and conductivity and temperature of the electrolyte [20]. Since internal factors usually are not greatly modified after NPs addition; it is likely the discrepancies found in the bibliography are due to differences in MAO conditions instead of NPs addition itself. [19]

7.3. Microstructural characterisation of anodised samples by MAO process.

Figure 7.3 and **Figure 7.4** show the surface morphology obtained for MAO-TH40(TiN) and MAO-TH525(TiN) samples, respectively, after MAO treatments with different concentrations of ZnO NPs. As can be observed, a multiscale porous structure was achieved for both treated alloys. It appears that the pores obtained in the MAO-TH525 (TiN) samples are slightly smaller than those of MAO-TH40(TiN). Most pores exhibit a rounded morphology; however, for MAO-TH40(TiN) samples, treated without ZnO NPs and with an addition of 12 g/L of ZnO NPs, regions with large elongated pores were found (**Figure 7.3**a,k).

Moreover, some surface cracks (indicated with black arrows in **Figure 7.3**) were observed for most samples. Cracks are intrinsic to the anodising process, as they are formed due to quenching of the molten oxide generated during the spark discharges when it comes into contact with the electrolyte bath.

In general, the coating is uniform over the entire surface of the sample, showing good adhesion to the substrate. The only exception are samples treated with 12g/L of ZnO NPs (both MAO-TH40(TiN) and MAO-TH525(TiN)), which present large detached areas corresponding to the outer porous layer, nevertheless, without leaving the substrate surface exposed. This confirms the good adhesion among the inner layer of the coating and the substrate.

Shokouhfar et al. [11] propose a mechanism of adhesion and incorporation of NPs into the coatings obtained by MAO treatment. They state that the middle part of the coating, corresponding to the outmost/inner porous layer interface, contains a higher amount of NPs than the other parts. Although there is no evidence of this, coating detachments observed in samples treated with 12 g/of ZnO, have likely been caused by possible ZnO agglomerates, due to the high ZnO NPs concentration in the electrolyte.

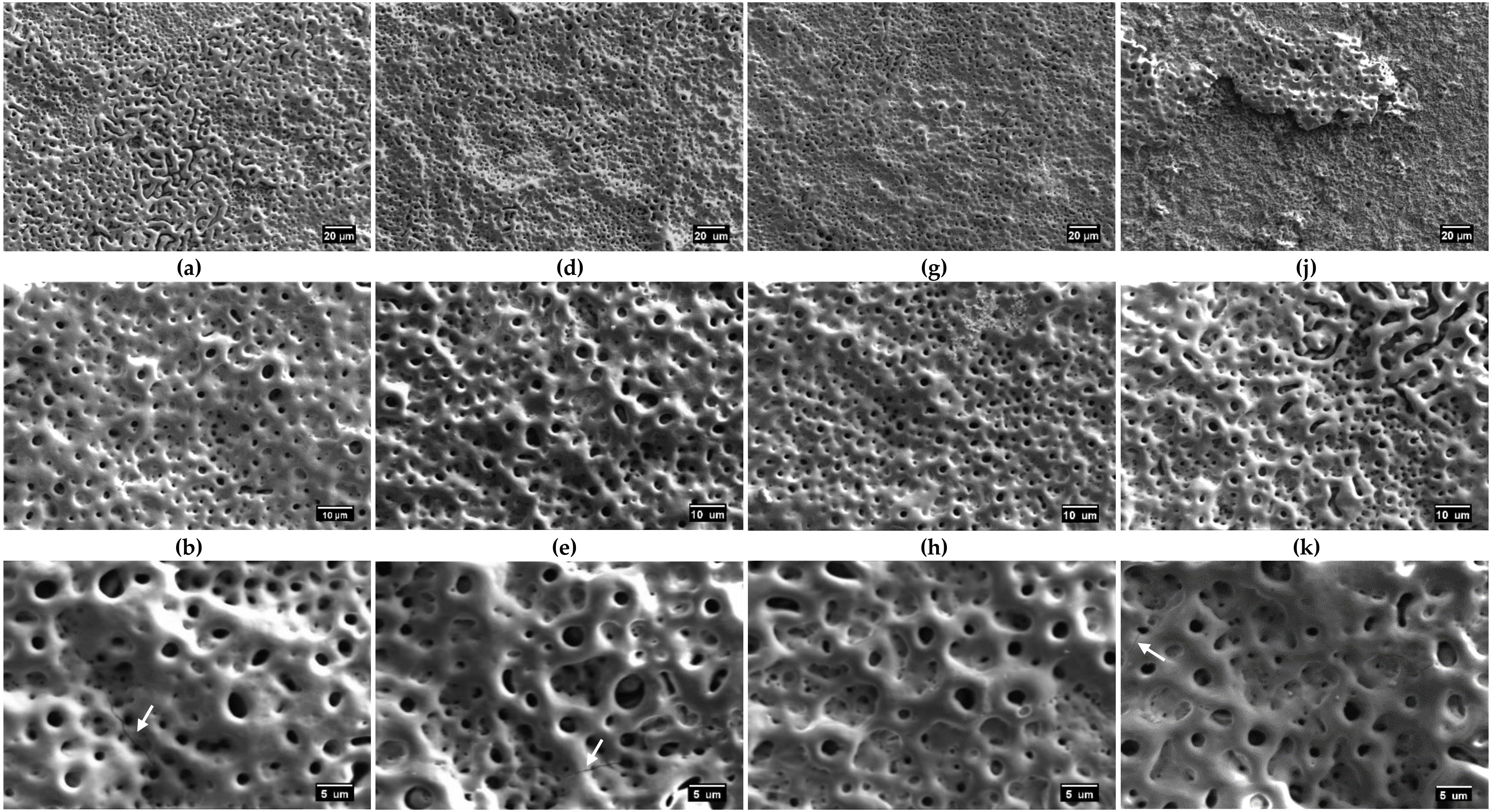

(a) (d) (g) (j)

(b) (e) (h) (k)

(c) (f) (i) (l)

Figure 7.3. SE-SEM images of anodised MAO-TH40(TiN) samples with different ZnO NPs concentrations: (a-c) No ZnO 0g/L; (d-f) 4 g/L; (g-i) 6 g/L and (j-l) 12 g/L.

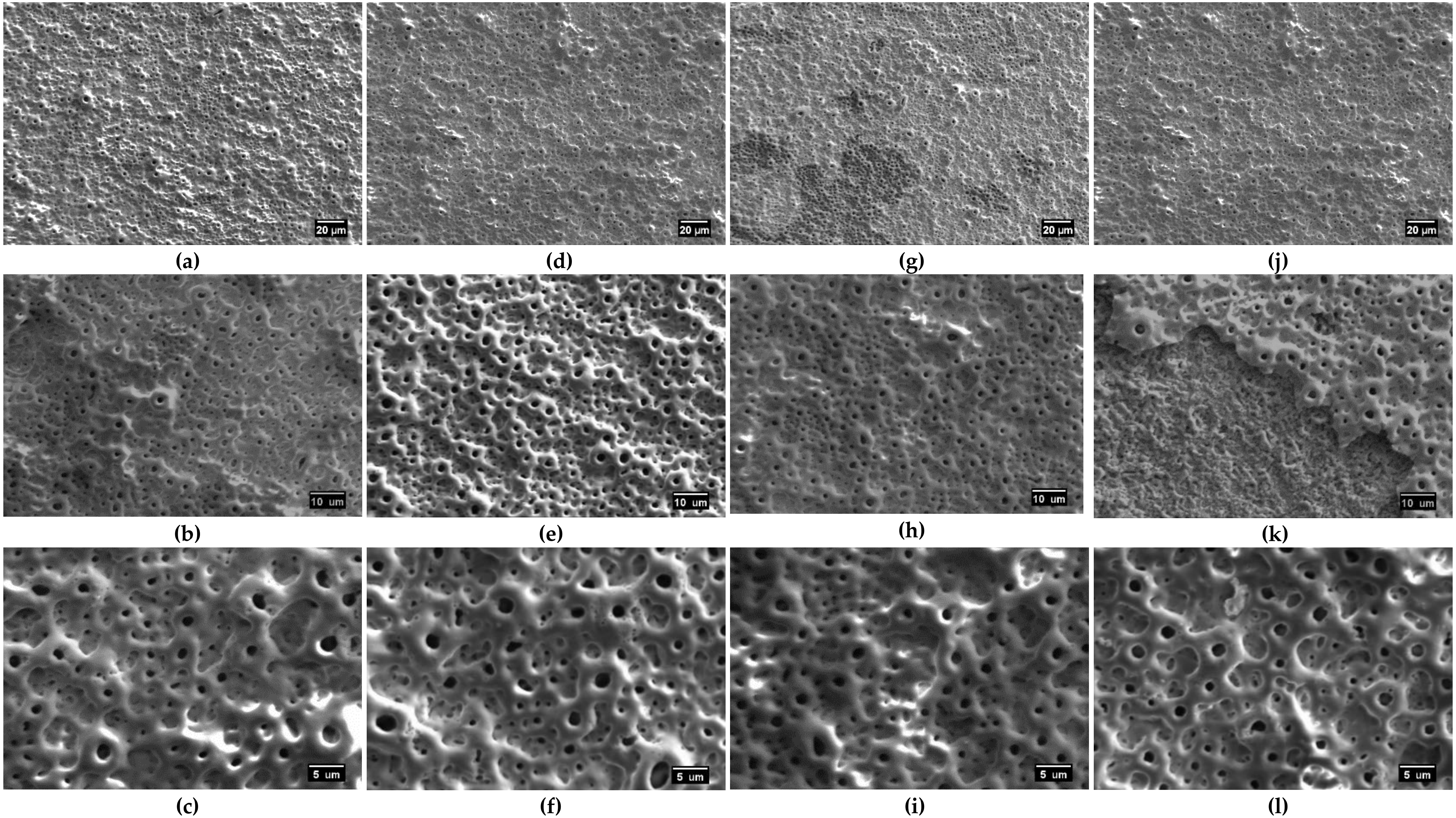

(a) (d) (g) (j)

(b) (e) (h) (k)

(c) (f) (i) (l)

Figure 7.4. SE-SEM images of anodised MAO-TH525(TiN) samples with different ZnO NPs concentrations: (a-c) No ZnO 0 g/L; (d-f) 4 g/L; (g-i) 6 g/L and (j-l) 12 g/L.

Formation of large agglomerates may reduce the bond between the inner and the outer porous layer, producing outer layer detachment. Hence, to enhance the adhesion and homogeneity of the coating with high NPs concentration (12 g/L), further studies should be carried out focused on achieving higher colloidal dispersion of the ZnO NPs.

Figure 7.5 displays the cross-section of the coated samples with a concentration of 6 g/L of ZnO and without ZnO NPs. Similar features were observed for the other ZnO concentrations. It can be seen that the obtained MAO films are composed of three layers. A thin and compact passive layer at the metal interface, followed by two porous sub-layers. It is noted that pore size increase from the inner to the outer porous layer, which could be related to powerful discharges produced as layer oxide grows. The formation of an inner and outer porous layer is typical in coatings produced by MAO. [21]

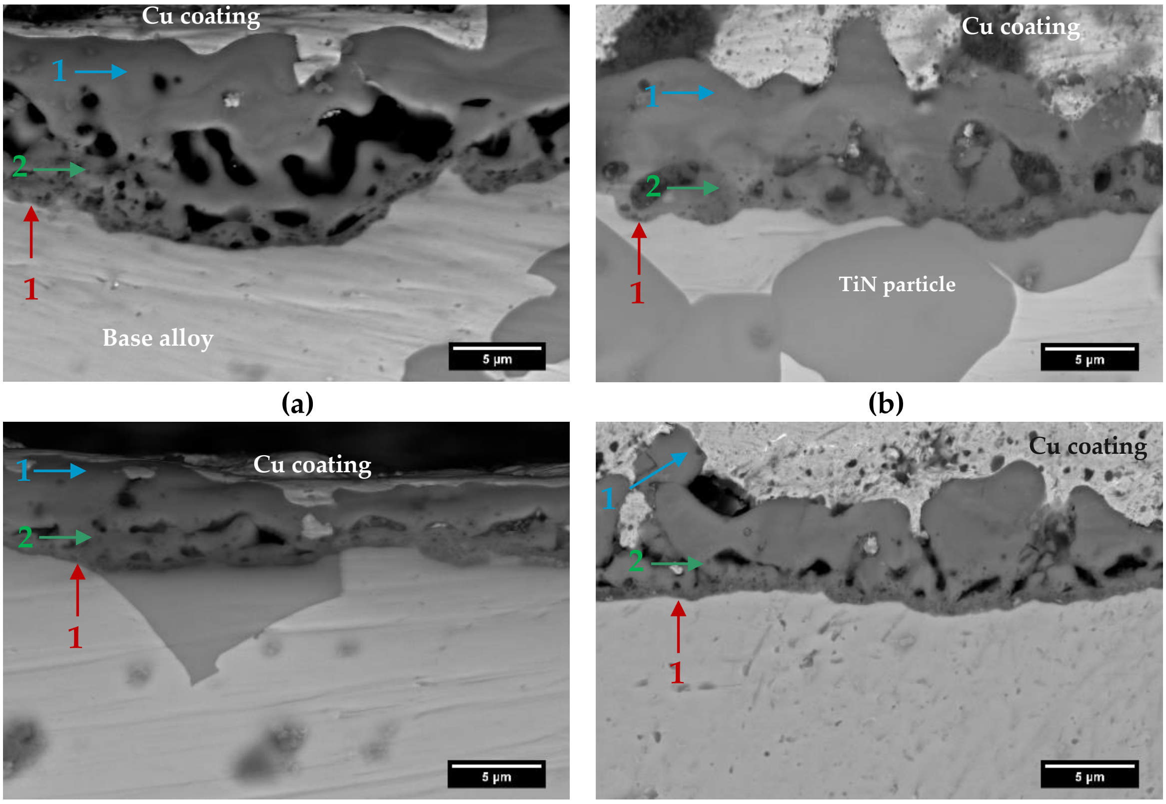

(a) (b)

(c) (d)

Figure 7.5. BSE-SEM images of the cross-section of MAO treated samples without ZnO NPs addition and with a concentration of 6 g/L: a) MAO-TH40(TiN) (No ZnO); b) MAO-TH40(TiN) (6 g/L); c) MAO-TH525(TiN) (No ZnO) and d) MAO-TH525 (TiN) (6 g/L). The numbers on the images indicate the different layers in the MAO coatings.
1: Outer porous layer. 2: Inner porous layer. 3. Passive layer.

The concentration gradient along the cross-section indicated in **Figure 7.2**g was confirmed by EDS measurements, which were done in the outmost and inner layers of the coatings. All samples exhibited the same trend. Representatively, the results obtained for MAO-TH40(TiN) sample with 6 g/L of ZnO NPs, are included. The outmost layer shows 29 Ti wt.%, 5 Nb wt.%, 11 Ca wt.%, 7 Zn wt.%, 2 P wt.%; whereas the inward layer shows 33 Ti wt.%, 8 Nb wt.%, 6 Ca wt.%, 2 Zn wt.%, 2 P wt.%,. It can be seen that Ca and Zn content increases from the inner to the outmost surface, whereas Ti and Nb slightly decrease. No significant changes were observed concerning P content.

Moreover, **Figure 7.5** suggests the coatings are well-adhered to the substrates, even in the sections where there are TiN reinforcement particles. This coincides with previous anodic treatments, performed with the same conditions in reinforced (with 5 TiN vol.%) and unreinforced Ti5Fe25Nb alloy [38], where no adhesion differences were found in MAO coating. It is possible that TiN particles on the MAO surface are favouring the formation of the anodic layer. A MAO study [39], performed over Ti substrates and TiN-coated substrates, reveals that the partial ionic bond of TiN compared to the metallic bond of the substrate may aid its dissolution in the electrolyte, accelerating the electrochemical reactions in the TiN-coated samples, which increases the growth rate of the oxide layer. On the other hand, ZnO NPs addition does not seem to affect the bonding with the substrate. Nevertheless, large concentrations of ZnO NPs (12 g/L) may weaken the bond between the inner and outer porous layer, producing the aforementioned coating detachments.

Although no significant differences are observed in pore size between both compositions, the cross-section reveals differences in porosity inside the coating. The MAO-TH40(TiN) samples appear more porous and thicker, showing larger cavities than the MAO-TH525(TiN) samples. It is known that coating porosity increases the electrical resistivity of coating, which reduces the current flow through the anodic layer [40]. This may explain the electrical response observed in the current-time curves (**Figure 7.1**) during the MAO process. For MAO-TH40(TiN) samples, current tends to stabilise at lower values than MAO-TH525(TiN) samples, likely because MAO-TH40(TiN) coating exhibits apparent higher porosity.

Coating thickness was measured for all samples. The obtained results are shown in **Figure 7.6**. It can be seen that the thickness of MAO-TH40(TiN) samples tends to be higher than that of MAO-TH525(TiN) samples, except for the treatment with 12 g/L of ZnO NPs. As it can be seen in **Figure 7.1**, this sample (MAO-TH40(TiN)_12) showed the lowest spark density, presenting a smoother current-time curve, compared to the other MAO-TH40(TiN) samples treated. Given that the lower the spark density, the lower the coating thickness; this could explain the decreases in thickness.

Different effects are observed concerning ZnO NPs addition in coating thickness. For MAO-TH40(TiN) alloy, thickness keeps almost constant (about 10 μm) for samples anodised without ZnO NPs and up to 6 g/L addition; while for a concentration of 12 g/L, coating thickness decreases to about 7 μm. For MAO-TH525(TiN) alloy, the thickness increases with the ZnO NPs concentration, reaching about 4.5 μm without ZnO; and 6 μm, 7 μm and 9 μm with the addition of 4, 6 and 12 g/L, respectively.

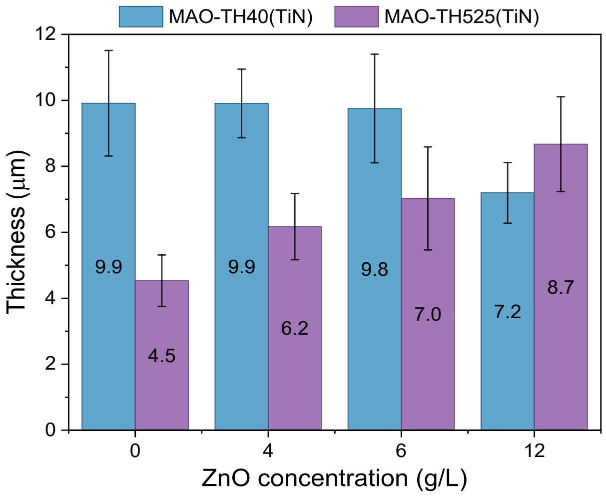

Figure 7.6. The thickness of MAO coatings for MAO-TH40(TiN) and MAO-TH525(TiN) alloys treated with different concentration of ZnO NPs.

On the other hand, the difference in thickness among MAO-TH40(TiN) and MAO-TH525(TiN) alloys could be attributed to the large pore cavities observed in MAO-TH40(TiN) samples, which may increase the coating thickness. Thicker coatings are desired to improve corrosion and wear resistance [41], [42]. Nevertheless, a relatively dense coating is also desired to provide good mechanical properties [43]. If the coating is too porous, it can break away easily, which is not suitable. Nevertheless, the presence of some porosity in the MAO coating could be beneficial. Coating porosity provides strain tolerance, distributing the stresses generated by the difference in properties between substrate and oxide coating, such as difference in thermal expansion coefficient [44]–[46]. Besides, it has been reported that good interfacial bonding adhesion between substrate and MAO coating, surface connected porosity, and high coating hardness enhance the tribological behaviour [44]. Hence, there must be a balance between porosity and coating resistance in order to improve both the biological response of the material and wear resistance.

MAO is one of the most effective and useful surface modification technique for the biofunctionalisation of Ti alloys. Incorporating the electrolyte elements (Ca, P and ZnO) is an important factor to be evaluated since these elements are related to improvement in biological behaviour. Ca and P promote apatite formation, found naturally in bones; while ZnO provides antibacterial properties and can improve wear resistance. In order to determine how these elements are distributed along the coating surface, the atomic Ca/P ratio and ZnO amount were obtained by EDS measurements; which were conducted in three different regions for each sample, considering three samples for each condition. The obtained results are summarised and displayed in **Figure 7.7.**

As shown in **Figure 7.7**, MAO-TH40(TiN) samples reached a higher Ca/P ratio and Zn content than MAO-TH525(TiN) samples. For both alloys, the Ca/P ratio keeps almost constant with ZnO NPs addition, reaching about 3.2 and 2.7, for MAO-TH40(TiN) and MAO-TH525(TiN), respectively. The amount of Ti, Nb and Fe along the surface also remains constant for all samples. Specifically, 14 Ti at.% and 5 Nb at.% were detected for MAO-TH40(TiN) samples; whereas for MAO-TH525(TiN) samples, 18 Ti at.% , 3 Nb at.% and 0.5 Fe at.% were detected. Hence, the Ca/P element distribution and the ratio is not affected by the ZnO NPs addition.

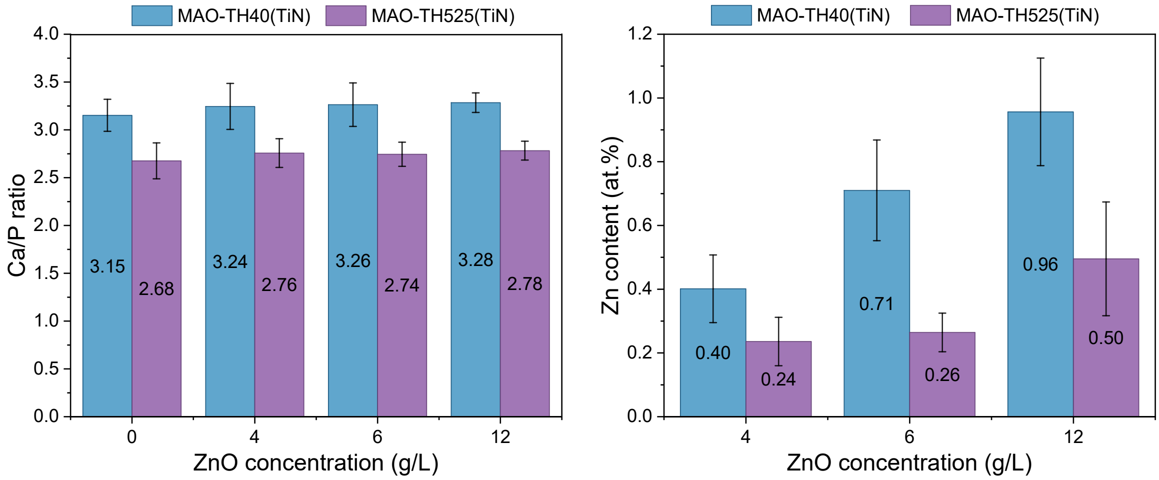

(a) **(b)**

Figure 7.7. EDS measurements of the top surface after MAO process with different ZnO NPs concentration. a) Ca/P atomic ratio and b) Zn atomic content.

On the other hand, it can be seen that the higher the ZnO NPs concentration, the higher Zn content is detected, which indicates successful incorporation of ZnO NPs into the coatings. Despite the fact that the samples treated with a ZnO NPs concentration of 12 g/L reached the highest amount of Zn, around 1 at.% for MAO-TH40(TiN) and 0.5 at.% for MAO-TH525(TiN), they would not be suitable for implant application since the achieved coatings were no uniform throughout the whole sample surface. The maximum Zn amount incorporated into the coating, without affecting its regularity, was obtained for 6 g/L, reaching 0.7 at.% (1.9 wt.%) and 0.3 at.% (0.7 wt.%) for MAO-TH40(TiN) and MAO-TH525(TiN), respectively.

It has been stated that Ca/P ratio above the stoichiometric ratio of hydroxyapatite (1.67) favours the early osteoblast cell response and could accelerate the osseointegration process [13], [19], [41]. Olesko et al. report that controlled Zn ions release would be suitable to promote both osteogenic and antibacterial effects [47]. In principle, a high Zn ion concentration improves the antibacterial response, while a low concentration of Zn ions, is enough to enhance the biological activity [48]. Hence, from these viewpoints, it can be deduced that all tested samples would be suitable to enhance bioactivity.

7.3.1. Phases identification by X-ray diffraction (XRD)

Figure 7.8 shows the diffractograms obtained for untreated alloys, and MAO treated samples with different ZnO NPs concentrations. Predominant peaks corresponding with the substrates, as β-Ti (ICDD 01-089-4913) and $TiN_{0.3}$ (ICDD 01-041-1352), can be identified. Both alloys show well-defined peaks of anatase phase (ICDD 01-071-1168). However, different effects are observed for each composition.

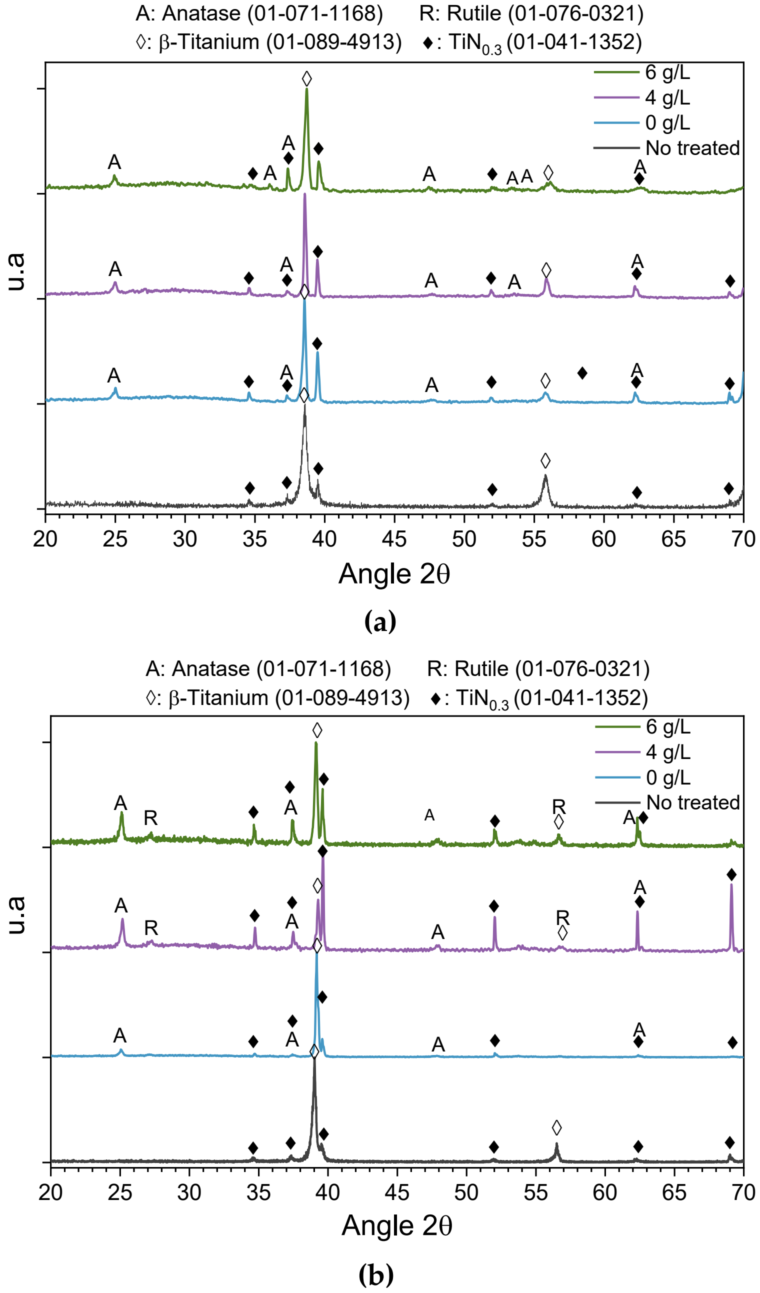

Figure 7.8. XRD for untreated alloys and MAO treated samples with different ZnO NPs concentration: a) MAO-TH40(TiN) samples and b) MAO-TH525(TiN) samples.

For MAO-TH525(TiN) samples, the intensity of anatase peaks increases for samples with higher ZnO content. This fact could be related to the growth of the oxide layer as the ZnO concentration increases (**Figure 7.6**). Furthermore, small peaks corresponding to rutile phase (ICDD 01-076-0321) are identified for samples with 4 g/L of ZnO NPs. In MAO-TH40(TiN) samples, less intense anatase peaks are observed than those of MAO-

TH525(TiN). The anatase peaks intensity remains almost constant for all ZnO additions. Despite no rutile peaks being detected in any MAO-TH40(TiN) treated sample, a broad diffuse peak was found between 25-30°, suggesting the formation of an amorphous phase of Ti oxide.

During the MAO process, spark discharges cause melting in localised areas that quickly solidify due to contact with the electrolyte bath. This high solidification rate produces an amorphous TiO_2 phase, since it cannot be transformed into a crystalline phase. [14], [49]

Phase composition observed for MAO samples agrees with those reported in the bibliography for Ti alloys. Most MAO coatings, performed on Ti or Ti alloys substrates, are composed of anatase and rutile [17]. Some studies reveal only the presence of anatase phase, while few studies show only the rutile phase presence. This is because rutile is formed from the transformation of metastable anatase, where oxygen vacancies act as rutile nucleation sites [32]. This transformation is highly influenced by processing parameters, like voltage and current density. It has been reported that anatase amount decreases and rutile increase as the applied voltage, current density and time increase [50], [51].

Despite the fact that MAO treatments were conducted under the same processing parameters for both compositions, only MAO-TH525(TiN) samples present rutile. This could be related to alloying elements acting as promoters or inhibitors of rutile transformation [52]. In the case of Nb, it has been stated it may hinder the rutile transformation because Nb^{+5} ions reduce the oxygen vacancies required for this transformation [53]–[55]. Hence, the absence of the rutile phase in MAO-TH40(TiN) samples could be associated with the higher Nb amount in this alloy.

According to the electrolyte composition, MAO coatings may exhibit Ca-P-rich phases such as hydroxyapatite, α-tricalcium phosphate, $CaTiO_3$, β-$Ca_2P_2O_7$. These phases could enhance the biological behaviour of the components [50]. Ca and P-rich phases were not detected in the current work.

It is known that MAO coating has a gradient structure composition where the Ca and P amount incorporated in the oxide increases as coating becomes thicker. Ribeiro et al. [56] and Dos Santos et al. [57] indicate that Ca is preferably present on amorphous regions of the oxide layer compared to the crystalline regions. Hence, the amorphous phase detected in MAO-TH40(TiN) could be related to higher Ca amount retained in the oxide, which could be favourable to improving the coating bioactivity since it has been reported that these amorphous areas, being Ca-rich, could be more effective in enhancing cell adhesion and cell viability [14], [56].

Although there is no evidence of peaks corresponding to Zn or ZnO in any sample, XRD results suggest that the addition of ZnO NPs slightly changes the phase composition of the oxides formed during MAO for MAO-TH525(TiN) samples, favouring the anatase and rutile formation and increasing the crystallinity of the coating. In contrast, a mixed crystalline/amorphous oxide phase is obtained for MAO-TH40(TiN), but it does not seem to be influenced by the ZnO NPs addition.

Several authors have reported that the presence of anatase and rutile may enhance the biological, electrochemical and tribological properties of Ti alloys [24]. On the one hand, anatase possesses high reactivity than rutile, which is advantageous for enhancing the alloy bioactivity and promoting the apatite formation in simulated body fluid [57]. In contrast, rutile reduces the coefficient of friction of the alloy and improves wear resistance since it has higher hardness than anatase, reaching about 1733 HV and 815 HV, respectively. Besides, rutile may exhibit a self-lubricant behaviour, which is also related to improvement in tribocorrosion resistance [24], [51], [58].

Since anatase was found in both treated alloys, bioactivity improvement is expected as compared to untreated samples. Additionally, higher wear resistance would be expected for treated samples MAO-TH525(TiN) due to the rutile formation.

7.4. Partial conclusions.

The main conclusions of the MAO treatment can be drawn as follow:

1. **MAO coatings were successfully deposited for both treated alloys**. All MAO coating showed a multiscale surface porous morphology and apparent high roughness, which are desirable to provide a suitable environment to promote different biological processes.

2. Samples **MAO-TH40(TiN) present a thicker coating with larger internal pores** than MAO-TH525 (TiN), due to higher spark density observed in the current evolution curves. The coating thickness remains constant in the MAO-TH40(TiN) samples, around 10 μm, regardless of ZnO NPs addition. While for MAO-TH525(TiN), the thickness increases with the ZnO NPs addition, increasing from 4.5 to 8.7 μm for samples without ZnO NPs and 12 g/L of ZnO NPs electrolyte concentration.

3. Addition of ZnO NPs into the coatings had no significant effect neither on the electrical response during the MAO process nor surface morphology features.

Addition of 4 g/L and 6 g/L of ZnO NPs, does not modify the MAO coating structure, which is composed of a thin and dense oxide layer, followed by an inner porous layer, with smaller pore size; and an outer porous layer, with larger pores. In contrast, some areas of porous layers are detached with an electrolyte concentration of 12 g/L of ZnO NPs.

4. The Ca/P ratio achieved for all treated samples remains constant regardless of the ZnO NPs concentration. The obtained **Ca/P ratio values are higher than the stoichiometric hydroxyapatite Ca/P ratio**, reaching about 3.2 and 2.7 for MAO-TH40(TiN) and MAO-TH525 (TiN), respectively. Moreover, Zn was incorporated into the coatings, although a relatively low concentration was achieved. Additionally, all samples contain anatase. These results suggest that the conducted MAO treatment is a suitable alternative to **improve the bioactivity** of the MAO-TH40(TiN) and MAO-TH525(TiN) samples, and likely to enhance also tribocorrosion behaviour for MAO-TH525(TiN) alloy.

References

[1] T. R. Rautray, R. Narayanan, T. Y. Kwon, and K. H. Kim, "Surface modification of titanium and titanium alloys by ion implantation," *J. Biomed. Mater. Res. - Part B Appl. Biomater.*, vol. 93, no. 2, pp. 581–591, 2009.

[2] L. Thair, U. K. Mudali, N. Bhuvaneswaran, K. G. M. Nair, R. Asokamani, and B. Raj, "Nitrogen ion implantation and in vitro corrosion behavior of as-cast Ti-6Al-7Nb alloy," *Corros. Sci.*, vol. 44, pp. 2439–2457, 2002.

[3] E. Peón Avés *et al.*, "Hydroxyapatite coating by sol-gel on Ti-6Al-4V alloy as drug carrier," *J. Mater. Sci. Mater. Med.*, vol. 20, pp. 543–547, 2009.

[4] H. Q. Nguyen, D. A. Deporter, R. M. Pilliar, N. Valiquette, and R. Yakubovich, "The effect of sol-gel-formed calcium phosphate coatings on bone ingrowth and osteoconductivity of porous-surfaced Ti alloy implants," *Biomaterials*, vol. 25, no. 5, pp. 865–876, 2004.

[5] C. S. Yip, K. A. Khor, N. L. Loh, and P. Cheang, "Thermal spraying of Ti-6Al-4V/hydroxyapatite composites coatings: Powder processing and post-spray treatment," *Journal of Materials Processing Technology*, vol. 65. pp. 73–79, 1997.

[6] J. G. Odhiambo, W. G. Li, Y. T. Zhao, and C. L. Li, "Porosity and Its Significance in Plasma-Sprayed Coatings," *Coatings*, vol. 9, 2019.

[7] Q. An, J. Chen, Z. Tao, W. Ming, and M. Chen, "Experimental investigation on tool wear characteristics of PVD and CVD coatings during face milling of Ti[sbnd]6242S and Ti-555 titanium alloys," *Int. J. Refract. Met. Hard Mater.*, vol. 86, no. 800, p. 105091, 2020.

[8] J. Li *et al.*, "CVD growth of graphene on NiTi alloy for enhanced biological activity," *ACS Appl. Mater. Interfaces*, vol. 7, pp. 19876–19881, 2015.

[9] R. Ali, M. Sebastiani, and E. Bemporad, "Influence of Ti-TiN multilayer PVD-coatings design on residual stresses and adhesion," *Mater. Des.*, vol. 75, pp. 47–56, 2015.

[10] G. M. Uddin *et al.*, "Experimental investigation of tribo-mechanical and chemical properties of TiN PVD coating on titanium substrate for biomedical implants manufacturing," *Int. J. Adv. Manuf. Technol.*, vol. 102, pp. 1391–1404, 2019.

[11] M. Shokouhfar and S. R. Allahkaram, "Formation mechanism and surface characterization of ceramic composite coatings on pure titanium prepared by micro-arc oxidation in electrolytes containing nanoparticles," *Surf. Coatings Technol.*, vol. 291, pp. 396–405, 2016.

[12] A. Santos-Coquillat, R. Gonzalez Tenorio, M. Mohedano, E. Martinez-Campos, R. Arrabal, and E. Matykina, "Tailoring of antibacterial and osteogenic properties of Ti6Al4V by plasma electrolytic oxidation," *Appl. Surf. Sci.*, vol. 454, pp. 157–172, 2018.

[13] M. Mohedano, R. Guzman, R. Arrabal, J. . López Lacomba, and E. Matykina, "Bioactive plasma electrolytic oxidation coatings-The role of the composition, microstructure, and electrochemical stability," *J. Biomed. Mater. Res. B Appl. Mater.*, vol.

101B, no. 8, pp. 1524–1537, 2013.

[14] D. R. N. Correa, L. A. Rocha, A. R. Ribeiro, S. Gemini-piperni, B. S. Archanjo, and T. Hanawa, "Growth mechanisms of Ca- and P-rich MAO films in Ti-15Zr-xMo alloys for osseointegrative implants," *Surf. Coat. Technol.*, vol. 344, pp. 373–382, 2018.

[15] C. Garcia-Cabezon *et al.*, "Application of Plasma Electrolytic Oxidation Coating on Powder Metallurgy Ti-6Al-4V for Dental Implants," *Metals (Basel).*, vol. 10, p. 1167, 2020.

[16] B. L. Jiang and Y. M. Wang, "Chapter 5: Plasma electrolytic oxidation treatment of aluminium and titanium alloys," in *Surface Engineering of Light Alloys: Aluminium, Magnesium and Titanium Alloys*, D. Huang, Ed. Woodhead, 2010, pp. 110–154.

[17] I. A. J. van Hengel, M. W. A. M. Tierolf, L. . Fratila-Apachitei, I. Apachitei, and A. A. Zadpoor, "Antibacterial titanium implants biofunctionalized by plasma electrolytic oxidation with silver, zinc, and copper: a systematic review," *Int. J. Mol. Sci.*, vol. 22, no. 7, 2021.

[18] W. H. Song, S. R. Hyun, and S. H. Hong, "Antibacterial properties of Ag (or Pt)-containing calcium phosphate coatings formed by micro-arc oxidation," *J. Biomed. Mater. Res. - Part A*, vol. 88, no. 1, pp. 246–254, 2009.

[19] X. Lu *et al.*, "Plasma electrolytic oxidation coatings with particle additions – A review," *Surf. Coatings Technol.*, vol. 307, pp. 1165–1182, 2016.

[20] A. Fattah-alhosseini, M. Molaei, N. Attarzadeh, K. Babaei, and F. Attarzadeh, "On the enhanced antibacterial activity of plasma electrolytic oxidation (PEO) coatings that incorporate particles: A review," *Ceram. Int.*, vol. 46, no. 13, pp. 20587–20607, 2020.

[21] M. Shokouhfar and S. R. Allahkaram, "Effect of incorporation of nanoparticles with different composition on wear and corrosion behavior of ceramic coatings developed on pure titanium by micro arc oxidation," *Surf. Coatings Technol.*, vol. 309, pp. 767–778, 2017.

[22] A. C. Alves *et al.*, "Effect of bio-functional MAO layers on the electrochemical behaviour of highly porous Ti," *Surf. Coat. Technol.*, vol. 386, 2020.

[23] M. Qadir, Y. Li, K. Munir, and C. Wen, "Calcium Phosphate-Based Composite Coating by Micro-Arc Oxidation (MAO) for Biomedical Application: A Review," *Crit. Rev. Solid State Mater. Sci.*, vol. 43, no. 5, pp. 392–416, 2018.

[24] F. Toptan, A. C. Alves, A. M. P. Pinto, and P. Ponthiaux, "Tribocorrosion behavior of bio-functionalized highly porous titanium," *J. Mech. Behav. Biomed. Mater.*, vol. 69, no. December 2016, pp. 144–152, 2017.

[25] X. He, X. Zhang, X. Wang, and L. Qin, "Review of Antibacterial Activity of Titanium-Based Implants' Surfaces Fabricated by Micro-Arc Oxidation," *Coatings*, vol. 7, no. 3, p. 45, 2017.

[26] E. Matykina, R. Arrabal, P. Skeldon, and G. E. Thompson, "Transmission electron microscopy of coatings formed by plasma electrolytic oxidation of titanium," *Acta Biomater.*, vol. 5, pp. 1356–1366, 2009.

[27] R. Chiesa, E. Sandrini, M. Santin, G. Rondelli, and A. Cigada, "Osteointegration of

titanium and its alloys by anodic spark deposition and other electrochemical techniques: A review," *J. Appl. Biomater. Biomech.*, vol. 1, pp. 91–107, 2003.

[28] B. L. Jiang and Y. F. Ge, *Micro-arc oxidation (MAO) to improve the corrosion resistance of magnesium (Mg) alloys*. 2013.

[29] M. Roknian, A. Fattah-alhosseini, S. O. Gashti, and M. K. Keshavarz, "Study of the effect of ZnO nanoparticles addition to PEO coatings on pure titanium substrate: Microstructural analysis, antibacterial effect and corrosion behavior of coatings in Ringer's physiological solution," *J. Alloys Compd.*, vol. 740, pp. 330–345, 2018.

[30] X. Lu, C. Blawert, M. L. Zheludkevich, and K. U. Kainer, "Insights into plasma electrolytic oxidation treatment with particle addition," *Corros. Sci.*, vol. 101, pp. 201–207, 2015.

[31] I. A. J. Van Hengel *et al.*, "Biofunctionalization of selective laser melted porous titanium using silver and zinc nanoparticles to prevent infections by antibiotic-resistant bacteria," *Acta Biomater.*, vol. 107, pp. 325–337, 2020.

[32] Y. Wang, H. Yu, C. Chen, and Z. Zhao, "Review of the biocompatibility of micro-arc oxidation coated titanium alloys," *Mater. Des.*, vol. 85, pp. 640–652, 2015.

[33] R. Kumari, C. Blawert, and J. D. Majumdar, "Microstructures and Properties of Plasma Electrolytic Oxidized Ti Alloy (Ti-6Al-4V) for Bio-implant Application," *Metall. Mater. Trans. A*, vol. 47, no. 2, pp. 788–800.

[34] D. Quintero *et al.*, "Anodic films obtained on Ti6Al4V in aluminate solutions by spark anodizing: Effect of OH− and WO4−2 additions on the tribological properties," *Surf. Coat. Technol.*, vol. 310, pp. 180–189, 2017.

[35] H. Li, Y. Sun, and J. Zhang, "Effect of ZrO2 particle on the performance of micro-arc oxidation coatings on Ti6Al4V," *Appl. Surf. Sci.*, vol. 342, pp. 183–190, 2015.

[36] Y. Wang, D. Wei, J. Yu, and S. Di, "Effects of Al2O3 Nano-additive on Performance of Micro-arc Oxidation Coatings Formed on AZ91D Mg Alloy," *J. Mater. Sci. Technol.*, vol. 30, no. 10, pp. 984–990, 2014.

[37] K. M. Lee, B. U. Lee, S. Il Yoon, E. S. Lee, B. Yoo, and D. H. Shin, "Evaluation of plasma temperature during plasma oxidation processing of AZ91 Mg alloy through analysis of the melting behavior of incorporated particles," *Electrochim. Acta*, vol. 67, pp. 6–11, 2012.

[38] I. Çaha *et al.*, "Improved tribocorrosion behavior on bio-functionalized β-type titanium alloy by the pillar effect given by TiN reinforcements," *Surf. Coat. Technol.*, vol. 415, 2021.

[39] H.-P. Teng, H.-Y. Lin, Y.-H. Huang, and F.-H. Lu, "Formation of strontium-substituted hydroxyapatite coatings on bulk Ti and TiN-coated substrates by plasma electrolytic oxidation," *Surf. Coat. Technol.*, vol. 350, pp. 1112–1119, 2018.

[40] Y. Hu, Z. Wang, J. Ai, S. Bu, and H. Liu, "Preparation of Coating on the Titanium Surface by Micro-Arc Oxidation to Improve Corrosion Resistance," *Coatings*, vol. 11, p. 230, 2021.

[41] I. Çaha, A. C. Alves, L. . Rocha, and F. Toptan, "A Review on Bio - functionalization

of β - Ti Alloys," *J. Bio- Tribo-Corrosion*, vol. 135, no. 6, 2020.

[42] Y. Wang, T. Lei, B. Jiang, and L. Guo, "Growth , microstructure and mechanical properties of microarc oxidation coatings on titanium alloy in phosphate-containing solution," vol. 233, pp. 258–267, 2004.

[43] C. Wang *et al.*, "The influence of alloy elements in Ti-6Al-4V and Ti-35Nb-2Ta 3Zr on the structure, morphology and properties of MAO coatings," *Vacuum*, vol. 157, pp. 229–236, 2018.

[44] J. M. Wheeler, C. A. Collier, J. M. Paillard, and J. A. Curran, "Evaluation of micromechanical behaviour of plasma electrolytic oxidation (PEO) coatings on Ti-6Al-4V," *Surf. Coatings Technol.*, vol. 204, pp. 3399–3409, 2010.

[45] Y. Zhong, L. Shi, M. Li, F. He, and X. He, "Characterization and thermal shock behavior of composite ceramic coating doped with ZrO2 particles on TC4 by micro-arc oxidation," *Appl. Surf. Sci.*, vol. 311, pp. 158–163, 2014.

[46] P. K. Wright and A. G. Evans, "Mechanisms governing the performance of thermal barrier coatings," *Curr. Opin. Solid State Mater. Sci.*, vol. 4, no. 3, pp. 255–265, 1999.

[47] O. Oleshko *et al.*, "Biocompatibility and Antibacterial Properties of ZnO-Incorporated Anodic Oxide Coatings on TiZrNb Alloy," pp. 1–15.

[48] A. Sirelkhatim *et al.*, "Review on Zinc Oxide Nanoparticles: Antibacterial Activity and Toxicity Mechanism," *Nano-Micro Lett.*, vol. 7, no. 3, pp. 219–242, 2015.

[49] A. R. Rafieerad, M. R. Ashra, R. Mahmoodian, and A. R. Bushroa, "Surface characterization and corrosion behavior of calcium phosphate-base composite layer on titanium and its alloys via plasma electrolytic oxidation: A review paper," *Mater. Sci. Eng. C*, vol. 57, pp. 397–413, 2015.

[50] Q. Dong, C. Chen, D. Wang, and Q. Ji, "Research status about surface modification of biomedical Ti and its alloys by micro-arc oxidation," *Surf. Rev. Lett.*, vol. 13, no. 1, pp. 35–43, 2006.

[51] F. G. Oliveira *et al.*, "Understanding growth mechanisms and tribocorrosion behaviour of porous TiO2 anodic films containing calcium, phosphorous and magnesium," *Appl. Surf. Sci.*, vol. 341, pp. 1–12, 2015.

[52] M. Echeverry-Rendón, O. Galvis, R. Aguirre, S. Robledo, J. G. Castaño, and F. Echeverría, "Modification of titanium alloys surface properties by plasma electrolytic oxidation (PEO) and influence on biological response," *J. Mater. Sci. Mater. Med.*, vol. 28, no. 169, 2017.

[53] J. Arbiol *et al.*, "Effects of Nb doping on the TiO2 anatase-to-rutile phase transition," *J. Appl. Phys.*, vol. 92, no. 2, pp. 853–861, 2002.

[54] D. A. H. Hanaor and C. C. Sorrell, "Review of the anatase to rutile phase transformation," *J. Mater. Sci.*, vol. 46, pp. 855–874, 2011.

[55] B. Grzmil, B. Kic, and M. Rabe, "Inhibition of the Anatase-Rutile Phase Transformation with Addition of K2O, P2O5 and Li2O," *Chem. Pap*, vol. 58, no. 6, pp. 410–414, 2004.

[56] A. R. Ribeiro, F. Oliveira, L. C. Boldrini, P. E. Leite, P. Falagan-lotsch, and A. B. R.

Linhares, "Micro-arc oxidation as a tool to develop multifunctional calcium-rich surfaces for dental implant applications," *Mater. Sci. Eng. C*, vol. 54, pp. 196–206, 2015.

[57] A. Dos Santos *et al.*, "A study of the physical, chemical and biological properties of TiO2 coatings produced by micro-arc oxidation in a Ca-P-based electrolyte.," *J. Mater. Sci. Mater. Med.*, vol. 25, no. 7, pp. 1769–1780, 2014.

[58] A. F. Yetim, "Investigation of wear behavior of titanium oxide films, produced by anodic oxidation, on commercially pure titanium in vacuum conditions," *Surf. Coat. Technol.*, vol. 205, pp. 1757–1763, 2010.

CHAPTER 8

General Conclusions

General Conclusions

In this Thesis work, novel low-cost, low modulus and biocompatible β-Ti alloys, belonging to Ti-Nb and Ti-Nb-Fe systems were developed and processed by powder metallurgy. Additionally, different approaches (development of composite materials and nitride-coating) were proposed to obtain improved mechanical, wear and bioactive properties of the developed β-Ti alloys for load-bearing implant applications.

The partial objectives listed in Chapter 2 have been successfully achieved, reaching reduced elastic modulus, improved wear properties and bio-functionalised surfaces. Overall, the materials developed are attractive and promising alternatives to be considered for use as implant materials, especially gas nitrided samples (GN-TH40 and GN-TH525) that combine low elastic modulus and higher wear resistance.

The main goal, described in Chapter 2, was divided into three sections focused on: (1) designing and developing low modulus β-Ti alloys reducing raw material cost; (2) enhancing wear performance and (3) adapting surface features to mimic the implant with the surrounding tissue. The conclusions will be exposed following the same sections.

Conclusions related to developing low modulus β-Ti alloys from TiH_2.

- The use of TiH_2 is a viable alternative for the processing of Ti alloys by powder metallurgy. It allows the reductions of the production costs without compromising the alloy performance.
- Heating conditions, atmosphere and heating rate, are critical parameters for the dehydrogenation of TiH_2. Vacuum heating facilitates hydrogen removal over the heating in an argon atmosphere. In addition, TiH_2 decomposition is slightly modified by the presence of other elements: Fe and Nb alloying elements accelerate the dehydrogenation initiation, reducing the onset temperature of the first decomposition stage by about 50-95 °C; and delaying the end of the final stage between 15-50 °C compared to pure TiH_2.
- Combining TiH_2, Fe and Nb powders, β-Ti phase is formed at a lower temperature than expected. The early stabilisation of the β-Ti phase may favour the diffusion process of other elements because diffusion of some elements occurs faster in β-Ti (BCC) than in α-Ti (HCP).

- Fe addition leads to reduction in the Nb amount required to fully stabilise β-Ti phase, which reduces the cost and density of the alloy. In addition, it contributes to increasing the alloy homogenisation and densification.
- Regarding sintering, the importance of a complete and controlled TiH_2 decomposition to obtain better densification values was established. Reducing the heating rate during the most intense decomposition reaction, from 5 to 2 °C/min, promotes full dehydrogenation. Moreover, the particle size of the starting powders (especially Nb, that shows slow diffusivity) significantly influences the diffusive processes. The larger the particle size of alloying elements, the higher the sintering temperature required to obtain complete diffusion and homogenisation. High sintering temperature should be avoided not only to reduce the energy consumption of processing but also to prevent grain growth, that might impair mechanical properties.
- Three novel PM compositions were developed: Ti-12Nb, Ti-40Nb and Ti-5Fe-25Nb. The more alloyed compositions (Ti-40Nb and Ti-5Fe-25Nb) are mainly composed of β-Ti phase, whereas Ti-12Nb is a biphasic (α+β)-Ti alloys; that may compete against the usually employed Ti6Al6V alloy.
- TH40Nb and TH5Fe25Nb β-Ti alloys, sintered at 1450 °C (C5), exhibit lower elastic modulus than biphasic (α+β) TH12Nb. Elastic modulus decreases up to 44% and 14% for TH40Nb and TH5Fe25Nb, while just 5% for TH12Nb with respect to Ti-6Al-4V alloy.
- Fatigue resistance could be influenced by the presence of TiC. Hence, both β-Ti alloys (TH40Nb and TH5Fe25Nb), having a higher amount of TiC, showed a lower fatigue limit at $2x10^6$ cycles than TH12Nb alloy, reaching 338 MPa for TH5Fe25Nb, 321 MPa for TH40Nb and 368 MPa for TH12Nb.

Conclusions related to enhancing wear performance.

- Samples of Ti-Nb-Fe system outperformed samples of Ti-Nb system in both hardness and wear resistance. Nevertheless, the main disadvantage of the Ti-Nb-Fe system samples is that they exhibit a slightly higher elastic modulus than those of Ti-Nb system
- Modified β-Ti alloys, either by reinforcement addition to produce a composite material or by deposition of nitriding coatings, allowed increase in the hardness values with respect to untreated alloys. Among these, gas nitrided samples exhibited better wear resistance than TiN reinforced alloys. This is because detached TiN reinforcement particles worsen wear, acting as a third body.
- Gas nitriding is an effective treatment to develop suitable load-bearing implants. Gas nitrided samples show the best results, combining improvement in dry sliding behaviour and maintaining low elastic modulus values, similar to those obtained for

untreated samples, achieving a wear rate reduction between 43-86% with respect to untreated base alloys (TH40Nb and TH5Fe25Nb) and elastic modulus values between 73 and 105 GPa.

Conclusions related to biocompatibility.

- Biological tests performed using pre-osteoblast cells (MC3T3-E1) in as-sintered samples indicated a non-cytotoxic response, exhibiting a biological response similar to Ti. Cells exhibited good adhesion and proliferation, as well as osteoblasts differentiation after 72 hours of culturing. They also show mineralisation evidence after 21 days of culturing.
- Modified surfaces of TiN reinforced alloys by MAO treatments show suitable features related to improved biological response. Both MAO-TH40-TiN and MAO-TH525-TiN samples achieved well-adhered coatings with a thickness between 5-10 µm. Both MAO coated samples exhibited multiscale surface porosity, and high apparent roughness. In addition, coatings have a high Ca/P ratio, between 2.7 and 3.2, which will promote the osseointegration process, and Zn content that provides antibacterial effects. All these suggest that MAO treated samples could provide a suitable environment to promote improved biological behaviour.

In order to give a more complete appreciation of the processed materials, some relevant conclusions about their tribocorrosion behaviour, derived from a collaboration work with Minho University, are included. They performed tribocorrosion tests of some alloys developed in this work. The tests were carried out in phosphate buffer solution (PBS; 0.2 g/l KCl, 0.24 g/l KH_2PO_4, 8 g/l NaCl, 1.44 g/l Na_2HPO_4) at body temperature (37 °C) against alumina ball, using a load of 1 N.

They found that as-sintered Ti12Nb alloy shows similar tribocorrosion behaviour to Ti6Al4V. The same study compared the corrosion resistance of cast and powder metallurgy (PM) Ti12Nb alloy. It was found that PM Ti12Nb alloys present better corrosion resistance than cast Ti12Nb alloys due to the fact that PM alloys exhibit a more homogeneous microstructure.

TH525-TiN and TH5Fe25Nb alloys were MAO treated, under similar conditions to those employed in this work (without ZnO NPs). Both MAO-treated alloys exhibit negligible wear damage and improved wettability than untreated samples. Hence, an enhanced biological response could be expected.

The results obtained from tribocorrosion are positive. This validates that these materials are attractive alternative candidates to produce load-bearing implants.

CHAPTER 9

Future Lines

Future Lines.

Based on the obtained results, there are some suggested studies to continue improving mechanical, wear and biological performance on more suitable β-Ti alloys for biomedical applications.

- Processing the alloys using smaller particle size of alloying elements (Nb and Fe), in order to further reduce the sintering temperature and hence, limit the excessive grain growth of the alloys.
- Evaluate elastic modulus and fatigue resistance of heat-treated alloys with heat treatment 6 (HT6: heating up 900 °C at 10°C/min, maintaining at this temperature for 6 h, followed by fast cooling at 600 °C/min), which exhibited a smaller amount and smaller size of titanium carbide precipitates, in order to validate the adequate mechanical behaviour and their reliability.
- Further tests should be performed to find the optimal conditions for reinforced alloys processing, attempting to improve interfacial bonding of reinforcement particles. After sintering, hot isostatic pressing (HIP) could be applied as an additional consolidation step for TiN reinforced alloys to reduce the porosity in the matrix and also inside reinforcement particles. This would also improve the interfacial bonding between TiN reinforcement particles and the β-Ti matrix, avoiding the particle detachment when the sample is subjected to wear.
- The high elastic modulus achieved for TiN reinforced alloys is not suitable for biomedical Ti. Nevertheless, these materials could be used as "coating" for beta-Ti alloys, improving the surface features but maintaining low-modulus in the core.
- Study dry sliding behaviour of MAO treated surfaces. Moreover, it would be interesting to perform in vitro biological tests to evaluate the osseointegration process of Ca/P rich surface; and study the Zn ion release and antibacterial effect of ZnO containing samples.
- MAO surface modification treatments carried out in this work could be used for a wide range of titanium alloys. Results obtained in the MAO treatment of TiN reinforced alloys suggest that there are no differences in the anodised areas above TiN reinforcements or above the β-Ti matrix. Since base alloys and gas nitrided samples presented the lowest elastic modulus values, it would be convenient to perform MAO treatments in these samples in order to evaluate their biological response.